Imperial College London

IMPERIAL COLLEGE LONDON

DEPARTMENT OF EARTH SCIENCE AND ENGINEERING

Novel Characterization Method of Ceria-Based Catalyst and Electrode in Solid Oxide Fuel Cells

Author:

Mengzheng Ouyang

Supervisors:

Prof. Nigel P. Brandon

Dr. Paul Boldrin

Submitted in part fulfilment of the requirements for the degree of

Doctor of Philosophy in Department of Earth Science and Engineering of

Imperial College London

March 2019

Declaration of Originality

I hereby declare that this thesis and the work reported herein was composed by and originated entirely from me. Information derived from the published and unpublished work of others has been acknowledged in the text and references are given in the list of sources.

Mengzheng Ouyang, March 2019

Copyright Declaration

The copyright of this thesis rests with the author. Unless otherwise indicated, its contents are licensed under a Creative Commons Attribution-Non Commercial 4.0 International Licence (CC BY-NC).

Under this licence, you may copy and redistribute the material in any medium or format. You may also create and distribute modified versions of the work. This is on the condition that: you credit the author and do not use it, or any derivative works, for a commercial purpose.

When reusing or sharing this work, ensure you make the licence terms clear to others by naming the licence and linking to the licence text. Where a work has been adapted, you should indicate that the work has been changed and describe those changes.

Please seek permission from the copyright holder for uses of this work that are not included in this licence or permitted under UK Copyright Law.

Preface

This dissertation is submitted for the degree of Doctor of Philosophy at the Imperial College London. The research described herein was conducted under the supervision of Professor Nigel P. Brandon and Doctor Paul Boldrin in the Department of Earth Science and Engineering, Imperial College London.

Part of this dissertation has been presented in the following publications and conference presentations:

M. Ouyang, P. Boldrin, N. P. Brandon, Methane Pulse Study on Nickel Impregnated Gadolinium Doped Ceria, ECS Transactions, 2017. 78: p. 1353-1366.

M. Ouyang, P. Boldrin, R. C. Maher, X. Chen, X. Liu, L. Cohen, N. P. Brandon, A mechanistic study of the interactions between methane and nickel supported on doped ceria, Applied Catalysis B: Environmental, 2019. 248: p. 332-340.

M. Ouyang, A. Bertei, S. J. Cooper, Y. Wu, P. Boldrin, X. Liu, M. Kishimoto, M. N. Marlow, J. Chen, X. Chen, Y. Xia, B. Wu, N. P. Brandon, Model-Guided Design of a Novel Nanofiber-Ni/Ceria SOFC Electrode Microstructure, Submitted to Energy & Environmental Science.

M. Ouyang, P. Boldrin, N. P. Brandon, Controlling TPB Length through Calcination Temperature, and its Influence on the Microstructure and Electrochemical Performance of Ni Infiltrated CGO anodes, 12th European SOFC & SOE Forum.

M. Ouyang, P. Boldrin, R. C. Maher, N. P. Brandon, The Methane Pulse Study of Impregnated Ni/CGO, 15th International Symposium on Solid Oxide Fuel Cells.

Abstract

Due to the worldwide rising awareness for environmental protection, there is a need for novel energy sources with high efficiency and low pollutant emission. Solid oxide fuel cells (SOFCs) have received more and more attention for their ability to fulfill such requirements and their fuel flexibility. Materials with mixed ionic and electronic conductivity (MIEC) have emerged to be a promising class of candidates for SOFCs' electrodes. However, due to the participation of dual-phase boundary and the resulting complex electrochemical and chemical reaction mechanism, the knowledge on the properties of MIEC materials is still insufficient. Therefore, it is difficult to quantitatively assess the relation of microstructures and performance of MIEC electrodes and efficiently improve the design strategy.

In this thesis, efforts are made on the development of characterization method for gadolinium-doped ceria anode for SOFCs, to investigate the mechanism of hydrogen and methane reaction on the electrodes and the relationship between the performance and microstructures.

A meliorated methane pulse transient experiments is first performed on impregnated Ni/CGO catalyst along with in-situ Raman spectroscopy. Through qualitative and quantitative analysis of the peaks, the mechanism of methane oxidation on Ni/CGO is revealed. Furthermore, the relationship of Ni surface area, CGO oxidation state, CGO surface oxygen with the methane uptake and carbon resistance is revealed. This implication is further applied in combined with electrochemical impedance spectroscopy in the characterization of aged Ni/CGO electrodes, to investigate the influence of aging to its performance. The influence of co-impregnation of Cu is also investigated via methane pulse transient experiment.

In the final chapter, a general approach of deconvoluting the DPB and TPB processes in MIEC electrodes is developed and applied to summarize a general design strategy for this class of materials. According to the strategy a novel structure is synthesized and shows better performance compared with conventional structures.

Table of Content

Title Page i

Declaration of Originality ii

Copyright Declaration iii

Preface iv

Abstract v

Table of Content vi

Chapter 1 Introduction and Background 1

1.1. Fuel Cell 1

1.1.1. History 1

1.1.2. Solid Oxide Fuel Cell 4

1.1.2.1. History and Recent development 4

1.1.2.2. Electrochemistry and Thermodynamics of SOFCs Operation 6

1.1.2.3 Materials of SOFC 9

1.2. Anode Materials 11

1.2.1. Conventional Cermet 12

1.2.1.1 Ni/Zirconia 12

1.2.1.2 Ni/Ceria 16

1.2.1.3 Other metal cermets 21

1.2.2 Perovskite, Double Perovskite and Pyrochlores 24

1.2.2 Other Structures 25

1.2.2.1 Impregnated Anodes 25

1.2.2.2 Other Structures 28

1.3. Characterization 30

1.3.1. Catalytic Reactivity 31
1.3.1.1 Temperature-Programmed Procedures 31
1.3.1.2 Pulse Reaction 32
1.3.2 Electrochemical Performance 33
1.3.2.1 Electrochemical Impedance Spectroscopy 33
1.3.3 Structural Techniques 36
1.3.3.1 X-Ray Diffraction 36
1.3.3.2 Raman Spectroscopy 38
1.4. Conclusion 42
Chapter 2 A Mechanism Study on by Methane Pulse 43
2.1 Methane as Fuel in SOFCs 43
2.1.1 Reactions and Mechanisms 43
2.1.2 Carbon Deposition 46
2.1.3 Implications ..... 52~~51~~
2.2 Methane Pulse on Ni/CGO ..... 54~~53~~
2.2.1 Experiment Setup ..... 54~~53~~
2.2.1.1 Powder Sample Preparation and Characterization ..... 54~~53~~
2.2.1.2 Powder Analysis ..... 55~~54~~
2.3.1.3 In-situ Raman Spectroscopy ..... 57~~56~~
2.2.3 Data Collection and Analysis ..... 59~~57~~
2.2.3.1 Mass Spec Calibration ..... 59~~57~~
2.2.4 Results and Discussion ..... 60~~58~~
2.2.4.1 Morphology and Crystallinity of Impregnated Ni/CGO ..... 60~~58~~
2.2.4.2 Mechanism Indication of Methane Pulse Experiment ..... 62~~60~~
2.2.4.3 Methane Pulse with In-Situ Raman Spectroscopy ..... 68~~67~~
2.2.4.4 Re-oxidation of Ceria by Steam ..... 75~~74~~

2.3 Conclusions and Implications....8079
Chapter 3 Ageing Studies of Impregnated Ni/CGO Anodes....8381
3.1 Introduction....9381
3.2 Experimental....9583
3.2.1 Sample Preparation....9583
3.2.2 Symmetrical Cell Analysis....9684
3.2.3 Powder Structure Characterization....9785
3.2.4 Powder Catalytic Activity Analysis....9785
3.3 Results and Discussion....9886
3.3.1 Morphology Change....9886
3.3.2 Ageing of Ni/CGO Symmetrical Cells....9987
3.3.3 Ageing of Ni/CGO powder....10391
3.4 Conclusions....10795
Chapter 4 Methane Pulse to Investigate Catalytic Performance of Different Materials....8397
4.1 Variation of Impregnated Ceria Based Anode Materials....8397
4.2 Experiment....8498
4.2.1 Preparation of Ni-Cu and Cu/CGO anodes....8498
4.2.2 Powder characterization of Ni-Cu and Cu/CGO....8498
4.2 Investigation of Cu/Ni Co-impregnated CGO by Methane Pulse....8598
4.2.1 Methane Pulse....8598
4.2.2 Raman Spectroscopy....88102
4.4 Conclusion and Implications....91105
Chapter 5 Model Guided Design of Ni/CGO Fibre Electrode....109107
5.1 Background....109107
5.1.1 Setup and Control of Fibre Morphology....109107
5.1.2 Recent Development of Electrospinning in Fuel Cells....111109

5.2 Materials and Methods 112110
5.2.1 Fabrication of Fibre-Matrix-Structure (FMS) Ni/CGO Symmetrical Cells 112110
5.2.2 Fabrication of Impregnated Ni/CGO Symmetrical Cells 114111
5.2.3 Fabrication of Cermet Ni/CGO Symmetrical Cells 114111
5.2.4 Morphology Characterization 114112
5.2.5 Definition of DPB Boundary weighted by distance to nickel 115113
5.2.6 Electrochemical Modelling 117114
5.2.7 Electrochemical Characterization of the Symmetrical Cells 120117
5.3 Results and Discussion 120117
5.3.1 Contribution of DPB and TPB on Conventional Electrodes 120117
5.3.1.1 EIS and Morphology of Conventional Electrodes 120117
5.3.1.2 Decoupling DPB vs TPB contribution via modelling 124121
5.3.1.3 The influence of electron conductivity 126123
5.3.1.4 The Contribution of DPB vs TPB and Implications 126124
5.3.2 Characterization of Novel Structured Ni/CGO 128126
5.3.2.1 Performance of FMS Ni/CGO Anode 128126
5.3.2.2 Microstructural and Electrochemical Characterization of FMS Ni/CGO 130128
5.3.2.3 Performance Stability during Degradation 135133
5.3.2.4 Implications from the Pseudo-2D Model for FMS Electrode Optimisation. 137135
5.4 Conclusions 139137
Chapter 6 Conclusion and Future Prospects 141139
6.1 Conclusion 141139
6.2 Future Prospects 144141
Reference 147144
Appendix A List of abbreviations and symbols 163162
Abbreviations 163162

Symbols ..... 165~~164~~

Appendix B List of Figures ..... 168~~167~~

Appendix C List of Tables ..... 175~~174~~

Acknowledgement ..... 176~~175~~

Chapter 1 Introduction and Background

As the world approaches the middle decades of the 21st century, the environment has been raised as a major problem that is threatening the wellbeing of human kind. A great part of harmful and greenhouse gases, particularly carbon dioxide (CO_2) carbon monoxide (CO), oxides of sulfur (SO_x), oxides of nitrogen (NO_x), and ozone (O_3) come from the emissions from our present energy structure, in which combustion of fossil-based fuel provides >90% of energy in the world. Feasible ways to reduce the air pollution include: 1. Developing new sources of low carbon energy; 2. Enhancing the energy efficiency of the energy sources we currently have. Fuel cells are proved to be a promising solution for both options.

1.1. Fuel Cell

1.1.1. History

Fuel cells are a type of energy conversion device that convert the chemical energy in fuels directly into electricity. First invented by Sir William Grove in 1839 [1], fuel cells were put to application in the 1960s as the power source for National Aeronautics and Space Administration (NASA)'s space flights, and participated in a series of space projects. In the late 1980s, the interest in fuel cell research grew significantly due to the global trend of emission reduction. Until now, thousands of publications have been produced to deal with the complex questions in science and engineering related to this technology. Fuel cells exhibit several intrinsic advantages: 1. High specific energy density; 2. High energy conversion efficiency; 3. Silent operation compared with fossil fuel engines; 4. Lower pollutant emission, for hydrogen-fueled fuel cells, the only product is water.

A schematic diagram of a fuel cell with an oxygen ion conducting electrolyte is shown in figure 1.1.1. A fuel cell single cell consists of two electrodes: cathode and anode, and an electrolyte sandwiched in between. The cathode, also known as the air electrode, is where oxygen combines with electrons to form into oxygen ions that are transported into the electrolyte. The anode, also known as the fuel electrode, is in contact with fuel gas; oxygen from the cathode reacts here with the fuel gas and generates electrons. If the fuel is hydrogen, then water will be produced. The electrolyte is a dense insulated layer separating air/oxygen and fuel gas. The electrolyte can be oxygen or proton conductive to provide reactants for

either anode or cathode. The electrons are conducted around an external circuit for application. The overall reaction for a hydrogen fueled fuel cell is the oxidation of hydrogen to water.

There are five major types of fuel cell being developed, which differ from each other mainly by their electrolyte. Their name, operation condition and major pro and cons are listed in table 1.1.1.

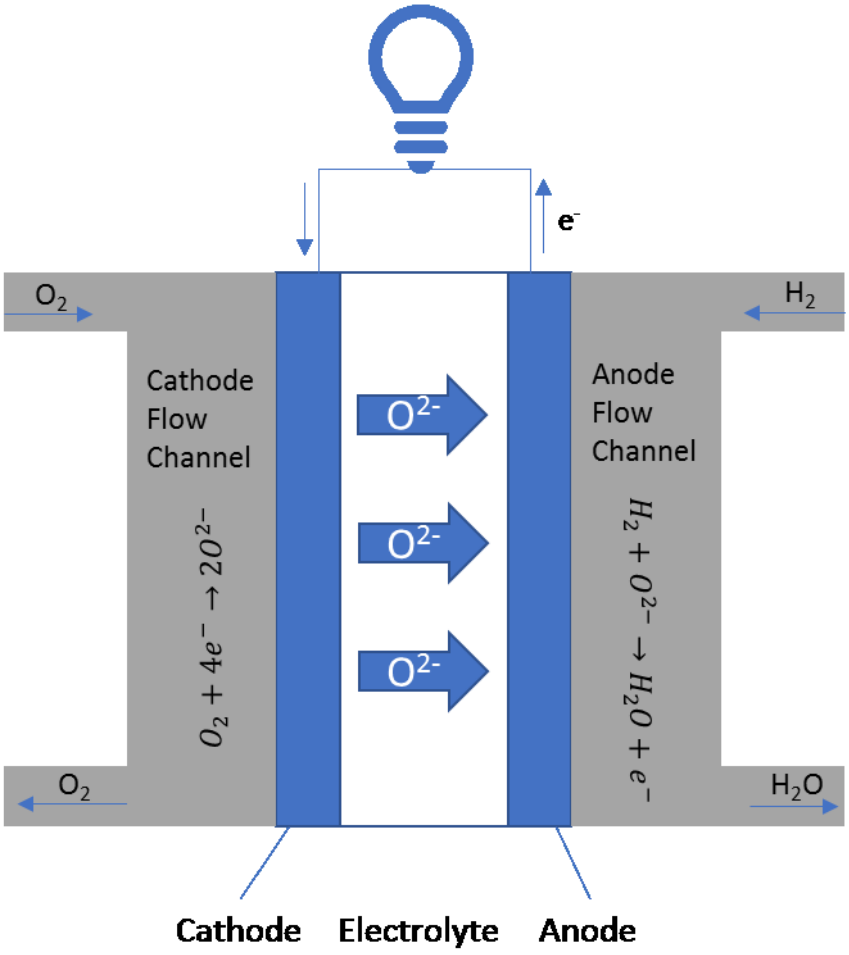


Figure.1.1.1 Schematic diagram of a fuel cell single cell with an oxygen ion conducting electrolyte

Table. 1.1.1 Features, pro and cons, and major applications of different types of fuel cells.

Fuel Cell Types	Operation Temperature	Electrolyte	Pros & Cons	Applications
Phosphoric acid fuel cell (PAFC)	150-240 ℃	liquid phosphoric acid	Can tolerate a variety of fuels and fuel impurities; low power density; moderate operating temperature	stationary power generators
Alkaline fuel cell (AFC)	25~250 ℃	aqueous alkaline solutions	Low Cost, Low operating temperature; CO_2 acts as a poison	Generators on Space Shuttles, Waste water treatment
Molten carbonate fuel cell (MCFC)	600-700 ℃	molten carbonate salt	Fuel flexibility, low cost; High operating temperature, molten salt corrosion	large-scale CHP (Combined Heat and Power), CO_2 separation
Solid-oxide fuel cell (SOFC)	500-1000 ℃	thin ceramic membrane	Precious-metal free fuel flexibility, high efficiency; High operating temperature	large to micro-sized CHP systems, APUs (auxiliary power units)

The solid oxide fuel cell (SOFC) stands among these types because of its highest tolerance to various types of fuel, high power density and high energy conversion efficiency on hydrocarbon fuels.

1.1.2. Solid Oxide Fuel Cell

1.1.2.1. History and Recent development

Solid-oxide fuel cells were first invented in 1853 by Gaugain who made the discovery of solid electrolytes. In the 1940s Baur [2] and his colleagues applied Y_2O_3 doped ZrO_2 (YSZ) in fuel cells. Later, in the late 1950s SOFCs drew a lot of attention, and a paper from scientists of Westinghouse Electric Corporation was published in the early 1960s announcing fuel cells with thin layer YSZ as electrolyte [3]. Later patents were filed using innovative cell designs such as planar and tubular cells [4]. This is believed to be the origin of modern SOFCs. ZrO2-based materials remain the most common electrolyte material nowadays.

SOFCs, together with PEMFCs have received significant attention among fuel cell systems, for their high efficiency, and simplicity in installation. However, PEMFCs' low operating temperatures limit their catalysts to precious metals such as Pt, and efforts to find a substitute have not yet been successful. Also, Pt is vulnerable to impurities in hydrogen, requiring high-purity H_2. In contrast, SOFCs can utilize ceramics with relatively abundant metals (such as Ni) as a catalyst, and are more tolerant to varieties of fuels[5]. With a high operating temperature, hydrocarbons can be internally reformed inside the cell. The use of hydrocarbons further lowers the cost for SOFCs because most of hydrogen is currently converted from hydrocarbons such as natural gas. A study by Winkler in 2002 states that direct use of hydrocarbons can enhance the energy efficiency by 5-7%[6]. Nowadays the combination of SOFCs and gas turbine (GT) can enhance the overall electricity efficiency to as high as 90% (including both heat and power supply)[7].

SOFCs can work in both fuel cell mode and electrolysis mode. Excess energy can be stored in chemicals (eg. H_2, CO, CH_4) through SOEC, and when needed, can be converted to electricity again [8]. Such grid-scale storage systems will be needed to match fluctuations in supply and demand when renewables grow to comprise a large proportion of total electrical grid generation capacity.

SOFCs have several advantages over other fuel cell systems, such as fuel flexibility, high power density and energy conversion efficiency on hydrocarbon fuels. Despite this, there are still some major challenges regarding material science inhibiting the commercialization of SOFCs [4]:

Poisoning of anode from hydrocarbon fuel or impurities[9]: Carbon easily deposits on nickel based catalysts through the pyrolysis of hydrocarbons or disproportionation of CO, and further blocks the reaction sites or destroys the structure. Also, nickel is vulnerable to H_2S impurities as it will strongly adsorb on the nickel surface and block the reaction sites. This reduces the working lifetime of electrodes and forces the cells to be restarted more frequently, increasing operational cost. Also, such poisoning prevents the direct usage of carbon and sulphur-containing fuels, resulting in additional costs for fuel pre-treatment.

Insufficient O^{2-} conductivity of the electrolyte hinders the electrochemical reaction rate. Large efforts have been made in the discovery and modification of ion conducting electrolyte materials in recent years. Yet electrolyte resistance is still one of the main losses in an SOFC.

The high operation temperature of SOFCs causes an increase in cost and limits the materials selection for components, impacting commercialization such as in vehicle's and in-home mCHP. Traditionally, the operation temperature of SOFCs is 800-1000°C. With the development of electrolytes such as YSZ, CGO and La(Sr)Ga(Mg)O_3 (LSGM), the operating temperature is now below 800 °C[10]. However, it would be desirable for the operating temperature to be lowered further.

There has been a huge amount of research aiming at dealing with these matters on material aspects, including new materials discovery [11-14], modifying fabrication methods[15-18], developing numerical models[19-21], etc. The optimisation of electrode materials involves modifying the particle size, morphology, and interactions of different materials. Different strategies have emerged so it would be very useful to examine them. The research focus of this thesis sits in the investigation of reactions on the anode of SOFCs, especially hydrocarbons on impregnated Ni/CGO anodes. This research is looking to explore the kinetics and electrochemistry behind the catalysis, the location, rate determining step, and selectivity of reactions to provide guidance on how to enhance the performance of anodes by manipulating the microstructure, and how the microstructure changes with fabrication method. Therefore, this review will contain two main aspects of the literature: Studies in the fabrication of SOFC anodes, and studies into the kinetics of fuel oxidation in SOFCs.

1.1.2.2. Electrochemistry and Thermodynamics of SOFCs Operation

In the case of an SOFC, an oxygen ion conducting electrolyte is usually used. Oxygen reduction happens at the cathode:

$$O_2 + 4e^- \rightarrow 2O^{2-}(s)$$

The anode catalyses the oxidation of various fuels:

For hydrogen: $H_2(g) + O^{2-}(s) \rightarrow H_2O(g) + 2e^-$

For carbon monoxide: $CO(g) + O^{2-}(s) \rightarrow CO_2(g) + 2e^-$

For methane: $CH_4 + 4O^{2-} \rightarrow CO_2 + 2H_2O + 8e^-$

The electrons produced are carried through the current collector to an external circuit and then back to the cathode to participate in oxygen reduction. The oxidation of fuel is assumed to happen on the triple phase boundary (TPB) of fuel, catalyst and ion-conducting scaffold[22, 23]. However, with the emergence of mixed ion and electron conducting anode materials, several studies revealed that, in the case of hydrogen, the reaction zone is then extended to the double phase boundary (DPB) of fuel and scaffold[24, 25], and that the metal phase primarily acts to improve the electron conductivity while the H_2 oxidation pathway is dominated by electrocatalysis at the oxide/gas interface[24]. This will be discussed in detail later.

The potential of a cell is given by the Nernst equation, exemplified by the case where hydrogen is the fuel:

$$E = E_0 - \frac{RT}{nF}\ln\frac{P_{O_2\ Cathode}}{P_{O_2\ Anode}}$$

Where E_0 is the standard cell potential, which indicates the reaction potential measured at standard conditions (1atm, 1M, 25°C), for hydrogen oxidation, E_0 is 1.23V [26]. R is the universal gas constant, T the absolute temperature in K, n is the charge transfer number per number of oxygen molecules reacted, and F is the Faraday constant, 96,485 C/mol.

The actual cell potential during operation is always lower than the theoretical one because of the polarization or irreversible losses in the cell. Such losses can usually be attributed to

three main parts: Ohmic polarization, activation polarization, and concentration polarization. An ideal i-V curve of an SOFC is shown in figure 1.1.2, in which i represents cell current density and V represents cell voltage.

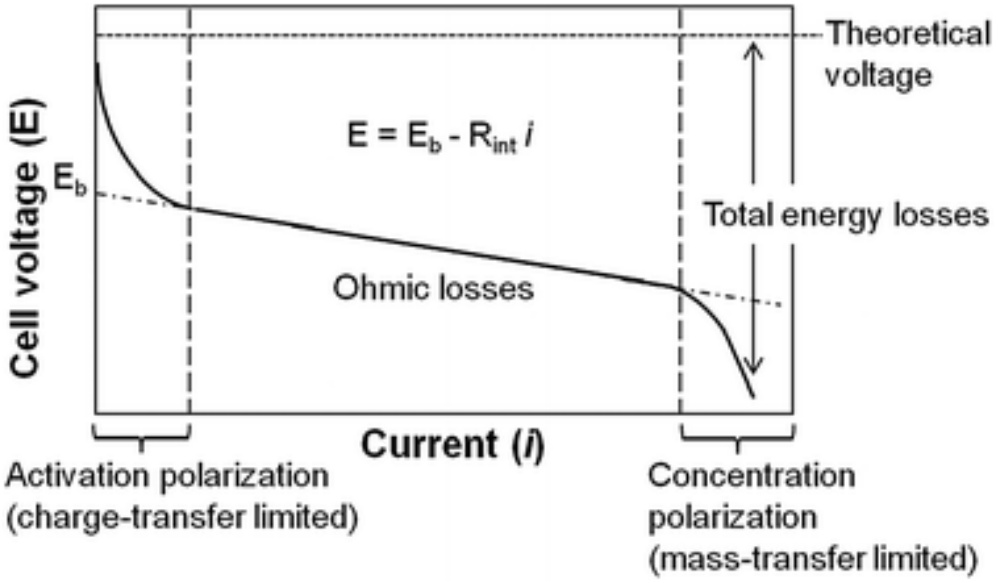


Figure. 1.1.2 An ideal i-V curve of SOFC including activation polarization, Ohmic loss and concentration polarization [Reproduced with permission from [27]]

Ohmic polarization is due to the Ohmic resistance from the bulk of electrodes and electrolyte, and their interfaces. It accounts for both electron and ion conductivity, but in SOFCs is normally dominated by the resistance of the electrolyte. Enhancing the electron and ion conductivity of electrodes or enhancing the ionic conductivity of the electrolyte will reduce Ohmic polarization. Also, the Ohmic polarization (η_{Ohmic}) is proportional to the current flowing through the cell. In which R_{elec} and R_{ionic} are the Ohmic resistance of electron conduction and ion conduction process, respectively.

$$\eta_{Ohmic} = i(R_{elec} + R_{ionic})$$

The activation polarization is the voltage loss associated with the activation energy for charge transfer reactions. It is described by the Butler-Volmer equation:

$$i = i_0(e^{\frac{\alpha n F \eta_{Act}}{RT}} - e^{\frac{(\alpha-1) n F \eta_{Act}}{RT}})$$

The equation gives the current density *i* as a function of activation polarization η_{Act}. In which α, the symmetry factor, varies with the nature of electrochemical reactions. The exchange current density i_0 gives the equilibrium rate at which reactant and product species are exchanged in the absence of an activation polarization, and is a measure of the electrodes electrocatalytic activity. At equilibrium, the reactants and products of an electrochemical reaction are in dynamic equilibrium, so that the forward and backward currents are the same. α and i_0 alters with the nature of electrochemical reactions, higher α and i_0 indicates a facile reaction. From the equation we can see that with larger η, the current can be enhanced to a higher degree by increasing i_0.

i_0 is expressed as follows:

$$i_0 = \mathrm{nF}c_R^* f_1 e^{-\frac{\Delta E}{RT}}$$

ΔE is the activation energy in the equilibrium state, c_R^* is the concentration of reactants and f_1 is the probability of activated species changing to the product. i_0 is increased and therefore activation overpotential is minimized with the following factors: increase in reactant concentration, which correlates to higher fuel and oxygen partial pressure; decrease in activation barrier, e.g. from better catalysts; and increase in temperature. The effective i_0 can also be increased by increasing the number of reaction sites by increasing the TPB or DPB.

Concentration polarization is the voltage loss caused by the concentration gradient in an electrode. It is described below:

$$\eta_{conc} = c \ln \frac{i_L}{i_L - i}$$

In which c is a constant, i is the measured current density and i_L is the maximum current density when the gradient of reactant concentration is at maximum.

$$i_L = nFD^{eff} \frac{c_0}{h_{ed}}$$

D^{eff} is the effective diffusion coefficient of the given gas in electrode, c_0 is the initial bulk reactant concentration and h_{ed} is the electrode thickness. The concentration polarization has a significant effect especially at high current density.

1.1.2.3 Materials of SOFC

The requirement for the materials used in different parts are different. For anode and cathode, because they are where the electrochemical reactions happen, they need to satisfy the following requirement: 1. High electron and oxygen ion conductivity; 2. Minimum CTE (coefficient of thermal expansion) mismatch with other components of SOFC; 3. Good chemical capability with electrolyte and interconnect; 4. Sufficient porosity for gas diffusion; 5. High catalytic activity for activation of fuels oxidation or oxygen reduction; 6. Good stability under reducing (anode) or oxidizing (cathode) atmosphere.

Therefore, composite materials are widely used as the anode of an SOFC, such as Ni/ceria, Ni/zirconia. In these materials, metal serves as the electron conducting phase and ceramic mainly as the oxygen ion conductive phase. TPBs, and/or in MIECS the double phase boundary (DPB) of pore-ceramic, are the sites of electrochemical reaction. Anode materials for SOFCs will be reviewed in more detail later.

For cathodes, noble metal/zirconia or ceria were first used for oxygen reduction[28]. perovskite structured materials with a general formula ABO_3 have emerged as the cathode of SOFCs since the 1960s and large amount of research has been done on this class of materials. Now it has become the most investigated class of SOFC cathode materials. To increase oxygen ion conductivity, the A-site or B-site of perovskites are usually doped with acceptor cations such as Sr^{2+}, Ca^{2+}, and Ba^{2+} or the reduction of Mn^{3+} (Co^{3+}) to Mn^{2+} (Co^{2+}) results in the formation of oxygen deficient perovskites. Other perovskites include LSCM (Sr, Co doped $LaMnO_3$), LSCF (Sr, Co doped $LaFeO_3$), LNO ($LaNiO_3$) and so on.

The electrolyte in an SOFC is the part separating the gases and conducting oxygen ions or protons between anode and cathode. The electrolyte for SOFCs needs to satisfy the following requirements: 1. High oxygen ion conductivity; 2. Low electron conductivity; 3. Chemical compatibility with electrode materials; 4. Small CTE mismatch with electrodes; 5. Sufficient mechanical properties; 6. Chemical and mechanical stability under high temperature; 7. Chemical stability under both reducing and oxidizing atmosphere. Fluorite-structured materials are widely used as the electrolyte of SOFCs. The most common examples being doped ZrO_2 and CeO_2. ZrO_2 is usually doped with 8% yttrium oxide to stabilize it in fluorite phase from room temperature to 2500 °C[29]. On the other hand, CeO_2 can maintain its

fluorite phase from room temperature to operation temperatures of ~500-700°C. CeO_2 is usually doped with different lower valent cations such as Gd^{3+}, Eu^{3+}, Sm^{3+} to increase its oxygen ion conductivity[30]. The structure and modification of ceria will be discussed in a later chapter in detail.

A SOFC stack is composed of tens or hundreds of SOFC single cells. The interconnect is the part that provides electricity connection between single cells in the stack. The requirement for the materials for interconnects are listed below[4, 31]: 1. High electron conductivity at SOFC working temperature (500-1000°C); 2. High mechanical strength as the interconnect is also a loading-bearing structure in an SOFC stack; 3. Chemically and mechanically stable in both oxidizing and reducing atmosphere, and also resistive to chemical reaction with all sorts of fuel compositions (hydrocarbon, hydrogen sulfide, etc.) at working temperature for the whole lifetime of a SOFC stack (>20000 h); 4. Matched CTE with other parts of SOFC stack; 5. Low cost in material and manufacturing. Materials for interconnects can be selected from both ceramics and metallic alloys. Ceramic materials have better stability in oxidizing condition, and also possess better CTE match with other part of SOFC due to the similar CTE in ceramic materials. However, ceramic interconnects can work only at higher temperature (>600°C), and are expensive and difficult to manufacture. The most common ceramic interconnect is $LaCrO_3$. Metallic alloys have lower cost and better availability than ceramic interconnects and can work in lower temperature and therefore they are favored over ceramic interconnects where possible. Among metal alloys, Fe–Cr based alloys, Cr-based alloys, Ni(Fe)–Cr-based heat resistant alloys, austenitic and ferritic stainless steels are being extensively used as interconnect materials.

Sealing prevents the leakage of gas from anode and cathode chambers. It is important in planar design SOFC but can be effectively eliminated in tubular or other special shaped SOFCs. The materials for sealants need to possess the mechanical and chemical stability at the condition similar with interconnects but must be intrinsically insulating. Glass, glass-ceramic, and mica-based composites are widely used as the sealant of SOFC. Their detailed review can be found in the literature and will not be shown here[32].

Figure 1.1.3 is a comprehensive list of materials that have been used in each component of an SOFC.

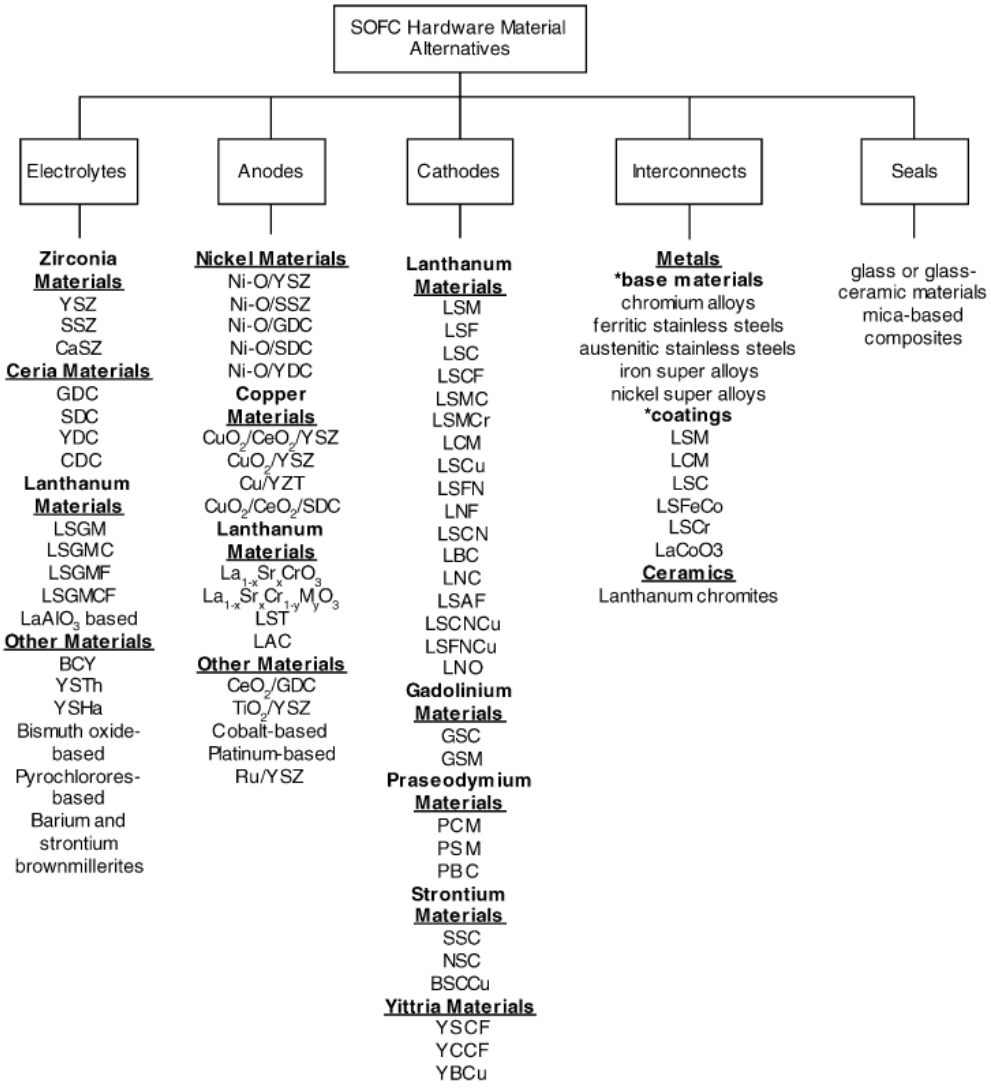


Figure. 1.1.3 Comprehensive lists of materials used in each component of an SOFC [Reproduced with permission from [33]]

1.2. Anode Materials

The oxidation of hydrogen on anode of SOFC mainly takes place at TPB (for zirconia) or dual phase boundary (DPB) (for perovskite, ceria). It can be written as:

$$H_2(g) + O_O^{\times} \rightarrow H_2O + 2e^{-} + V_{\ddot{O}}$$

In which $O_O^{\times}$ is the lattice oxygen from oxygen ion conducting ceramic, $V_{\ddot{O}}$ is the oxygen vacancy site after H_2 oxidation. Electrons were conducted out from the reaction site by the metal phase or mixed conducting ceramic phase. The oxygen conduction, H_2 diffusion in pores, H_2 surface adsorption, and H_2 charge transfer reaction all contribute to the anode polarization.

Therefore, the performance of the anode is extensively dependent on the microstructure, including porosity, grain size, particle morphology, surface area, TPB, DPB between phases and so on.

YSZ, doped-ceria and perovskites are three classes of materials commonly used as the oxygen ion conducting phase for anode for SOFCs because their superior ion conductivity. Also because of their ion conductivity and lack of electron conductivity, these materials are usually modified with metals to make a composite in order to satisfy the requirements for anodes. Among the choice of electron conducting phase, nickel has received the most attention, due to its high catalytic activity towards hydrogen oxidation and relatively low cost.

1.2.1. Conventional Cermet

A cermet is a composite material composed of ceramic and metal. Due to its simplicity of manufacturing, good stability and reasonable performance, cermets made by mechanical mixing of ceramic and metal phases are now the most commonly used structure as SOFC anode.

1.2.1.1 Ni/Zirconia

With increasing temperature, zirconia goes through two phase conversion processes[34]. At room temperature, it is stabilized as monoclinic structure which transforms to tetragonal at 1170 °C. Then it will transform to a cubic fluorite structure which is desired for application in SOFC at a high temperature of 2370 °C. In order to be used in SOFCs, YSZ needs to be doped with acceptor ion to be stabilized at cubic fluorite structure from room temperature to operation temperature (<1000 °C). Y_2O_3 stabilized ZrO_2 (YSZ) is the most commonly used doped zirconia, in which 8 mol% YSZ shows the highest oxygen ion conductivity[35]. Ni/YSZ cermets were first developed by Spacil[36]. They are now the most common SOFC anode materials and have been extensively studied.

Sc_2O_3 stabilized ZrO_2 (ScSZ) is another promising type of doped zirconia and has now attracted more and more attention. The Sc_2O_3-ZrO_2 composite above 5mol.% Sc_2O_3 content show a tetragonal structure. By doping with over 9 mol% Sc_2O_3, ScSZ is stabilized in a cubic fluorite phase. 11 mol% ScSZ shows double the oxygen ion conductivity than 8YSZ at 850 °C[37], it has high oxygen ion conductivity across a wide range of pO_2 and operating temperatures, and it is suitable for application in low to intermediate temperature (500-

800 °C) SOFC[38]. Gu's[39] work applied ScSZ as the anode as SOFC working at 600 °C, and shows a decent 0.06 W/cm^{-2} power density.

Different Structures and Fabrication Route

The most common means to fabricate Ni-YSZ cermets is the mechanical processing route[40]: first of all, NiO and zirconia powders are mixed together by either planetary or attrition milling; then the mixture is dispersed in an ink with solvent and binder followed by screen printing on an electrolyte pellet (for electrolyte-supported cells); after that, the printed cell is sintered to make a well-attached anode layer; finally, the NiO is reduced under a reducing atmosphere. Sato[41] used high-speed attrition equipment to process NiO/YSZ mixtures. High shear and compression force exerted during the milling resulted in nano-sized particles (NiO 160 nm, YSZ 75 nm) and a narrow size distribution. Additionally, chemically bound hetero-interfaces were formed between NiO and YSZ phases and these contributed to smaller polarization and better long-term stability. High-energy ball-milling (HEM) is also used for synthesizing Ni/YSZ[42]. Compared to conventional ball milling, HEM results in a much smaller average particle size (270 nm vs 700 nm) and thus have greater TPB density, leading to much smaller impedance and better performance. Mechanical processing is favoured for its low cost and simplicity. However, conventional mechanical mixing will not achieve a uniform distribution of Ni in the ceramic[43].

The fabrication of Ni/doped zirconia cermets by wet chemistry routes are also widely investigated. Combustion methods are widely used for synthesizing ultrafine particles[44]. These utilize the exothermic nature of reactions propagating in a self-sustained manner at a relatively high speed. Also, combustion is a good way to dope equivalent or heterovalent ions into the crystal lattice, making it an ideal method for ion-conducting materials. Ni/YSZ cermets have been synthesized by citrate/nitrate combustion[45] and Ni/CSO anodes (samarium doped ceria) by the urea-combustion route[46, 47], by way of two examples. The as-prepared samples exhibit smaller particle sizes (~50 nm) and high surface area compared to conventional mechanical processes.

Co-precipitation is a facile wet chemistry route to synthesize nano ceramic particles. The atomic-level mixing of species in solution can be maintained by such methods therefore it is ideal to prepare doped nano particles. Ni/YSZ is synthesized by co-precipitation with ammonia

[48]. The sample shows more homogenous distribution of NiO phases, narrower particle size distribution, and better conductivity with same Ni amount than samples prepared by conventional solid-state reaction. Also, various anode materials have been synthesized by precipitation, proving it to be a method of wide applicability[49-52].

The Pechini process is a type of sol-gel method. In this method metal salts are introduced into a citric acid solution with ethylene glycol. Then the excessive liquid is dried at controlled pH to produce a homogenous gel-like system in which ions are uniformly distributed. Finally, the gel is calcined and the desired sample is obtained. Morphology and sizes of particles can be controlled by changing the citric/metal ratio, drying rate and calcination conditions, [53, 54]. The process has been applied to synthesizing Ni/YSZ[55, 56], ceria[57, 58], and perovskite [59, 60] based anode materials.

The Electrochemical Reaction and Degradation on Ni/Zirconia Anode

The reaction mechanism of fuel gas on Ni/doped zirconia electrodes has been extensively studied. When hydrogen is used as fuel, Ni/YSZ patterned electrode was prepared by Vogler and Bieberle[61, 62] by dc magnetron sputtering. Surface processes on nickel and YSZ including hydrogen spill-over, TPB charge transfer reactions, and water desorption were investigated by impedance under different bias and a quantitative elementary kinetic model was developed. Four rate-determining steps at different water concentrations were determined in this work: hydrogen spill-over to oxide ions, water association on YSZ, water desorption from YSZ, and surface diffusion of YSZ-adsorbed hydroxyl ions. Another pattern cell study by Mizusaki[63] found that the electrode interface conductivity is proportional to the length of TPB, and the rate of the electrode reaction is essentially determined by the reaction process on the Ni surface close to TPB. Tanner's work[64] has similar conclusions, suggesting that as long as there is sufficient porosity so that gas transfer is not limiting, the electrode performance will increase as the TPB density becomes larger. This validate the advantage of wet chemistry method, as it can make electrodes with finer structures.

The degradation of Ni/zirconia electrodes after long-term operation is mainly due to sintering or structure failure of nickel due to its higher mobility than zirconia at operation temperature[65]. The sintering of nickel happens by diffusion of vacancies, particles and grain boundaries, driven by minimisation of surface free energy. Vaßen[66] developed a model that

takes into account the curvature of two neighbouring particles and describes the Ni grain growth. According to this model, due to varying gas pressures near two particles having different radius, diffusive vacancy flux will be induced, which controls the growth kinetics. The rate of nickel growth is different in dry or humid environments. Holzer[67] found that nickel coarsening on Ni/YSZ in humid environment (60 vol% H_2O, 40 vol% N_2/H_2) are very high (up to 140%/100 h) during the initial period (<200 h). At longer exposure time (>1000 h) the growth rates decrease significantly to nearly 0%/100 h. In contrast, under dry conditions (97 vol.% N_2, 3 vol.% H_2) the growth rates during the initial period are much lower (ca. 1%/100 h) but they do not decrease over a period of 2000 h. This behaviour has been described in terms of $Ni(OH)_2$ formation, which has been described to be responsible for evaporation and loss of Ni from anode as well. Ioselevich[68] found the performance loss from sintering of nickel mainly comes from the connection loss of TPBs from percolating nickel phase, and therefore loss of electrochemical reaction site.

In the case of hydrocarbons, the reforming kinetics of methane on a Ni/YSZ electrode at 800 °C including 42 reaction steps was thoroughly investigated by Hecht[69]. Restrepo[70] found the removal of carbon deposition will be more difficult with time when operating in methane and anodic polarization would supress carbon deposition when operating in methane. More works on hydrocarbon fueled SOFC will be reviewed in later chapters.

Drawback and Future Prospect

Although Ni/YSZ cermets have been developed for over forty years, there are some drawbacks yet to be overcome: 1. Reduction of NiO to Ni is accompanied with a decrease in particle volume, thus frequent redox cycling of the electrode will cause disconnect between the metal and ceramic phases, and fracture of electrodes and electrolyte, which could cause mechanical failure; 2. The thermal expansion coefficient of Ni and YSZ is different, which contributes to structural failure; 3. In order to acquire structure integrity, the preparation of the cermet involves high temperature processing (~1400 °C), which causes significant sintering and grain growth of both the Ni phase and YSZ phase[71], and high cost in terms of energy consumption; 4. the nature of a cermet will produce a lot of inactive Ni not exposed to the fuel atmosphere, and not connecting with other metal phases. As investigated in experiments and models, 30 vol% of Ni loading is required for percolation[72, 73], most of which is not contributing to TPB, nor acting as current collector; 5. Ni-Zirconia based

electrodes are susceptible to carbon deposition by hydrocarbon fuel[74]. Thus, novel fabrication methods were developed to enhance the performance of such materials, this will be reviewed in 1.2.2.

1.2.1.2 Ni/Ceria

CeO_2 shares a similar fluorite-type structure with YSZ and also has good ionic conductivity. Under reducing atmospheres, it shows mixed ionic and electronic conductivity (MIEC), about 1 S/cm at 900 ℃ at PO_2 of 10^{-18} atm. It has also been found to have catalytic activity towards various fuel oxidation reactions [75-77], including hydrogen oxidation[78] and methane oxidation[79].

With decreasing oxygen partial pressure and increasing temperature, ceria exhibits the property of an n-type electronic conductor. Oxygen vacancies form with charge compensation through two electrons, localized on trivalent cerium cations, forming polarons[80]:

$$2Ce_{Ce}^{x} + O_{O}^{x} \rightarrow V_{\ddot{O}} + 0.5O_2 + 2Ce_{Ce}^{\prime}$$

The transportation of such polarons is the origin of the electron conductivity in ceria[81].

The ionic conductivity σ_{ion} of doped ceria can be described as:

$$\sigma_{ion}T = A[V_{\ddot{O}}]exp(-\frac{\Delta H_m}{kT})$$

Where ΔH_m is the activation entropy of electron diffusion, A is a pre-exponential factor. The oxygen ion conductivity and electron conductivity of doped ceria has been thoroughly investigated, e.g. by Yahiro [82] and Wang [83]. The electronic conductivity of doped ceria is proportional to $pO_2^{-1/4}$.

The ionic conductivity of ceria is further improved by doping with heterovalent metal ions, such as rare earth metals Gd and Sm. Alkaline earth elements including Ca, Mg and Sr have also been studied. These dopants are soluble in the ceria lattice and can create oxygen vacancies to compensate charge imbalance, which can be expressed by the Kröger–Vink notation as follows:

$$M_2O_3 \xrightarrow{2CeO_2} 2Ce_M^{\prime} + V_{\ddot{O}} + 3O_O^x$$

The introduced oxygen vacancies can increase the oxygen mobility because oxygen ions migrate through vacancies.

Influence of Doping to Ni/Ceria Anode

Doping with lower valent cations is also found to decrease the volume change of ceria and improve the electronic conductivity[84]. 10 at% gadolinium doping can enhance the electronic conductivity of ceria to ~0.1 Scm^{-1} at 700 ℃, and increase the ionic conductivity to ~0.9 Scm^{-1} [85] figure 1.2.1 [86]. Samarium doping is the best concerning the enhancement of bulk mix-conductivity, followed by Pm. However Sm tends to aggregate to the grain boundary, blocking the charge transfer between grains and increasing total resistance[87]. To further increase the ionic conductivity of ceria electrodes, co-doping is used. Andersson [30] investigated the ionic conductivity change when different rare earth cations were doped into ceria. They found that the ideal dopant should have an effective atomic number between 61 (Pm) and 62(Sm) due to their appropriate ion radius. And the combinations of Nd/Sm and Pr/Gd co-doping was applied and showed enhanced ionic conductivity (figure 1.2.2). Various combinations have been tested around these radiuses and achieved good conductivity (figure 1.2.3) [84, 88, 89].

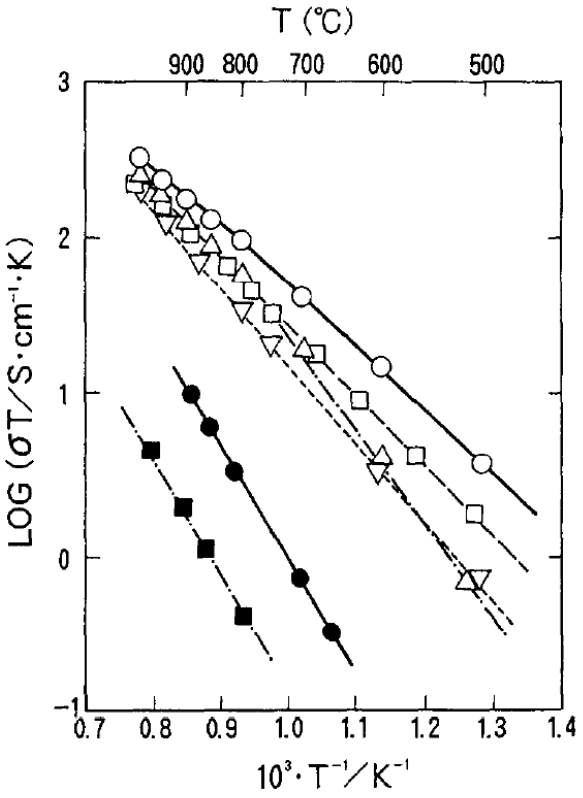


Figure. 1.2.1. Arrhenius plots of ionic conductivity of ceria based oxides doped with rare-earth oxides: (○) $(CeO_2)_{0.8}(SmO_{1.5})_{0.2}$; (Δ) $(CeO_2)_{0.8}(GdO_{1.5})_{0.2}$; (∇) $(CeO_2)_{0.8}(YO_{1.5})_{0.2}$; (□) $(CeO_2)_{0.8}$ $(CaO)_{0.2}$; (▪) CeO_2; (●) $(ZrO_2)_{0.85}(YO_{1.5})_{0.15}$ [Reproduced with permission from [86]]

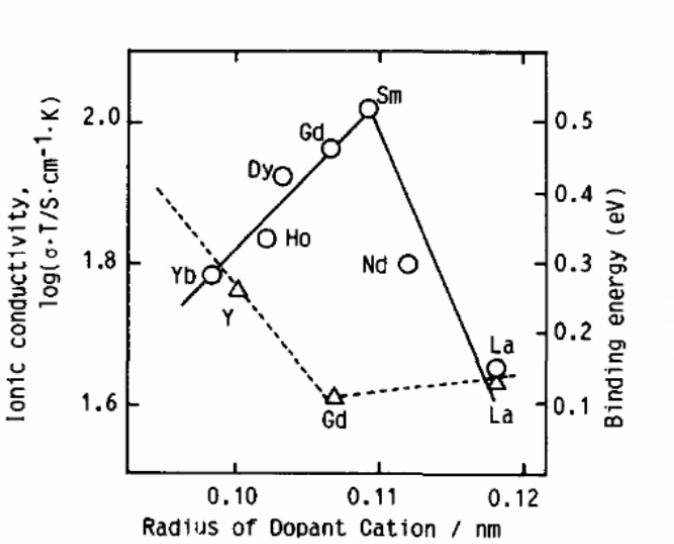


Figure. 1.2.2. Ionic conductivity of doped ceria at 1073 K against the radius of dopant cation, shown in the horizontal axis is the critical radius of the divalent or trivalent cation [Reproduced with permission from [86]]

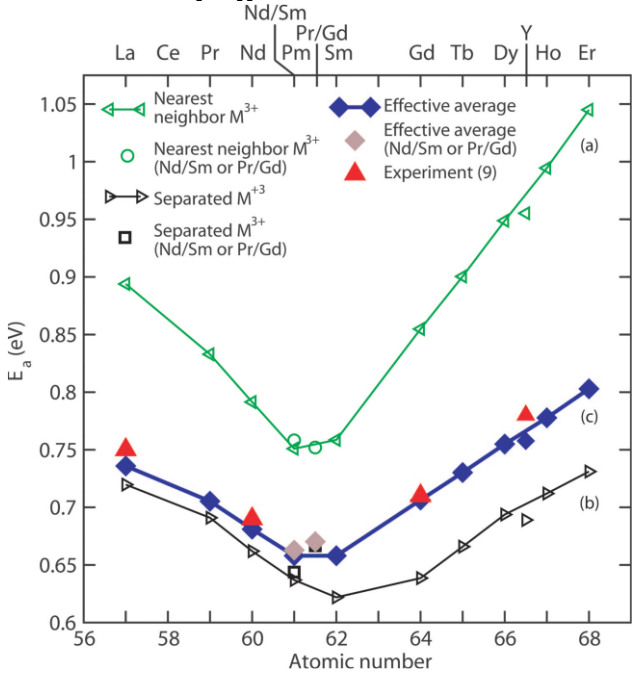


Figure. 1.2.3. E_a for dopants sitting next to each other (a) and separated from each other (b) and an effective average of the former two (c) (see text). The results were obtained within the 3*2*2 supercell, which implies a dopant concentration of 4.2%. The experimental values refer to the same doping level. Nd/Sm and Pr/Gd represent a mixture

of dopants and have been placed according to their average atomic numbers [Reproduced with permission from [30]].

CeO_2 itself is a good oxygen storage material, oxygen can be released by reduction of Ce^{4+} to Ce^{3+}. The reaction can be expressed following Kröger-Vink notation:

$$2Ce_{Ce}^{\times} + O_O^{\times} \rightarrow V_{\ddot{O}} + 2Ce'_{Ce} + \frac{1}{2}O_2$$

At elevated temperatures (above 685 °C) and low oxygen pressures, $V_{\ddot{O}}$ is joint together and formed a continuum of oxygen deficient non-stoichiometric oxides, the so-called α phase, with compositions in the range of $0 < y < 0.286$ for CeO_{2-y}[90]. Yao[91] studied the transient oxidation of CO by ceria using pulse chromatographic systems. The oxygen storage capacity (OSC) values of ceria range around 50−100 μmol O g^{-1}, and they are strongly dependent on surface area, and therefore on particle size, thermal or chemical pre-treatment, and synthetic procedure. The OSC properties of ceria can be further enhanced by compositing with metal[92] (Ni, Cu, Pt, Nb, and so on) via interaction with metal. It is found that the metal-ceria interaction leads to a build-up of a net positive charge on metal particles supported on stoichiometric cerium oxide, and a net negative charge on metal particles on reduced ceria[93]. This is believed to be the driving force of oxygen spill-over from metal to ceria or ceria to metal. Vayssilov[94] also observed the electron transfer from metal to ceria and oxygen spill-over from ceria to metal, however it was indicated that nano-structured ceria is required for such a transfer. This makes it ideal catalytic oxidation substrate in cermet anodes of SOFCs.

The Electrochemical Reaction and Degradation on Ni/Zirconia Anode

Because of the catalytic activity and MIEC property of ceria, the reaction site of hydrogen oxidation on metal/ceria can be extended away from TPBs towards the DPB of pore-ceria. Chueh[24] prepared striped Pt/ceria electrodes with controlled DPB and TPB density, and found that change of DPB affects the performance more than change of TPB, which barely influences the electrochemical reaction rate of hydrogen. Ciucci[95] built a 2-D model of a similar striped electrode and found that the electrochemical active zone can extend more than 2.5 μm from TPB to ceria-pore DPB. The importance of DPBs in ceria-based electrodes has inspired researchers to design materials structures in different ways from zirconia-based

electrodes. Jung[96] synthesized $Sm_{0.2}Ce_{0.8}O_{1.9-\delta}$ (CSO) films with highly porous and vertically oriented morphology (figure 1.2.4) which exhibited superior performance compared with traditional cermet Ni/CGO.

Ceria based electrodes also show superior tolerance to undesirable side reactions in fuel oxidation. When hydrocarbon fuel is used, carbon deposition could be greatly suppressed with ceria backbones compared with conventional YSZ. Murray[97] deposited a 0.5 µm layer of YDC ($(Y_2O_3)_{1.5}(CeO_2)_{0.85}$) on both sides of a Ni-YSZ/YSZ/LSM full cell, as the interlayer between the electrolyte and electrodes. When CH_4 was used as fuel, it achieved 0.37 W/cm^2 maximum power density which is identical with hydrogen fuelled SOFC, and no carbon deposition was observed at <700 °C. It was proposed that the catalytic activity and OSC property of ceria enhanced the methane oxidation rate. Zhang[98] performed a comparative study of H_2S poisoning on electrode behaviour of Ni/YSZ and Ni/CGO anodes of SOFCs, using EIS at 800 °C on SOFCs in pure H_2 and H_2S-H2 fuel with H_2S increasing from 5 ppm to 700 ppm. The cell voltage of Ni/YSZ anode supported SOFCs decreased from 0.61 V to 0.34 V at 200 A/cm^2 current density while the cell voltage of SOFCs with Ni/CGO anode decreased from 0.78 V to 0.72 V.

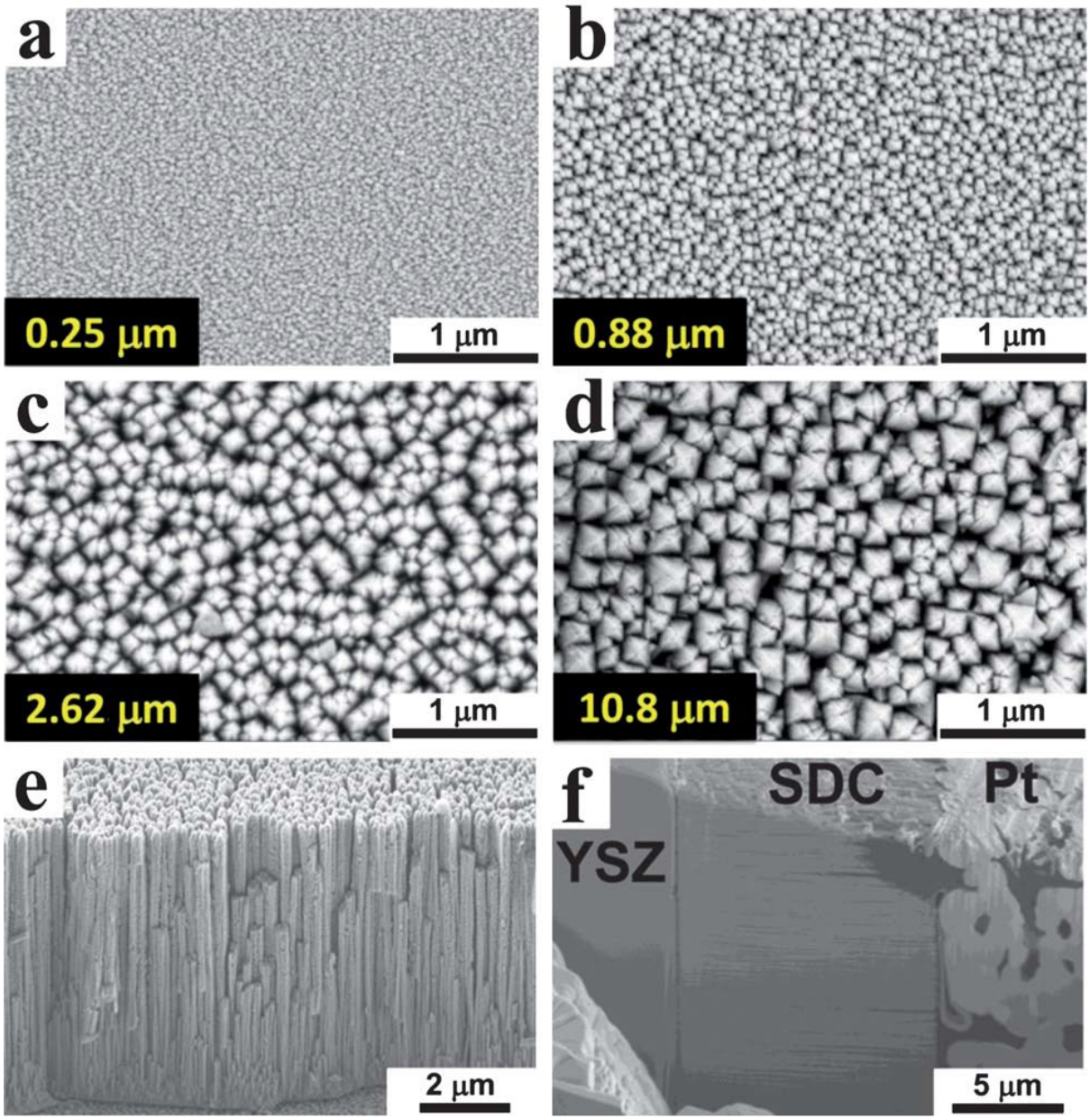


Figure. 1.2.4 Scanning electrode microscope micrographs of the porous columnar CSO films prepared in 100 mTorr O_2 at 650°C. (a–d) Top view image as a function of the layer thickness (250 nm to 10.8 mm). (e–f) Cross-section view images with the Pt current collector on top. Image (f) was obtained after focused ion beam (FIB) milling of the sample.[Reproduced with permission from [96]]

1.2.1.3 Other metal cermets

Apart from nickel and noble metals, cermets made by other metals with YSZ or ceria as backbones have also been investigated in the anode of SOFCs.

Co has similar catalytic properties for hydrogen and hydrocarbon fuels and widely used as a substitution of Ni, it has reported to have good performance in ethanol and with Ni or Cu[99, 100]. It is found the addition of Co can inhibit the dehydrogenation reaction of hydrocarbon and suppress carbon accumulation. Cu is rarely used alone because of its electrochemical inactivity and low melting point and it is commonly added along with nickel or cobalt. It has been widely reported that Cu could significantly enhance the carbon and sulphur tolerance of anodes in hydrocarbon fuels at a cost of small performance drop[78, 101]. It was found the addition of Cu can break down the surface continuity of Ni and therefore suppresses carbon deposition.

The choice of metal is broader in impregnated electrode, due to its lower sintering temperature. Cu was co-impregnated with Ni to alleviate carbon deposition [102-104] when operating with hydrocarbon fuels and to enhance the electronic conductivity. Also, the interaction between Ni and Cu enhanced the catalytic activity towards the steam reforming of methane [101, 105, 106]. The carbon and sulphur poisoning of Ni catalysts will be discussed in the chapter two. However, copper is a poor electrochemical catalyst and encounters serious sintering problem at the operating temperature of SOFCs, resulting in poor connectivity of the metal phase and a decrease in conductivity. Kaur developed a solution by adding iron into the Ni/Cu co-impregnated electrodes and gained an increased long-term stability in both hydrogen and methane[107]. Apart from Cu, Ag[108, 109], Ru[110], Rh[106], Pd[12, 102, 111], Au[112] and Sn[106, 113] have all been tested as the additive of Ni-impregnated electrodes. As with Cu, Au and Ag merely act as current collector in the electrodes and have no catalytic enhancement. Other noble metals such as Rh, Ru and Pd exhibited greater oxidation catalytic reactivity, not only to fuels, but also to impurities such as deposited carbon and sulfur, despite their high cost. In these noble metals, Pd is the most widely used and shows the best performance up to now. Rh has a high specific rate for the water gas shift reaction and it is the best catalyst for internal reforming[114]. Apart from the noble metals, Co has been found to have good activity on the oxidation of both hydrogen and hydrocarbon, similar to Ni but has less carbon deposition and better stability [100, 115, 116]. However, Co is found to aggregate on the backbones, especially on the TPB to cover the surface and block fuel transport to reaction sites.

The Discussion on the Function of Metal Phases

Although the metal phase has been long thought to play a vital role in metal-ceramic composites, Chueh [24] used Pt-patterned electrodes to test the cell with fixed TPB lengths and various DPB areas (Figure. 1.2.5). The research found that when hydrogen is used as the fuel, for an electrode using an electrochemically active ceramic such as CGO as the backbone, electrodes with smaller distance between metal electrodes perform better. This suggests that the metal phase is more of an electronic conductor than a catalyst. The research also found that the electrochemically active region of CGO is limited to the near-TPB area because of poor electronic conductivity of CGO. So that nanostructuring of the ceria oxide component, to enhance the DPB area specific surface area, may be equally or more important than the nanostructuring of metal catalysts to enhance the TPB length. The study explained the enhanced performance when non-catalytic metals such as Cu and Au were added to the electrodes, and cast light on a new study direction of electrode morphology. The role of metal phases in hydrocarbon fuels needs to be further looked into.

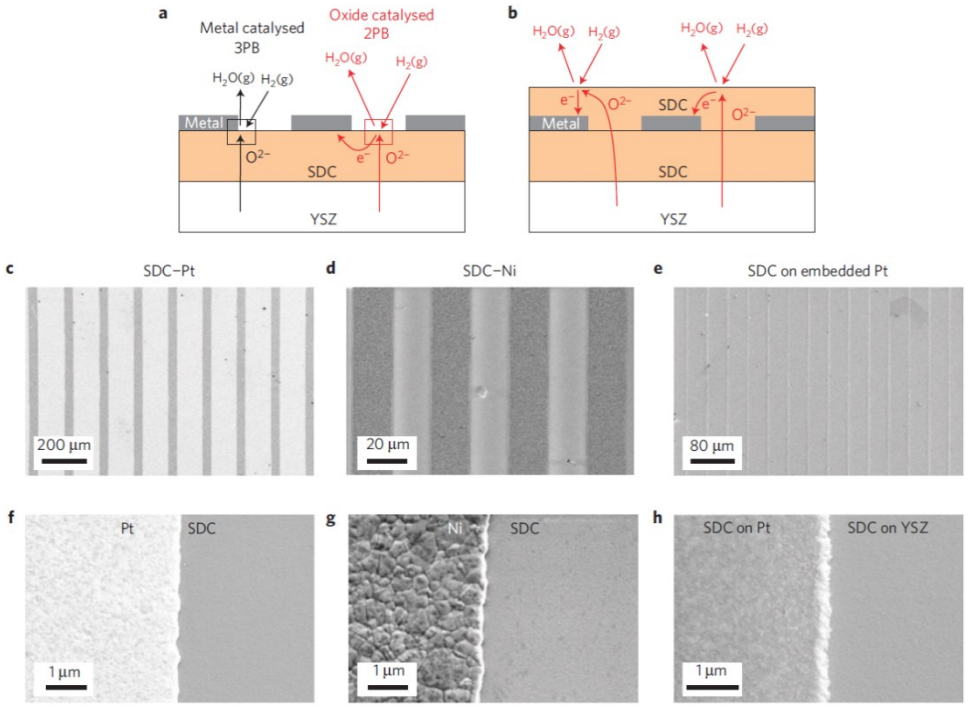


Figure. 1.2.5 Patterned metal on thin-film ceria as a model system to study competing electrochemical reactions. a. Schematic depicting the two macroscopic reaction sites present in a ceria–metal patterned electrode and the corresponding surface reaction and bulk diffusion steps. Bulk pathways involving the metal are not shown. b. Patterned electrode with an embedded current collector that eliminates contribution from the metallic phase. c–h, Planar SEM images of corresponding electrode structures, recorded

after electrochemical characterization under H_2–H_2O–Ar atmospheres at 650 ℃. [Reproduced with permission from [24]]

1.2.2 Perovskite, Double Perovskite and Pyrochlores

To eliminate sulfur and carbon poisoning, other MIEC materials have been investigated as nickel free anodes for SOFCs. Including perovskite LST ($Sr_{1-x}La_xTiO_3$)[117], LSCM ($La_{1-x}Sr_xCr_{1-y}Mn_yO_3$)[118], LSV ($La_xSr_{1-x}VO_3$)[119], double perovskite SMMO ($Sr_2Mg_{1-x}Mn_xMoO_{6-\delta}$)[120], and pyrochlore $Gd_2Ti_{2-x}Mo_xO_7$[121]. Perovskites are a class of oxides with the ABO_3 structure (figure 1.2.6). Usually a 4+ or 3+ transition metal ion are collated at the B site and a 3+ or 2+ rare earth ion or transition metal ion in the A site [122]. It is intrinsically a p-type conductor with interstitial oxygen (O_i'') as its major defect. As a result, the oxygen vacancy content in perovskites is small, even at low pO_2. However, increasing the vacancy concentration is important for enhancing the oxygen conductivity. Many research studies found that doping of A and B sites by acceptor ions[123], such as Sr, Mn can improve the oxygen conduction as well as stabilize the structure of perovskite at low pO_2. Tao [124] evaluated the effects of combining different A-cations (such as La, Sr and Ca) and different B-cations (such as Cr, Ni, Ti and Mn) in the perovskite structure. They found $La_{0.75}Sr_{0.25}Cr_{0.5}Mn_{0.5}O_3$ has comparable electrochemical performance to Ni/YSZ cermets in hydrogen fuel, and showed great carbon resistance when operating in hydrocarbon and good redox cycling performance.

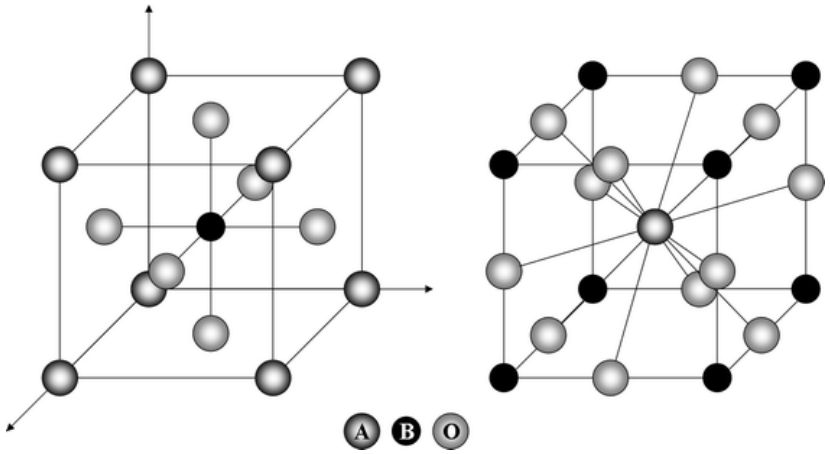


Figure. 1.2.6 Structure of an ideal perovskite ***ABX***$_3$ with ***X*** = O^{2-} (***left hand side A*** in origin; ***right hand side B*** in origin)

However, there are several disadvantages of perovskites as the anode of SOFCs: Perovskites are less active in fuel oxidation than ceria, and without TPB like in Ni/YSZ, the catalytic kinetics are slower and due to absence of metal percolation, the electron conductivity is lower than a metal/ceramic composite. Therefore, the addition of perovskite as a component to other SOFC anode materials was investigated. Chen prepared a ceria-LSCM composite anode and operated it in sulfur containing hydrogen and methane[125, 126]. It showed comparable performance with Ni/ceria cermet anodes while exhibiting better stability in methane and sulfur-containing hydrogen. Ye[127] prepared a Pd-impregnated LSCM/YSZ composite anode. The addition of Pd enhanced the performance in CH_4. When operating with LSM as cathode, the full cell showed 60 $mWcm^{-2}$ in 100% humidified CH_4, and no carbon deposition was detected after 15 h of operation.

1.2.2 Other Structures

1.2.2.1 Impregnated Anodes

Although wet impregnation has long been used in preparing heterogeneous catalysts, its application in SOFC electrodes is more recent[128]. Impregnation of metal salts into already sintered ceramic electrode scaffolds avoids the agglomeration of catalytic particles. Research has proved that the impregnation route can enhance electrode performance by modifying the microstructure [73, 129]. An infiltration process involves the precipitation and decomposition of a metal salt solution inside a porous electrode or electrolyte structure. The solution should wet the ceramic backbone to ensure good uniformity of nanoparticles, therefore the wetting of the scaffold plays an important role in the impregnation process, and it can be enhanced by lowering the surface energy of the scaffold by adding metal oxides(Figure. 1.2.7)[130]. Take Ni/CGO ($Ce_{1.8}Gd_{0.2}O_{2-x}$) as an example, first of all a drop of $Ni(NO_3)_2$ ethanol solution is placed on a sintered porous CGO scaffold and infiltrates by capillary force. Then the infiltrated electrode is calcined at 800 ℃ to decompose the $Ni(NO_3)_2$ salt to NiO nano-particles. The infiltration-deposition process is repeated until NiO reaches the desired amount. A typical infiltration synthesis is shown in Figure. 1.2.8 [129]. The infiltration can be facilitated in vacuum conditions[131]. While repeating drops of low-

concentration solution is required to achieve non-aggregated particles, it is highly time-consuming and difficult to commercialize. Therefore, there have been some efforts on developing a single-step or reduced step infiltration [132, 133]. This is an ideal way to combine the electrochemical active materials and the electron/ion conducting materials to fabricate an electrode with good performance. Also, it is possible to tune the electrode by infiltrating different catalytic species on different backbones.

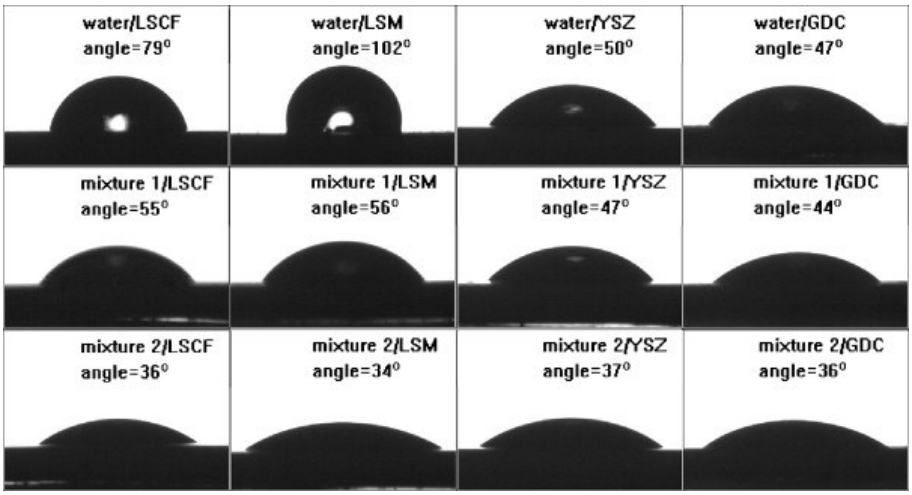


Figure. 1.2.7 Wetting angles of different SSC precursor solutions on LSCF, LSM, YSZ and CGO substrates (*note*: mixture 1 had a water-to-ethanol volume ratio of 1:0.3 and mixture 2 has a water-to-ethanol volume ratio of 1:0.6). [Reproduced with permission from [130]]

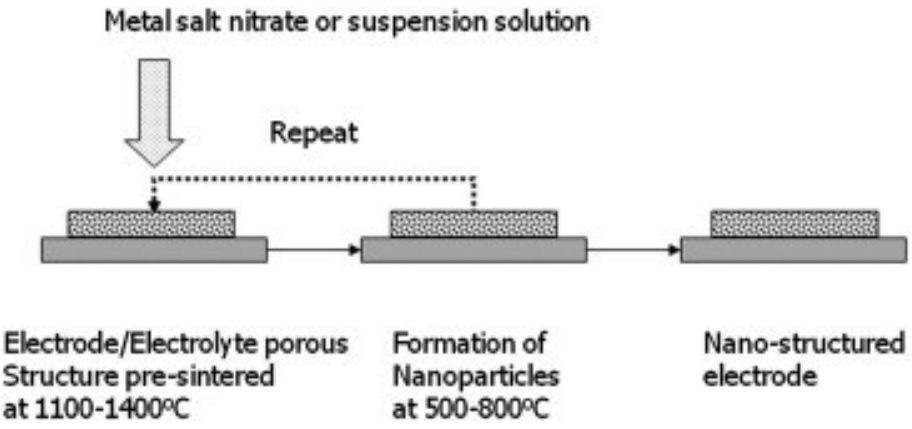


Figure. 1.2.8 Typical process for the infiltration of metal salt nitrate solution or nanoparticle suspension into pre-sintered electrode or electrolyte porous structure. [Reproduced with permission from [129]]

The impregnation process can be improved by adding additives such as urea and ethylene glycol. Urea can optimize the distribution and morphology of impregnated metals[134, 135] by forming an organic network and then through the micro-combustion reaction inside the pores[136]. Similarly, ethylene glycol and citric acid were used as chelating agents to facilitate a Pechini process in the micro-pores of electrodes [108, 137]. Electrodeposition and electrolysis deposition have also been used to accelerate the infiltration process [109, 138, 139].

The most widely used combination is ion-conducting backbones with infiltrated electron-conducting nanoparticles exemplified by Ni impregnated YSZ. In these electrodes, the ceramic backbone provides mechanical strength and ion conductivity while the infiltrated species provide electron conductivity and catalytic activity. Ni has been impregnated on zirconia and ceria-based backbones to improve their performance as cermet electrodes [140-142]. Ni impregnated electrodes have been proved experimentally and theoretically to have superior electrochemical performance compared to conventional cermets at similar catalyst loading. Zhu[143] compared Ni/YSZ made by both the cermet and infiltration process and found that infiltration results in lower resistance, they also estimated the TPB length of both electrodes and indicated that the improvement is due to the larger TPB length of the infiltrated electrode. A similar result was shown by Wang [144] when both hydrogen and methane were used as fuel, and it was further found that there was less carbon deposition on infiltrated electrodes in methane. Also, 9 wt% of Ni infiltrated on porous YSZ is enough to produce a percolating electrode while for a cermet electrode of ~1 µm thickness, the Ni loading has to be >25 wt% [145, 146], while 12 wt% Ni infiltration already showed sufficient conductivity[145].

However, due to the smaller particle size of impregnated nickel, impregnated metal/ceria composites show more degradation in operation. Work by Busawon[147] found that infiltrated YSZ has a similar TEC (Thermal Expansion Coefficient) with YSZ and does not suffer from redox-cycle degradation but would probably have more long-term isothermal degradation caused by Ni sintering. Klemensø[146] further addressed the long-term degradation of infiltrated electrodes and found that adding metal oxides (CGO, TiO_2, Al_2O_3, MgO) could inhibit Ni agglomeration at a price of a slight conductivity drop.

Because of the low calcination temperature of the impregnation process, the solid-state reaction of NiO with perovskites can be prevented. Recently, the co-impregnation of Ni and CGO on LST ($La_{0.57}Sr_{0.15}TiO_3$) [148] and LSCM ($La_{0.75}Sr_{0.25}Cr_{0.5}Mn_{0.5}O_{3-\delta}$) [149] has been investigated and they all showed good electrochemical performance and fuel tolerance.

Additional metals have been added along with Ni to optimize the performance of electrodes. Cu was co-impregnated with Ni to alleviate carbon deposition [102-104] when operating with hydrocarbon fuels and enhance the electronic conductivity. Also, the interaction between Ni and Cu enhanced the catalytic activity towards the steam reforming of methane [101, 105, 106].

1.2.2.2 Other Structures

Apart from conventional cermets and impregnated metal/support structures, a large amount of effort has been made on other structures that meets the requirement of SOFC anodes.

A micro-tubular SOFC using Ni/CGO as anode was made based on a Ni/CGO dual-layer hollow ceramic fiber structure[150]. The hollow fiber (HF) structure was prepared by coextrusion methods, a LSCF-CGO multilayered structure was deposited on the outer surface of HF, as shown in figure. 1.2.9, AS1, AS2 and AS3 stand for the HF prepared with different NPM-ethanol ratio, resulting in different pore structure. This preparation method provides the possibility to adjust the porosity of anodes and acquire better connectivity between anode and electrolyte. The resulting power density is 2.32 W/cm^2 at 600 °C, about two times the average power density of other micro-tubular SOFC.

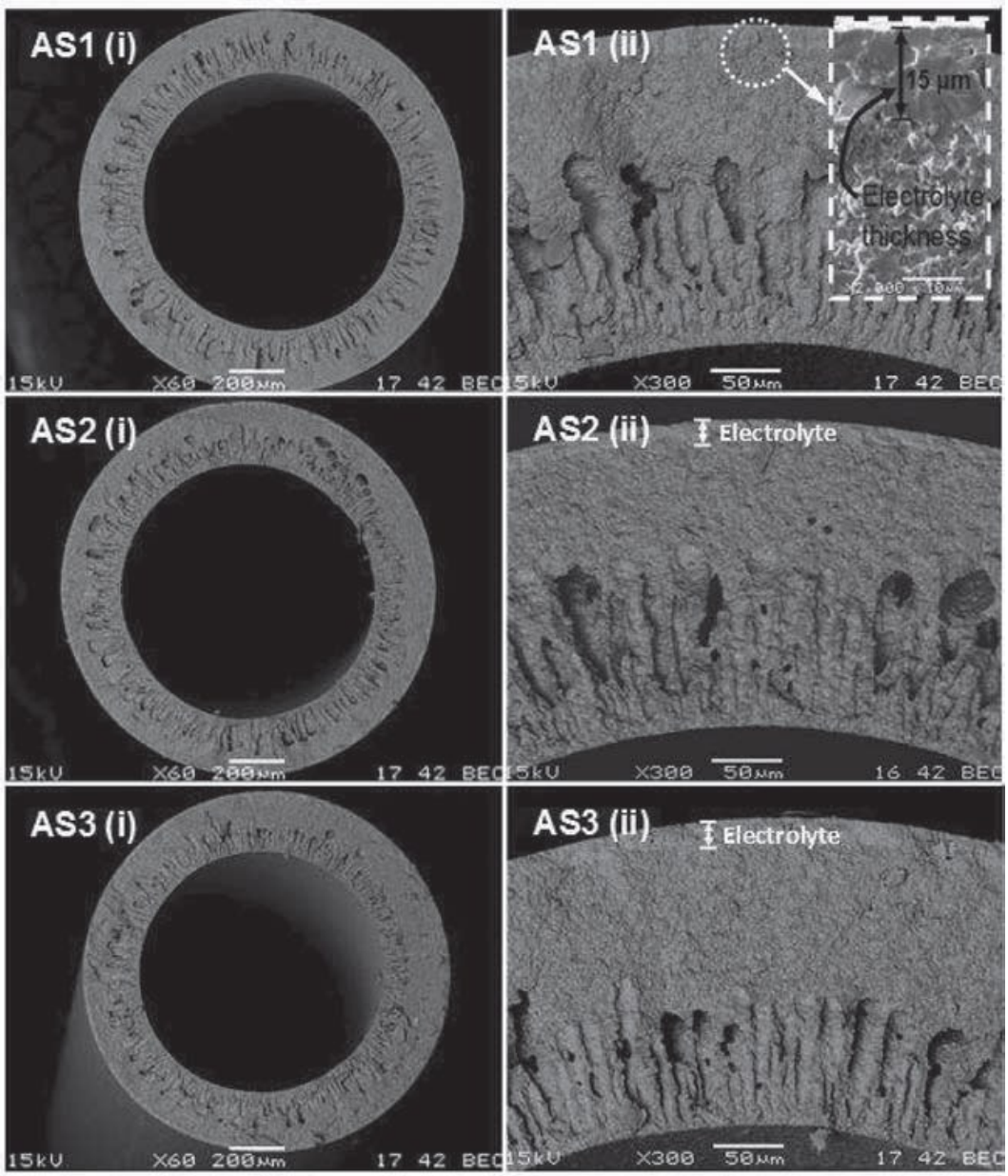


Figure. 1.2.9 SEM images of the i) overall view and ii) cross-section of the dual-layer HFs co-sintered at 1500 ° C for 12 h and reduced at 550 °C for 2.5 h. [Reproduced with permission from [150]]

An ordered mesoporous Ni/CGO cermet anode was prepared from a silica hard template (KIT-6)[151]. The Ni and CGO are both impregnated in the template to make an interconnected meso-network structure, as shown in figure. 1.2.10. The structure exhibits good connectivity, low tortuosity and enough porosity. EIS measurements were performed at 650 °C in wet 5% H_2/N_2 and the anode showed a low polarization resistance of 0.5 Ω/cm^2.

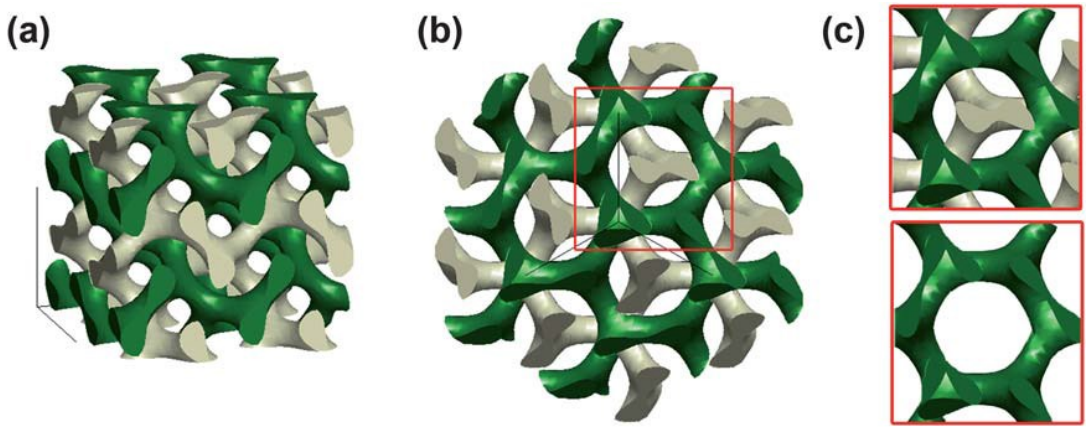


Figure. 1.2.10 Sketch of the replica resulting from a double gyroid KIT-6 mesoporous template. (a) Two sets of interpenetrating mesoporous channels in the template, Ni and CGO was impregnated separately in these two channels; (b) [111] projection of the mesostructure and (c) bimodal pore size distribution obtained after filling one or two of the channels. [Reproduced with permission from [151]]

Electrospinning techniques have also used in the development of SOFC anodes. The eletrospun nanofiber of ceramic or metal were ground and made into slurry before tape-casting into an electrode[152]. A Ni coated YSZ fiber anode was developed by Li consisting of electrospun YSZ anode and electroless-plated of Ni[153] and exhibits good electrochemical performance. The electrospun polymer fiber was used as the pore-former by Pan [154]in a Ni/YSZ cermet anode and shows improved gas transportation and electron conductivity. As a newly developed technique, the application of electrospinning on SOFC is still in its infancy, and requires more exploration.

Although the electrodes with novel structure generally show superior performance compared with conventional cermets, the preparation process is usually complicated and costly and therefore difficult to scale up. More efforts are therefore needed for the replacement of conventional cermet electrodes.

1.3. Characterization

Characterization is of great importance to the development of SOFCs. The common aspects to characterize in an SOFC anode include: 1. catalytic activity of surface reaction of fuel gas; 2. Overall electrochemical performance of electrode, including the influence of mass transportation in bulk of electrodes and pores and charge transfer in electrode; 3. Structural

characterization of the morphology, crystal structure, chemical-bonding information of electrodes.

1.3.1. Catalytic Reactivity

1.3.1.1 Temperature-Programmed Procedures

Temperature-programmed procedures, including temperature-programmed reduction (TPR), temperature-programmed oxidation (TPO), and temperature-programmed desorption (TPD) are useful tools to extract chemical information from heterogeneous catalysts and are widely used in the catalysis field.

TPD is often employed to obtain information about the nature of adsorption of certain gas species on sites of catalyst, indicated by the temperature of desorption and rate of desorption[155, 156]. Because of the strong chemisorption at room temperature, H_2, N_2O and CO are often used to determine the surface area of metal such as copper and nickel[157, 158]. TPD is also widely used to investigate the surface oxygen activity of reducible catalysts, Cordatos[159] found part of the adsorbed CO were oxidized by oxygen from ceria lattice, and proposed the oxygen reverse spill-over from ceria to Rh.

The principle of TPO and TPR are similar with TPD, in which the consumption of reductant or oxidant are recorded as a function of temperature. These techniques are often used to evaluate the oxidizing and reducing behavior of heterogeneous catalysts. Marrero-Jerez [155]applied TPR, TPD and TPO on freeze dried NiO/CGO with different metal oxide loading (figure 1.3.1). TPR showed two hydrogen consumption peaks, with the 400°C peak assigned to the reduction of surface nickel, and the 500°C to the reduction of bulk nickel. CO TPR also shows two peaks, the TPD afterwards shows four desorption peaks, indicating four different CO desorption processes. Finally, the TPO shows two peaks, indicative of two different species of carbon deposited during CO-TPR test.

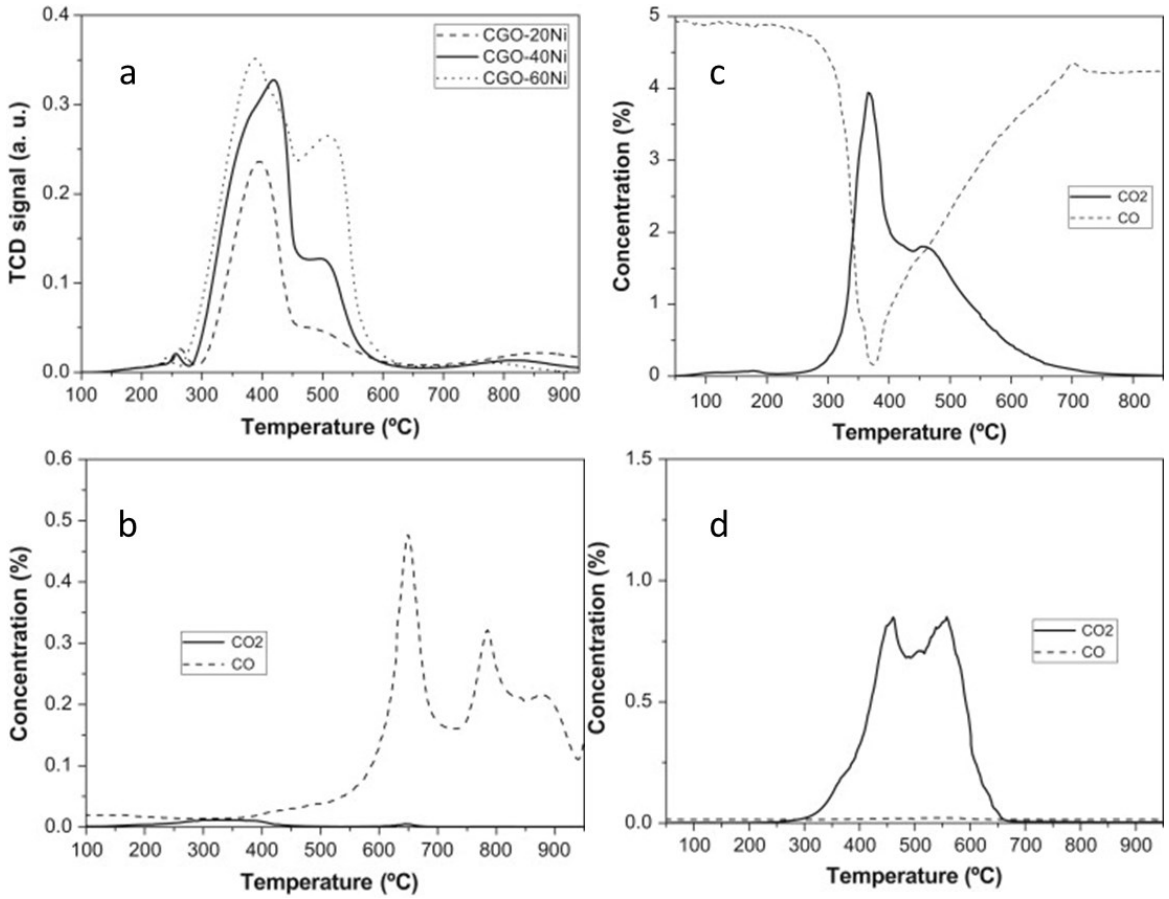


Figure. 1.3.1 a. The H_2-TPR of Ni/CGO samples with different Ni loading; b. CO-TPR of 40wt% Ni/CGO sample; c. TPD of 40wt% Ni/CGO sample after CO-TPR; d. O_2-TPO of 40wt% Ni/CGO sample. [Reproduced with permission from [155]]

However, it is difficult to extract quantitative information on surface kinetics or energetics via temperature-programmed procedures because many factors may affect the peak intensity and position, including temperature ramp rate, gas flow rate, temperature of adsorption, and the microstructure of sample, etc[160].

1.3.1.2 Pulse Reaction

Pulse experiments are a type of transient analysis method that record the response of heterogeneous catalyst system to perturbation of concentration or temperature, which is useful in describing the non-steady-state catalytic processes[161]. The technique involves injection of small amount of reactant gas into certain catalyst under controlled conditions and use of a mass spectrometer or gas chromatograph to analyze the composition change of in-coming and outlet gas.

It is a highly tunable technique which can be used with TPD in the determination of surface adsorption site density (pulse chemisorption)[162]; oxygen storage capacity of reducible catalysts towards the oxidation of CO, hydrogen or methane [163] ; and reaction of gas species with the surface of a catalyst[164, 165].

Temporal analysis of products (TAP) is a technique developed from conventional pulse experiments. The catalyst is usually under vacuum conditions while small amounts of gas molecules are pulsed over the bed of catalyst particles (ca. 10^{15} molecules per pulse)[161]. The vacuum condition eliminates all the gas phase reaction and enhances the desorption of reactive intermediates, while the small number of molecules ensure the surface of catalyst is only slightly occupied[166]. Due to the more controlled condition of TAP, the kinetic parameters can be estimated based on the analysis results.

Dewaele[167] studied the activation of methane on an industrial Ni/Al_2O_3 catalyst in a TAP reactor between 723 and 823 K, in which 20 small CH_4/Ar pulses were injected to the sample at a frequency of 1 to 2 pulses per second. It was found that methane was activated on the nickel surface via three different pathways, two involving oxygen and the other empty sites. The activation energy and rate constant of these three adsorptions were calculated by the TAP results. The oxygen chemisorbed on Ni enhanced the rate of dehydrogenation of methane on the surface of catalyst.

1.3.2 Electrochemical Performance

1.3.2.1 Electrochemical Impedance Spectroscopy

Electrochemical impedance spectroscopy (EIS) is an experimental method of characterizing electrochemical systems. It measures the response current from input AC signals of different frequencies (roughly in the mHz to MHz range for processes relevant to SOFCs), and gives different impedance responses of the processes of a system over a range of frequencies. The impedance can be expressed as a complex number[168]:

$$Z(j\omega) = Z' - jZ''$$

Where $j = \sqrt{-1}$, Z' and Z'' are frequency dependent real numbers, which are related to the magnitude of the impedance and the phase by:

$$|Z(j\omega)| = \sqrt{Z'^2 + Z''^2}$$

$$\tan\varphi = -\frac{Z''}{Z'}$$

The results of EIS analysis are usually expressed graphically in a Bode plot or a Nyquist plot. The Bode plot is a combination of Bode magnitude plot and Bode phase plot. The former expresses the magnitude of the signal by the function of frequency response. The latter expresses the phase shift by the function of frequency response. The Nyquist plot expresses the imaginary part of the signal transfer function by the function of real part of the function. Figure 1.3.2 shows an EIS result of a solid oxide fuel cell, made with LSM/YSZ cathode, YSZ electrolyte and Ni/YSZ anode, presented by Nyquist plot and Bode plot. In Nyquist plot, each point on the complex plane plot represents the impedance at a certain frequency, and each semi-circle represents a rate-determining step at given frequency.

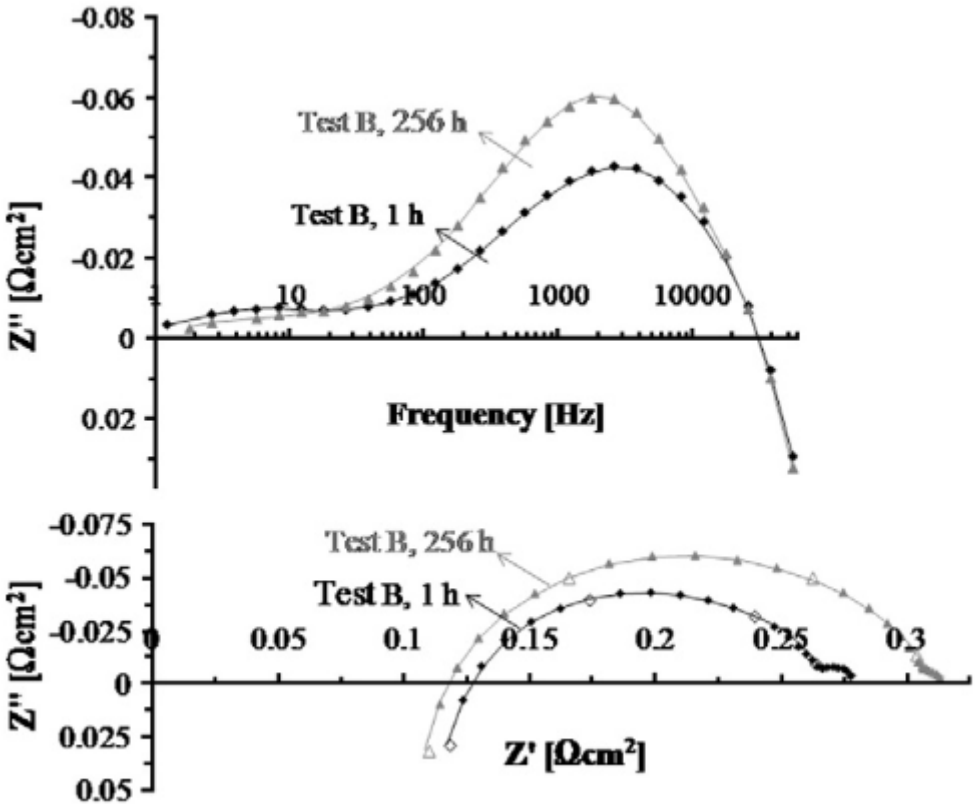


Figure. 1.3.2 The impedance of the anode in a solid oxide fuel cell using YSZ as electrolyte: (a) Bode plot; (b) Nyquist plot. [Reproduced with permission from [169]]

The power of EIS lies in the fact that it is essentially a steady-state technique that can access relaxation phenomena whose relaxation times vary over many orders of magnitude. It is widely used in the evaluation of performance of SOFC electrodes and determination of electrode reaction mechanism[170-173]. In a Nyquist plot, the value of the high frequency intercept of the impedance curve on x-axis represents the total Ohmic resistance of electrodes, electrolyte and current collector. The information on polarization processes can be obtained by fitting the impedance data to an appropriate equivalent circuit (EC), which consists of electric circuit elements (resistors, capacitors, inductors, etc.). A charge process is represented by the parallel connection of a resistor (R) and a constant phase element (CPE). A Warburg element may be added in parallel to R(CPE) to represent a simple diffusion situation. Figure 1.3.3[174] shows a EC describing EIS of a symmetrical cell made by Ni/YSZ electrodes. R_e is the ohmic resistance of cell components, R_t is the charge transfer resistance, C_{dl} is the double layer capacitance. $R_3(CPE_3)$ is the high-frequency process, $R_1(CPE_1)$ and $R_2(CPE_2)$ are two low-frequency processes, each of these processes corresponds to a semi-circle on the Nyquist plot.

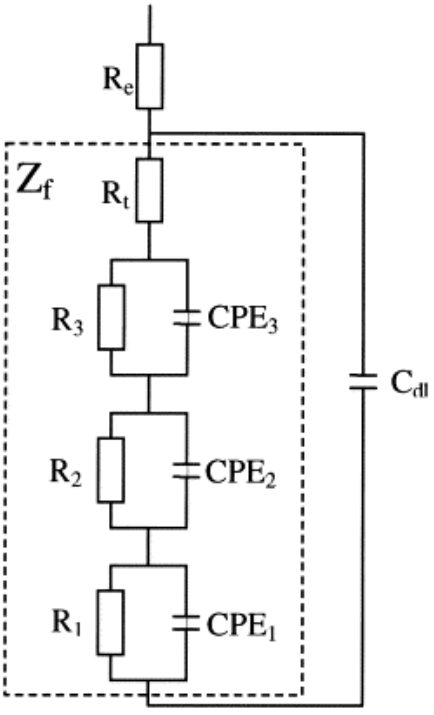


Figure. 1.3.3. Equivalent circuit used for fitting the electrochemical impedance spectra of a symmetrical cell made by Ni/YSZ electrodes [Reproduced with permission from [174]]

By changing the experimental parameters, it is straight forward to determine the governing factors of each processes via the equivalent circuit[172, 175]. The impact of H_2S on Ni/CGO as the anode for SOFC was studied by EIS[172], which was fitted by a EC $\mathbf{R_eR_{HF}(CPE_{HF})R_{LF}(CPE_{LF})}$. The EIS results from different pH_2O and pH_2S were compared with each other and it was found that increasing pH_2S enhanced the interaction of sulphur with Ni but such interaction is mitigated with ceria substrate.

For mixed ion and electron conductors such as ceria, a more generalized EC was developed by Jamnik and Maier[176], which allows for the description of different experimental set-ups as well as of a variety of devices. Following this work, Lai[177] derived EIS of Sm doped ceria from first principle and compared it with experimental data. The results suggest that ceria is electrochemically active for hydrogen electro-oxidation and that the reaction is limited by the rate of removal of electrons from the ceria surface.

1.3.3 Structural Techniques

1.3.3.1 X-Ray Diffraction

X-ray diffraction (XRD) is a commonly used technique in determining the bulk crystal structure and composition of heterogeneous catalysts[178]. The wavelength of x-rays is typically 1-100 Å, therefore, in powder analysis, XRD can identify the specific lattice planes that produce peaks at corresponding angular position 2θ. As shown in figure. 1.3.4, when a beam of x-ray comes through two parallel planes in a crystal, a small portion of the beam intensity will be scattered by the electrons within atom in the lattice. The scattered spherical waves will be diffracted with each other at specific angular direction θ when Bragg's law is satisfied:

$$2d \sin\theta = n\lambda$$

d is the spacing between diffracting planes, θ is the incident angle, n is an integer, and λ is the wavelength of the beam. The generated peaks at each position θ can be used as a signature to determine the composition and crystal structure of solid phase and thus has proved to be a standard tool in materials research. An example of XRD pattern is shown in figure 1.3.5, which indicates the pattern of $Ce_{0.8}Gd_{0.2}O_{1.9}$ fluorite structure[179]. XRD can also

be used to estimate the average crystallite size of powders. The peaks on XRD pattern are intense and sharp only if the sample has sufficient long-range order but become broader for crystallite sizes below about 100 nm. The crystallite size is determined by the Scherrer equation:

$$\tau = \frac{K\lambda}{\beta \cos\theta}$$

In which K is a dimensionless shape factor, with a value close to unity. The shape factor has a typical value of about 0.9, but varies with the actual shape of the crystallite, τ is the mean crystallite size, β is the full width of half maximum intensity (FWHM) of given peak.

For example, Bandsal[180] used XRD to determine the phase of perovskite $Sm_{0.5}Sr_{0.5}CoO_{3-x}$ and $La_{0.6}Sr_{0.4}CoO_{3-x}$ nanopowders synthesized by combustion method. The nanopowders had an average particle size of ~12 nm as determined from X-ray line broadening analysis using the Scherrer equation.

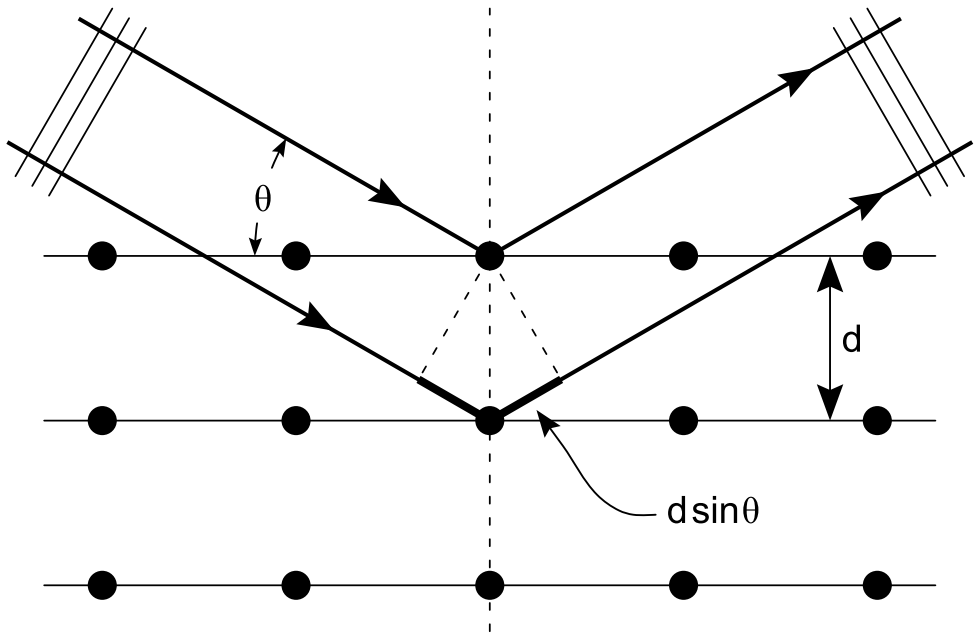


Figure. 1.3.4 A diagram of diffraction of an x-ray beam scattered at a crystal plane

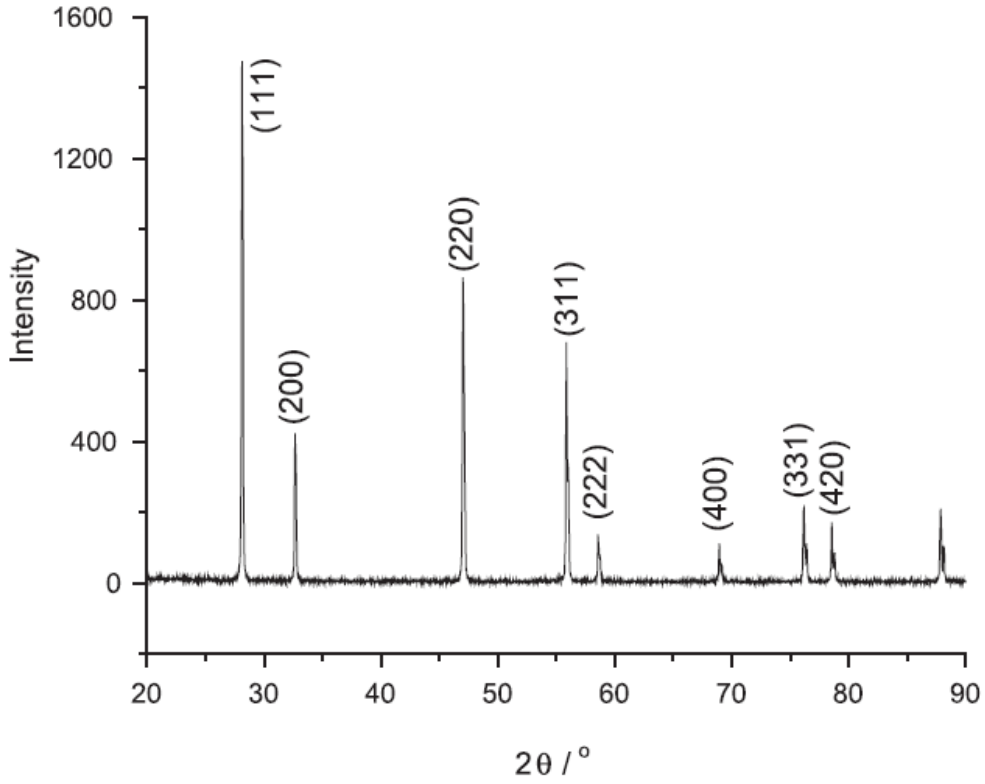


Figure. 1.3.5 XRD pattern of $Ce_{0.8}Gd_{0.2}O_{1.9}$, the brackets above shows the Miller index of the crystal plane [Reproduced with permission from [179]]

On the other hand, XRD does have some limitations[160]: 1. It cannot provide useful information on amorphous or highly dispersed solid phases; 2. Due to its low sensitivity, the concentration of the crystalline phase in the sample needs to be reasonably high in order to be detected; 3. XRD probes bulk phases and is not able to selectively identify the surface structures where catalytic reactions take place.

1.3.3.2 Raman Spectroscopy

Raman spectroscopy is a spectroscopic technique used to observe the vibrational, rotational, and other low-frequency modes in a system. Raman scattering is a type of inelastic scattering which happens when a photon excites the molecules of sample to a virtual energy state. After a short time, the molecules are moved to a different state and another photon is emitted which has a different energy to the incoming photon, as shown in figure.1.3.6. The difference between incoming and excited photons depends on the rovibronic states of the molecule, and thus are widely used to acquire the vibrational information of chemical bond

in solid state, it is especially ideal for the identification of oxygen species in covalent metal oxides. Therefore, Raman was used to determine the oxidation state of ceria[181].

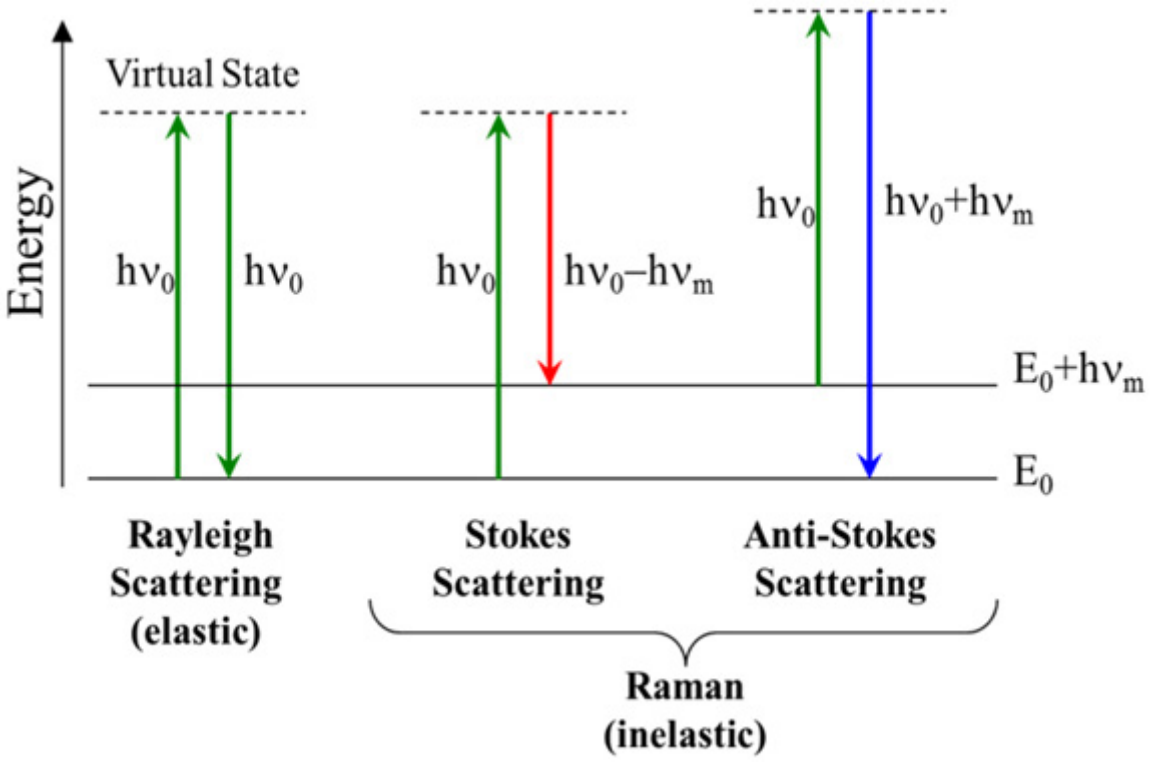


Figure. 1.3.6 Jablonski Diagram of Raman Scattering, *h* is the Planck's constant, v_0 is the frequency of in-coming photon. v_m is the frequency difference between in-coming and excited photon.

Figure. 1.3.7[181] is the Raman spectrum of Ni, CGO and Ni/CGO, it shows the counts of Raman scattered photon as a function of wavenumber shifting between excited photon and in-coming photon. The broad peak at 1170 cm^{-1} in figure 1.3.6a is the Ni-O vibrational peak. The sharp peak at 400 cm^{-1} in figure 1.3.6b and c is the vibrational Ce-O peak, which reflects the oxidation state of ceria. Figure 1.3.8 shows the integrated intensity of Ce-O peak and Ni-O peak changing with time, the significant drop is when hydrogen started to flow. The intensity of integrated peak decreased as the sample became more reduced.

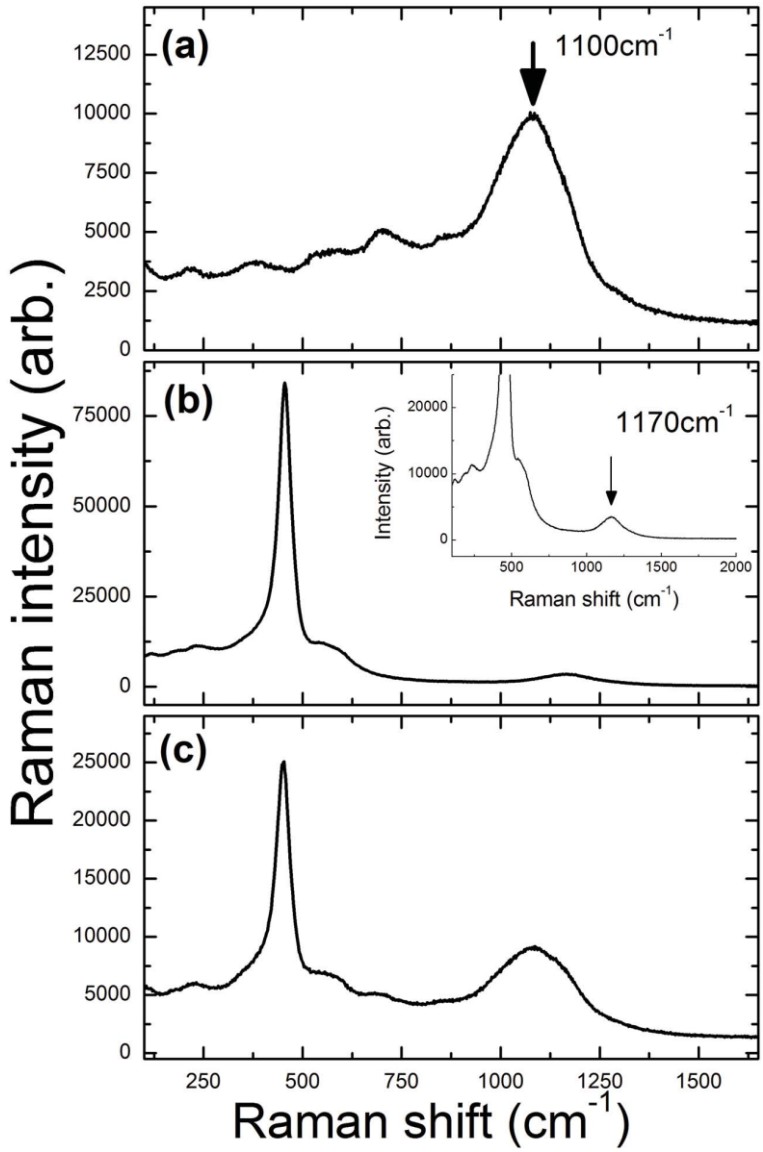


Figure. 1.3.7 Extended Raman spectra of a) NiO, b) CGO, and c) NiO-CGO cermet taken at 600 °C in flowing nitrogen using a 514 nm laser. Inset to (b) shows the Raman spectrum obtained from CGO at 600 °C emphasizing a small second-order Raman mode at 1170 cm^{-1} close to the position of the principle NiO mode. [181]

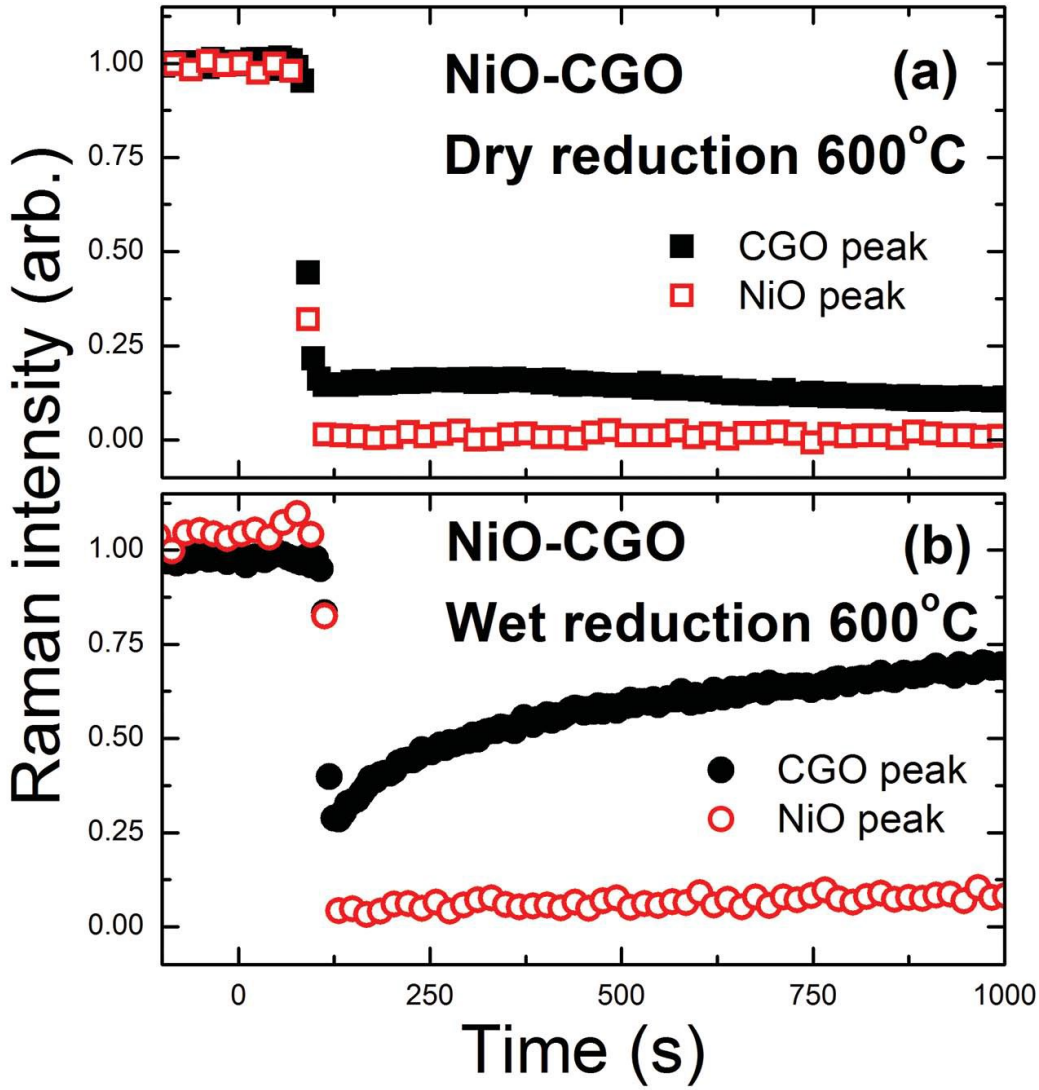


Figure. 1.3.8 Normalized intensities of the NiO and CGO Raman peaks monitored as a function of time from a NiO-CGO composite exposed to a) dry and b) wet 75% N_2:25% H_2 flowing at 100 ml/ min. Reduction of NiO and CGO appears to be strongly coupled in both cases, although the oxidation state of the CGO surface strongly recovers for the cermet exposed to the wet atmosphere. [181]

Raman spectroscopy does suffer from some limitations. For example, Raman intensities of surface species are often quite low. Also, the high laser powers needed for Raman characterization tend to heat the sample, and often cause changes in the physical properties of the solid. Finally, strong sample fluorescence typically masks the weaker Raman signals[182].

1.4. Conclusion

As reviewed in the previous sections, the mechanism of electrochemical processes of hydrogen and hydrocarbon fuels has been extensively investigated in pure ion conducting YSZ based anode materials, by all kinds of characterization technique. It was found that fuel oxidation on Ni/YSZ mainly occurs at the TPB. Based on this, the structure of Ni/YSZ was modified towards the direction of high TPB and small particles.

While ceria-based materials have also been widely used as anode of SOFCs, the study on their mechanism and modification is not as abundant as on YSZ. This is partly due to ceria's complex mixed ion and electron conductivity, which extends the electrochemical area from TPB to ceria-pore DPB; and oxygen storage capacity, which provides catalytic reactivity towards hydrogen and hydrocarbon, and would change the surface chemistry of supported metal particles by oxygen spillover. Due to these properties, in the characterization of ceria-based electrodes, we need to consider more of the participation of support than on YSZ-based materials, in which techniques that can take account for the influence of support individually is needed. While conventional characterization technique for SOFCs and catalysts are usually not capable of separating different steps in a process, novel technique needs to be developed.

In this thesis we will be focusing on the development of analytic techniques that can better describe the influence of ceria in catalytic and electrochemical reaction of SOFC anodes based on already existing techniques. We also use the technique to investigate the mechanism when ceria-based anode is operated under hydrogen and methane as fuels.

Chapter 2 A Mechanism Study on by Methane Pulse

In this chapter, the preparation and characterization of sample, methane pulse experiment are done by the thesis author. In-situ Raman spectroscopy is done by Dr Robert Maher. The idea of methane pulse comes from literature review, the application of In-situ Raman on methane pulse experiment is inspired by Dr. Paul Boldrin.

This chapter is partly reproduced from a published paper M. Ouyang, P. Boldrin, R. C. Maher, X. Chen, X. Liu, L. Cohen, N. P. Brandon, A mechanistic study of the interactions between methane and nickel supported on doped ceria, Applied Catalysis B: Environmental, 2019. 248: p. 332-340.

2.1 Methane as Fuel in SOFCs

In recent decades, natural gas has been developed as a new source of cleaner energy than coal because of the greater hydrogen-to-carbon ratio in its molecular composition and because it contains smaller quantities of N and S impurities. Methane is the major component of natural gas. The conventional use of natural gas includes direct combustion, electricity generation, and hydrogen production through steam reforming. Hydrocarbons have been used as the fuel of SOFC for a long time with an external reformer to conduct steam reforming before pumping the gas into the cell[183]. However, external reforming increases the overall costs of the system because it needs heat exchanger to transfer heat to a separate facility[184]. The direct utilization of methane without external informing in a SOFC was first reported in detail by Steele[185]. In 2000, Gorte[75] presented the first direct hydrocarbon fuel cell with reasonable power density (0.12 Wcm^{-2}), and thus direct hydrocarbon fuel cells began to attract a lot of attention.

2.1.1 Reactions and Mechanisms

In a methane molecule, four hydrogen atoms are tetrahedrally coordinated around a carbon atom, forming a sp^3 hybridization. The symmetrical structure of methane grants it superior stability. Therefore, usually a high temperature is required to break the C-H bond and form bonds with other molecules.

Methane can undergo many reactions with an oxidant:

Total Oxidation:

$$CH_4 + 2O_2 \rightarrow CO_2 + 2H_2O$$

Partial Oxidation:

$$CH_4 + 1/2O_2 \rightarrow CO + 2H_2$$

Steam Reforming:

$$CH_4 + H_2O \rightarrow CO + 3H_2$$

Dry Reforming:

$$CH_4 + CO_2 \rightarrow 2CO + 2H_2$$

The mechanism of these reactions has been extensively studied for decades. However, a consensus on the mechanistic pathways of the oxidation of methane is still lacking. A large amount of research has been done on resolving the reaction mechanisms of methane and oxygen on nickel and platinum catalyst surfaces[186-190]. The methane oxidation on electrochemically active metals represented by nickel and platinum supported on inert supports (YSZ, Al_2O_3, SiO_2) is best described by the Langmuir–Hinshelwood (L–H) mechanism, in which methane and oxygen adsorb on different surface sites of the catalyst before reacting with each other. After adsorption, methane usually undergoes a multi-step dehydrogenation process:

1. $CH_4(g) + * \rightarrow CH_4*$
2. $CH_4* \rightarrow CH_3* + H* \rightarrow CH_2* + 2H* \rightarrow CH* + 3H* \rightarrow C* + 4H*$
3. $O_2(g) + * \rightarrow O_2*$
4. $O_2* + * \rightarrow 2O*$
5. $CH_x* + O_y* \rightarrow product$

In which * denotes a surface site on the catalyst, CH_x being adsorbed hydrocarbyl species adsorbed on the surface of metal, O_y being the O* or O_2* adsorbed on the metal surface. Except for step 5, the adsorbed oxygen would also participate in the adsorption and dehydrogenation of methane. Taking methane oxidation on a Pt surface as an example, the rate determining step of this route varies with different oxygen coverage on the surface of the catalyst. At high coverage, methane is quickly activated at an O*-O* pair or *-O* pair at the metal surface, therefore step 5 is rate-limiting. As the oxygen coverage is decreased, step

4 becomes rate determining. While at low coverage the activation of methane is slow at a *-* pair, and step 2 is rate-limiting[190]. The process on a Ni surface is similar to that of Pt.

On the other hand, Seimanides[191] found that methane oxidation on Ag can be described by an Eley–Rideal (E-R) mechanism, in which gas phase methane directly reacts with the oxygen adsorbed on metal surface. The reason is probably that methane interaction with Ag is much weaker than with Ni. It was further supported by Nagamoto[192], who found oxygen atoms on the surface of catalyst to be more active than those coming from the gas phase:

1. $O_2(g) + * \rightarrow O_2 *$
2. $CH_4(g) + O_2 * \rightarrow product$

Hurtado[193] found that methane oxidation on Pd/Al_2O_3 follows the Mars-van Krevelen (MvK) mechanism, in which oxygen is supplied from the catalyst support to react with adsorbed methane. Schwartz[194] studied methane oxidation on Pd/ZrO_2 and suggested it also went through a MvK route:

1. $CH_4(g) + * \rightarrow CH_4 *$
2. $CH_4 * \rightarrow CH_3 * + H * \rightarrow CH_2 * + 2H * \rightarrow CH * + 3H * \rightarrow C * + 4H *$
3. $CH_x * + O_{sup} \rightarrow product$

When metal catalysts are supported on reducible supports (e.g. ceria, perovskite based), a strong metal-support interaction has been widely recognized and studied[93, 195, 196]. Sevcikova [93] found Rh-ceria interaction leads to a build-up of a net positive charge on Rh particles supported on stoichiometric cerium oxide, and a net negative charge on Rh particles on reduced cerium oxide. Also, the oxygen spillover from metal to support and support to metal on Rh particles supported on partially reduced ceria was supressed. Vayssilov[94] identified the oxygen transfer from ceria to Pt surface as an essential part of the metal-support interaction and found such interaction can be greatly enhanced by the nanostructure of both Pt and ceria.

The reaction mechanism of methane on metals with reducible supports is controversial. Kundakovic [197] found the methane oxidation on Cu or Ag/ceria follows the L-H mechanism described above. Lykhach [198] applied in-situ XPS on an operating SOFC cell and found methane oxidation on Pt/ceria went through a MvK route, in which oxygen was supplied from

the bulk of ceria. During oxidation of methane on the metal surface, oxygen migration from ceria to metal surface has been widely recognized in parallel with oxygen from gas phase[93, 199], though which of these two is the majority oxygen source is still under debate.

Although not as strong as ceria supported metal catalyst, ceria itself is a decent oxidant for methane even without a metal catalyst. Although fully oxidized ceria is not active as a catalyst, partially reduced ceria is highly active for methane adsorption[200]. Therefore, high surface-area ceria was investigated as the catalyst for methane partial oxidation[201] and exhibited good oxidation activity towards methane and also, no carbon deposition was found.

2.1.2 Carbon Deposition

Nickel is a good catalyst for the methane splitting reaction[202]: $CH_4 \overset{Ni}{\rightarrow} C + 2H_2$, so carbon tends to accumulate on the anode and leads to rapid degradation. Therefore, large efforts have been devoted to inhibiting carbon and sulphur poisoning in recent years.

Carbon growth on Ni catalysts is generally accepted to occur via the dissolution −precipitation mechanism[203-205]. Methane is first adsorbed on the surface of nickel and then decomposes into C and H; later the carbon dissolves into the Ni bulk and diffuses through it, at last precipitating on the surface. Sehested[206] investigated the growth of carbon on Ni surfaces and found there are three types of carbon formed. Pyrolytic carbon is formed by exposure of higher hydrocarbons to high temperatures. Encapsulating carbon (gum) may be formed during reforming of heavy hydrocarbon feeds with a high content of aromatic compounds. Whisker carbon is the most destructive form of carbon, it may grow into the Ni bulk and destroy the catalyst structure. Whisker carbon is formed during steam reforming of methane, first nickel carbide is formed and then carbon is dissolved into bulk nickel and thus forms the whisker.

The factors controlling carbon formation can be summarised as followed:

Thermodynamics underpins coke formation. Sasaki[207, 208] suggests that dry methane would decompose to carbon and hydrogen at high temperature (> 300 °C). When the steam/carbon ratio (s/c) is 1.0, the formation of carbon is inhibited after 750°C. When s/c is increased to 1.5, no observable carbon was found to form (Fig. 16). Therefore, if we control the temperature and s/c ratio we can reduce carbon deposition on the catalyst. However, the

tendency of SOFC usage is lowering the operation temperature while higher s/c reduces the power density and efficiency.

Nickel particle size has been proven to affect coke formation greatly. Ermakova[209] looked into methane decomposition at temperatures under 550 °C . They found that nickel with 10-40 nm particle size is most prone to coke formation. Increasing or decreasing the nickel size would result in a sharp decrease of carbon deposition. Chen[210] further confirmed the size effect and found 34 nm as the optimum size for carbon tube growth. And they further investigated the kinetics behind coking. Small sized Ni particles were found to have an increased saturation concentration of carbon, and large particles had lower surface area for carbon growth. However small nickel particles are desired for higher TPB density and specific surface area. Therefore, the prevention of nickel sintering is of specific importance.

In conventional cermet anodes, the nickel content is usually over 40 wt%, higher than usually used in methane reforming catalysts. Also, Ni in the cermet is sintered at 1300 °C or more to form a robust cermet anode. In this case, the Ni particle size is usually as large as 20 μm[40] and the anode suffers even more coke formation than methane reforming catalyst. Since impregnation, as stated before, is a great route to reduce Ni particle size, it also enhances coke resistance of anode greatly. Kim [211] modified the impregnation method and produced Ni particles with various size. They found 7 nm to be the minimum size for carbon whisker growth.

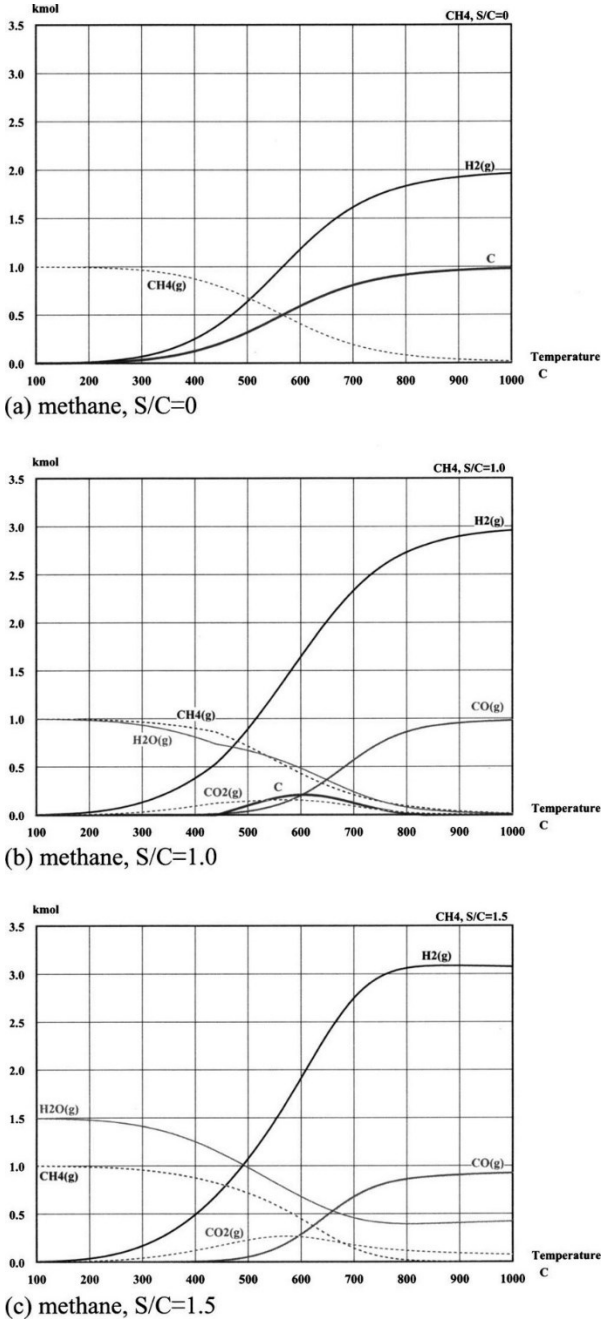


Figure. 2.1.1 Equilibrium products from methane (CH_4) mixed with H_2O in different steam-to-carbon ratios (S/C): (a) S/C = 0, (b) S/C = 1.0, and (c) S/C = 1.5. [Reproduced with permission from [207, 208]]

Coke formation on nickel is initiated by the strong adsorption of carbon atoms on Ni surface sites[212]. Therefore, if another metal is added to form an alloy with nickel, and to passivate Ni 3d electrons, the production of nickel carbide might be inhibited. A number of metals have been investigated when alloying with Ni at methane reforming conditions, including Co[213], Fe[214], Sn[215, 216], Ru[217] etc. Co can reduce carbon deposition from methane splitting due to the synergic effect of Co and Ni. Sn-Ni alloys also exhibit good carbon

resistance, by selectively oxidizing deposited carbon atoms rather than forming C-C bonds. Farrell[218] reported 1% Sn/Ni can reduce carbon deposition and increase power density in ethanol operation. They suggest that, after forming an alloy, Sn is aggregated to the under-coordinated sites on the surface of Ni, eliminating nucleation sites for carbon growth. Also, by breaking the ensembles of Ni surface atoms, the room for carbon filament growth is limited, similar to the size effect discussed above.

The support is another determinative factor of carbon resistance, when nickel is present. Guo [219] found $MgAl_2O_4$ inhibits coke formation in methane dry reforming compared with Al_2O_3 supports, because $MgAl_2O_4$ assists the dispersion of Ni particles and adsorbs more CO_2 to conduct the reforming reaction. Further research indicates that basic surfaces that favour water adsorption and OH surface mobility can decrease the coke formation rate. Therefore additives such as alkaline metal oxides (MgO, CaO) were added to adjust the acidity of the support surface[220, 221]. Horiuchi[221] looked into the effect of alkaline metal oxide on Ni/Al_2O_3 and found that it changes the CH_4 adsorption favoured surface to CO_2 adsorption favoured, and thus suppresses coke formation. Rare-earth metal oxides such as CeO_2 can also inhibit coke deposition by enhancing the carbon gasification rate[222, 223]. Wang[224] tested La_2O_3, CeO_2, Pr_2O_3, Sm_2O_3 and Gd_2O_3 as additives in Ni/Al_2O_3 catalyst for methane reforming reactions. While all oxides show enhancement towards catalytic activity and inhibition of coke formation, Gd, Pr, La are the best. Also, research found that Ni on CeO_2 support is more active than Al_2O_3 support for hydrocarbon fuels[225].

The composition of fuel gas in the SOFC system has a great influence on coke deposition. Watwe[226] found that CH dehydrogenation is the limiting step of CH_4 decomposition, therefore the addition of H_2 facilitates the equilibrium of reactions moving towards CH_4. Laosiripojana[225] applied H_2/O_2 co-feed during the steam reforming of ethanol at Ni/CeO_2 and coke formation was significantly suppressed,. However, adding O_2 in an SOFC will lower the operating voltage and adding too much H_2 would reduce the catalytic activity because of the active site competition on Ni surface. Nikooyeh[227] found that adding pure hydrogen in methane would reduce carbon deposition (~30% carbon deposition when H_2/CH_4 ratio is 1.5), as shown in Fig. 2.1.2. Also, hydrogen can be used to remove carbon, and results in less damage to microstructure compared to oxygen.

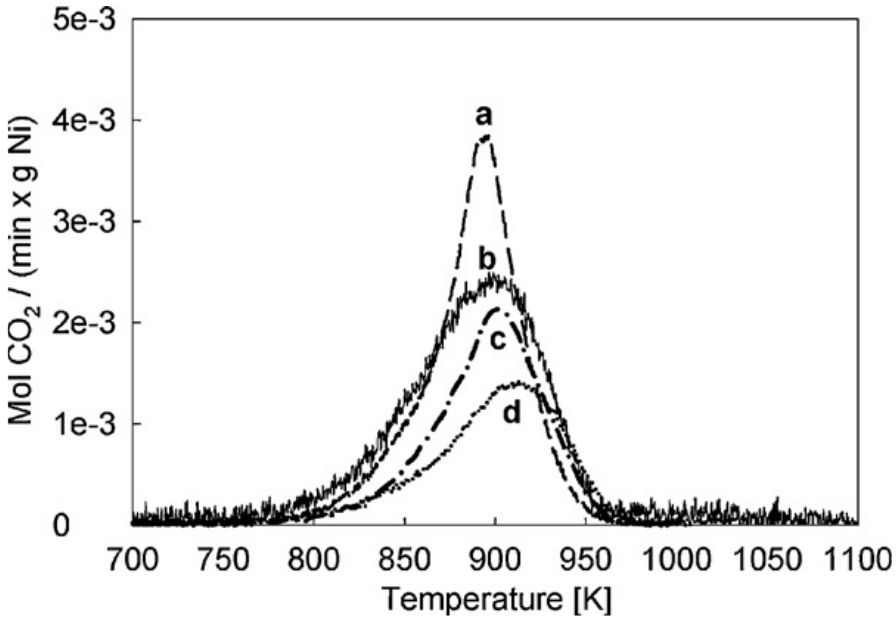


Figure. 2.1.2 TPO spectra of Ni/YSZ exposed for 3 h at 1073 K to feed streams with H_2:CH_4 ratios of (a) 0, (b) 0.5, (c) 1 and (d) 1.5. [Reproduced with permission from [227]]

For SOFCs under hydrocarbon fuel, adding a **polarization current** can inhibit carbon deposition. As the polarization current increases, the ionic current flux from cathode to anode increases and therefore accelerates the removal of deposited carbon[228, 229]. Alzate[70] reported that carbon formed under load is more reactive and easier to remove while carbon formed at OCV is more stable (Fig. 2.1.3). Also the amount of carbon decreases as the current density increases from 1 $mAcm^{-2}$ to 50 $mAcm^{-2}$ but the reactivity remains the same.

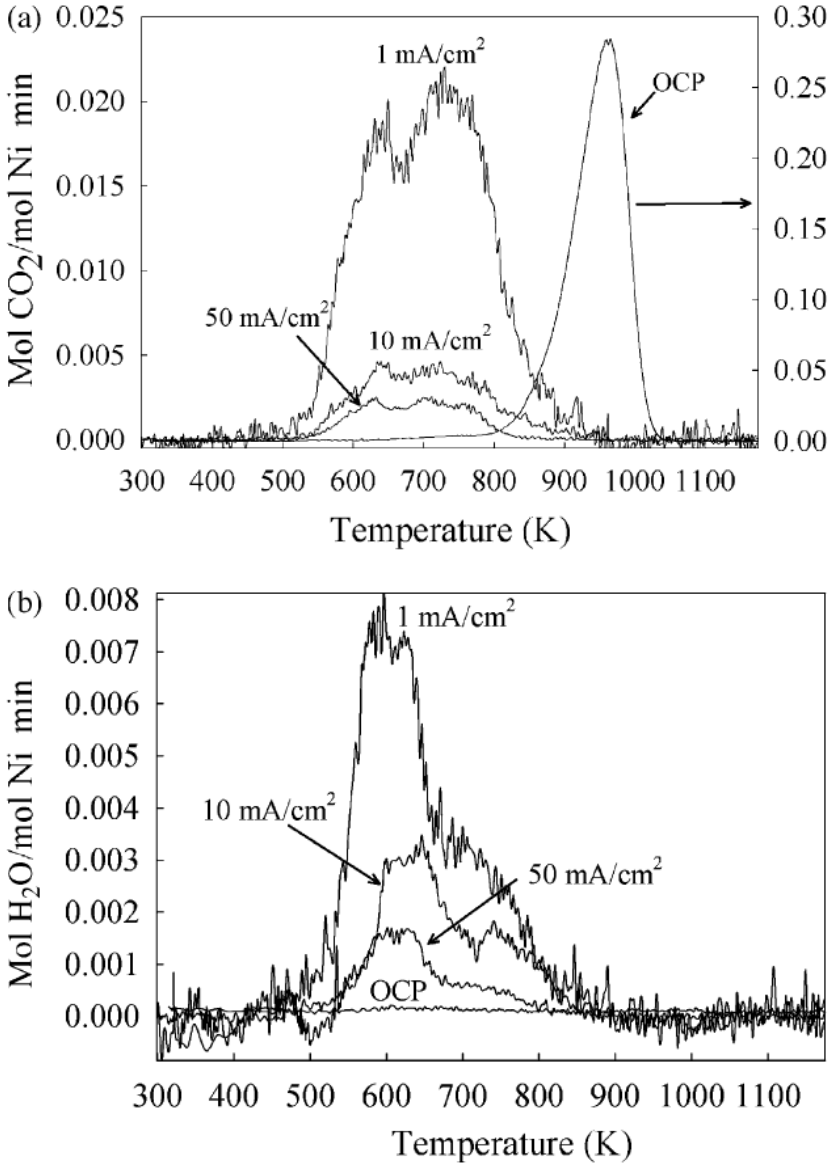


Figure. 2.1.3 TPO analysis of Ni/YSZ anodes exposed to methane for 6 h at 1073 K with current densities of 0 mA/cm^2, 1 mA/cm^2, 10 mA/cm^2 and 50 mA/cm^2: (a) CO_2 production and (b) H_2O production. [Reproduced with permission from [70]]

2.1.3 Implications

Much work has been done on Ni/ceria catalysts to explore their activity-structure relationships, mostly done by steady-state approaches [181, 230, 231], which are facile and readily scaled up to industrial scale. However, steady-state approaches suffer from several intrinsic disadvantages: 1. The kinetic data of steady-state approaches is usually related to only the rate determining step and does not provide detailed information of a complex multi-step process such as catalytic oxidation of methane[232]. 2. The observed kinetic corresponds with factors other than the structure of the catalyst, such as gas composition and time of reaction. Therefore, detailed activity–structure relationships are difficult to establish using steady-state kinetic data.

Transient studies can generate a perturbation in the system and then the relaxation/response of the system is monitored. Therefore, some short-lived intermediate species that are not seen in steady-state approaches can be investigated[233]. Transient methods have been widely applied on ceria-based catalysts to determine the oxygen storage capacity (OSC)[234, 235] or to investigate the mechanism of methane catalysis[167, 236]. Although in these works the kinetic data were well-interpreted quantitatively, the qualitative information such as shape and broadening of peaks that can also provide information related to reaction mechanism more intuitively were somewhat overlooked. In the literature on solid state chemistry, transient experiments such as electrical conductivity relaxation[237, 238] and gravimetric relaxation[239, 240] have been used to measure parameters such as the chemical diffusion coefficient (D_{Chem}) and the surface exchange coefficient (k_s) over a wide pO_2 range but these experiments need certain geometries of samples, custom-designed equipment and are not appropriate for studying real electrode or catalyst structures.

On the other hand, transient methods have not been applied on any attempt aiming at relating the carbon resistance of Ni/CGO with its intrinsic properties which is of much importance in industrial processes like catalytic partial oxidation or steam reforming of methane (POM, SRM), and the actual application of SOFC and CLR on methane fuel. In different conditions the catalyst will be at a different equilibrium state depending on the gas

composition (for example the steam/carbon ratio) and the composition of the catalyst (for example the level of doping of the support or active metal). These different equilibrium states could mean differences in parameters which may affect the performance of the catalyst, such as the surface coverage of carbon or the oxidation state of the bulk and the surface of the catalyst support. As a simple example, the energy of a surface oxygen atom on CeO_2 will be different to the energy of a surface oxygen atom on $CeO_{1.95}$, and this will change the rates of certain steps of the reaction. The effect of this on the performance of ceria and doped-ceria catalysts has not yet been investigated. Work to fill in the gap on a real-life catalyst environment is therefore a pressing need.

2.2 Methane Pulse on Ni/CGO

2.2.1 Experiment Setup

2.2.1.1 Powder Sample Preparation and Characterization

The Ni/CGO sample was prepared via the tape casting and impregnation method in order to produce a microstructure similar to an SOFC electrode in a powder form. At first, a CGO ink was prepared by mechanically mixing commercial gadolinium doped ceria ($Gd_{0.9}Ce_{0.1}O_{1.95}$, Praxair, particle size = 0.5 μm) with carbon black as a pore former, Hypermer KD15 as a dispersant and an ethylcellulose binder (Hercules EC N-7) in a triple roll mill. Secondly, the ink was tape cast onto an alumina plate followed by calcination in a muffle furnace (Elite Co.). at 1350 °C, with a ramping rate of 5 °C/min, and dwelled for 3 h. Thirdly the calcined sample was scraped down from the plate and ground. Then the powder with total weight of 1 g was impregnated with 2 M $Ni(NO_3)_2{\cdot}6H_2O$ (Sigma-Aldrich) ethanol solution, the impregnation was conducted as follows: 4 μL of solution was dropped onto the sample along with grinding in the mortar to acquire uniformity; then the powder was calcined in a muffle furnace at 500 °C, with a ramping rate of 5 °C/min for 30 min to convert $Ni(NO_3)_2{\cdot}6H_2O$ to NiO. After that the powder was weighted on an analytical balance to determine the actual amount of NiO introduced, and the nickel amount after reduction was calculated accordingly. The above process was repeated until the amount of nickel reached more than 20 wt% (21.3 wt% after the last impregnation). After impregnation, the sample was further calcined at 800 °C for 4 h, with a ramping rate of 5 °C/min.

The impregnation process is shown in figure 2.2.1.

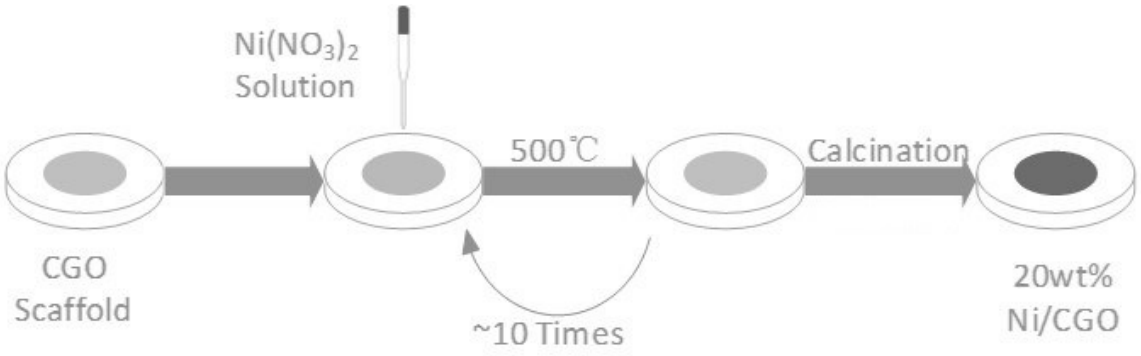


Figure. 2.2.1 Impregnation process of Ni/CGO using 2 M $Ni(NO_3)_2.6H_2O$ ethanol solution

Commercial Ni/CGO, Ni/YSZ and Ni were provided by Fuel Cell Materials. The Ni/CGO and Ni/YSZ had metal loadings of 54.1 wt% and 61.7 wt% NiO respectively, with a NiO particle size of 500-1000nm.

Powder X-ray diffraction (XRD) of the impregnated sample was recorded using Panalytical X'Pert³ Powder X-ray diffractor with Cu Kα radiation. The particle size of NiO and CGO was calculated using the Scherrer equation. The SEM images of CGO and impregnated Ni/CGO were taken by LEO Gemini 1525 FEGSEM, using in-lens detector and 5 kV acceleration voltage.

2.2.1.2 Powder Analysis

The powder experiments were conducted using an AutoChem II 2920 (Micromeritics). The powder sample was placed on a piece of quartz wool inside a U-shaped quartz tube. The composition of outlet gas was analysed using a Cirrus 2 Quadrupole Mass Spectrometer (MKS).

A series of temperature programmed procedures were used to analyse the morphology and reactivity with methane, as shown in figure 2.2.2. The sample was first reduced in a temperature programmed reduction procedure (TPR), the temperature was raised to 600 °C with 5 °C/min ramping rate in 50 mL/min 20% H_2/Ar mixing gas. H_2 (amu 2) and H_2O (amu 18) were monitored in the mass spectrometer.

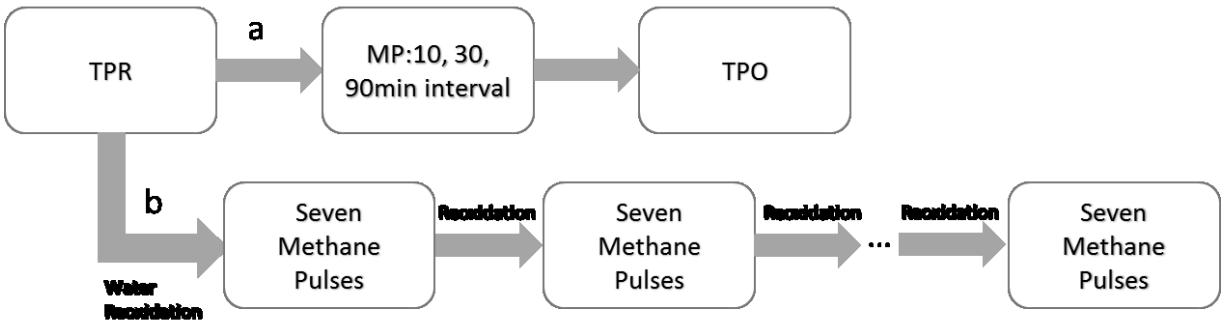


Figure. 2.2.2 Analysis process of Ni/CGO using Autochem powder analyser

In a methane pulse (MP) experiment, 0.3793 mL of methane was injected into 0.1 g of 20 wt% Ni/CGO sample at 600 °C in each pulse, followed by flushing of 50 mL/min of Ar during the pulse interval, the pulse number and time of interval were adjusted as variables. A Sigma-Aldrich molecular sieve moisture trap was added in the pipeline to avoid the influence of trace amount of water in Ar. CH_4 (amu 15), CO (amu 28), CO_2 (amu 44), H_2 (amu 2), and H_2O (mass 18) were monitored in a mass spectrometer. MP was performed in two ways. First a series of pulses with different intervals were performed to investigate the difference when changing interval and pulse numbers. 30 pulses were injected when the interval was 10 min, and 15 pulses were injected when interval was 30 min or 90 min. Commercial powders of Ni/CGO, Ni/YSZ and Ni were used to provide a comparison. After the different interval experiments a steam reproducibility test was performed along with MP.

As a final step last, temperature programmed oxidation was performed to investigate the amount and form of carbon deposition in each methane pulse experiment. 50 mL/min 2% O_2/Ar mixing gas was used in the oxidation with the temperature raised to 1000 °C at a 5 °C·min^{-1} ramping rate. Ar (amu 40), CO_2 (amu 44) and O_2 (amu 32) were monitored in the mass spectrometer.

Methane pulse with water re-oxidation experiments were performed on impregnated Ni/CGO powder, as shown in figure. 2.2.2b. 0.2326 mL methane pulses were injected at 15 min intervals. Every seven methane pulses, pulses of 0.2326 mL 12.3vol% H_2O/Ar were injected with an interval of 0.5 min until no hydrogen production was observed. This indicates

that ceria was oxidised to a certain oxidation state. CH_4 (amu 15), CO (amu 28), CO_2 (amu 44), H_2 (amu 2), and H_2O (amu 18) were monitored in a mass spectrometer.

Calibration was performed before the recording of all mass spectrum of methane pulses by pulsing a known volume of standard gas or gas mixtures (H_2, CH_4, 1% CO/Ar) through the mass spectrometer. The mass spectrometer data was analysed by OriginLab 8.6.

During the development of the methane pulse method, several parameters have been adjusted to better extracting the information we need. The interval between pulses and volume of CH_4 both can greatly influence the shape and extending of the peaks. If the volume of pulse is too large while the interval too short, the CGO oxidation state would decrease quickly and information from higher oxidation state will be missing, also carbon will accumulate and deactivate the catalyst. On the other hand, if the volume is too small and interval too large, the time period of the whole experiment would be greatly extended to order for CGO to fully reduce. Therefore, the oxidation of CGO by trace amount of steam in the background would play an important role in the experiment and cause an imprecision. So we have decided to use an loop size of 0.3793 ml in combine with pulse interval of 30 min, and 0.2426 ml in combine with 15 min. The former combination allow us to see better the process during the interval, while the latter allow us to observe more peaks before the full reduction of CGO.

2.3.1.3 In-situ Raman Spectroscopy

The in-situ Raman Spectroscopy is applied to characterize the change of surface chemical bonding of CGO during methane pulse experiment. The development of in-situ Raman Spectroscopy encountered several difficulties in the beginning: Because of nature of in-situ Raman, the sample has to be exposed under laser and under stream of Ar and CH_4 while being heated at the same time. The catalyst analyser-mass spectrum used in previous methane pulse experiments are unable to achieve these conditions. Therefore, another experiment platform is assembled with help from Dr. Paul Boldrin and Dr. Robert Maher, as shown in figure 2.2.3 which consists of: Benchtop Raman spectrum platform, for laser emission and Raman scatter signal sampling; Sample holder, for the holding of powder catalyst sample, made of stainless-steel shell and quartz window which allows laser to go through. Manual gas

injection valve, for injection of loop gas into sample; Gas phase mass flow controllers, for controlling of flow rate of carrier (N_2) and loop gas (CH_4, H_2); Desktop mass spectrometer, for detection of different gas species; Pipelines, for connection of gas.

After the system was assembled, it is found that the water level detected by the mass spectrometer is high, ~100 times higher than in catalyst analyser. This is thought to because of the steam from the pipelines. In integrated catalyst analyser, the pipelines are all heated to >100 °C to make sure no water reside inside it. While in our assembled system, the pipelines are under room-temperature. A molecular sieve is added in the pipeline to eliminate the water originally in the gas, and the whole system is vented under N_2 for 12h before the experiment started. The water level decreases 20 times after the action. Although still higher than integrated catalyst analyser, the water baseline would not affect the result now.

In-situ Raman measurements were carried out using a Jobin-Jbvon LabRam HR-1000 confocal microscope. Spectra were collected using a 514 nm argon ion laser which was focused onto the sample using a ×20 long working distance objective. This resulted in a spot with a diameter of approximately 4 μm at the focal point. The incident laser power and integration times used for the measurements were optimized before for each to ensure a good signal-to-noise ratio was achieved while any possible laser heating was minimized. Integration times varied between 5 and 15 seconds and the laser intensity was constant at approximately 4 mW at the focal point.

In-situ Raman spectra were collected from the samples in real time using a high temperature catalytic stage from Linkam Scientific. Raman spectra were collected at 600 °C as reported by the stage controller. Continuous flows of N_2 and H_2 were delivered through the stage to the samples using a system of calibrated mass flow controllers. Samples were reduced using a mixture of 90 % N_2: 10% H_2 for at least an hour and then purged at 105 °C for 12 hours in pure N_2 in order to minimize the presence of any water in system. All gas mixtures passed through the system at a total rate of 100 cm^3 min^{-1}. The scheme of gas connection is shown in figure 2.2.3.

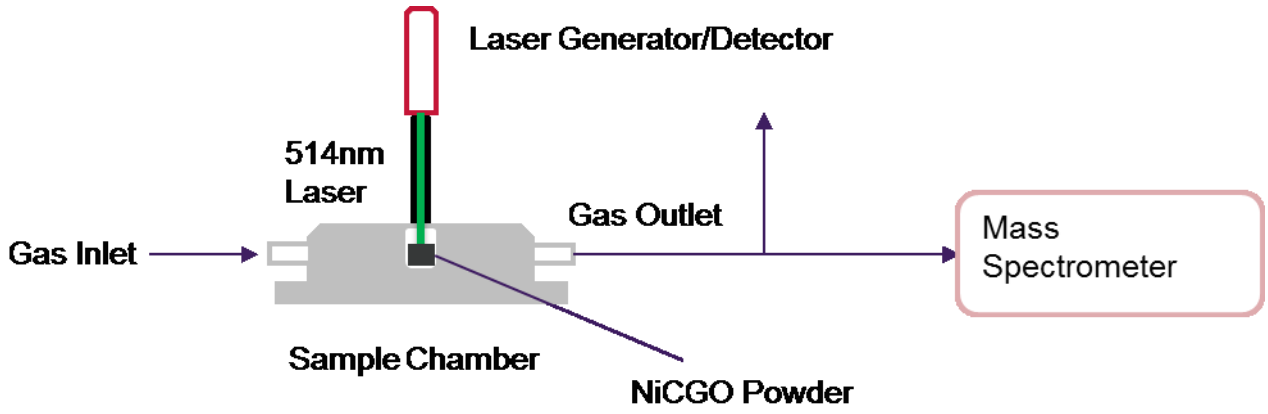


Figure.2.2.3 Schematic indication of gas connection in in-situ Raman experiment, the powder sample is stored in sample chamber, heated to 600 °C while being immersed in the required gas. The laser is emitted onto the sample through a quartz glass window on the chamber and the detector is located at the same position as laser generator; The gas outlet is connected to a vent while a branch line is connected to a desktop mass spectrometer.

During the experiment, 100 cm^3 min^{-1} Ar passed through 0.1 g impregnated Ni/CGO powder and 0.3793 mL methane was injected manually by a Rheodyne 7010 injector every 20min. H_2, CO, CH_4, CO_2 and H_2O were monitored by a Thermo Fisher ProLab Benchtop Mass Spectrometer at the same time.

All Raman spectra collected were analysed using a combination of the JY LabRam software, Peakfit v4 and OriginLab 8.6. Spectra were normalized to their total intensity in order to compensate for any differences in focal conditions. They were then background corrected and fitted to Voigt modes using Peakfit v4 or integrated over regions of interest using OriginLab. The resulting data was then further analysed using OriginLab 8.6.

2.2.3 Data Collection and Analysis

2.2.3.1 Mass Spec Calibration

The mass spectrometer ionizes gaseous species and directly measures the ion current of ions with different mass/charge ratio ($\varepsilon=m/e$). If ions with a mass/charge ratio of ε are ionized from one gas species *x*, then the ion current I_ε can be converted to partial pressure by dividing sensitivity of gas x at mass/charge ratio ε, S_ε^x [A·Pa^{-1}]: $px = \frac{I_\varepsilon}{S_\varepsilon^x}$. The absolute value of sensitivity depends on many factors other than the physical properties of gas including the

instrument, ionizer and mass filter design, which means for given instrument at the same period of time S_ε^x is constant.

The goal of calibration is to relate the signal of mass spec I_ε with volume of gas V_x. The flow rate r_x *[mL·min^{-1}]* can be determined by $r_x = r_t \frac{px}{p_t}$, in which r_t is the total flow rate of gas species *x*, p_t is the total pressure, in our case r_t is 50 mL·min^{-1}, p_t is 3.7×10^{-6} mbar as indicated in mass spec. So $r_x = Cpx$, *C* is a constant. Let us consider one pulse of CH_4 (*ε=15*), the volume of CH_4 in one pulse V_{CH_4} can be expressed as:

$$V_{CH_4} = \int_0^t r_{CH_4}(t)dt = \int_0^t Cp_{CH_4}(t)dt = \int_0^t CS_{15}^{CH_4} I_{15}(t)dt = C_1 \int_0^t I_{15}(t)dt \quad (1)$$

t is the width of amu 15 signal peak on mass spec. C_1 is a constant that determined by condition of instrument, and gas species. So, if we inject a pulse of CH_4 with known volume V'_{CH_4} through the mass spec, and the mass spec signal reads $I'_{15}(t)$. Then we have:

$$V_{CH_4} = \frac{V'_{CH_4}}{\int_0^t I'_{15}(t)dt} \int_0^t I_{15}(t)dt \quad (2)$$

Therefore, 20 pulses of 0. 3793 mL methane was injected to pass through mass spec before each methane pulse experiment. Then signal peaks of amu 15 were integrated by the width of the peak. Finally, the volume of CH_4 during methane pulse experiment can be determined by eq. (2). The calibration of H_2 and CO were performed in same way.

2.2.4 Results and Discussion

2.2.4.1 Morphology and Crystallinity of Impregnated Ni/CGO

The SEM images of CGO and impregnated Ni/CGO powder is shown in figure 2.2.4. The large particles with size of 300-600 nm are CGO. There were dispersed particles of ~50-100 nm diameter sitting on CGO particles both shown in Fig. 3a and b, EDS showed it was CGO. These particles might be generated from the high temperature sintering of CGO backbone. The small particles with particle size of 5-20 nm evenly distributed on the surface of CGO in Fig.3b are impregnated nickel. No agglomerated nickel particles were observed in the structure. The SEM images show that impregnated nickel particles acquired good contact with CGO particles.

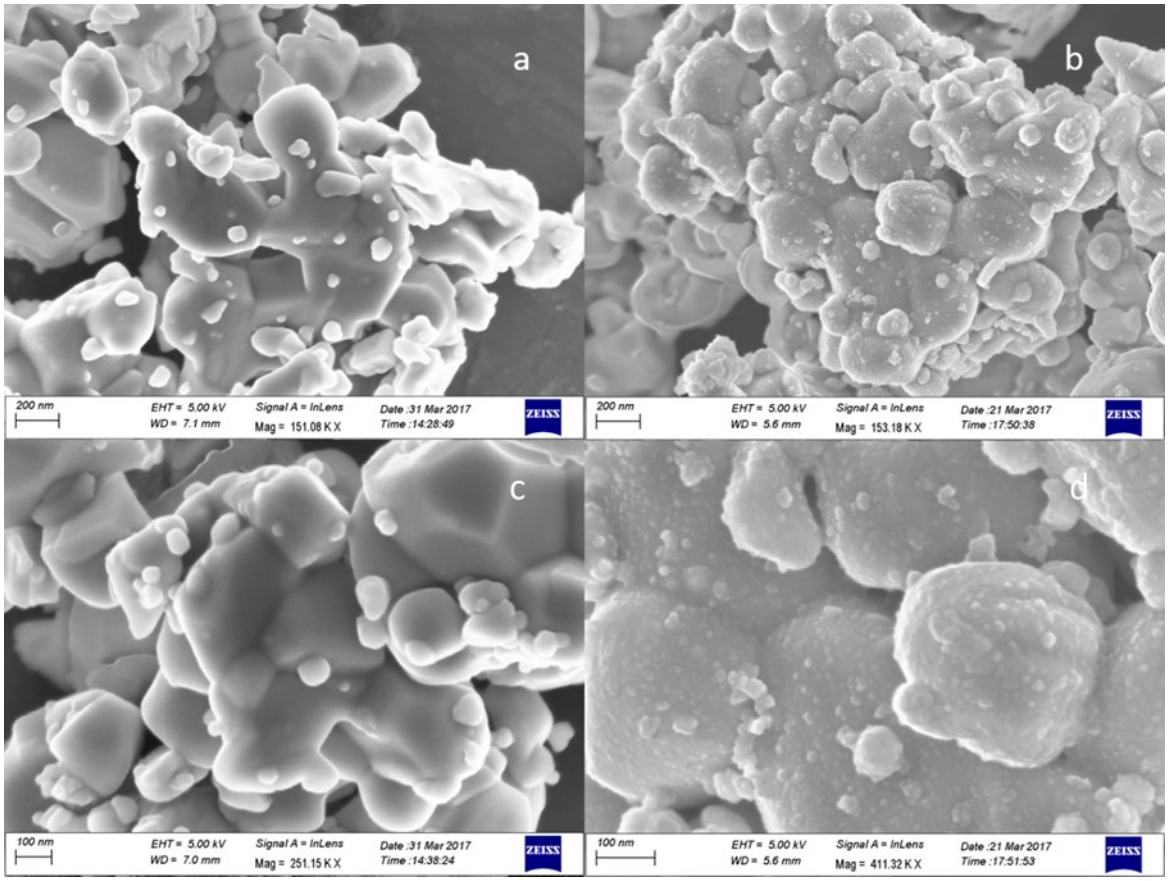


Figure. 2.2.4 SEM image of reduced a and c. CGO; b and d Ni impregnated CGO powder

The XRD pattern of NiO/CGO before reduction and pristine CGO is shown in figure 2.2.5, The peaks of CGO phase are indicated by ♦, NiO indicated by *. All peaks were assigned to either CGO or NiO meaning no impurities were found in the sample. NiO particle size calculated via (111) peak by Scherrer equation is 33.7 nm which was significantly larger than the size acquired from SEM image due to 40% volume loss during reduction.

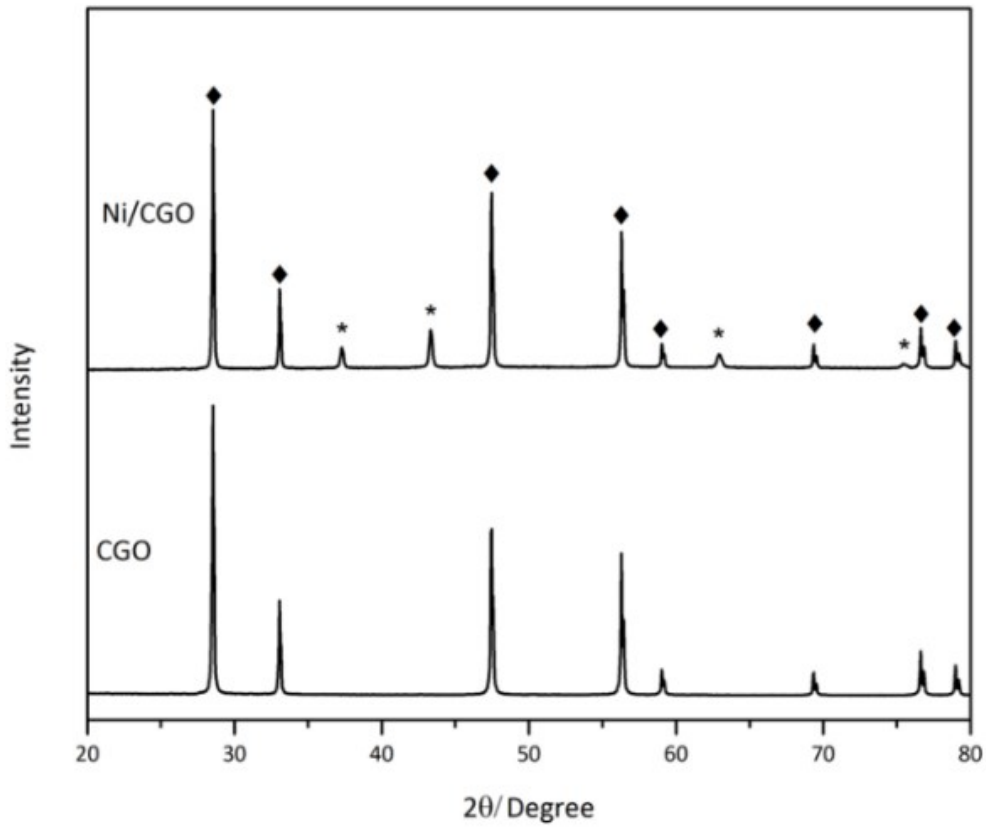


Figure. 2.2.5 XRD pattern of CGO and Ni/CGO, ♦ indicates doped CeO_2 phase, * indicates NiO phase

2.2.4.2 Mechanism Indication of Methane Pulse Experiment

During the methane pulse experiments, a loop valve is used to pass 0.3793 mL of pure methane over the sample. When the sample is Ni/CGO, the methane reacts with the surface producing a mixture of CO_2, CO, H_2 and H_2O (figure 2.2.6a). The main reaction on Ni/CGO was the partial oxidation of methane (POM) producing CO and H_2: $CH_4(g) + O \rightarrow CO(g) + 2H_2(g)$. There was also a small amount of CO_2 and H_2O produced. The form of oxygen on Ni/CGO is currently unknown, it could either be adsorbed oxygen on nickel, oxygen as the compound of nickel oxide, oxygen adsorbed on surface CGO or oxygen from the lattice of CGO. The signal of the mass spectrometer is proportional to the partial pressure of the monitored gas species and the relative intensity of different mass of such gas species, the signal was calibrated and converted into a production rate ($mL \cdot min^{-1}$), the calibration process was described in former chapter. An identical experiment using only CGO as the sample showed much lower conversion of methane (figure 2.2.6b), confirming that the main site of

methane interaction with Ni/CGO is either on the surface of nickel or at the nickel-CGO boundary. Interestingly, in this first pulse the amount of CO_2 produced by total oxidation of methane (TOM) producing CO_2 and H_2O: $CH_4(g) + 4O \rightarrow CO_2(g) + 2H_2O(g)$ was identical with CO produced by partial oxidation of methane (POM). On Ni/CGO, CO_2 and H_2O were detected by the mass spectrometer earlier than CH_4, CO and H_2. This is not observed on CGO, indicating that the total oxidation of methane on Ni/CGO is a direct oxidation step, rather than further oxidation of CO and H_2. It also indicates that the source of the oxygen used for TOM on these two samples are from different sites; on CGO the reaction involves surface oxygen, while on Ni/CGO it is either oxygen spilled-over to nickel[241] or oxygen at the interface between nickel and CGO[196]. In both cases, the concentration of all gases drops to background levels within 30 s.

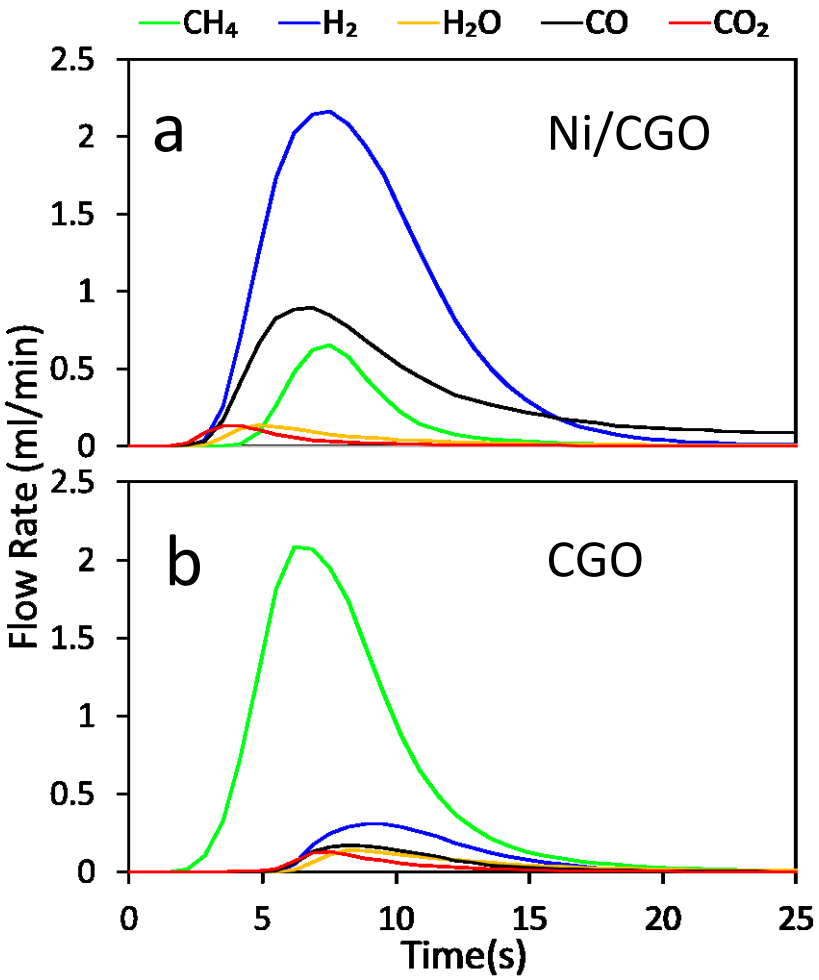


Figure. 2.2.6 The products of the first methane pulse on a. Ni/CGO; b. CGO. The y axis is the flow rate of each species in ml/min CH_4 (amu 15), H_2 (amu 2), H_2O (amu 18), CO (amu 28) and CO_2 (amu 44) are monitored. The methane pulse is injected from 0s. After 25s, all species except for CO has escaped from the system.

Because the methane reacting with the surface of the sample causes an oxygen gradient in the sample and possible carbon deposition, after the pulse a period of time (10, 30, and 90 min intervals were used, the results here are from pulses with 30 min interval) was allowed for the sample to reach equilibrium before another pulse of methane was passed over the sample. In this second pulse the CO_2 production fell by 80% in both samples (figure 2.2.7a and b), while by the third pulse there was negligible CO_2 production, indicating that this CO_2 is produced by surface oxygen via the total oxidation of methane (TOM), rather than by the water gas shifting reaction: $CO(g) + H_2O(g) \rightarrow CO_2(g) + H_2(g)$. It also suggests that the TOM process requires highly oxygenated sites on the surface of CGO and Ni, since the CGO becomes more reduced with each pulse.

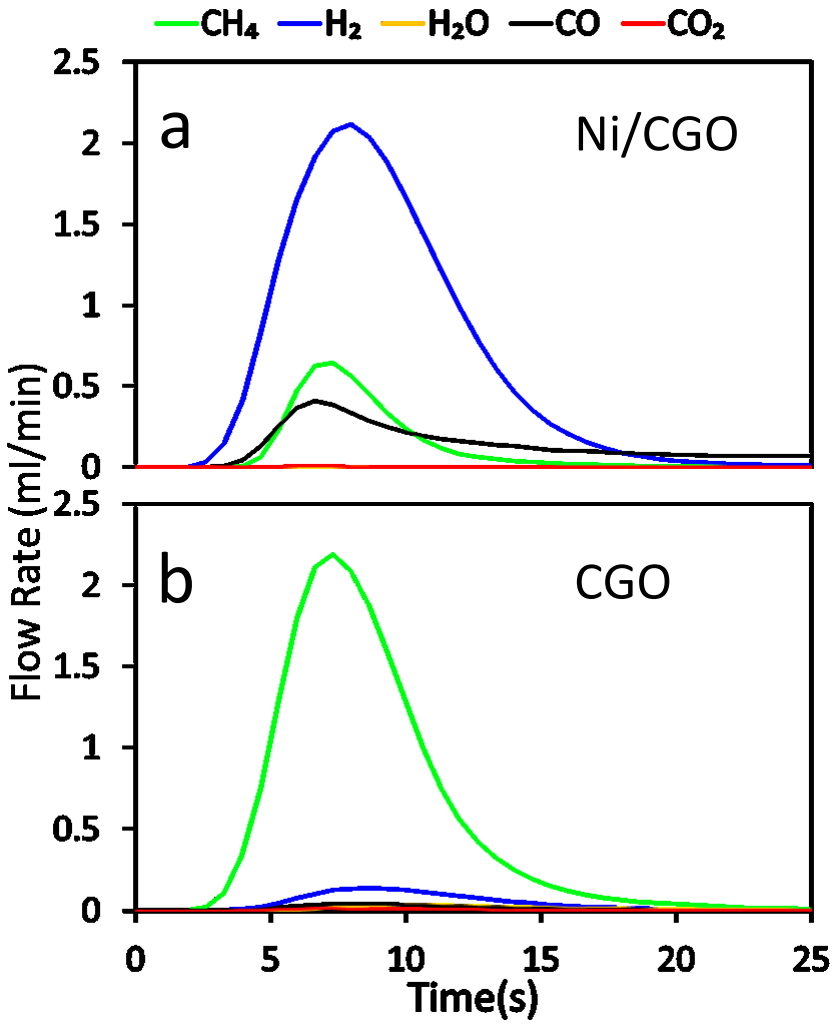


Figure. 2.2.7 The products of the second methane pulse on a. Ni/CGO; b. CGO. The y axis is the flow rate of each species in mL/min CH_4 (amu 15), H_2 (amu 2), H_2O (amu 18), CO (amu 28) and CO_2 (amu 44) are monitored. The methane pulse is injected from 0s. After 25s, all species except for CO has escaped from the system.

Starting from the second pulse, it becomes clear that CO is still being produced for a period of time after all the other gases have exited the reactor (figure 2.2.8). Identical experiments with either no sample or with Ni/YSZ (figure 2.2.8) showed no such behaviour, indicating that it is not the result of an interaction between gaseous CO and the reactor or the nickel particles. This leaves the reaction of carbonaceous species on the nickel surface with oxygen from the CGO as the likeliest explanation. With subsequent pulses, this tail of CO production becomes longer, eventually reaching over 30 minutes. This indicates that whatever reaction is producing the CO is becoming slower as the CGO becomes more reduced.

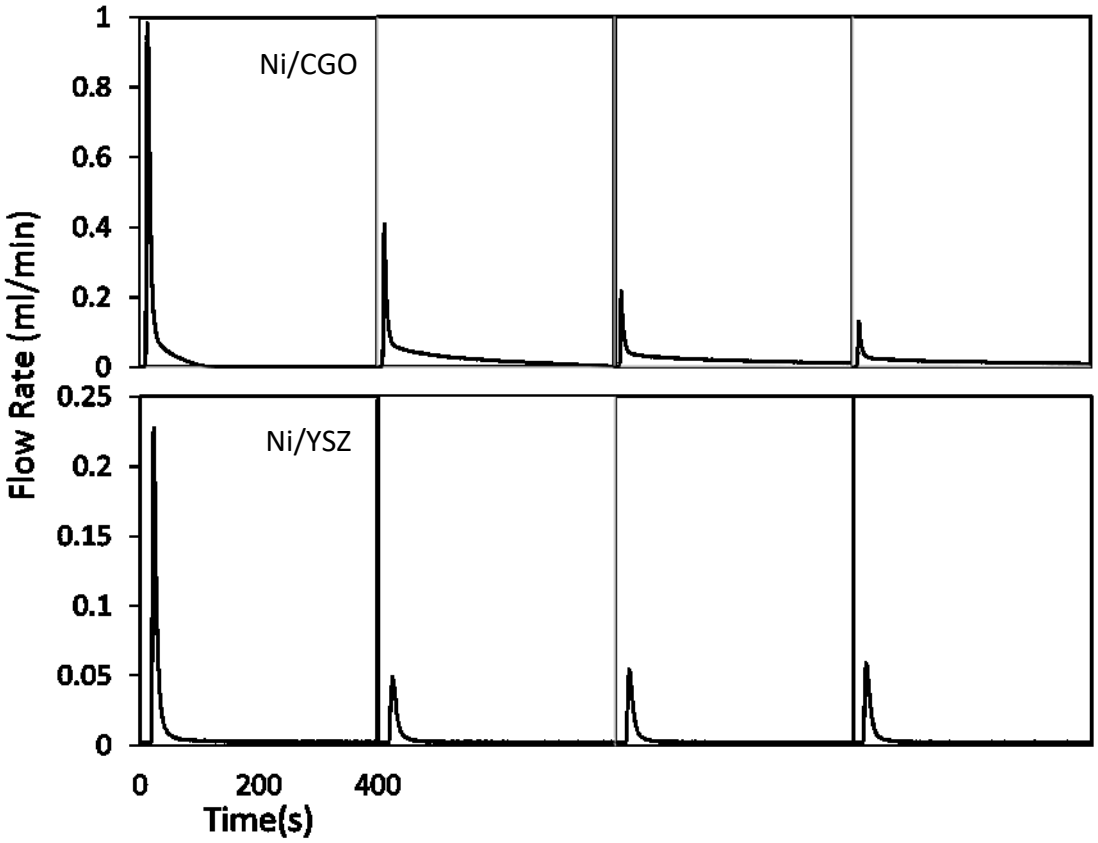


Figure. 2.2.8 The first to fourth CO production peak of a methane pulse on Ni/CGO and on Ni/YSZ. From the second methane pulse, the CO production peak consists of an initial peak and a tail, the length of tail extends with pulsing number.

In these later pulses, the CO production can be divided into two phases – the initial peak coincident with the other species from the methane pulse, and the tail which continues after all the other gas species have fallen to background levels. The shapes of the two peaks suggest these are two oxidation processes. In all the pulses from the second pulse onwards, and

before the tail overlapped with the next pulse (fifth pulse), the total amount of CH_4 consumed and CO produced, which is the area under the consumption/production peak, remains constant within the range of error (<±2%) (figure 2.2.9), despite the massive change of the peak shape. The initial peak is determined by fitting the CO production peak with peak functions, it is found that the initial peak is best fitted by the asymmetric double sigmoidal function:

$$y = A * \frac{1}{1 + e^{-\frac{x - x_c + \frac{w_1}{2}}{w_2}}} * \left(1 - \frac{1}{1 + e^{-\frac{x - x_c - \frac{w_1}{2}}{w_3}}}\right)$$

This function has been widely used in chemical and physical studies[242, 243]. In which A, x_c, w_1, w_2, w_3 are fitting parameters, x represents the time axis and y represents the CO production rate. The area under the fitted peak is used as the CO produced in the initial major peak. The original second CO production peak and the fitted peak are shown in figure 2.2.9a.

The ratio of the CO amount in the initial peak to the amount in the tail is depicted in figure 2.2.9b, it decreases with number of pulses. This suggests that the two processes are competing with each other and involve a reaction on nickel sites. The spill-over of oxygen onto metal sites from doped ceria has been widely observed previously [94, 195, 199]. Due to the oxygen deficiency on nickel surface, the oxygen for CO production can only come from the lattice oxygen of CGO. It is likely that the initial peak is methane cracking at the surface of nickel with any deposited carbon species (C/CH_x) being oxidized by the surface oxygen from CGO. The tail is caused by oxidation of the deposited carbon species by oxide ions migrating from the bulk of CGO after the surface oxygen is depleted (the Mars-van Krevelen mechanism). When the tail of CO production overlaps with the next pulse at the fifth pulse, this means that at the time of the fresh injection of methane, it is likely that there is still carbon remaining on the surface of the nickel from the previous pulse, blocking the reactive sites. Because of this, the consumption of methane and the production of CO decrease after the fifth pulse. This deduction is further proved by methane pulse with 90 min interval, in which the CO tailing did not reach the next injection during all 15 pulses. The consumption and production of all species remained constant after the first few pulses whereas these are changing with number of pulses in the 30 min interval experiment shown in figure 2.2.8, suggesting the tailing is oxidation of carbon species deposited on Ni.

Temperature-programmed oxidation (TPO) experiments following these methane pulse experiments show that there is no carbon deposition on the sample, as long as enough time has been left between pulses to allow the concentration of CO to drop to baseline levels. For example, at high oxidation states carbon can be eliminated within 20 s, while after the second methane pulse the carbon elimination time increases to 100 s. As the CGO oxidation state decreases, the time required can increase to 60 mins. In methane pulse with 90 min interval, the CO tailing did not extend to the next pulse during the whole duration, and no carbon is detected in subsequent TPO, as opposed to TPO after 10 min and 30 min interval methane pulse experiment (The TPO results of methane pulse with different intervals is included in figure 2.2.14). Conversely, if not enough time is left between pulses (i.e. if CO is still being detected at the time of the next pulse of methane) then there is carbon deposition detected by subsequent temperature-programmed oxidation (TPO) experiments (figure 2.2.14). Even if some pulses have overlapped, if enough time is left after the final pulse then no carbon is detected by TPO.

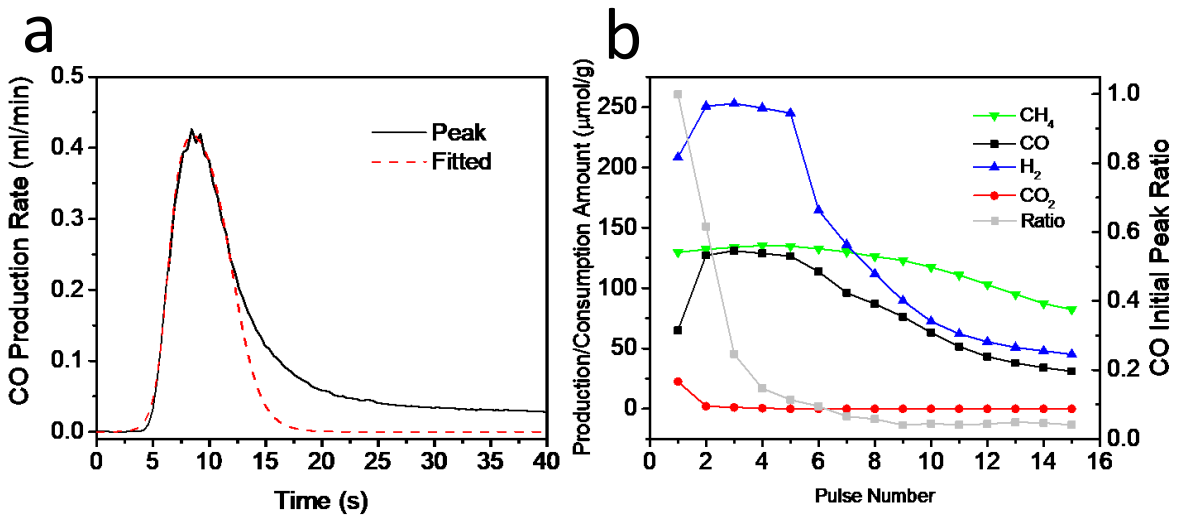


Figure. 2.2.9 a: The second CO production peak in methane pulse experiment and the fitted initial peak; b: Red, green and black lines are the amount of CO and CO_2 produced, and CH_4 consumed, in each methane pulse; the grey line is the proportion of CO produced in initial peak versus the total CO produced in each methane pulse. The methane pulses were injected with 30min intervals.

These observations strongly suggest that the initial carbon deposition is fully reversible on metal-CGO based catalysts if there is still reducible CGO present. The carbon deposits are oxidized at a low temperature of 450 °C in the TPO measurement, compared with other's

work, in which highly amorphous carbon is oxidized at ~530 °C and graphitic carbon at 650 °C [244]. This suggests that carbon deposits caused by the methane pulses are in more disordered form, likely in the form of clusters made only of several atoms, as reported by Hofmann to be the initial stage of carbon formation[245]. Amorphous carbon resulting from methane reforming was oxidized at ~600 °C[187], which further suggests that the carbon deposition here was not agglomerated. Since methane cracking on nickel would readily result in crystallized carbon (graphite for example) [246], these observations suggest that when carbon deposits at a rate which is faster than oxygen can be supplied, then carbon would aggregate on nickel and with increasing carbon concentration would turn from dispersed clusters to aggregated amorphous carbon, and finally to graphitic carbon.

To confirm these hypothesis, in-situ Raman was performed.

2.2.4.3 Methane Pulse with In-Situ Raman Spectroscopy

The experiment setup and data acquisition were described in chapter 2.2.1. Figure 2.2.10 shows the Raman spectrum of the impregnated Ni/CGO sample obtained in-situ at 600 °C after it had been reduced in hydrogen. The sharp peak at approximately 450 cm^{-1} is the main F_{2g} Raman peak of ceria which corresponds directly to the Ce^{IV}-O bond[181]. The small shoulder observed at approximately 600 cm^{-1} arises due to oxygen vacancies within the lattice. The broad peak at 900-1330 cm^{-1} is the second order mode of the Ce^{IV}-O vibration peak. Ordinarily the NiO peak would also be located in the same position, however we expect that very little evidence of NiO should be present after reduction and as a result do not expect it to contribute. The main F_{2g} peak is a direct indication of the percentage of Ce^{IV} at the sample surface (determined by the penetration depth of Raman laser, which changes with different oxidation state) relative to the initial state during monitoring. As a result, the relative oxidation state of the ceria surface can be monitored in-situ and in real time using the integrated intensity of the F_{2g} peak.

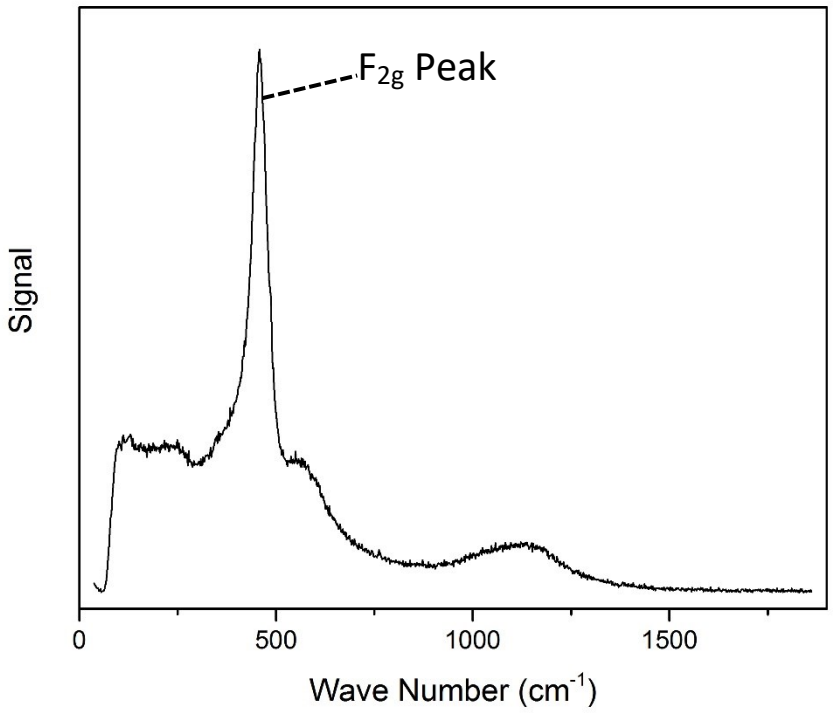


Figure. 2.2.10 The Raman spectrum for reduced Ni/CGO sample, recorded from 0-1780 cm^{-1}

Five gas species were monitored using the mass spectrometer during the pulse experiment: H_2, CH_4, CO, CO_2 and H_2O, the production and consumption amount of which are plotted in figure 2.2.11. The integrated intensity of the F_{2g} Raman peak was monitored during the methane pulse experiment and the integrated intensity is plotted in figure 2.2.12a along with the CO signal. TPO was performed on the Ni/CGO sample after pulse experiments to examine any carbon deposition.

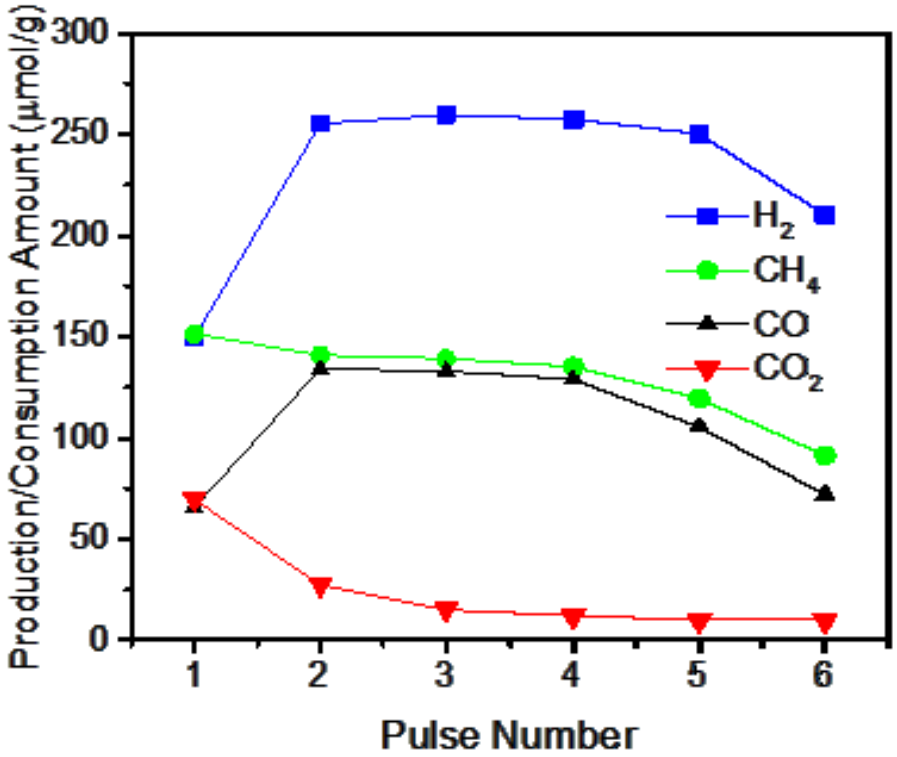


Figure. 2.2.11 Production/consumption amount of gas species in the methane pulse experiment with in-situ Raman by mass spectrometer versus pulse number

The result of the mass spectrometry test was similar to previous methane pulse experiments. POM was the major reaction. While a large amount of CO_2 and H_2O were produced in the first pulse, they dropped quickly in the second and nearly disappeared in the third pulse. A CO tail appeared from the second pulse and extended with the number of pulses. The total production of CO was identical in the second and third pulse, and after the third pulse the CO tail extended longer than the interval time (20 min) and CO production reduced. The change in the amount of H_2 produced was similar to that of CO.

The integrated intensity of the F_{2g} peak decreased sharply immediately after each methane pulse. It then gradually recovered during the interval before the next pulse, although not to the same intensity as prior to the previous pulse. As the number of pulses increased, the rate of recovery decreased significantly, and the intensity recovered to a lower level. Although TPO showed that there was carbon deposition on Ni/CGO after the methane pulse experiments, no peak of carbon was observed in the Raman spectra during the pulse experiment, which would normally appear as two peaks, the D and G, at 1350 cm^{-1} and 1580

cm^{-1} respectively. The absence of these peaks indicates that the carbon was only present in a dispersed atomic form below the Raman spectrometer detection limit rather than an aggregated amorphous or crystalized form.

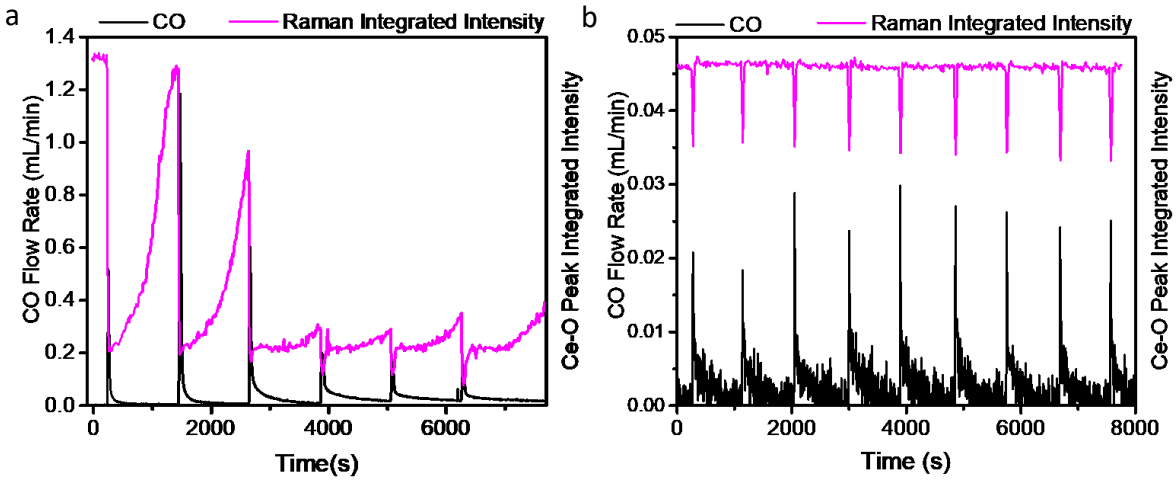


Figure. 2.2.12 CO signal from the mass spectrometer and integrated Ce^{IV}-O peak intensity with time in methane pulse on a) Ni/CGO; b) CGO

While a significant drop of the F_{2g} peak intensity after each pulse was observed in experiments on Ni/CGO, on CGO the reduction of the peak intensity was much smaller (as shown in figure. 2.2.12b). This indicates that the near surface oxygen of ceria was consumed immediately after the pulse by the oxidation of intermediate CH_x/C species on the nickel surface. The recovery of the peak indicates that the surface oxygen was resupplied by bulk oxygen of CGO. As the pulses continue, CGO oxygen stoichiometry decreases and bulk migration rate decreases resulting in the decrease of carbon re-oxidation rate. This suggests that bulk oxygen migration is the rate determining step of carbon oxidation.

After the third pulse, the oxidation state was maintained at a plateau at a low level for 18 min, and then the recovery of the oxidation state accelerates. The mass spectrometry data showed the CO tail on the third pulse faded to the baseline value at the same time. This suggests that, after the depletion of surface oxygen, oxygen migrating from bulk ceria preferentially spills-over to the nickel surface to react with the carbon. After the carbon is removed, oxygen from the bulk of CGO remains on the surface of the CGO and results in the acceleration of the recovery of the F_{2g} peak.

The combination of in-situ Raman and mass spectrometry provides direct evidence of the nature of the reaction of CH_4 on Ni/CGO, proving that methane was first adsorbed and decomposed on nickel before being oxidized by oxygen migrated from the surface of the CGO. Bulk oxygen from CGO then migrates to the surface to fill the vacancy. It also indicates that oxygen migration from bulk CGO to the surface is the rate-limiting process in carbon oxidation.

From the preceding conclusions, a mechanism for the reaction can be derived (CO and H_2 desorption are rapid at 600 °C and so have been omitted) [247, 248]:

a. $\boldsymbol{O_{CGO}^{surface} \rightarrow O_{Ni}^{*}}$

b. $\boldsymbol{CH_4(g) + S_{Ni}^{*} \rightarrow C_{Ni}^{*} + H_2\,(g)}$

c. $\boldsymbol{CH_4(g) + O_{Ni}^{*} \rightarrow CO_2(g) + H_2O\,(g)}$

d. $\boldsymbol{O_{CGO}^{surface} \rightarrow O_{Ni}^{*} + C_{Ni}^{*} \rightarrow CO(g)}$

e. $\boldsymbol{O_{CGO}^{bulk} \rightarrow O_{CGO}^{surface}}$

f. $\boldsymbol{C_{Ni}^{*} \rightarrow C_{amorphous}}$

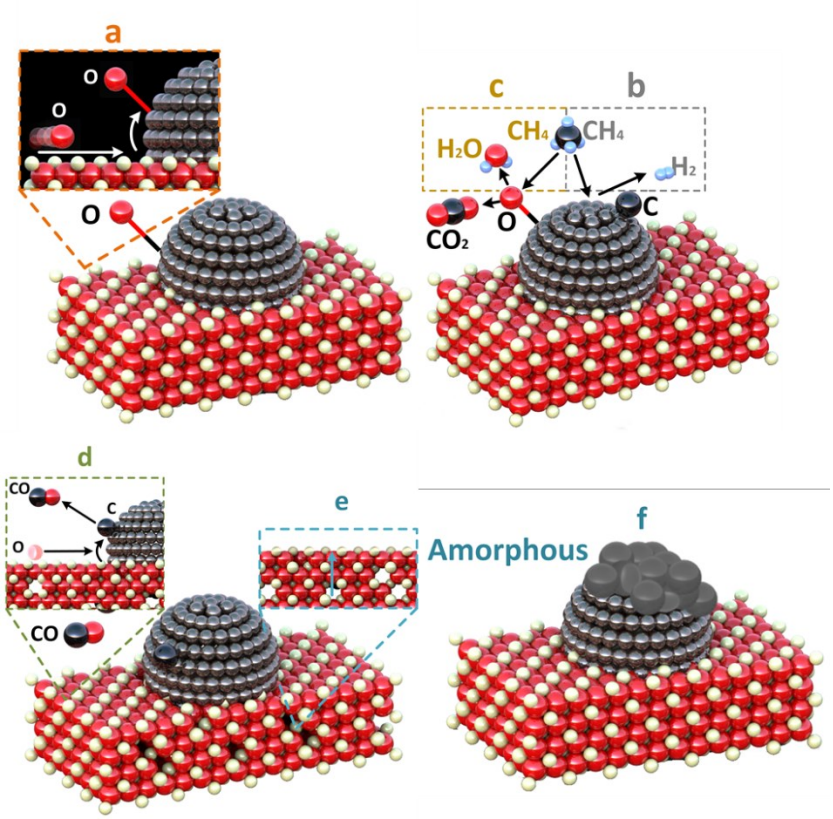


Figure. 2.2.13 Proposed mechanism for methane oxidation in given conditions: a. Oxygen is first migrated to the surface of Ni; Then methane either: b. Decomposes at the surface of ceria or c. Reacts with adsorbed oxygen, then d. Carbon species are oxidized by oxygen spilled-over from the ceria surface; after depletion of surface oxygen, e. Oxygen from the bulk ceria migrates to the surface; If carbon is not oxidized, f. It will accumulate and form amorphous and eventually crystalized carbon deposits.

As shown in figure 2.2.13, the process of methane oxidation on nickel/CGO consists of six elementary steps: a. oxygen migration across the CGO surface and spill-over to the nickel surface; b. methane cracking at the surface sites of nickel; c. methane total oxidation by adsorbed oxygen on the nickel surface; d. oxygen reaction with adsorbed carbon species; e. oxygen migration from bulk to surface CGO; Finally e. if carbon species are not oxidized timely they form amorphous carbon on nickel. Surface migration and spill-over of oxygen is generally believed to be very fast compared with bulk diffusion (10^5 times faster according to Holmgren's work[249]). The reaction between adsorbed carbon species and oxygen spilled-over from CGO is fast compared with methane dehydrogenation according to literatures [188, 250]. In this work, the dehydrogenation of methane in each pulse is completed in the major peak less than 20 s after the pulse was injected, as can be seen by the fact that there is no hydrogen production after the initial pulse, while the length of the CO production tail ranged from 30 s to 30 min after the major peak, indicating that the reaction between surface carbon and oxygen is not the rate-limiting step of sequent carbon oxidation. Therefore, it is reasonable to conclude the rate determining step is oxygen migration from bulk to surface CGO.

According to Chin's work, at $\boldsymbol{pO_2/pCH_4}$< 0.08 methane is deduced to mainly activate at empty sites of metal catalysts, without the participation of oxygen[190]. In our case, sample is reduced in $\boldsymbol{pO_2}\approx10^{-14}$atm, and oxygen is absent when methane is injected, it is safe to say the participation of oxygen in activation of methane is negligible. The absence of H_2O from the second pulse suggests the absence of ***OH**-group-producing processes on the nickel surface, as H_2O is mainly produced via: $\boldsymbol{OH*+H*\rightarrow H_2O*}$ or $\boldsymbol{OH*+OH*\rightarrow H_2O*+H*}$ [251]. This suggests in the POM at given conditions, the oxygen from CGO participates in the reaction only by oxidizing carbon species on Ni.

Temperature-programmed oxidation experiments following these methane pulse experiments show that there is no carbon deposition on the sample, as long as enough time has been left between pulses to allow the concentration of CO to drop to baseline levels. For example, at high ceria oxidation states carbon can be eliminated within 20s, while after the second methane pulse the carbon elimination time increases to 100s. As the ceria oxidation state decreases, the time required can increase to 60 mins or more. Conversely, if not enough time is left between pulses (i.e. if CO is still being detected at the time of the next pulse of

methane) then there is carbon deposition detected by subsequent temperature-programmed oxidation (TPO) experiments (figure 2.2.14 inset). Even if some pulses have overlapped, if enough time is left after the final pulse, then no carbon is detected by TPO.

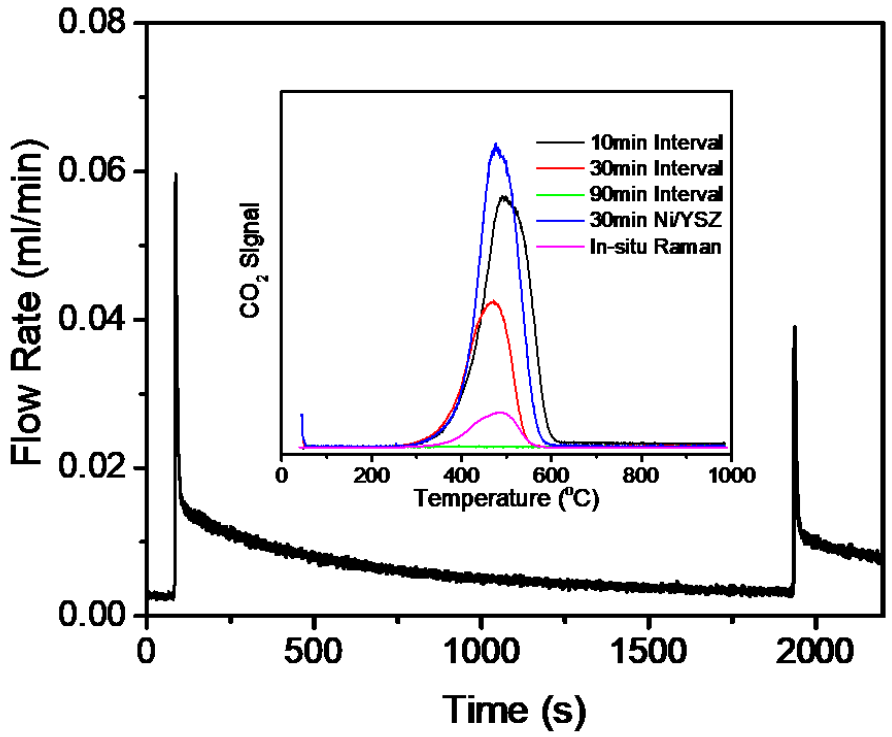


Figure. 2.2.14 An excerpt from the CO production of methane pulse with 30min interval, showing the CO production from the fifth methane pulse. It indicates the overlaps of the CO tail with the next pulse, inset is the temperature programmed oxidation after the methane pulse with different interval on Ni/CGO and Ni/YSZ indicated by CO_2 production.

These observations strongly suggest that the initial carbon deposition is fully reversible on metal-ceria based catalysts if there is still reducible CGO present. The carbon deposits are oxidized at 420 °C in the TPO measurement, but on the same sample the Raman spectra does not show any carbon peak, suggesting that carbon deposits caused by the methane pulses are highly dispersed over the nickel surface, likely in the form of clusters made only of several atoms[245]. Since methane cracking on nickel would readily result in crystallized carbon (graphite for example)[246], these observations suggest that when carbon deposits at rate which is faster than oxygen can be supplied, then carbon would aggregate on nickel and with increasing carbon concentration would turn from dispersed clusters to aggregated amorphous carbon, and finally to graphitic carbon.

2.2.4.4 Re-oxidation of Ceria by Steam

Before applying moisture trap to Ar pipeline in all our experiment, in the methane pulse with a 90 min interval, the baseline of water was observed to drop after the major peak of the pulse, while the baseline of hydrogen increased at the same time, as shown in figure 2.2.15. After ~40 min, the H_2 baseline decreased and H_2O increased again. This is due to the oxidation of reduced ceria by trace amounts of water in Ar (<10ppm):

$$H_2O + V_o^{\cdot\cdot} + 2Ce'_{Ce} \rightarrow H_2 + O_O^{\times} + 2Ce_{Ce}^{\times}$$

Following each methane pulse, after ~40 min of exposure to trace amounts of water, ceria was replenished to a certain level of oxidation state. This suggests steam can be used to control the oxidation state of ceria.

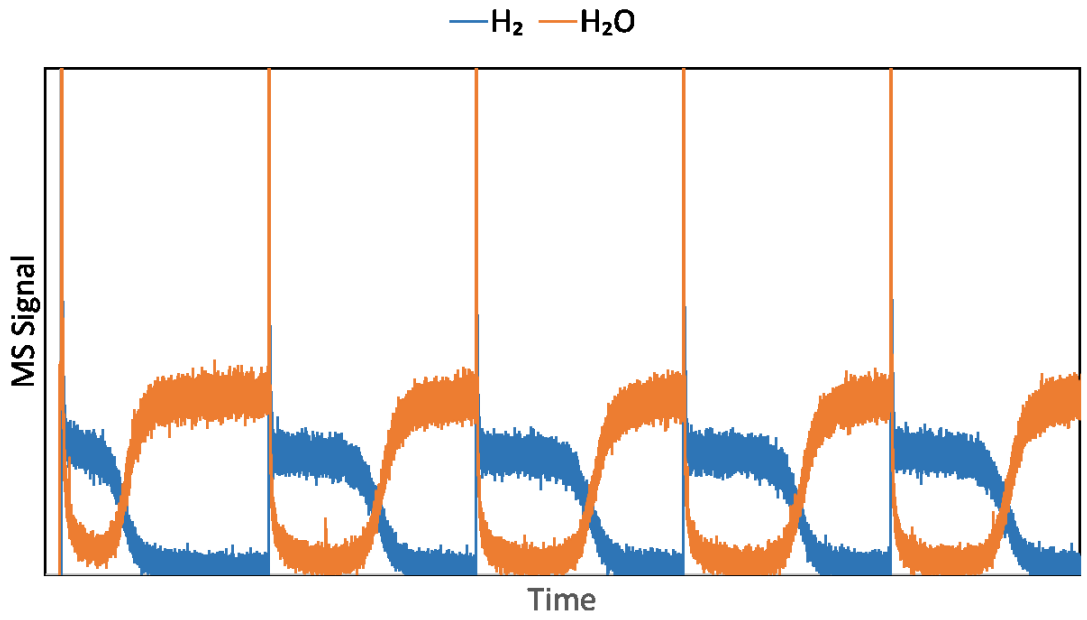


Figure. 2.2.15 The decrease of H_2O baseline and increase of H_2 baselines after each methane pulse. The y-axis is logarithmic-scaled to better show the low content.

Therefore, to confirm that the changing carbon oxidation rate is related with oxygen stoichiometry of CGO, CGO was re-oxidized in between pulses of methane, using pulses of 12.3% steam. To avoid the influence of carbon deposition, a smaller loop size is used. Seven methane pulses of 0.2326ml (equivalent to 103.8 µmol·g^{-1} CH_4) were injected at 600°C with

20min interval in each cycle. Similar steam pulses performed on nickel powder of 50 nm particle size did not show noticeable consumption of steam, therefore the nickel oxidation is negligible, suggesting that it can be assumed that only CGO was oxidized in the steam pulse. Pulses of 12.3% steam/Ar mixing gas is injected to the sample and produced only hydrogen. CO production peaks of the first cycle are shown in figure 2.2.16, and the integrated production amount is concluded in figure 2.2.17. The CO production amount is constant in the second to sixth pulse in a cycle despite the shape change, which is consistent with previous observations, and steam pulses are able to fully reoxidise the sample to its initial state, as evidenced by the fact that CO production in all four cycles are identical with each other (figure 2.2.17). The methane pulse features recover at the start of each cycle, suggesting that the CGO oxidation state is the determining factor in the carbon oxidation rate.

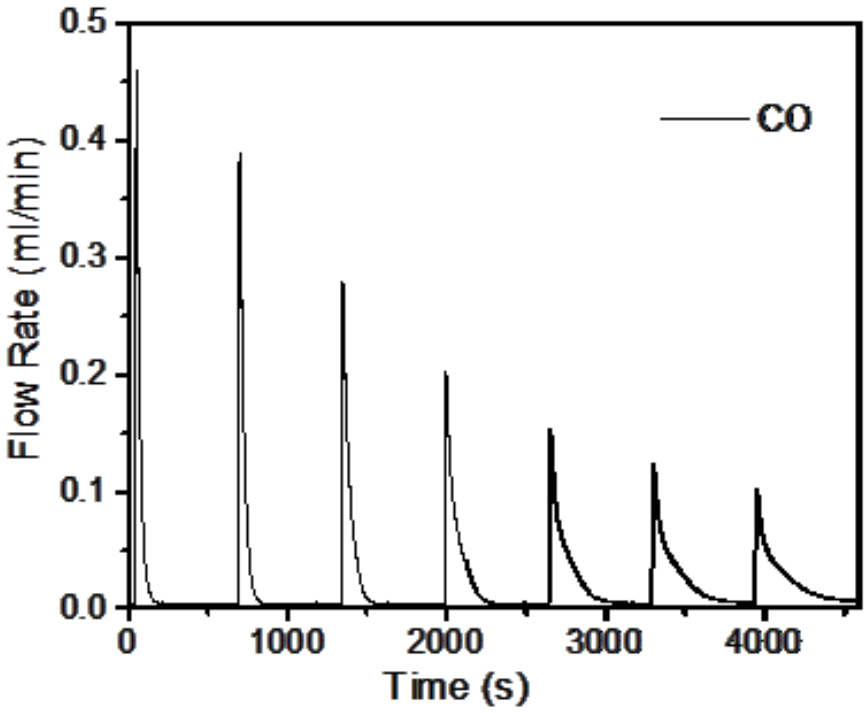


Figure. 2.2.16 The CO production peaks in the first cycle of methane pulse with steam reoxidation

Oxygen non-stoichiometry δ after each pulse relative to the initial oxidation state of CGO at the start of each cycle is calculated by CO and CO_2 production. As shown in figure 2.2.18, the selectivity towards POM in all four cycles followed the same trend as a function of oxygen non-stoichiometry of CGO, which are over 85% at δ = 0.027, and further increases to >99% at

δ=0.073. Indicating the selectivity of methane oxidation is closely related with oxidation state of CGO, a high selectivity towards POM can be achieved by slightly increasing the oxygen non-stoichiometry of CGO and maintaining oxygen supply by steam. Therefore, while oxygen often over-oxidizes the metal compound in catalyst, making it prone towards TOM[252], steam, and potentially CO_2 as they share similar oxidation ability towards CGO, can be used in methane CLR for controlling of CGO oxidation state for high POM selectivity.

The CO production amount in the initial peak as a function of CGO non-stoichiometry also showed good reproducibility for all cycles. According to the mechanism deduced previously, the CO production amount in the initial peak indicates oxygen on the surface of CGO that is consumable by oxidation of carbon species. The oxygen consumption in the first initial peak of each cycle is ~90 $\mu mol \cdot g^{-1}$, equivalent to two oxygen monolayers on CGO, calculated using the condition of full oxygen stoichiometry ($Gd_{0.1}Ce_{0.9}O_{1.95}$), and specific surface area of 100 $\mu m^2 \cdot \mu m^{-3}$. On the other hand, using the total reducible oxygen (~830 $\mu mol \cdot g^{-1}$) and reducible surface oxygen ratio at 100 nm (~10%) from Xu's work[253], the estimated reducible surface oxygen at full oxidation state of CGO is 83 $\mu mol \cdot g^{-1}$, which is in good accordance with our experiment data. This in turns adds the credibility of our proposed mechanism.

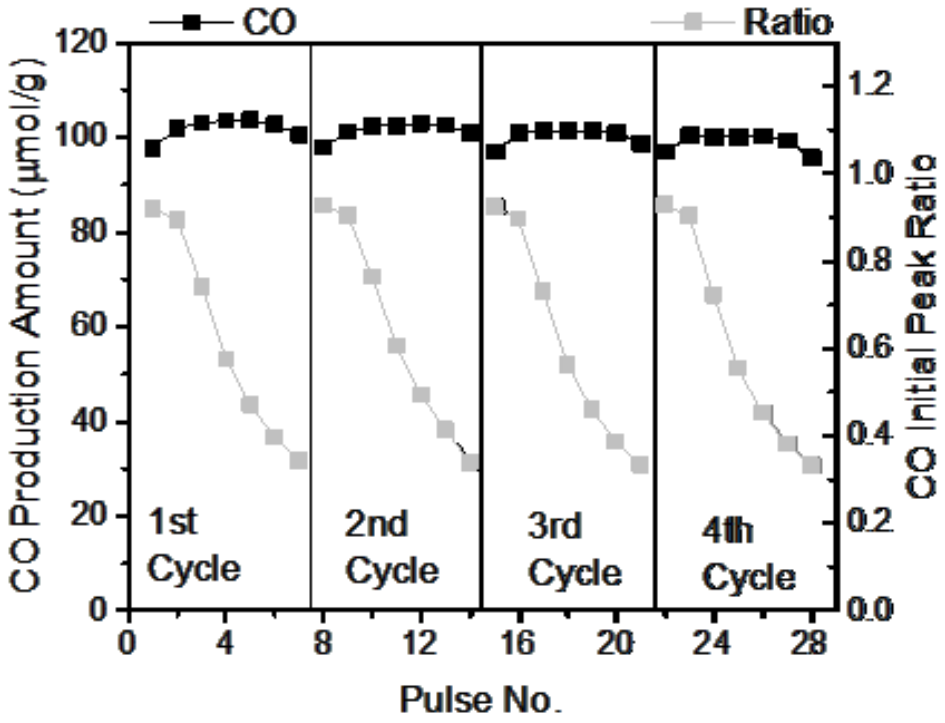


Figure. 2.2.17 The CO production and initial peak ratio in methane pulse with water oxidation experiment. The black line is the CO production amount in each methane pulse; the grey line is the proportion of CO produced in the initial peak versus the total CO production in each pulse.

Some literature suggests that the metal sites at the metal-CGO interface are more active because the adsorbed species would dissociate faster at the interface due to formation of bridging bonds of adsorbed species (-CH_4) with metal and oxygen ions on the support [94, 196, 254], therefore, such an effect is closely related to the concentration of surface oxygen vacancies [255]; However, here it was found that the production of CO and consumption of methane of each cycle did not change with decreasing CGO oxidation state, which suggests the activation of methane is not affected by the oxygen concentration on CGO surface. Such irrelevance has also been found by Wei [256], who concluded the support is not involved in the activation of methane. Also, if we consider a nickel surface site density of 3.3×10^{-3} $\mu mol\cdot cm^{-2}$ [257], and nickel average diameter of 20nm, assuming the nickel particles are all in hemispheric, the concentration of gravimetric surface site on the nickel surface is then 91.9 $\mu mol\cdot g^{-1}$, which is slightly smaller than the CO production in each methane pulse. However, the concentration of perimeter sites is 2.3 $\mu mol\cdot g^{-1}$, which is too small for the amount of methane consumed. It is still difficult to conclude that methane does not preferably activate on the perimeter, but it is safe to say that in this condition the top of nickel also contributes significantly to the activation of methane. However the high activity of metal-oxide interface has been well accepted in the field of catalyst, the reason it is not significant here is probably: 1. The nickel particle size in this work (~20 nm) is not small enough to give a high perimeter/surface ratio; 2. In the given oxygen free condition, there is already a high concentration of oxygen vacancies on the surface of CGO, so the decrease of oxygen concentration at the interface is not significant during the methane pulse.

If the steam pulse is introduced while there is still CO being produced (figure 2.2.19a), the observation is that there is a spike of hydrogen and an increase in the rate of CO production concomitant with an increase in the oxidation state of the CGO. Parallel experiments on Ni/YSZ after methane pulses did not show similar hydrogen peaks and increment of CO (figure 2.2.19b). The results are consistent with the steam reacting exclusively with the CGO, and not with the carbonaceous species present on the surface of the nickel. The increasing of CGO oxidation state in turn enhance the carbon oxidation rate. This shows that even when steam is present to react with carbon species on the nickel, the reaction still proceeds via the Mars-van Krevelen mechanism, with oxygen migration being the rate limiting step.

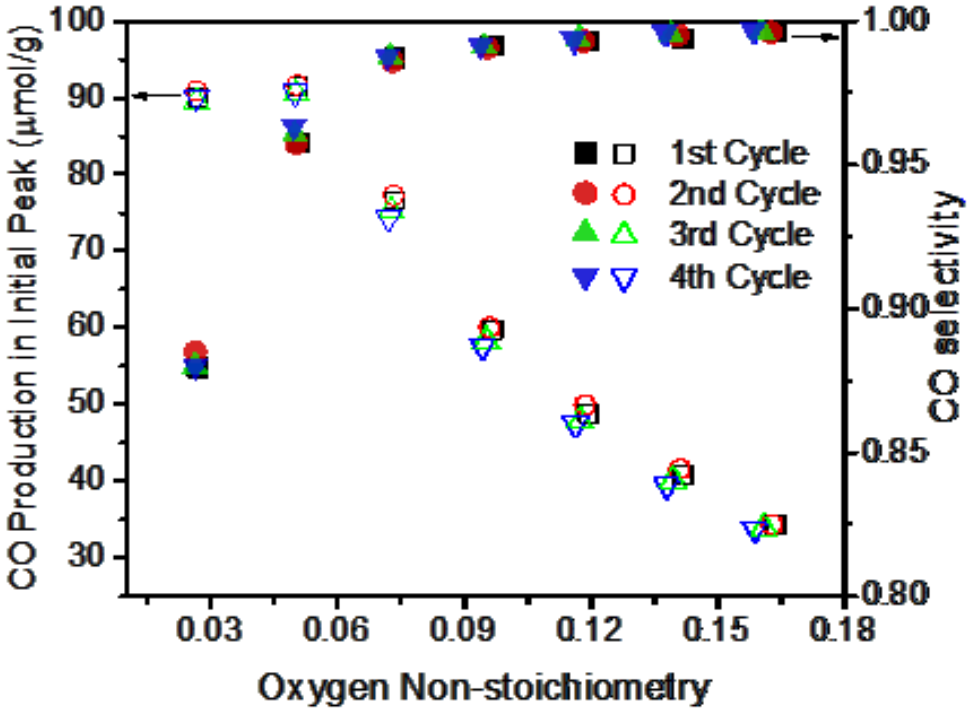


Figure. 2.2.18 The CO production amount in the initial peak and selectivity towards POM plotted with changing oxygen non-stoichiometry in four cycles of methane pulse with water reoxidation

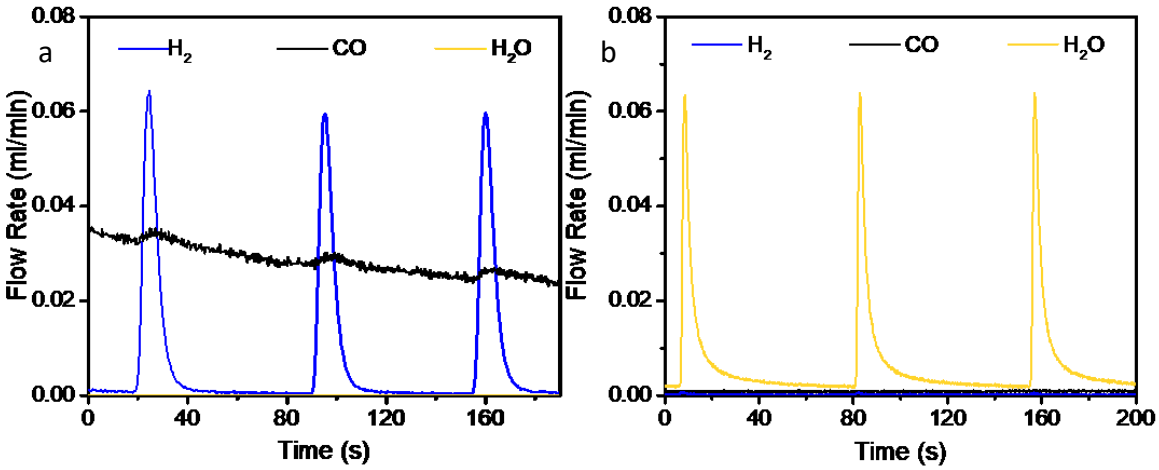


Figure. 2.2.19 a) An excerpt from water pulse oxidation in the methane pulse with water oxidation. It shows that all water was converted to hydrogen and that the rate of CO oxidation was enhanced. b) An excerpt from water pulse oxidation on Ni/YSZ after methane pulses. In the methane pulse with water re-oxidation experiment 12.3% water/Ar pulses were injected every seven pulses of methane until no hydrogen is produced.

From the methane pulse experiments and water oxidation shown in 2.2.4, we have found that the oxidation of methane on Ni/CGO mainly went through a MvK route instead of L-H or E-R route, with oxidation migration from bulk from the surface being the rate-determining step and the key step of carbon deposition. These reaction mechanisms were introduced in section 2.1.1. This information about the mechanism and the fact that a single rate-determining step is identified for the process can potentially provide access to the intrinsic properties of heterogeneous catalysts. Apart from the qualitative deduction of the reaction mechanism, a great deal of quantitative information can be extracted from these pulse experiments, such as integrated intensity of peaks and fitting of decay of peaks. Taking this work as an example, ceria non-stoichiometry can be calculated from the consumption of oxygen. Metal surface area is closely related with the consumption of methane in the initial peak. The diffusion coefficient and diffusion distance can potentially be extracted from the fitting of the decay of the CO peak. Also, carbon deposition amounts and carbon oxidation rate of every pulse on Ni/CGO can easily be extracted. The combination of these two reflects the carbon resistance of the catalyst. These can surely be worked out in the future.

2.3 Conclusions and Implications

To summarise, we have applied facile methane pulse experiments on Ni impregnated CGO powder catalyst to investigate the reaction of methane in oxygen free conditions. The CO tail is observed for the first time and related with the mechanism and kinetic of methane oxidation. By analysing the shape of peaks and the production amount of species, following conclusions were drawn:

1. Partial oxidation of methane on Ni/CGO catalyst goes through a Mars van-Krevelen type mechanism, in which methane is first activated on nickel, forming carbon species (CH_x*) and then oxidized by oxygen migrated from CGO. Total oxidation of methane only happens when CGO oxidation state is high, and likely involves oxygen adsorbed on nickel. Nickel has no appreciable solubility in CGO Ni [258] so the presence of Ni in the CGO lattice was discounted:
    a. The activation of methane is not affected by the CGO oxidation state. All the surface of nickel contributes to the activation of methane.

b. There are two oxidation stages of carbon species: first is oxidation by surface oxygen of CGO, the second is by the oxygen migrated from the bulk CGO after surface oxygen is depleted. The rate limiting step of the second oxidation process is the oxygen migration from bulk to surface of CGO, whose rate decreases with increasing oxygen non-stoichiometry of CGO.

2. The highly amorphous carbon deposition after methane pulse deactivates the catalyst by blocking the active sites on nickel surface, and can be eliminated by oxygen from CGO, if enough time is allowed for the migration of oxygen from bulk.
3. The oxygen migration and POM selectivity is closely related with oxidation state of CGO. Low concentration of steam can replenish the oxidation state of CGO without significant oxidation of nickel and thus can be used to control the oxidation state.

These results have implications for the design of nickel on doped ceria supports for both SOFC anodes and for methane chemical looping combustion/reforming catalysts.

The results indicate that the rates of carbon oxidation by oxygen on nickel, the spill-over of oxygen onto nickel, and the surface transport of oxygen on CGO are rapid compared to the bulk transport of oxygen in CGO, and this has different consequences for catalysts compared to SOFC anodes. In SOFC anodes, methane is continuously supplied, and the oxygen is always supplied from the bulk of the oxygen-conducting phase, so the rate of methane oxidation will be limited by the rate of oxygen transport through the bulk. The activation of methane, however, is determined by the surface area of nickel. Therefore, to mitigate carbon deposition in SOFCs, the rate of methane activation needs to be smaller than the carbon oxidation. In other words, the surface area of nickel needs to be matched to the thermodynamic equilibrium of the system and the structure of CGO support.

The methane pulse experiment used in this work has proven to be a useful tool to analyse the catalytic properties of heterogeneous catalysts, especially those reactions that contain various steps with different rates, such as the oxidation of methane. As discussed in 2.2.4, it can be useful in extracting intrinsic information on electrode materials and catalyst.

In this chapter a facile ambient-pressure transient method is developed based on conventional pulse experiment. The qualitative analysis of shape of peaks is added to the quantitative analysis to reveal the methane oxidation mechanism on Ni/CGO catalyst under

different ceria oxidation states. Also, the methodology is capable of evaluating the activity and carbon resistivity of catalyst in methane fuel. In the later chapters, the methodology here will combine with EIS to investigate the ageing of Ni/CGO and activity of Cu/CGO in methane.

Chapter 3 Methane Pulse to Investigate Catalytic Performance of Different Materials

In former chapter, a facile methane pulse method has been developed to evaluate the catalytic ability and carbon resistance of catalyst. Other metals apart from Ni have been widely used in heterogeneous catalyst and anode of SOFCs, including Cu, Fe, and Co. This chapter would be focused on applying methane pulse method to investigate the effect of addition of other metal to CGO backbones to methane oxidation reaction. Due to the insufficient time, only the experiment of Cu has finished.

3.1 Variation of Impregnated Ceria Based Anode Materials

Nickel is the most widely used metal in the SOFC anode partly because of its high activity for methane activation, especially for YSZ based materials. For the same reason, nickel is highly susceptible to carbon deposition. Because of the surface catalytic activity of ceria-based materials, the metal phase does not have to have as high a catalytic activity. Metals with better carbon resistance can thus be combined with ceria to produce applicable anodes for SOFC.

Cu has been widely investigated as a replacement or additive for Ni, because of its low cost and toxicity, and high carbon and sulfur tolerance. He[78] investigated a Cu/CeO_2 anode in 450ppm H_2S/H_2 fuel and such a high content of H_2S did not influence the performance. A $CuNi-CeO_2$-YSZ anode was investigated by Hornés[104] in dry methane. The full cell was stable for at least 100 h of operation at 1023 K. Li[102] investigated the different performance of Pd, Cu, Ni and Ni-Cu impregnated $BaZr_{0.1}Ce_{0.7}Y_{0.1}Yb_{0.1}O_{3-\delta}$ (BZCYYb) anodes, and found Ni and Pd impregnation reduced the polarization resistance of the anode in both H_2 and CH_4, while Cu reduced the ohmic resistance while preventing carbon deposition. Ni-Cu impregnated BZCYYb combined the advantages of both. Cobalt is another potential replacement of nickel that possesses moderate catalytic activity but better carbon and sulphur resistance. It often works with copper to further mitigate carbon and sulphur poisoning. Fuerte's work[259] prepared Cu-Co-ceria co-precipitated anodes, and tested them with biogas mixture. No evidence of carbon or sulphur poisoning was found after 740 h of operation. Iron often works with nickel

to form a bimetallic catalyst in ceria-based anodes. A Ni-Fe supported on CGO anode was investigated by Park[260] and showed good performance in hydrogen. Kan[214] further tested the Ni-Fe/CGO anode in dry methane. Compared with Ni/CGO anodes, Ni-Fe/CGO exhibited slightly lower power density but much higher stability.

This chapter was meant to be an application of methane pulse method on several other metals/CGO catalyst, including Cu, Fe and Co, to compare their catalytic ability towards methane oxidation and carbon resistivity. However, due to insufficient time and the demission of collaborator, only the experiment of Cu has finished. Therefore, in this chapter, the transient methane pulse and in-situ Raman spectroscopy methods, introduced in chapter 2, are applied on Cu and 1:1 Cu-Ni/CGO anodes. The results are analysed and the features and performance of Ni and Cu/CGO on methane oxidation at oxygen-free condition are summarised.

3.2 Experiment

3.2.1 Preparation of Ni-Cu and Cu/CGO anodes

The 1:1 Ni-Cu and Cu/CGO powders was prepared using a similar impregnation method as Ni/CGO, described in chapter 2. The same CGO ink was first tape-casted on an alumina plate, and then sintered at 1350 °C, then the powder was scraped off and roughly ground in an agate mortar for further impregnation.

2 M $Cu(NO_3)_2$ (Sigma-Aldrich) ethanol solution was used in the preparation of the impregnated Cu/CGO. 4μL of solution was dropped onto the powder for each impregnation step, followed by calcination at 500 °C for 30 min. The impregnation-calcination process was repeated until the mass loading of Cu has reached 20 wt%, and finally the powder was calcined at 800 °C. In the preparation of 1:1 Ni-Cu/CGO, the same impregnation process was used except that a 2 M $Cu(NO_3)_2$-$Ni(NO_3)_2$ in ethanol solution was used in the impregnation. The metal loading was 20 wt% 1:1 atom percentage Ni-Cu.

3.2.2 Powder characterization of Ni-Cu and Cu/CGO

The as-prepared powder was examined using the similar route described in chapter 2. In powder analysis, 15 pulses of 0.2326 mL methane were injected into the samples at 600 °C every 15 min, followed by temperature programmed oxidation. The emerging gas was

monitored by mass spectrometer. In methane pulse with in-situ Raman spectroscopy experiments, 0.3793 mL of methane was pulsed on Ni/CGO while 0.2326 mL pulses were used on Ni-Cu and Cu/CGO and CGO every 15 min. The integrated Raman Ce-O peak was smoothed and analyzed. The production/consumption of species were acquired by integration of the mass spectrometer signal.

3.3 Investigation of Cu/Ni Co-impregnated CGO by Methane Pulse

3.3.1 Methane Pulse

The consumption amount of CH_4 and production amount of H_2, CO and CO_2 from methane pulses on Ni, 1:1 Ni-Cu, Cu/CGO and CGO samples are plotted in figure 3.3.1. In the first methane pulse on each sample, it can be seen that the production of different gas species is quite different between Ni, Ni-Cu/CGO and Cu/CGO.

For Ni/CGO, the CH_4 conversion ratio for first nine pulses is ~92%. The ratio of CO and H_2 production is almost 1:2. After the first pulse, the production of CO_2 was negligible. H_2O is almost not detected. The production/consumption of species dropped after the ninth pulse, as described in chapter 2. This indicates that the major reaction on Ni/CGO is methane partial oxidation. The ratio of species production is similar on Ni-Cu/CGO. However, the methane conversion ratio is only ~30%, suggesting that the replacement of 50 wt% Ni by Cu lowered the catalytic activity by 60%, and the methane conversion per surface area of Ni remains basically the same. The consumption and production of species are stable for Cu-Ni/CGO throughout the whole pulse experiment, this can be explained by: the methane did not reduce ceria in Ni-Cu/CGO to the same degree as Ni/CGO, and the carbon species deposited on the metal phase can be eliminated by oxygen from ceria during the interval between pulses and hence not block the active sites on the metal. This can be confirmed by the comparison of CO production on Ni/CGO and Ni-Cu/CGO as a function of ceria non-stoichiometry (figure 3.3.2): Ni-Cu/CGO was only reduced to δ=0.1 at the 15th pulse while Ni/CGO was already reduced to δ=0.1 in the fifth pulse. The TPO afterwards showed a considerable amount of carbon deposition on Ni/CGO but negligible carbon on Ni-Cu/CGO, suggesting there is less carbon deposited on Ni-Cu/CGO at a cost of lower catalytic activity. As introduced in Chapter 2, the oxygen flux from CGO could eliminate carbon deposited on Ni and therefore is critical in preventing carbon deposition. It is possible that the less carbon deposition in Ni-Cu/CGO may

solely be the result of lower methane conversion, and oxygen flux is enough to remove most of the carbon deposition.

The methane pulse result on Cu/CGO is different to Ni and Ni-Cu/CGO. The methane conversion ratio is low (6%) and remains constant during the whole experiment. The production of CO decreased while CO_2 increased with pulse number. H_2O formation is still not observed over the experiment. This indicates that the total oxidation of methane is identical to partial oxidation on Cu/CGO. And the activation of methane on Cu is slow, as is found in the literature [102, 261, 262]. The result on Cu/CGO is compared with CGO in figure 3.3.1d. Similar ratios and trends for gas species are observed on CGO, except for two aspects: 1. Methane conversion is slightly higher on CGO (8.5%) than Cu/CGO (6%); 2. Water production is observed on CGO, with a H_2O:CO_2 ratio of nearly 2:1, but not on Cu/CGO. The fact that the production of CO and H_2 decreases with pulse number while CH_4 consumption remain the same, and CO_2 production increases on Cu/CGO and CGO, suggests that the selectivity of methane oxidation changed towards total oxidation as the ceria non-stoichiometry increases. The conclusion seems non-intuitive at first glance. However, Cu is a conventional catalyst for water-gas-shifting reaction[263]: $CO + H_2O \rightarrow CO_2 + H_2$, in which H_2O and CO are both adsorbed on Cu $H_2O + * \rightarrow O* + H_2$, $CO + * \rightarrow CO*$, before reacting ($O* + CO* \rightarrow CO_2$)[264] [265]. Since we did not observe any H_2O production along with CO_2, it is likely that produced water by TOM is further dissociated on Cu surface. Therefore, the concentration of resulting oxygen radical on Cu increases with number of pulses, and the reaction is more prone to water-gas-shifting, converting CO produced by POM route to CO_2. This seems the likeliest explanation for the decreasing CO and increasing CO_2 production from the third pulse. On the other hand, it is also possible that the partially reduced ceria surface is more active towards the further oxidation of CO to CO_2 : $CO* + O* \rightarrow CO_2*$, as found in Binet's work.[266] The higher conversion of methane on the pure CGO sample strongly suggests that the activation of methane on these two samples are mainly on the surface of CGO rather than Cu, and the impregnation of Cu blocked the active site on surface of ceria.

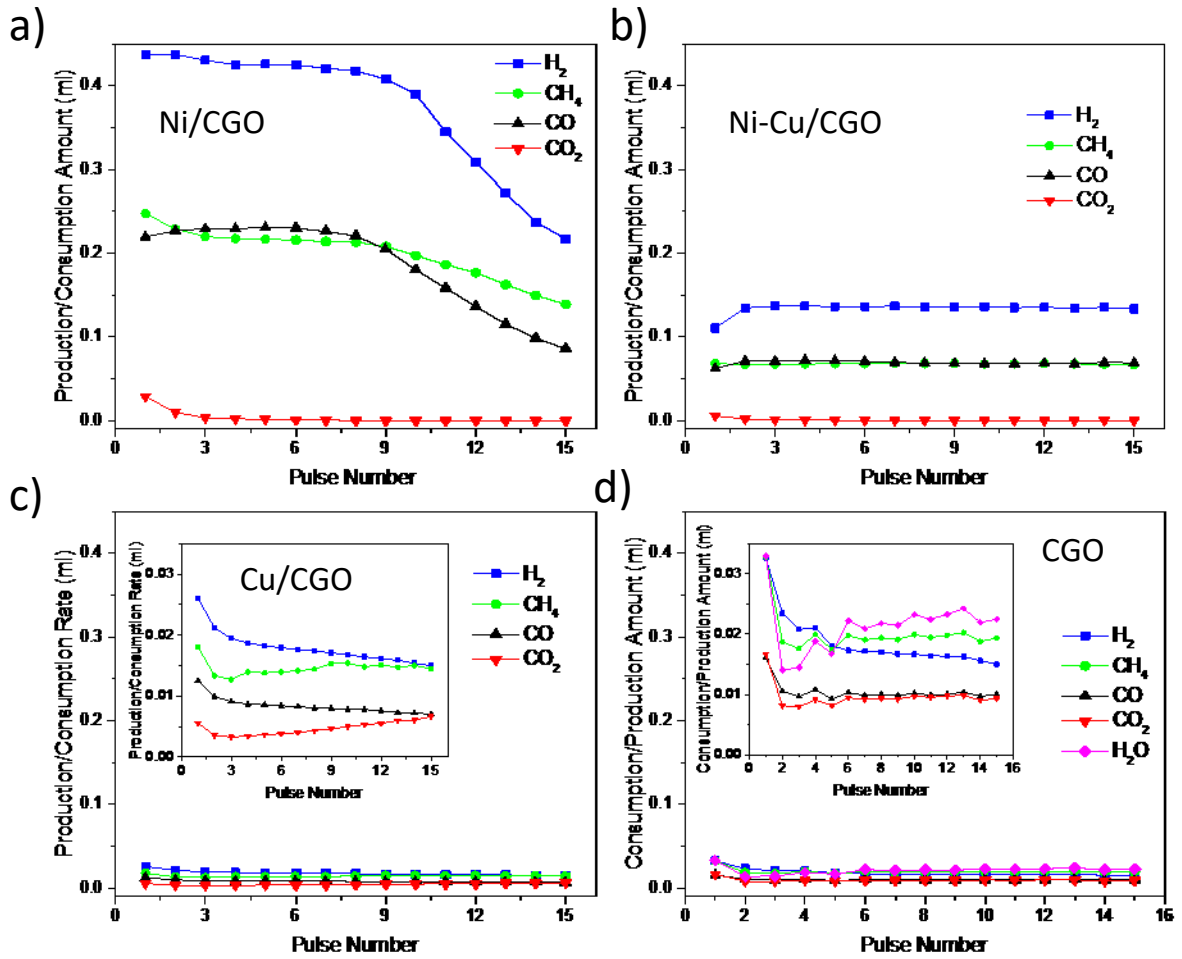


Figure 3.3.1 Consumption/production of species in methane pulse as a function of pulse number on a) Ni/CGO; b) Ni-Cu/CGO; c) Cu/CGO and d) CGO; The inset of c and d presents figure in a magnified scale to better show the detail

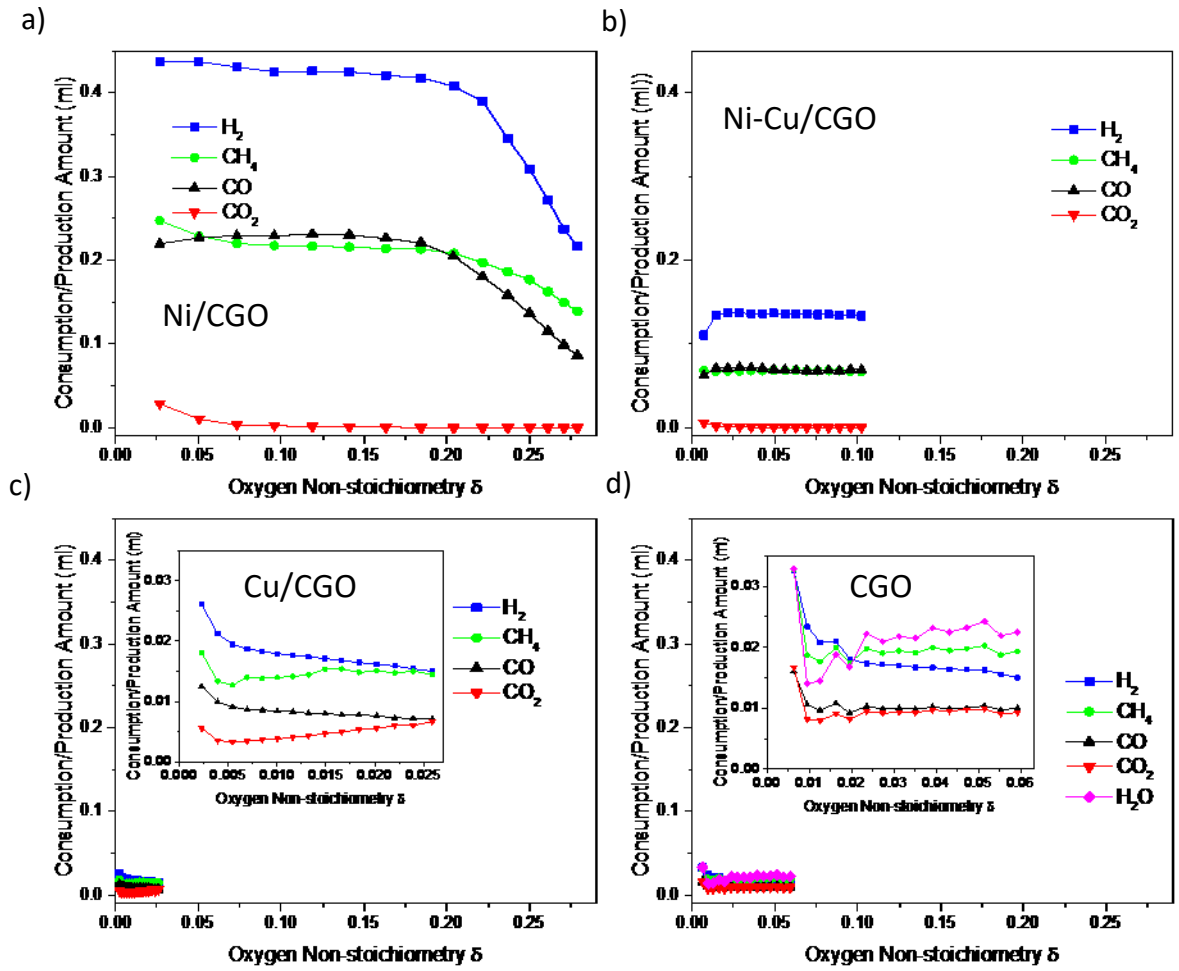


Figure 3.3.2 Consumption/production of species in methane pulse as a function of ceria oxygen non-stoichiometry on a) Ni/CGO; b) Ni-Cu/CGO; c) Cu/CGO and d) CGO; The inset of c and d presents figure in a magnified scale to better show the detail

To summarize, when supported on CGO, Cu itself did not show obvious activity for the catalytic activation of methane. On the contrary, it blocks the active sites on CGO and lowers the methane conversion rate. Also, the selectivity becomes prone to total oxidation of methane as the oxygen non-stoichiometry of ceria increased. When 1:1 Ni-Cu is supported on CGO, compared with Ni/CGO, 50% Ni replacement by Cu brought a 60% decrease of methane conversion ratio and negligible carbon deposition. This is likely to be the result of lowered methane conversion.

3.3.2 Raman Spectroscopy

To address the different results of the methane pulse experiment between different metals, in-situ Raman was performed. The in-situ Raman spectrum during a methane pulse on Ni, Ni-

Cu, Cu/CGO and CGO sample is shown in figure 3.3.3. Note that the experiment on Ni/CGO and CGO used a larger loop (0.3793 mL) than Ni-Cu and Cu/CGO (0.2326 mL) so only a qualitative comparison is presented between Ni/CGO and other two samples. The consumption and conversion of species on the three samples show similar characteristic with individual methane pulse experiments. Methane conversion ratios are ~80%, ~30%, ~10%, ~8% on Ni, Ni-Cu, Cu/CGO, and CGO respectively. However, the CO_2 production is much higher on Ni-Cu and Cu/CGO in the in-situ Raman experiment (figure 3.3.3b and c), and the CO production is significantly lower than CO_2 on Cu/CGO (so CO_2 is presented in the figure 3.3.3 c for Cu/CGO). This is probably due to a trace amount of air leakage in the in-situ Raman sample chamber as experiments on these two samples were done at the same time. However, oxygen (amu 32) was monitored in a separate experiment but no obvious increase in the oxygen background was observed. This probably suggests that the oxygen leakage is smaller than the detection limit of mass spectrometer, and that the mechanism of methane conversion is highly sensitive to the background oxygen concentration. Even in this condition, no water production was detected throughout the experiment. This suggests that the produced water is consumed by other species that has high reducibility. Due to the lower reactivity of copper compared with nickel, Cu should not be easily oxidized by water in this condition [267], the water can only be consumed by partially reduced ceria. Knapp found [268] that CO is preferably oxidized by ceria compared with H_2, this may explain the absence of an H_2O peak.

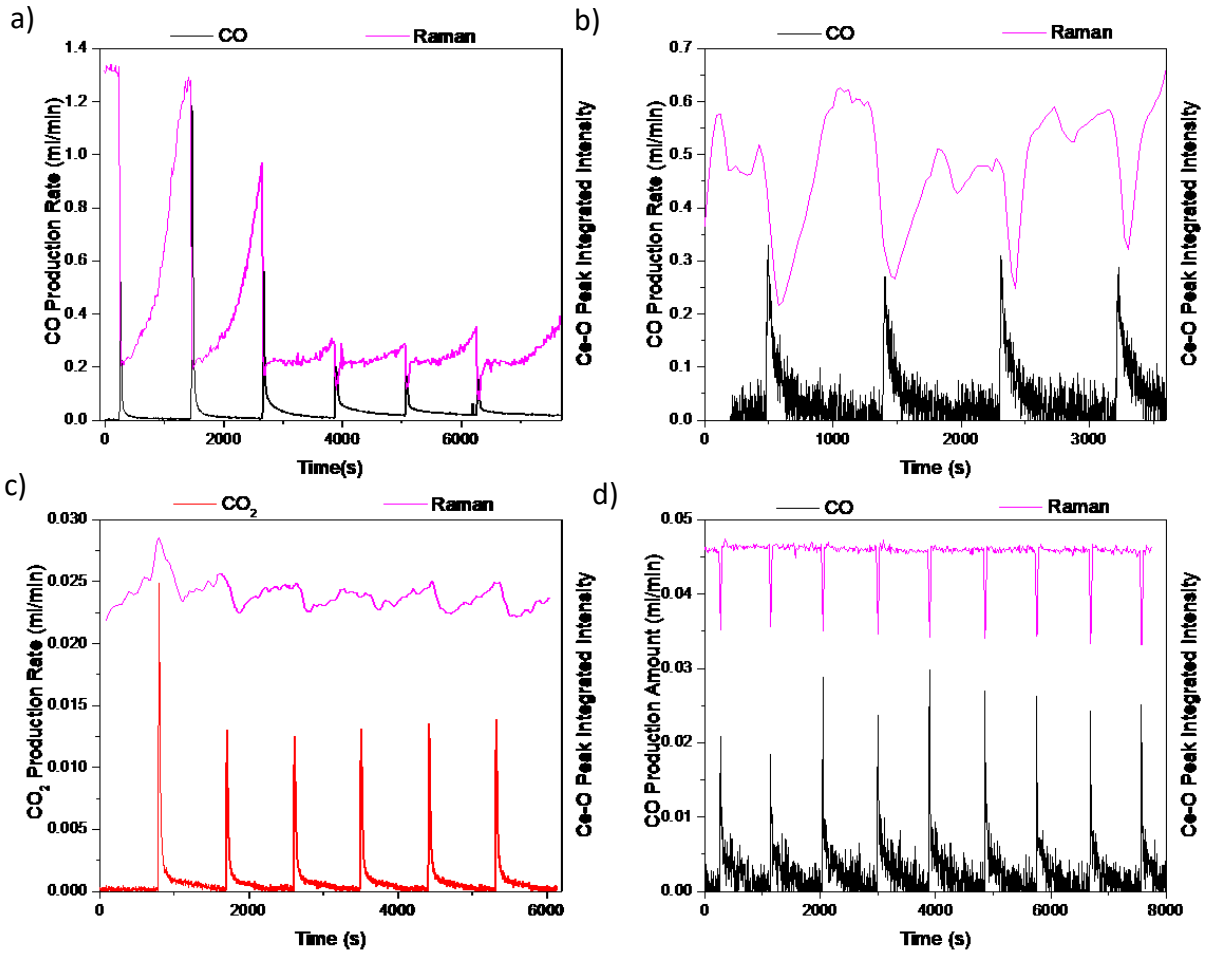


Figure 3.3.3 The integrated Raman Ce-O peak and CO/CO_2 production rate with time on a) Ni/CGO, b) Ni-Cu/CGO,c) Cu/CGO and (d) CGO

The exact reading of the Raman signal is not shown here is because the reading changes with different sample and position on sample, however the relative percentage of change after each pulse remained the same. This hinders the further quantified analysis of the Raman data. After the first methane pulse, the Raman signal dropped 84.6%, 57.1%, 25.4%, 16.8% and 22.9% on Ni, Ni-Cu, Cu/CGO and CGO, respectively. The is in good accordance with the methane conversion in the previous methane pulse experiments. Also, the peak shapes are different for these four samples. Raman peaks on Ni-Cu and Cu/CGO recovered quickly and stabilized within five minutes, peaks on CGO exhibit sharp drops with instant recovery in 1 min although the degree of drop is higher than Cu/CGO and identical with Cu-Ni/CGO. Unlike Ni/CGO, there is no visible decrease in the signal level after stabilization after several pulses on other samples. The fact that the Raman peak showed a greater drop for Cu/CGO than CGO indicated Cu is not active for methane activation. The similar peak result of Cu-Ni and Ni/CGO

indicates that the methane oxidation on Ni-Cu also features a Mars van-Krevelen mechanism, in which methane was first activated on either the metal or ceria surface and then the consumption of ceria surface oxygen by methane pulses is small and is quickly resupplied by bulk oxygen. And it confirmed that the catalytic activity of Cu is much lower than Ni-Cu and Ni. The slow recovery of the Raman peak after each pulse on Ni and Ni-Cu/CGO is likely due to the carbon species residing on the metal surface that would constantly consume surface oxygen. In contrast the Raman peak recovered instantly on CGO, indicating that the lifetime of species residing on the CGO surface is short as it is quickly eliminated by oxygen from ceria. Because methane preferably adsorbs on 3fh (threefold hollow site in the lattice) oxygen atom sites on ceria[268], the adsorption and reaction with oxygen is at the same site, so no migration of oxygen is needed at this stage. Also, this means that oxygen facilitates the adsorption of methane on ceria, and most methane adsorbed on ceria can be oxidized by oxygen on the ceria surface. As a comparison, methane adsorption on Ni is independent of the oxidation state of ceria. As a result, the oxygen from ceria might not be enough to oxidize all methane and would result in carbon deposition. This may explain the good carbon resistance of ceria[201, 269]. On the other hand, although Cu itself did not show methane activation activity, the drop of Raman peak after each pulse follows the pattern of Ni and Ni-Cu/CGO, which features a gradual recovery after each pulse, instead of the sharp spike like on CGO. The oxygen migration from ceria to Cu has been observed previously[270]. So this phenomena looks like there is adsorbed species other than decomposed methane on Cu surface that is continuously consuming oxygen migrated from CGO. Correspondingly, we found instead of CO tails on Ni and Ni-Cu/CGO samples, there is a CO_2 tail after each CO_2 production peak on Cu/CGO, which was deduced to be the result of water gas shifting . So here we deduced that the gradual recovery of Raman peak on Cu/CGO sample is due to the adsorbed CO on Cu reacting with oxygen migration from CGO.

3.4 Conclusion and Implications

The methane transient pulse method with in-situ Raman spectroscopy has been applied on Ni, Ni-Cu, Cu/CGO and CGO at 600°C. The following conclusions are made by analysing the Raman spectra and mass spectrometer data:

1. Ni and Ni-Cu show reactivity towards methane activation, in which the activity of Ni is much higher than Ni-Cu. Cu did not show noticeable activity towards methane activation.
2. Cu/CGO is active in water gas shifting reaction, leading the oxidation of methane towards TOM.
3. Compared with Ni/CGO, 1:1 Ni-Cu/CGO exhibits much better carbon resistance at a cost of 60% less reactivity towards methane activation. So Cu is not an active component in methane conversion.
4. The oxidation of methane on Ni and Ni-Cu followed a similar Mars van-Krevelen type mechanism as described in chapter 2. However, the residence time of methane on the CGO surface is much shorter, the reason being adsorption and oxidation of methane on CGO occurs on the same site. This also explains the good carbon resistivity of CGO.

Although Cu has proved to be an inactive component in methane activation, it can still find its part in methane fuelled SOFCs or methane oxidation catalysts. As mentioned in section 2.3, carbon deposition can be mitigated by adjusting the surface area of nickel and the oxygen supply from substrate. Here the result indicates that the nickel surface area can be adjusted by replacing part of Ni with Cu for better stability in methane fuelled SOFCs or CLCs, at a cost of a decrease of conversion rate. However, there are still several questions that remain to be solved in future work:

1. The optimal ratio of Ni:Cu on CGO for methane conversion and carbon resistance is yet to be found.
2. The exact mechanism of methane oxidation on the ceria surface is not investigated.
3. The reason for the increase of CO_2 production with increasing ceria oxygen non-stoichiometry is not clear.

Chapter 4 Ageing Studies of Impregnated Ni/CGO Anodes

In Chapter 2, a facile methane pulse method was developed that has the potential of extracting the intrinsic properties of anode. For example, the consumption of methane is related with the nickel surface area, the CO tailing is related with the oxygen migration from support to nickel site. This enables us to monitor the evolution of microstructure, which is essential in investigating the degradation of anodes during operation. Electrochemical impedance spectroscopy (EIS) has been a conventional characterization method to monitor the microstructural change, but explanation of change of EIS can be controversial, it would be interesting to see what information methane pulse method can provide in combine with EIS. Therefore, this chapter is focused on a tentative application of methane pulse method on the investigation of microstructural change during anode degradation, in combination of EIS.

All the experiment in this chapter is done by thesis author.

4.1 Introduction

Due to its high operation temperature, the degradation of SOFCs is an essential topic for practical application, and a great technical issue hindering the commercialization of SOFCs. The degradation of SOFC single cells can be classified into the degradation of different components: anode, cathode and electrolyte and the connection between them. The major causes of degradation which have been identified can be concluded as: 1. Microstructure changes of metal or support by sintering at high temperature, resulting in the loss of TPB, porosity and percolation[271]; 2. The solid-state reaction of certain electrode materials with electrolyte. For example, LSM reacts with zirconia oxide based electrolyte, and results in non-oxygen-conducting $La_2Zr_2O_7$ and $SrZrO_3$ dense layer, blocking the oxygen ion conducting path[272], this would greatly deteriorate the performance of cell; 3. Reaction of electrodes and impurities in the fuel, or the side reaction of fuel on electrodes, such as carbon deposition by cracking of methane, and the nickel poisoning by sulfur[273]. Here the literature review is focused on the high temperature ageing degradation behavior and mechanisms of SOFC anodes.

The ageing of an anode is usually due to the sintering of metal phases. The sintering of nickel on YSZ support has been investigated intensively[68, 271, 274]. It was demonstrated that nickel coarsened mainly occurred through an Ostwald ripening mechanism[275]. The

increase in the Ni particle size results in a corresponding decrease in TPB density which, on one hand, increases the polarization resistance of the anode and on the other hand, results in a decrease of electrical conductivity due to the loss of Ni–Ni contacts[276]. Jiang found that the sintering behavior of Ni/ YSZ cermet electrodes was dominated by the agglomeration and grain growth of Ni particles in the cermet, and that the sintering of nickel was more serious with higher nickel content[274]. Similar findings were made by Matsui[277], who further added that the humidity of fuel also plays an essential role in the evolution of anode microstructures. Higher steam content accelerates the sintering of nickel and loss of TPBs. The application of FIB-SEM tomography provided a new method to characterize the micro-structural parameter change of SOFC anodes during degradation more precisely[278]. The parameters can therefore be correlated with decrease of both conductivity and electrochemical performance.

Nickel agglomeration on ceria-based supports is different from YSZ, which is affected by the properties of ceria. Holzer[67] conducted a thorough study on the influence of the humidity of the fuel gas to the degradation of Ni/CGO, and found that, similar to Ni/YSZ, humidity accelerates the sintering of Ni (up to 140% per 100 h). The morphology of ceria also changed on degradation after long exposure for 1000 h, a layer of CGO was formed on the surface of nickel, which prevents the nickel from further growing. Zekri[279] found that CGO would also agglomerate at 850°C, such agglomeration in turn promoting the agglomeration of Ni particles by offering more space for Ni mobility. Suzuki[280] looked into long term sintering of Ni/samarium doped ceria (SDC), and found nickel particles were stabilized on SDC by the strong interaction of nickel with SDC.

Focus ion beam scanning electronic microscopes (FIB-SEM) is a dual-beam SEM system set up for the quantitative study of the microstructure of materials. It utilizes an ion beam (usually gallium ion) to expose and polish the cross section of materials, and uses an electron beam to do imaging. FIB-SEM was developed during the late 1970s and early 1980s and was widely available in semiconductor research and processing environments, as well as in failure analysis and chip-design centers. It is also used in the preparation of specimens for transmission electron microscopy (TEM)[281].

In the milling operation of FIB-SEM, the Ga^+ beam spot is scanned over a solid sample. When energetic ions meet with the sample surface, they lose energy to excite electrons and to break down the bonds between atoms, thus causing the removal of several nanometers of material. Then the electron beam from the SEM is scanned over the material cross-section to take images of the microstructure. The milling-imaging process can be repeated hundreds of times. In the end, a sequence of cross-sectional images are acquired with several nanometers gap in between. After image processing, the 3D reconstruction of the materials microstructures can be acquired, based on which researchers can calculate the quantitative microstructural parameters such as porosity, surface area, and most importantly for SOFCs, the TPB density. Compared with a conventional 2D imaging technique, FIB-SEM provides a more accurate way to acquire detailed microstructural parameters from materials.

FIB-SEM was first used in research on SOFC electrode structures in 2006, by Wilson[282], who characterized a Ni/YSZ cermet. The application in this field has grown significantly in the last decade and gave impetus to the further development of modelling of electrochemical performance based on microstructure parameters. Hiroshi [283] first vacuum infiltrated epoxy resin into the pores of an electrode to increase contact between pore and solid phase. Shikazono [284] conducted a 3D numerical simulation of the anode overpotential of a Ni/YSZ cermet based on a microstructure reconstructed by FIB-SEM. The predicted anode overpotential agreed well with experimental results. Other than Ni/YSZ cermet, Ni/CGO[285] and LSCF[286] were also successfully characterized by FIB-SEM.

4.2 Experimental

4.2.1 Sample Preparation

The Ni/CGO symmetrical cells and powder were prepared via the same impregnation method as described in chapter 2.

At first, CGO ink was prepared by mechanically mixing commercial gadolinium doped ceria ($Gd_{0.9}Ce_{0.1}O_{1.95}$, Praxair, particle size ≈ 0.5 μm) with carbon black as a pore former, Hypermer KD15 as a dispersant and an ethylcellulose binder (Hercules EC N-7) in a triple roll mill.

Secondly, the ink was tape casted onto an 20mm diameter YSZ pellets for both sizes, followed by a calcination in a muffle furnace (Elite Co.) at 1350 °C.

For symmetrical cell preparation, after the calcination, the pellets were impregnated with 2 M $Ni(NO_3)_2 \cdot 6H_2O$ (Sigma-Aldrich) ethanol solution, the impregnation was conducted as follows: 4 µL of solution was dropped to the sample along with grinding in the mortar to acquire uniformity; Then the powder was calcined in a muffle furnace at 500 °C for 30 min. The above process was repeated until the amount of nickel reached 20 wt%. The weight of nickel was calculated by weighing the nickel oxide after calcination. After the impregnation, the sample was further calcined at 800 °C for 5h.

The powder preparation process is as described in Chapter 2.2.1.

4.2.2 Symmetrical Cell Analysis

Symmetrical cells were aged and tested using an in-house impedance rig.

The cells were aged in 10% H_2/N_2 mixing gas at 600 °C for a total of 100 h, and the impedance spectra were recorded every 15 min for the first 10 h and every 30 min for the rest of the ageing time. The EIS was recorded from 10000 - 0.02 Hz, with 100 points per decade. EIS is tested in a custom rig (figure 4.2.1).

The impedance results were fitted in ZView for equivalent circuit $\boldsymbol{LR_s(R_1CPE_1)(R_2CPE_2)(R_3CPE_3)}$.

Images of cross sections of unaged, 20 h aged, 50 h aged and 100 h aged symmetrical cells were acquired via focussed ion beam SEM (FIB-SEM) (Zeiss Auriga). The 3D reconstruction was performed from these images via Avizo (FEI Visualization Sciences Group) software.



Figure 4.2.1 The structure of custom rig used in the characterization of symmetrical cells.

4.2.3 Powder Structure Characterization

Powder X-ray diffraction of the as-prepared sample was recorded using Panalytical X'Pert³ Powder with Cu Kα radiation. The particle size of NiO and CGO was calculated using the Scherrer equation. The microstructure image was taken by LEO Gemini 1525 FEGSEM.

4.2.4 Powder Catalytic Activity Analysis

The powder experiments were conducted using an AutoChem II 2920 (Micromeritics). The powder sample was placed on a piece of quartz wool inside a U-shaped quartz tube. The composition of outlet gas was analyzed using a Cirrus 2 Quadrupole Mass Spectrometer (MKS).

A series of temperature programmed procedures were used to analyse the morphology and reactivity with methane. The sample was first reduced in a temperature programmed reduction procedure (TPR), and the temperature was raised to 600 °C with 5 °C/min ramping rate in 50 $mL \cdot min^{-1}$ 20% H_2/Ar mixing gas. Hydrogen (amu 2) and water (amu 18) were monitored in the mass spectrometer.

After the reduction, the powder sample was aged at 600 °C in 50 mL/min 20% H_2/N_2 for a total amount of 117 h. A methane pulse experiment was performed every 12 h of ageing,

starting from the fifth hour. CH_4, H_2, CO, CO_2 and H_2O were monitored by mass spec during methane pulse.

In each methane pulse (MP)experiment, 0.2336 mL of methane was injected into 0.1 g of 20 wt% Ni/CGO powder at 600 °C for 10 times, followed by flushing of 50 mL/min of Ar during the 15 min pulse interval.

To ensure that the ceria oxygen stoichiometry was the same at the beginning of each MP experiment, the sample was flushed by 50 mL·min^{-1} Ar for 1 h at 600 °C between the ageing and MP experiment to maintain its oxygen balance.

After the last pulse experiment, a temperature programmed oxidation was performed to investigate the amount and form of carbon deposition from the methane pulse experiment. 50 mL·min^{-1} 2% O_2/Ar mixing gas was used in the oxidation, the temperature was raised to 600 °C with a 5 °C·min^{-1} ramp rate.

4.3 Results and Discussion

4.3.1 Morphology Change

The SEM images and 3D reconstructions of symmetrical cells without ageing and aged for 96 h are shown in figure 3.3.1. The unaged sample shows CGO particles of 200 - 500 nm diameter and pores of ~200 nm size. The small particles on the top of CGO scaffold are impregnated nickel particles, the size of which ranged from 10 nm to 100 nm in diameter. Nickel particles were evenly distributed on the CGO scaffold.

There is a significant change on the morphology of the cell after 100 h of ageing in 10% H_2/N_2. The CGO scaffold and the pores remained of similar size. However, the nickel morphology changed dramatically. Although there were still small particles on the CGO scaffold ranging from 10 nm to 200 nm, most nickel particles aggregated within the pore and formed a continuous phase which blocked the pores as can be seen from the SEM. A great change in the nickel surface area and triple phase boundary (TPB) density can thus be expected.

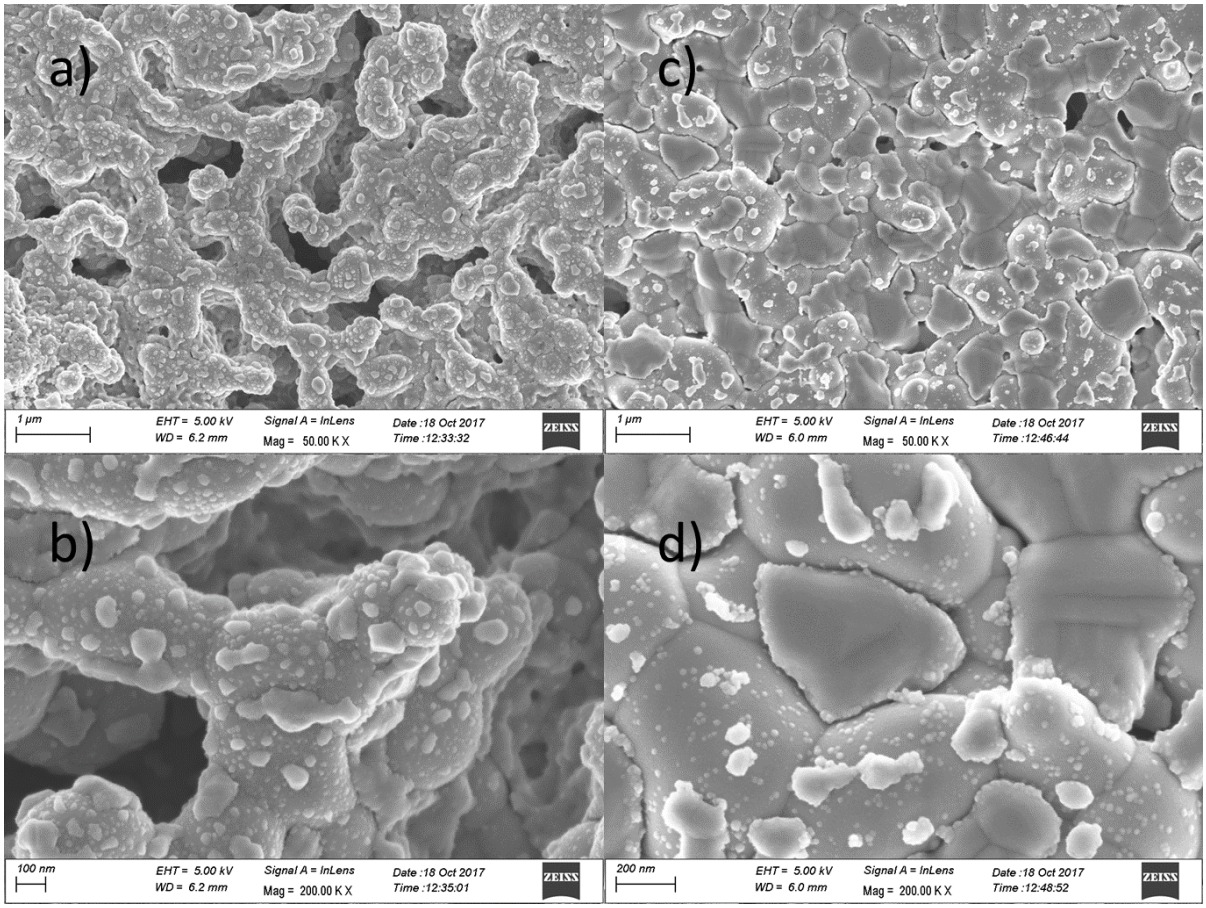


Fig. 4.3.1 SEM image of Ni/CGO electrode a) and b) as prepared; c) and d) after 100h aging

4.3.2 Ageing of Ni/CGO Symmetrical Cells

The impedance measurement was performed while the cell was aged in hydrogen. The EIS spectrum of the unaged cell is shown in figure 4.3.1a) Distribution of relaxation time (DRT) analysis was performed on these impedance results, shown in figure. 4.3.2a) inset, indicating there were three distinguishable processes in hydrogen, located at 10 – 100 Hz, 1 – 5 Hz and 0.02 - 0.5 Hz. The impedance result is fitted by the equivalent circuit $\boldsymbol{LR_s(R_1CPE_1)(R_2CPE_2)(R_3CPE_3)}$, as shown in figure 4.3.2c. In Zhu et al.'s work, the high-frequency (HF) process appeared only when certain metal current collectors were applied. Oh and Haile[287] as well as Nielsen et al.[288] suggest that this HF feature could represent the interfacial resistance between CGO and YSZ. Therefore, the HF process can generally be

attributed to the contact resistance caused by electrical constriction between current collector and electrodes or between electrodes and electrolyte[289, 290].

The medium frequency (MF) feature within 50 - 1 Hz is the only process showing high temperature-dependence with an activation energy of 0.79 eV. Later in table 5.3.4, considering its magnitude, frequency range and temperature-dependence, this process can be attributed to the transportation of oxygen ions in CGO and the electrochemical reactions between oxygen ions and hydrogen[287, 288, 291]. A thorough discussion about the MF feature and the DPB vs TPB contribution as a function of the electrode microstructure is reported later in this section.

The low frequency (LF) semicircle at 1 - 0.01 Hz accounts for roughly 10 % of the polarisation resistance at 600 °C and is weakly temperature-dependent. Previous experience with different anode materials in our laboratory indicates that the LF feature is mainly due to gas diffusion [292] and gas conversion [293] phenomena occurring within the test rig and the current collector mesh [290, 294, 295], as also reported by Aravind et al. [296], who used a similar experimental setup. An additional effect due to the CGO chemical capacitance, as reported by Lai et al. [177], cannot be excluded, although its contribution is expected to be minor considering the small thickness (~20 μm) of the electrodes and the weak temperature dependence. For similar arguments, low-frequency contributions associated to surface diffusion of adsorbed gas species [291, 297] are expected to be negligible.

The fitted data from the EIS measurements of symmetrical cells during the ageing process is summarised in figure 4.3.2b). R_s is the ohmic resistance, R_1 is the resistance for the high frequency process, R_2 is the resistance for the medium frequency process and R_3 is the resistance for the low frequency process.

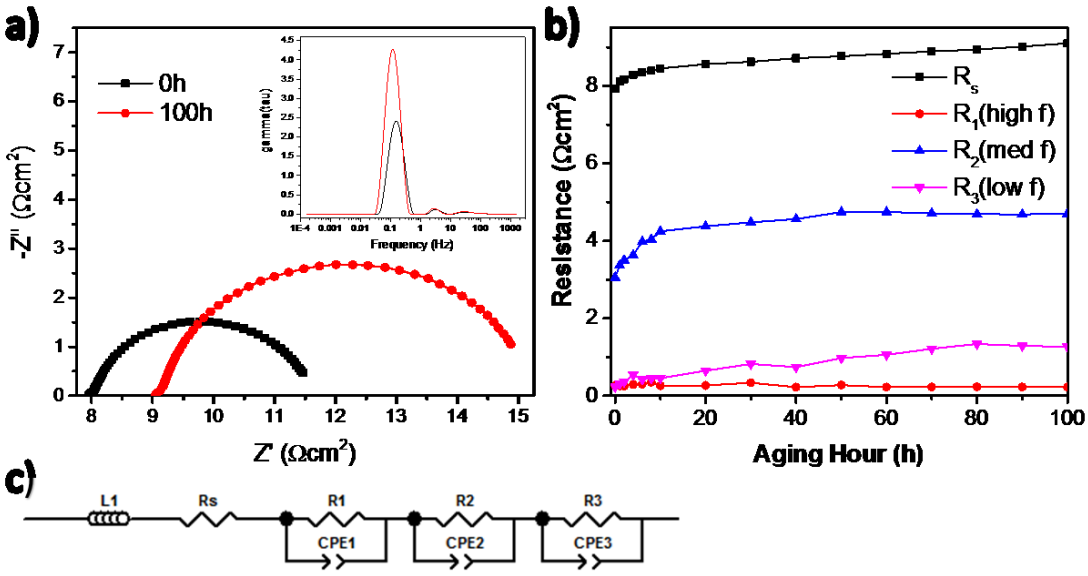


Figure 4.3.2 a) EIS spectrum of non-aged cell and 100h aged cell (inset is the DRT analysis); b) Summary of EIS of aging symmetrical cell, R_s is the ohmic resistance, R_1 is the resistance corresponding to the high frequency process, R_2 the medium frequency process and R_3 the low frequency process; c) The equivalent circuit used to fit EIS.

R_s is increasing throughout the whole ageing process. It quickly increases from 7.9 to 8.4 $\Omega \cdot cm^{-2}$ in first 5 h and then the rate of increase slowed down, turning to a steady linear increase, during which R_s increases from 8.4 to 9.1 $\Omega \cdot cm^{-2}$ from the 10^{th} hour to the 100^{th} hour. Such a linear pattern is also seen in R_2, which is related with the electrochemical oxidation of hydrogen. Therefore, such a degradation can be attributed to the loss of percolation of Ni network in the electrode.

R_2 increases in a similar pattern as R_s. In the first 10 h, in which it increases 38.7% from 3.1 to 4.2 $\Omega \cdot cm^{-2}$. After 20 h of ageing, R_2 stabilized at ~4.5 $\Omega \cdot cm^{-2}$ until the 100^{th} hour. This suggests that the electrochemical reaction rate is decreasing fast in the first 10 h and stabilized afterwards. The influence of ageing on the electrochemical performance on a Ni/CGO electrode is much smaller than Ni/YSZ as shown in Trine's work [298] or Tanasini's work [271], in which the polarization resistance increased 10 fold after 24 h operation at 650 °C.

R_3 goes through a steady increase from 0.23 to 1.26 $\Omega \cdot cm^{-2}$. Because 600 °C is a relatively mild temperature for CGO, as seen in Badwal et al.'s work[299], in which ceria is aged at 650 °C for 1000 h without significant increase in grain boundary. Also, SEM shows no change on CGO particle morphology, so here we assume there is no change in the morphology and chemical

properties of CGO. The increase of R_3 is likely to due to the blocking of pores by sintered nickel as can be seen in figure 4.3.2c and d.

The images analysis of different aged (10 h, 50 h and 100 h) and unaged samples is concluded in table 4.3.1. The TPB density decreases significantly from 41.2 μm^{-2} to 27.3 μm^{-2}, and Ni-pore DPB density decreases from 6.5 to 2.6 μm^{-1}. (Note that the TPB density here represents the TPB length per unit volume of electrode, therefore it has a unit of μm. μm^{-3}= μm^{-2}. Similarly, the DPB density is the DPB area per unit volume of electrode, with a unit of μm. μm^{-2}= μm^{-1}.) However, the CGO-pore DPB density increases from 2.1 to 3.7 μm^{-1}. These changes correlate well with the SEM images, the TPB density and Ni-pore DPB density decreased due to the sintering of nickel particles, which reduce the performance of cell. On the other hand, the sintering of nickel exposes more CGO surface, and in turn increases the reaction site density of hydrogen and CGO which enhances the performance of the cell.

Table 4.3.1 The measured microstructural parameters of unaged and aged Ni/CGO electrodes.

Ageing Hour / h	**TPB Density / μm^{-2}**	**CGO-Pore DPB Density / μm^{-1}**	**Ni-Pore DPB Density / μm^{-1}**	**Ni-CGO DPB Density / μm^{-1}**
0	41.2	2.1	3.5	3.4
10	32.8	2.7	3.1	3.1
50	28.3	3.4	2.8	2.8
100	27.3	3.7	2.6	2.7

Another major factor influencing the performance is percolation. Most of the nickel is percolated in the unaged electrode (98.3%). After ageing, nickel sintered into separate particles with an average diameter of 90 nm, there is no percolating Ni in the selected sampling volume. The loss of metal percolation has a major negative impact on zirconia-based electrodes. Due to the essentially zero electronic conductivity of the YSZ, the electrochemical active area is limited to a thin layer near the current collector[68]. However, ceria-based substrates can provide reasonable electronic conductivity (~0.1 $S \cdot cm^{-1}$) to make up for the loss of percolation, as depicted in Ciucci's work[95].

As a summary, the sintering of Ni by ageing caused a negative influence on the impregnated Ni/CGO anode in two ways: 1. Decrease of the TPB; 2. Loss of Ni percolation. Such a negative influence is mitigated by the larger interface of CGO and gas phase through ageing, plus the electronic conductivity offered by the reduced CGO.

4.3.3 Ageing of Ni/CGO powder

While EIS gives comprehensive information on how the cell degrades from an electrochemical aspect, the influence of changes of electron percolation and surface catalytic activity are entangled. Therefore, the change of catalytic properties of Ni/CGO with ageing is extracted with methane pulse experiments. The methane pulse as a method to evaluate the performance of Ni/CGO catalyst is introduced in the previous chapter 2. Unlike hydrogen, the surface activity of pristine CGO towards methane oxidation is low, as shown in chapter 2. Therefore, the change in methane activity can be completely assigned to the change of nickel surface or interface, which makes the analysis simpler. Here the methane pulse experiment is performed on Ni/CGO powder at 5 h, 12 h, 19 h, 26 h, 33 h, 45 h, 57 h, 69 h, 81 h, 93 h, 105 h and 117 h.

The amount of consumption/production of species in each pulse as a function of pulse number is shown in figure 3.3.3a. The CO_2 production amount is high in the first pulse, and dropped to nearly zero from the second pulse, indicating that the majority of methane is partially oxidized to H_2 and CO. This is further strengthened by the fact that in the first 4 pulses H_2 is nearly twice of the amount of CO produced (2% error). CO and H_2 production as well as CH_4 consumption levels went through a plateau which lasted for three pulses, and then went down at an accelerating rate. Such phenomenon was analysed in detail in chapter 2. Figure 4.3.3b shows the CO production from methane pulses on Ni/CGO samples after different ageing hours, the plateau is clearly shown for first three pulses of each ageing hour. The reaction of methane on Ni/ceria in an oxygen deficient environment thus goes through a Mars-van-Krevelen mechanism: At first the methane goes through a quick decomposition process on nickel surface and formed amorphous carbon, then the oxygen from ceria spills-over to nickel surface and oxidizes the carbon to CO. So when oxygen migration from ceria is quick, CO production remains unchanged with number of pulses. When the pulse interval was

not long enough for all carbon to be eliminated by oxygen, nickel surface sites were blocked, result in a fall in the amounts of CO, H_2, and CH_4 in the subsequent pulse. Due to this reason, the values of the plateau of CO, CH_4 and H_2 are closely related with nickel surface – i.e. the catalytic active area of Ni/CGO in methane partial oxidation.

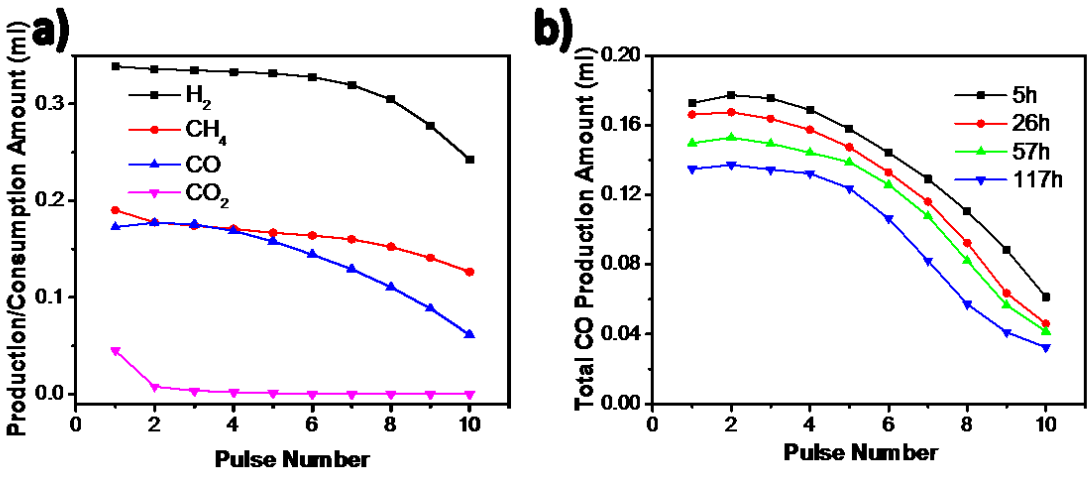


Figure 4.3.3a) The consumption/production amount of species in methane pulses on 5 h aged Ni/CGO; b) The CO produced in methane pulses on Ni/CGO of different ageing times.

The value for the plateau decreased with ageing time, as shown in figure 4.3.4a. The plateau value for CO and CH_4 decreased from 0.176 to 0.136 mL, H_2 decreased from 0.335 to 0.265 mL, and the production amount of all species dropped 22.7%. The degree of plateau decrease is similar to the nickel surface area (Ni-Pore DPB density) as shown in table 4.3.1, which decreased 25.7% from 3.5 to 2.6 μm^{-1}. This further confirmed that the consumption of CH_4 in oxygen deficient conditions is closely related with the surface area of nickel.

As demonstrated in chapter 2, each CO production peak after a methane pulse on Ni/CGO is composed of a major peak and a tail which extends even after all the species have escaped. It was demonstrated that the major peak is due to the oxidation of carbon species by the surface oxygen of CGO, while tail is the result of slow migration of oxygen from the bulk to the CGO surface. Because of the decreasing nickel surface area, the methane conversion is decreasing and therefore oxygen extraction from CGO by each methane pulse is also decreasing. The oxygen non-stoichiometry therefore cannot be related only with number of pulses but also related with ageing time. So, to relate the production of CO with the intrinsic

properties of Ni/CGO, the total CO production amount and CO production in the major peak of methane pulses on Ni/CGO at different ageing times is plotted against oxygen non-stoichiometry in figure 4.3.4a, and in b. Under the same oxygen non-stoichiometry, the total CO produced decreases with ageing.

As expected, the amount of CO in the major peak decreases with increasing oxygen non-stoichiometry, because the usable surface oxygen is decreasing as CGO is getting more reduced. However, CO in the major peak also decreased with ageing time. This unexpected result suggests the usable oxygen on the surface of ceria is decreasing with ageing. However, the structure and chemical properties of CGO should not have changed at such a low temperature over a relatively short time period[67]. Rather, such a change could be assigned to the result of nickel coarsening as well. It was found in the literature that nano-metal particles can enhance the activity of ceria surface towards oxidation of hydrogen or hydrocarbons[195, 196, 300]. The reason is that V_O formation energy of oxygen near the interface of metal/support is much lower. The aggregation of particles by ageing would decrease the concentration of such metal/support interface. In other words, the decrease in the TPB of Ni/CGO electrodes would also result in the decrease of surface oxygen reactivity.

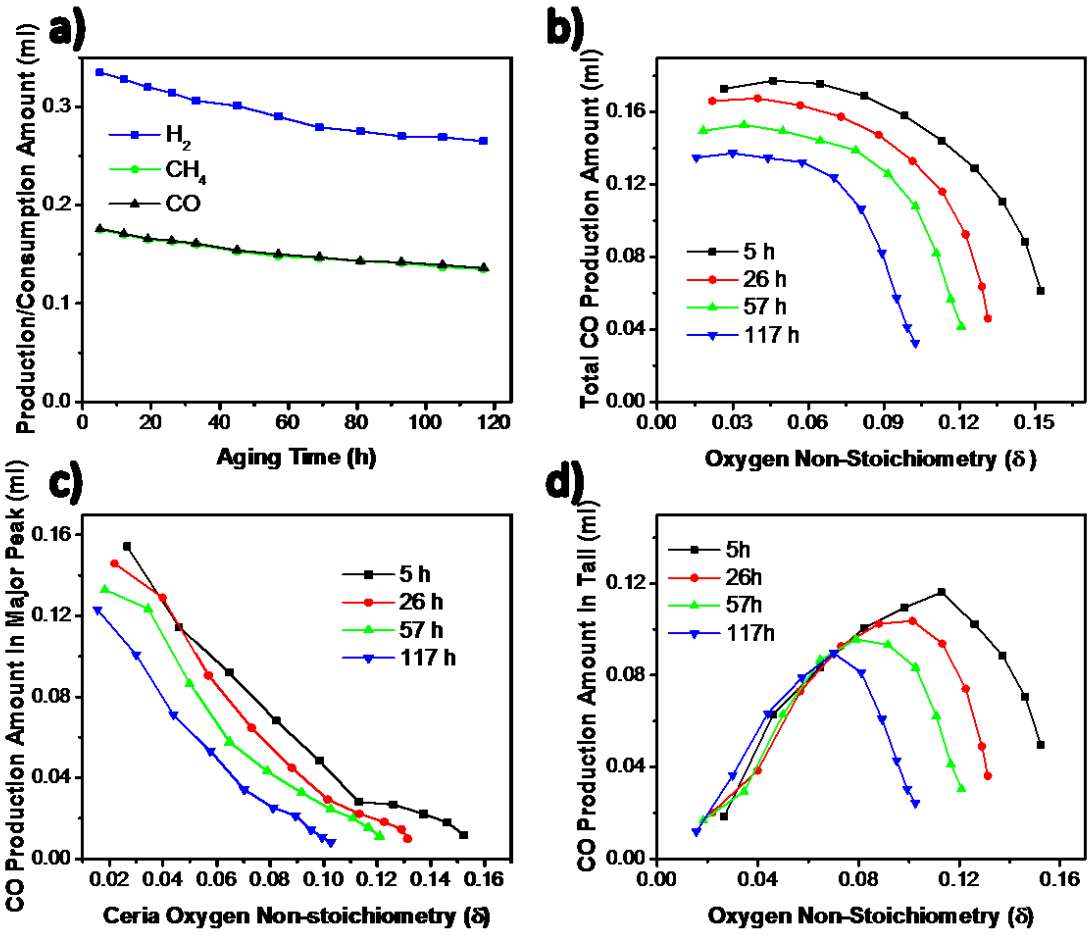


Figure 4.3.4 a) The plateau of species in methane pulses on Ni/CGO at different ageing hours; b) The total CO produced c) CO produced in major peaks d) CO produced in tails from methane pulses on Ni/CGO of different ageing times, plotted with oxygen non-stoichiometry.

The CO produced in the region of the tail also showed interesting trends with ageing. For all samples, CO production in the tail increases in the first five pulses and then decreases afterwards, reaching a maximum at the fifth or sixth pulse. This can be explained by the decrease of oxygen migration rate from bulk to surface CGO. Also, after the fifth pulse of each sample, the CO tail extends longer than the pulse interval, and carbon starts to deposit on nickel. These two factors make the CO in tail decrease after the fifth pulse.

Interestingly, in the first five pulses of each sample, the CO production amount in the tail followed a linear correlation with oxygen non-stoichiometry. This may suggest there is a correlation between the amount of oxygen migrated from CGO in each pulse interval and ceria oxygen non-stoichiometry, which will be investigated in the future.

The change of catalytic properties is mainly due to: 1. The decrease of nickel surface area, which reduces the initial adsorption of species on nickel; 2. Nickel becomes less dispersed, reducing the metal/ceria interface, and the average V_O formation energy of ceria surface is thus increased, this in turn decreases the available oxygen at the ceria surface in a given oxidation state. The importance of the previous point has been widely addressed [301, 302] but the influence of the latter has been rarely mentioned in studies into the ageing of SOFC anodes. As shown in chapter 2, carbon started to build up on nickel after the depletion of ceria surface oxygen. Therefore, the accessibility of oxygen on the surface of ceria is very important for carbon prevention. And so that ageing of Ni/CGO anode would have a detrimental effect on the carbon resistance through nickel aggregation. This can be confirmed from figure 4.3.4d: After ageing, the maximum amount of CO produced in the CO tail at the fifth or sixth pulse (amount of carbon oxidized by oxygen migrated from the bulk of ceria) decreases, and the maximum point shifts towards lower oxygen non-stoichiometry of ceria. This suggests that carbon removal is getting slower with ageing, which can also be explained by the increasing activation energy of oxygen removal from the surface of CGO.

4.4 Conclusions

By combining the analysis from EIS of Ni/CGO symmetrical cells and methane pulse on Ni/CGO powder, a picture of the initial degradation of nano-particle Ni/CGO electrode has been established. The structural degradation of the electrode after 100h of ageing at 600°C is mainly due to the aggregation and migration of nickel nano-particles. The impact of such a change in the nickel can be summarized in terms of three key structural factors:

1. The loss of percolation of nickel phase: This prevents electrons from accessing all the chemically active sites (TPB or DPB) and increases the ohmic resistance, which has been widely addressed in literatures. This is partly mitigated by the reasonable electron conductivity of CGO. Methane pulse method is not useful in capturing the loss of percolation, as it is an electrochemical reaction-related microstructural property.
2. The decrease of nickel surface area: This is intuitive and also widely addressed in literatures. The adsorption of fuel species on the nickel surface is therefore inhibited. For hydrogen, such an effect is not obvious as hydrogen can also be activated on CGO. On the other hand, a decrease of nickel surface area largely inhibited the adsorption

of methane and thus inhibited methane oxidation. The decrease of nickel surface area is not directly reflected in the EIS of hydrogen, but the decrease of surface area is directly proportionally indicated by the decrease of methane consumption in each pulse in methane pulse experiment. The quantitative relation is not yet clear and will be investigated in the future.

3. The less dispersed Ni particles:
    a. Enhanced the CGO surface exposed to the gas phase, and further increased the active CGO catalytic area. This effect is most evident for hydrogen, as the CGO surface is highly active towards hydrogen oxidation, but not obvious for methane. This is rarely mentioned in literatures, as it is difficult to deconvolute TPB process from DPB, and also, the activity of CGO DPB is sometimes overlooked. Although it is not possible to accommodate this in both EIS and methane pulse, the structural change is obvious as observed by FIB-SEM.
    b. The decrease of nickel dispersion reduces the metal-oxide interface density, and thus reduces the activity of CGO surface oxygen by increasing the V_O formation energy. The carbon resistance when methane is used as fuel is significantly lower. In field of catalyst, this effect has been mentioned and studied, but so far it is not related with the electrochemical performance of SOFCs in any literatures. EIS is not capable of showing this effect, but it is indicated by the slower CO tailing kinetic in methane pulse methods.

Chapter 5 Model Guided Design of Ni/CGO Fibre Electrode

Due to the existing problem of conventional MIEC electrode structures, there is increasing need to understand the mechanism and kinetic of DPB and TPB in MIEC materials. This chapter is aiming to find a way to relate the EIS of Ni/CGO with its microstructure, sequentially to help deconvolute the DPB and TPB process of hydrogen oxidation on Ni/CGO. In the end, the method shows the potential to predict the electrode performance from microstructure.

The NiO fibers membrane is fabricated by Dr. Xinhua Liu. The fiber-matrix-structure (FMS), impregnated, cermet 1 Ni/CGO symmetrical cells are prepared by the thesis author. The cermet 2 Ni/CGO symmetrical cell and EIS are done by Dr Masashi Kishimoto. All the other EIS experiments and all the EIS fitting are also done by the thesis author. The cellular automaton algorithm is programmed by Yufei Wu. The 2D model is developed by Dr. Antonio Bertei. The idea of the research comes from the thesis author under the supervision of Dr. Xinhua Liu and Dr. Paul Boldrin.

5.1 Background

Electrospinning is a technology widely used for fabricating polymer fibres. It utilizes electrical forces to produce polymer fibres with diameters from the nanometer scale to several micrometers[303]. The electrospinning technique was first patented to fabricate continuous fibres in 1934 [304]. It started to attract more and more attention from the start of 21st century due to the rising interest in nano-technology. It not only can be used to fabricate polymer or carbon fibres but can also synthesise fibres made of organic or inorganic materials by dispersing corresponding particles into a slurry. Up to now, hundreds of polymers and thousands of materials have been successfully electrospun into nanoscale fibres.

5.1.1 Setup and Control of Fibre Morphology

A schematic diagram of electrospinning is shown in figure. 5.1.1. The equipment is made of three components including a syringe that contains the raw slurry with a needle of controlled diameter, a metal plate to collect the electrospun fibre, and a high-voltage power supply. The positive electrode of the power supply is connected to the slurry and the negative electrode to the metal plate so that the direction of the electric field is from the tip of the syringe needle to the metal plate. During fabrication of fibrous membranes, as the intensity of the electric field is increased, the hemispherical surface of the fluid at the tip of the capillary

tube elongates to form a conical shape known as the Taylor cone[305]. Then the charged jet goes through an elongation process and fabricates fibres on the metal plate. The fibre membrane is then formed after a certain duration of fabrication.

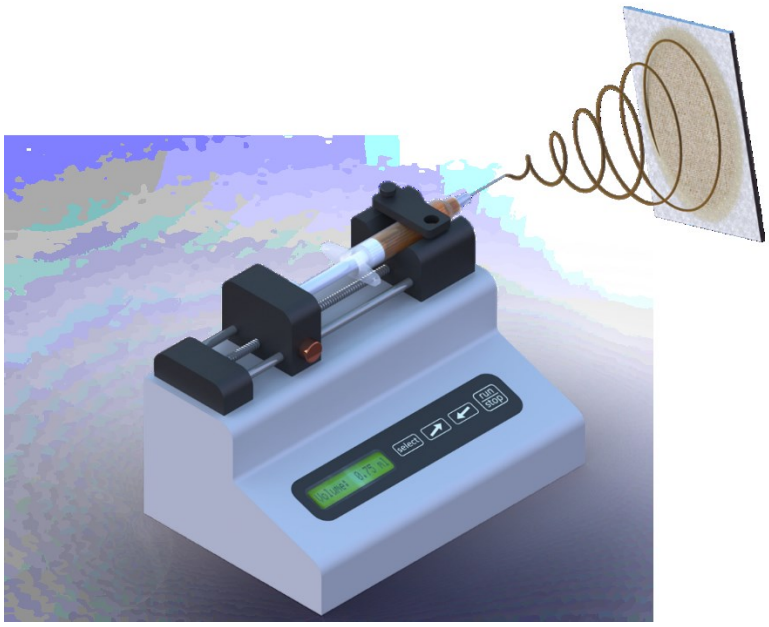


Figure. 5.1.1 A schematic diagram of setup for electrospinning.

The morphology of fibre membranes can be controlled by adjusting various parameters. To fabricate consistent and stable fibres, the viscosity of slurry, distance between tip and metal plate, feed rate of slurry, and temperature and humidity of the environment need to be carefully adjusted into a certain range, which varies with different types of polymer and loading of particles. Fibres cannot be formed if the viscosity is too high, the distance is too large or the feed rate is too high, and droplets and beads will be formed if the viscosity is too low, the distance too small or the feed rate too low[306]. One of the most important properties of a fibre membrane is the diameter of the fibres. The diameter of fibres can be increased by increasing viscosity and/or feed rate or decreasing the applied voltage and/or environmental temperature. This tremendous variety of electrospun nanofibres in terms of materials, structures, architectures and functionalities explains the increased use of the electrospinning technique for the production of nanofibres, fabrics and membranes.

5.1.2 Recent Development of Electrospinning in Fuel Cells

Due to its high adaptability and tuneability, electrospinning technique has been applied to the preparation of different components of energy conversion and storage devices, ranging from fuel cells (FCs), lithium-ion batteries (LIBs), and dye-sensitised solar cells (DSSCs)[307].

In the field of FCs, electrospinning has been widely used in fabricating the support of catalyst in the electrodes of proton exchange membrane fuel cells (PEMFCs). Because in electrospinning, the catalyst such as platinum can be easily loaded on polymers, and then can be carbonized under controlled condition. The most used catalyst and polymer carrier in this case is Pt/PAN (Polyacrylonitrile). Park [308] prepared Pt/CNFs (carbon nano-fibres) by electrospinning and carbonization PAN slurry, and acquired high surface area and electrical conductivity with shallow pores with rough surfaces (as shown in figure. 5.1.2). Then the CNFs were loaded with nano-Pt particles. Such a method can increase the TPB density and make the use of Pt more effective. Li [309] prepared CFM (carbon fibrous mats) by thermally treating the electrospun polyacrylonitrile fibrous mats, and loaded with commercial Pt/C as catalyst exhibited higher chemical stability and catalytic activity towards hydrogen oxidation.

Although electrospinning has been explored in the field of PEMFCs, only a few studies concerning its use in SOFCs have been presented for the following reasons: Neither polymer nor carbon can withstand the high operation temperature of SOFCs; ion conduction is an essential step for SOFCs and requires a large volume percentage of ion conductive phase, so that electrodes with electrospun fibres usually do not perform well. Li [153] prepared 8YSZ fibre membranes with ~200nm diameter fibres and impregnated it with Ni. They illustrated the effect of the 1D morphology on the enhancement of ionic and electric transfer at the three-phase-boundary sites and acquired better performance than conventional cermet electrodes. Zhi [310] prepared similar YSZ fibres and infiltrated them with 50 wt% LSM as an electrocatalyst. The composites were used as the cathode of SOFCs and showed good performance in EIS. The potential utilization of electrospinning on SOFCs are still under exploration.

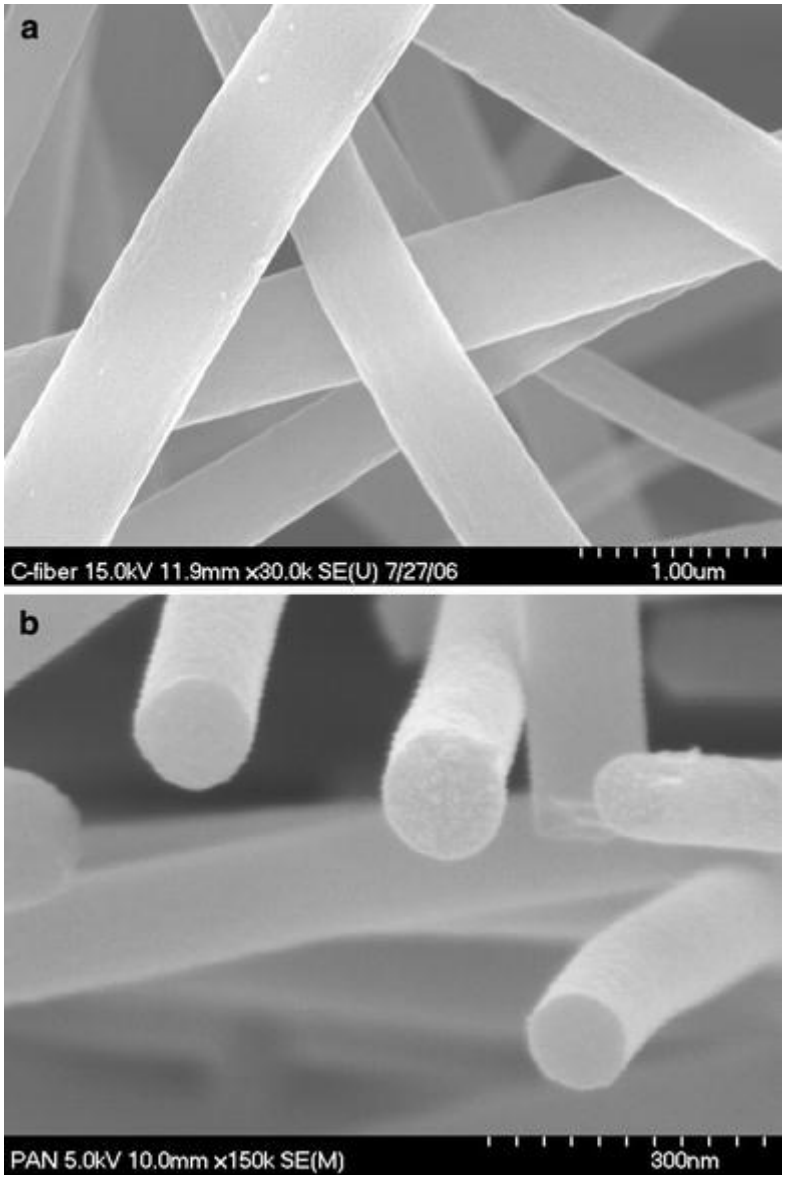


Figure. 5.1.2 SEM images of cross sections of electrospun CNF carbonized at 1000 °C [Reproduced with permission from [308]]

5.2 Materials and Methods

5.2.1 Fabrication of Fibre-Matrix-Structure (FMS) Ni/CGO Symmetrical Cells

The preparation method combined the use of electrospinning and the conventional tape-casting technique with a modified calcination process.

The CGO ink for tape casting was made by the same method as described in chapter 2.2.1.1.

The electrospinning precursor was prepared by mixing 2.4 g NiO, 0.3 g of polyacrylonitrile (PAN) powder (Goodfellow Cambridge Limited Huntingdon, mean particle size 50 µm, mean

molecular weight 230,000 g mol^{-1}) in 3 ml dimethylformamide (DMF, VWR chemicals, 99.90%) for 6 h at 60 °C. For electrospinning, the as-prepared precursor solution was filled into a syringe and then driven into the electrospinning nozzle (13 mm length, flat-tipped, 19 G, 0.69 mm inside diameter, 1.07 mm outside diameter) by a syringe pump (Graesby 3300) at a flow rate of 0.5 ml h^{-1}. The needle was held at 14 kV relative to a grounded aluminium collector plate by using a high voltage power supply (GenVolt 73,030) with a horizontal separation distance of 17.5 cm. The PAN based, NiO-carrying continuous nanofibres (NiO-PAN nanofibres) were collected after 15 min of spinning (25 °C, 50% of humidity), after which they were stabilized in air by heating at 1 °C min^{-1} up to 300 °C and holding for 2 h. Here, PAN is employed only as a spinning agent to produce the fibres, thus the stabilized NiO-PAN nanofibres were further heated at 2 °C min^{-1} to 550 °C and held for 1 h in order to burn off the PAN and obtain the pre-calcined NiO fibre membrane. Notably, the pre-calcined fibre membrane can maintain the fibre shape structure. To make a lab scale symmetrical pellet cell the membrane was then carefully cut to round pellets with diameters of 16 mm, then calcined at 1200 °C for 4 h on a zirconia substrate to oxidize all the carbon and add some minimal mechanical strength to the membrane by slightly sintering the NiO. After volume shrinkage, the final diameter of NiO membranes was c. 14 mm.

For the preparation of the CGO matrix, CGO ink was first tape-cast on a YSZ pellet (YSZ-8 20 mm pellets, Fuelcellmaterials). Then, a NiO membrane was put into the cast CGO ink and, after it was fully soaked, another layer of CGO ink was cast on the top of the NiO membrane. This composite structure was held in a vacuum desiccator to remove bubbles and improve wetting between the membrane and the ink. Finally, the electrode was calcined at 1250 °C for 5 h and the symmetrical cell was obtained.

We altered the initial sintering temperature of NiO fibre membrane to find the best temperature. When sintered below 1000 °C, the mechanical strength of membrane is not good enough to withstand contact and movement. If sintered at above 1200 °C, the membrane would sinter with the zirconia substrate and not able to be peeled off. Therefore, we use 1200 °C as the standard initial calcination temperature.

In the beginning of its development, the FMS electrode fell off the electrolyte easily after sintering. We later found the problem was caused by the insufficient contact of electrode and

electrolyte, which came from the air that was brought to the ink when the fibre membrane was soaked into the ink. After we applied vacuum treatment down to 5 Pa, the problem is solved.

5.2.2 Fabrication of Impregnated Ni/CGO Symmetrical Cells

The fabrication of impregnated Ni/CGO symmetrical cell is the same as described in chapter 3.2.1.

5.2.3 Fabrication of Cermet Ni/CGO Symmetrical Cells

Two conventional mixed powder cermet electrodes were also produced, using two approaches typical in the literature.

In the preparation of cermet 1, commercial Ni/CGO ink (Fuel Cell Materials) was tape-cast on both sides of a YSZ pellet. After drying in the oven, the cell was calcined at 1350 °C for 5 h.

Cermet 2 were prepared by our collaborator in Japan, NiO powder (Wako chemical industry, Japan) and CGO powder (Tosoh, Japan) were mixed to obtain Ni:CGO≈50:50 vol% composition. After ball-milling and sieving processes to remove agglomerates, the powder was mixed with terpineol-based binder (VEH, Fuel Cell Materials) and screen printed on both sides of a YSZ pellet (Tosoh, Japan). After drying, the cell was sintered at 1400 °C for 4 h. The thickness of electrodes are ca. 20 μm.

5.2.4 Morphology Characterization

SEM images were taken on a Zeiss LEO Gemini 1525, using an in-lens detector and 5 kV acceleration voltage. Focused ion beam scanning electron microscope (FIB-SEM) image sequences were taken on a Zeiss Auriga Crossbeam, with 240 pA milling current (FMS and conventional cermet electrodes) or 120 pA milling current (impregnated electrodes), using a backscattered detector with 1.5 kV acceleration voltage to acquire maximum contrast. Due to the presence of Ni nano-particles in the impregnated electrodes, a better voxel resolution (9.81×9.81×11 nm) was used in the reconstruction of impregnated electrodes compared to FMS and cermet ones (30.71×30.71×30 nm). The 3D structure of the electrodes was reconstructed, segmented into three different phases (Ni, ceria and pore) and analysed by Amira-Avizo and ImageJ. Structural parameters, including volume fractions of each phase,

surface areas, TPB and DPB densities were evaluated using the open-source TauFactor package[311]. The distribution of ceria-pore DPB weighted with respect to distance from the nearest nickel phase region was calculated using an algorithm developed in Python (see supplementary material). Afterwards, a pseudo-2D model was developed to describe the electrochemical reaction of hydrogen at the TPB and ceria-pore DPB of Ni/CGO. Polarization resistance of electrodes were extracted form EIS and used to fit the model and calculate the relative reactivity of electrochemical reaction on fibre, impregnated and conventional cermet electrodes.

5.2.5 Definition of DPB Boundary weighted by distance to nickel

Inspired by Rinaldi et al.[312], we define an intra-ceria distance to measure length of the shortest path through bulk ceria[313] from a ceria point to ceria-nickel DPB, which is connected to the percolated Ni network. Fig. 5.2.1 shows a cross section of three-dimensional tomography data in voxel grids and colour of each voxel represents its phase (Ni is shown in grey, the CGO is reported in white and the pore phase is in black). The intra-ceria distance is approximated with the length of the nearest path (marked in red) among all possible paths from a given ceria-pore DPB to ceria-nickel border, which is different from Euclidean distance (marked in blue).

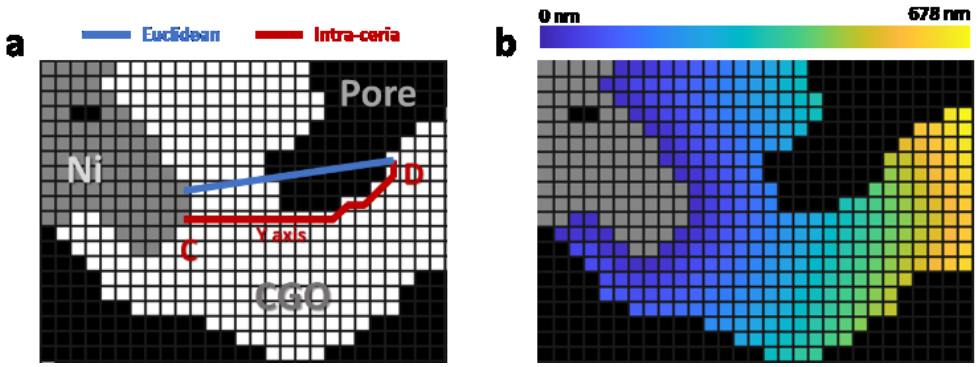


Fig. 5.2.1 a) a 2D cross section of 3-dimensional Ni/CGO electrode data in grids. Grey, white and black grids represent Ni, CGO, black and pore separately. Euclidean distance from a given point to Ni/CGO DPB is marked in blue, while intra-ceria distance is shown as the red curve (Note this shortest path is not unique in grid space). b) At the convergence of cellular automata, each ceria cell is assigned with a value representing the intra-ceria distance to Ni/CGO DPB.

Calculation of this non-Euclidean distance is non-trivial due to no analytical solutions. Usually, traversal is a straight-forward approach solving this problem by traversing all possible

paths from the chosen ceria-pore DPB point to any ceria-nickel DPB points and finding the shortest one. However, naïve traversal algorithm demonstrates critical drawbacks on computational complexity: time and space consumption grow exponentially as the traversal operation proceeds. Therefore, we propose here a cellular automata algorithm with parallel computing, which is equivalent to naïve traversal but reduces computational complexity dramatically

A brief mathematical description of the algorithm is presented as follow: We define a non-Euclidean measurement $D(i,j)$ as the distance-within-ceria between two cells, which can be expressed in a recursive form:

$$D(i,j) = \begin{cases} 0 & \text{if } i = j \\ \min_{\forall k \in Ni} E(i,k) + D(k,j) & \text{Otherwise} \end{cases} \quad (1)$$

where $E(i,k)$ is the Euclidean (L2) distance between two cells in grid space.

The aim of our cellular automata algorithm is to evolve from an initial state C^0 towards a final state C^*, which is the minimum distance map between each point within the bulk of ceria to its nearest ceria-nickel border. C^* satisfies:

$$C^*(i) = \min_{j \in S_{c\&n}} D(i,j) \quad (2)$$

where $S_{c\&n}$ represents the set of all ceria-nickel border cells. Combined with Eq. (1) above, Eq. (2) can be written as:

$$C^*(i) = \min_{j \in S_{c\&n}, k \in Ni} [E(i,k) + D(k,j)] \quad (3)$$

$$= \min_{k \in Ni} \left[E(i,j) + \min_{j \in S_{c\&n}} D(k,j) \right] \quad (4)$$

$$= \min_{k \in Ni} [E(i,j) + C^*(k)] \quad (5)$$

The entire continuous cellular automata algorithm is described as:

INPUT: set of ceria cells S_c, set of ceria-nickel border cells $S_{c\&n}$ (notice $S_{c\&n} \cap S_c = \emptyset$)

STEP1 Initialisation:

$$C^0(i) \leftarrow \begin{cases} 0 & if\ i \in S_{c\&n} \\ inf & Otherwise \end{cases} \quad (6)$$

STEP2 Repeat:

$$\forall i \in S_c, C^{t+1}(i) \leftarrow \min_{k \in Ni}[E(i,j) + C^t(k)] \quad (7)$$

Until $C^{t+1} = C^t$

OUTPUT: $C^* \leftarrow C^t$

The cellular automata starts with an initial state C^0 with only two values: 0 for ceria-nickel DPB cells and inf (unknown) for the rest. The updating rule of cellular automata is to find the length of the current optimal path towards the ceria-nickel DPB via different neighbourhood cells. After a finite number of repetitions, cellular automata will eventually converge to C^*.

With the distance map C^*, DPB within certain distance *d* of the ceria phase can be achieved by simply finding the number of cells satisfying:

$$i \in S_{cp}, C^*(i) < d \quad (8)$$

where S_{cp} is a set containing all ceria-pore DPB cells. This algorithm was developed in Python with CUDA acceleration. The source code can be found in the supplementary material*.

5.2.6 Electrochemical Modelling

The quantification of the microstructural contribution to the electrode polarisation resistance is performed by using a continuum pseudo-2D physically-based model, which takes into account the main transport and reaction phenomena taking place within the Ni/CGO anodes. Two reaction pathways for hydrogen oxidation are considered: a surface path (Eq. (9a)), taking place at the DPB (i.e., on the CGO-pore surface), and a TPB path (Eq. 9b))[24]:

$$H_{2(g)} + O^{2-}_{(CGO)} \rightarrow H_2O_{(g)} + 2e^-_{(CGO)} \quad (9a)$$

$$H_{2(g)} + O^{2-}_{(CGO)} \rightarrow H_2O_{(g)} + 2e^-_{(Ni)} \quad (9b)$$

Due to the small electrode thickness and the large diffusivities of gas species, gas transport resistances are neglected, so uniform hydrogen and water partial pressures are assumed

throughout the anode thickness[290]. Similarly, due to the large electronic conductivity of Ni, the reduced electrochemical potential of electrons in Ni is considered uniform[314] and equal to the applied electrode overpotential η_{ed}.

Under these simplifications, the conservation of ionic current flux J_O along the electrode thickness results as follows:

$$\frac{\partial J_O}{\partial x} = i^v_{TPB} + i^v_{DPB} \tag{10}$$

thus, taking into account the current generation per unit of electrode volume given by the TPB and the DPB reaction pathways, i^v_{TPB} and i^v_{DPB}, respectively. The ionic current density J_O is assumed to obey the diffusion-drift equation[95, 176, 177]:

$$J_O = -\sigma_O^{eff} \frac{\partial \tilde{\mu}^*_O}{\partial x} \tag{11}$$

where σ_O^{eff} is the effective ionic conductivity of CGO and $\tilde{\mu}^*_O$ is the reduced electrochemical potential of oxygen ions in CGO[95, 315]. Notably, $\tilde{\mu}^*_O$ is set equal to 0 V at the anode/electrolyte interface ($x = h_{ed}$, where h_{ed} is the anode thickness) as a reference potential and no ionic flux (i.e., $J_O = 0$) is set at the anode/current collector interface ($x = 0$).

The current density produced by the TPB reaction path i^v_{TPB} is assumed to follow linear Butler-Volmer kinetics[316]:

$$i^v_{TPB} = L^v_{TPB} k_{TPB} (\eta_{ed} - \tilde{\mu}^*_O) \tag{12}$$

which is a valid assumption near open-circuit conditions, where k_{TPB} is the kinetic constant of reaction (9b), L^v_{TPB} is the TPB density per unit volume and $\eta_{ed} - \tilde{\mu}^*_O$ is the activation overpotential, equal to the difference between the reduced electrochemical potential of electrons in Ni (η_{ed}) and the reduced electrochemical potential of oxygen ions in CGO ($\tilde{\mu}^*_O$). Any partial pressure-dependence on k_{TPB} is neglected for simplicity.

The current density produced by the DPB reaction path i^v_{DPB} is evaluated by solving for the electronic transport in CGO and the surface reaction (Eq. (9a)) along the local scale y. The local scale y runs from $y = 0$, which is a ceria-nickel border at any integral coordinate x, to $y = \delta_{CGO}$, which is the maximum distance of a CGO-pore surface cell as evaluated by the cellular

automata described in the previous section. Thus, while the integral scale *x* solves for the transport of oxygen ions along the electrode thickness, the local scale *y* solves for the lateral transport of electrons in CGO produced by the DPB reaction (Eq. (9a))[95].

The electronic charge balance on the local scale *y* is equal to:

$$\frac{\partial J_e}{\partial y} = -i_{DPB} a'_{DPB} \delta_{CGO} \tag{13}$$

where a'_{DPB} is the DPB density distribution, evaluated according to the cellular automata as a function of *y* for different electrode microstructures, and J_e is the electronic current flux in CGO, calculated according to the diffusion-drift equation:

$$J_e = -\sigma_e^{eff} \frac{\partial \tilde{\mu}_e^*}{\partial y} \tag{14}$$

where σ_e^{eff} is the effective electronic conductivity of CGO and $\tilde{\mu}_e^*$ is the reduced electrochemical potential of electrons in CGO. In particular, $\tilde{\mu}_e^*$ is equal to the electrochemical potential of electrons in the Ni phase, equal in turn to η_{ed}, at the ceria-nickel border ($y = 0$) while no electronic flux $J_e = 0$ is enforced at $y = \delta_{CGO}$.

The current density produced by reaction (9a) per unit of DPB surface i_{DPB} is evaluated according to Ciucci et al.[95] as:

$$i_{DPB} = k_{DPB,0} p_{O_2}^{-1/4} (\tilde{\mu}_e^* - \tilde{\mu}_O^*) \tag{15}$$

that is, proportional a surface-specific kinetic constant $k_{DPB,0}$, the oxygen partial pressure raised to the power -1/4 and the reduced electrochemical potential difference between electrons and ions in CGO. By integrating for the local scale *y*, the DPB current density per unit of electrode volume i_{DPB}^v to be used in Eq. (10) can be calculated from the electronic current at $y = 0$, as follows:

$$i_{DPB}^v = \frac{J_e(y=0)}{\delta_{CGO}} \tag{16}$$

The effective conductivities σ_O^{eff} and σ_e^{eff} are calculated by correcting the bulk conductivities σ_O and σ_e, which depend on temperature and oxygen partial pressure as from

Atkinson et al.[317], for the CGO volume fraction and tortuosity factor (i.e., $\sigma_i^{eff} = \frac{\rho_{CGO}}{\tau_{CGO}}\sigma_i$), which are evaluated by 3D microstructural analysis along with L_{TPB}^{v}, δ_{CGO} and a'_{DPB}. The set of Eqs. (10-16) represents a pseudo-2D model of the TPB and DPB reaction pathways to be solved in the variables $\tilde{\mu}_O^*(x)$ and $\tilde{\mu}_e^*(y)$, with two unknown fitting parameters, namely the kinetic constants k_{TPB} and $k_{DPB,0}$. By numerically solving the model, the electrode polarisation resistance R_{ed} is evaluated as:

$$R_{ed} = \frac{\eta_{ed}}{J_{ed}} \tag{17}$$

where the total electrode current density is equal to the ionic current evaluated at the electrolyte interface, $J_{ed} = J_O(x = h_{ed})$.

5.2.7 Electrochemical Characterization of the Symmetrical Cells

The symmetrical cells were placed in the same custom rig described in Chapter 3 (figure 3.2.1) and tested by using an electrochemical workstation (Autolab, Metrohm) in a two-electrode configuration. Electrochemical impedance spectroscopy (EIS) was performed from 600-800 °C, 0.02-100000 Hz, under flow of 3% humidified 10% H_2/N_2 gas mixture with a flowrate of 100 ml min^{-1}. EIS tests were also performed while during aging at 600°C for a total of 200 h and 800°C for 100 h to examine the stability and degradation pattern of electrodes at high temperature[294, 318].

The cermet 2 was tested by our collaborator in Japan using the same conditions as above.

5.3 Results and Discussion

5.3.1 Contribution of DPB and TPB on Conventional Electrodes

5.3.1.1 EIS and Morphology of Conventional Electrodes

Results of EIS measurements of cermet and impregnated electrodes are shown in figure 5.3.1a at 600 °C and 3% humidified 10% H_2/N_2. The EIS data was fitted by using the same equivalent circuit ***$LR_s(R_1CPE_1)(R_2CPE_2)(R_3CPE_3)$*** as chapter 3, where ***L*** stands for inductance, ***R*** for resistance and ***CPE*** for constant phase element, since at least three impedance contributions are expected in conventional electrodes, as also more evident at higher temperatures[289]. The fitted EIS result is shown in table 5.3.1.

Table 5.3.1 Summary of EIS fitting results of cermets and impregnated Ni/CGO. Fitted by the equivalent circuit $LR_s(R_1CPE_1)(R_2CPE_2)(R_3CPE_3)$

	R_s/ Ωcm^2	R_1/ Ωcm^2	R_2/ Ωcm^2	R_3/ Ωcm^2
Impregnated	3.40	0.12	2.03	0.28
Cermet 1	3.9	0.016	3.77	0.45
Cermet 2	5.57	0.43	6.21	1.08

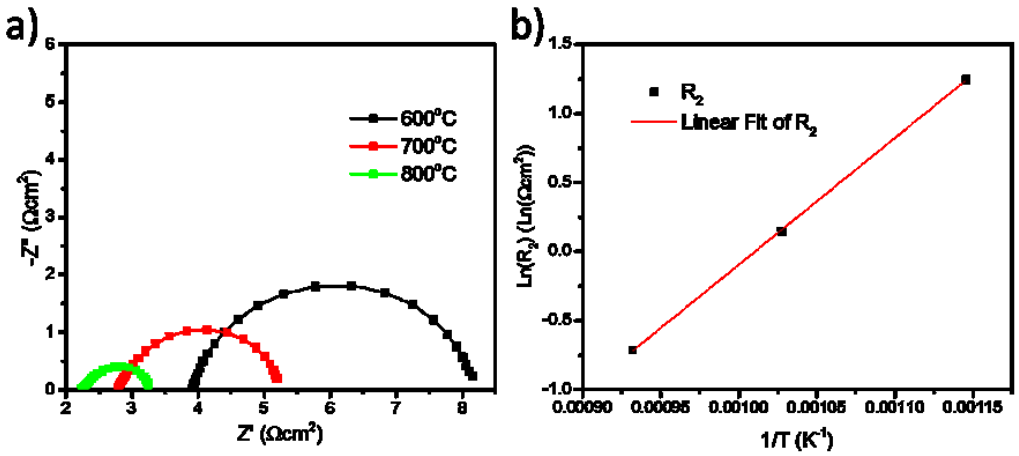


Figure 5.3.1 a) The EIS of cermet 1 electrode at 600, 700 and 800°C; b) The Arrhenius fitting of R_2.

According to the EIS deconvolution discussed in chapter 4, the resistance R_2 of the MF process is the only one relevant to the hydrogen electrochemical reaction and is affected by the electrode microstructure. Thus, the R_2 values of impregnated, cermet 1 and cermet 2 Ni/CGO, equal to 2.03, 3.77 and 6.21 Ω cm^2, respectively, must be compared with the microstructural parameters relevant for performance (i.e., volume fractions, as well as TPB and DPB densities), which are reported in Table 5.3.2 along with the electrode thickness, evaluated from SEM cross sections.

3D reconstruction through FIB-SEM tomography show that pore and ceria phases are entirely percolating within the impregnated electrode. Similarly, the nickel phase has mostly achieved percolation except for a few isolated nano-particles, accounting for less than 2 vol%.

Thus, full percolation of all the phases is achieved in the impregnated Ni/CGO electrode. On the other hand, in cermet 1, 24.3 vol% of Ni phase is not connected with the major metal network: these nickel regions were excluded from the determination of DPB density and subsequent model calculations.

Major differences between impregnated and cermet electrodes arise when comparing TPB and DPB densities. As shown in Table 5.3.2, the impregnated Ni/CGO anode shows a TPB density of 41.60 μm^{-2}, which is roughly one order of magnitude larger than in cermets (4.95 and 3.85 μm^{-2}), in agreement with previous investigations[285] and theoretical predictions[319]. The different TPB density in impregnated and cermet electrodes is due to the different Ni particle size, which is much smaller in the impregnated electrode than cermet electrodes (< 50 nm vs 500 nm, respectively). In particular, Ni nano-particles are evenly distributed on the ceria surface in the impregnated electrode. Such an even nano-particle distribution hinders the exposure of the ceria surface to the porous phase, so that 81.7 % of the potential CGO-pore surface is covered by nickel, as shown in figure 5.3.2c. On the other hand, only the 43.9% of CGO surface is covered by Ni in cermets (figure 5.3.2d). As a result, the exposed ceria-pore DPB density is smaller in the impregnated electrode than in cermets (1.70 μm^{-1} vs 2.31 and 1.91 μm^{-1}, respectively). In addition, cellular automata shows that most of the ceria-pore DPB of impregnated electrode lies within 0.5 μm from the nickel phase (figure 5.3.2b, red line). On the other hand, the DPB density distribution in cermets is more dispersed, with most of the DPB lying within 1.5 μm from nickel.

Table 5.3.2 Summary of relevant microstructural parameters of impregnated and cermets Ni/CGO.

	Thickness / μm	**Ni content / vol%**	**Porosity / vol%**	**Effective TPB Density L_{TPB}^{v} / μm^{-2}**	**CGO-Pore DPB Density / μm^{-1}**
Impregnated	15	16.37	30.23	41.60	1.70
Cermet 1	19	24.06	46.39	4.95	2.31
Cermet 2	15	25.97	50.69	3.85	1.91

The distribution of ceria-pore DPB density with different distances from metal phase were determined by a cellular automata algorithm described in Chapter 5.2.4, the distance is defined by the shortest distance within bulk ceria from the ceria-pore DPB point to its nearest

nickel phase. For the sake of simplicity, let us consider a 2-dimensional version of the electrode, as reported in Figure 5.3.2f, where Ni is shown in grey, the CGO surface is reported in blue and the pore phase is in white. Consider that the voxel side length is Δy = 1 µm and that the distance of any CGO surface voxel from the nearest Ni is measured according to a city-block approach, as presented by the numbers on blue blocks. The areas density within this distance as a function of the distance y is plotted in Figure 5.3.2c and used to generate the area distribution, as in Figure 5.3.2b.

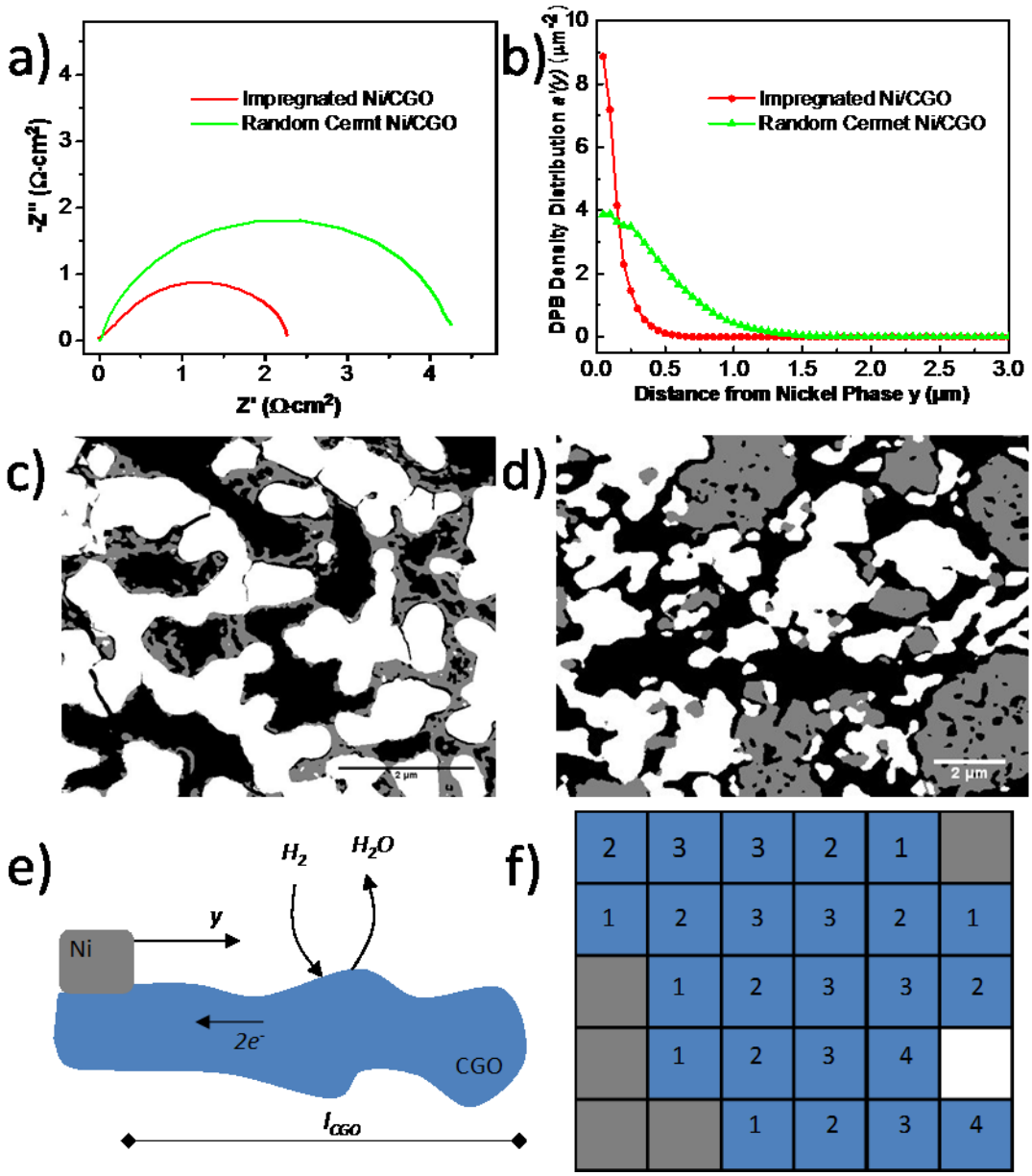


Figure 5.3.2 a) The EIS results of impregnated and cermet Ni/CGO at 600°C, 9.7% H_2/97.3% N_2/3%H_2O; b) The distribution of ceria-pore DPB density with distance to nickel phase A slice of FIB-SEM cross-section image of c. Impregnated Ni/CGO; d. Cermet Ni/CGO; white phase represents CGO, grey phase nickel, black phase pore; e) Sketch of the electron transport within the CGO phase and of the electrochemical reaction at the DPB along the y-scale; f) 2-dimensional example for illustration of the distribution of DPB area.

5.3.1.2 Decoupling DPB vs TPB contribution via modelling

A preliminary interpretation of the EIS results can be done on the basis of the microstructural parameters discussed in the previous section. The lower MF polarisation resistance R_2 of the impregnated electrode can be qualitatively justified by the larger TPB density compared to cermets. Actually, this is the general interpretation commonly accepted for anodes based on purely ionic ceramics, such as YSZ, wherein charge transfer reactions occur at the TPBs. However, the TPB density does not seem to be the only relevant microstructural parameter for Ni/CGO anodes. In fact, due to the MIEC properties of CGO, which allow for the extension of the electrochemically active zone within a certain distance on the CGO-pore surface, the DPB density distribution might be as important as the TPB density. More specifically, in Pt/SDC patterned electrodes Chueh et al. [24] reported that the main electrochemical reaction pathway is dominated by DPBs with minimal contributions from the TPBs. Such experimental evidence was confirmed by Ciucci et al. [95], who set up a 2-D model of Pt/SDC patterned anodes and found that the electrochemical active area on doped-ceria surface can extend from 0.6 µm up to 4 µm from the metal current collector. Thus, in MIEC-based anodes, the DPB density should matter more than the TPB density. On the other hand, despite the DPB density of the cermets being larger than the impregnated electrode (see table 5.3.2), the impregnated sample outperforms in terms of polarisation resistance. This suggests that, in composite Ni/CGO electrodes, both the TPBs and the DPBs contribute to hydrogen electro-oxidation and none of them on their own can be considered dominant.

The quantification of the DPB vs TPB contribution is made by fitting the R_2 values in the three different electrodes using the electrochemical model. The two unknown kinetic parameters, k_{TPB} and $k_{DPB,0}$, were estimated from the fitting, equal to $6 \cdot 10^{-6}$ S m^{-1} and $3.6 \cdot 10^{-5}$ S atm$^{1/4}$ m^{-2}, respectively, at 600 °C and 3% humidified 10% H_2/N_2. These values lie within the same order of magnitude of the kinetic constants of the TPB reaction in Ni/YSZ electrodes according to de Boer[320] and the DPB reaction in Pt/SDC anodes according to Ciucci et al.[95]. With only two adjustable parameters, the mechanistic model allows a satisfactory fitting of

the polarisation resistance of all three electrodes despite their very different microstructures, as reported in Table 5.3.3. In particular, an excellent match between model results and experimental data is achieved for the impregnated and cermet 1 samples and a relative error in R_2 in the order of 5 % is obtained for cermet 2.

Model results enable rationalization of the electrochemical response as a function of microstructural properties and allow for the quantification of the relative contribution of DPB and TPB reaction pathways to the overall hydrogen electrochemical conversion. Model predictions indicate that more than 80 % of the current produced in cermets comes from the DPB reaction pathway (last column in Table 5.3.3. This is a consequence of the broader DPB density distribution, which extends more than 1.5 μm from Ni internal contacts as shown in Figure 5.3.2b. This means that the Ni phase provides a good distribution throughout the cermet microstructure of electronic current, which is then converted into ionic current at the DPBs which extend from each Ni-CGO contact. This is in fair agreement with the conclusions reached by Chueh et al. [24] and Ciucci et al. [95]. On the other hand, in the impregnated anode the DPB is mostly hindered by Ni nanoparticles (Figure 5.3.2c), resulting in a narrow DPB distribution around the TPB: in such a situation, there is not enough extended DPB available for the surface reaction pathway (Eq. (9a)), so electrochemical conversion proceeds according to the TPB pathway (Eq. (9b)) thanks to the large TPB density. In particular, only 27.2 % of current is converted through the DPB pathway in the impregnated Ni/CGO anode, meaning that the TPB pathway compensates for the lack of extended DPB producing more than 72 % of current and allowing the impregnated electrode to outperform the others.

Table 5.3.3 The summary of calculation results from pseudo-2D model of impregnated and cermet Ni/CGO anodes

	Experimental R_2 / Ωcm²	**Fitted R_2 / Ω cm²**	I_{DPB}/I_{tot} **/ %**
Impregnated	2.02	2.02	27.2
Cermet 1	3.77	3.77	81.3
Cermet 2	6.21	5.89	82.1

Thus, the model allows for the quantitative estimation of the DPB vs TPB contribution to electrochemical activity of Ni/CGO anodes as a function of electrode microstructure,

suggesting that the extension of the DPB density distribution has an equally dramatic influence on the total performance of cermets as the TPB density.

5.3.1.3 The influence of electron conductivity

To investigate if the electron conductivity of CGO is rate-limiting on the DPB electrochemical reaction, the fitting results from models with and without considering DPB density distribution are compared. Without considering the DPB density distribution, we assume the electrochemical reactivity of all DPB is the same, irrelevant to its distance from Ni, as elaborated in more detail in the chapter 5.2. For both cermets and impregnated electrodes, same R_2 values are fitted with only 1% difference in k_{TPB} and $k_{DPB,0}$. This suggests the influence of CGO electron conductivity on electrochemical oxidation reactivity can be neglected and the surface reaction is rate-limiting. The result confirms Haile et al.'s[24] conclusion and extends it to real porous electrodes, indicating that conventional microstructures design of Ni/CGO electrodes are far from being able to exploit the potential of the DPB reactivity, and the performance of electrode can be effectively enhanced by increasing DPB density and the extension of DPB without reaching the limitation of CGO electronic conductivity.

5.3.1.4 The Contribution of DPB vs TPB and Implications

According to the experimental results and the mechanistic interpretation discussed in the previous sections, some recommendations can be made regarding possible strategies to enhance the performance of Ni/CGO anodes.

Cermet Ni/CGO electrodes are among the most commonly used electrode architectures due to the ease of fabrication and good thermal stability. However, as previously shown, the electrochemical performance of cermets have scope for improvement due to their limited active TPB and DPB densities. This is partly due to the large nickel particle size and particle distribution, which create disconnected and hence inactive Ni particles, hindering the electronic current percolation and making a large portion of the TPBs inaccessible along with limited DPB density. Both the TPB and DPB densities might be increased by reducing the Ni and CGO particle size, but in such a case the extension of DPB distribution would be quite

limited and gas concentration losses may become significant as the pore size decreases. Therefore, conventional cermets are far from an efficient structure for CGO-based anodes.

Impregnated Ni/CGO electrodes show better electrochemical performance but offer little room for improvement. In fact, nickel covers most of the CGO surface as a result of the tendency to decrease the surface energy during the impregnation process [130]. This hinders the exposure of the CGO surface to the pore phase, reducing the DPB density. The TPB reaction pathway can compensate for the lack of DPB due to the larger TPB density created by Ni nano-particles, but this does not make full use of the benefits of MIEC materials. Moreover, increasing the TPB density by reducing the size of Ni nano-particles has several drawbacks. Nickel nano-particles are highly susceptible to coarsening at normal SOFC operation temperatures[298, 321]. As pointed out by Holzer et al.[67], small average grain sizes, wide particle size distribution and high nickel volume fractions lead to higher coarsening rates, thus reducing TPB density, nickel percolation and, in turn, electrochemical performance. In fact, a significant decrease in TPB density, with corresponding increase in polarisation resistance by over an order of magnitude, were observed in both impregnated Ni/ScSZ[318] and Ni/YSZ[294] even at a relatively low temperature (550 °C) within the first 200 h of operation. Thus, long-term stability is an issue in all the electrodes that rely on large TPB density via Ni nano-particle impregnation.

Therefore, rather than pointing towards nano-particles and TPB maximization, modelling results suggest that modifying the ceria-pore DPB is an alternative strategy to effectively enhance the electrode performance of MIEC-based electrodes. Apart from Jung et al. works[96, 322], who developed a nano-columnar ceria scaffold, so far there has been little effort in maximizing the ceria-pore DPB of SOFC anode materials. According to this design strategy, in order to ensure maximum DPB while maintaining a robust structure, new MIEC-based electrode microstructures should fulfil the following requirements:

1. Full percolation of MIEC, pore and nickel phase;
2. Sufficient ion, electron conductivity and gas transport;
3. Maximum DPB and reasonable TPB;
4. Structure be able to inhibit degradation at operation temperature;
5. Sufficient contact between nickel and MIEC for charge transfer;

6. Facileness and flexibility of preparation route.

Because electron transport in nickel is much faster than ion transport in ceria (~10^6 times) [323], enough electronic conductivity can be achieved with small amount of nickel as long as nickel percolates. Also, to meet requirement no. 3, the volume fraction of nickel should be minimized: this requires the percolation threshold of nickel to be as low as possible. On the other hand, the requirement for ion conductivity suggests that the cross-section area of the ceria phase needs to be sufficiently large. These requirements lead to the combination of electrospinning and conventional tape-casting techniques: the former provides long nickel networks with a low percolation threshold while the latter provides ceria-based backbones with sufficient oxygen ion transportation. By controlling calcination processes and vacuum treatment, the electrospun nickel network can be implanted into cast ceria substrates, forming a percolating NiO fibre network and ceria matrix composite structure, whose performance and characterization are reported in the next section.

5.3.2 Characterization of Novel Structured Ni/CGO

5.3.2.1 Performance of FMS Ni/CGO Anode

SEM images of electro-spun NiO/PAN fibres, carbonized fibre membrane and pre-calcined fibre membrane are shown in figure 5.3.3a and b. The as electro-spun membrane is formed by aligned, continuous PAN fibres of ~500-1000 nm diameter, with NiO particles of 500-800 nm embedded inside the fibres. After carbonization at 500 °C, PAN decomposes into amorphous carbon [324], and the fibres remain intact with almost no fracture. After 1000 °C pre-calcination, all the carbon is oxidized and eliminated while NiO fibres of 400-1000 nm diameter formed a well-percolated network. The diameter grew larger because of sintering of smaller NiO particles. During pre-calcination, the volume of the membrane shrunk by ~30 %. After placing the membrane into the tape-cast slurry and calcination, apart from a thin layer (< 1 μm) of NiO fibres exposed on the surface for current collection, most of the fibres were embedded within the CGO matrix.

Results of EIS measurements of symmetric FMS cells at different temperatures are shown in figure 5.3.3c-e. The offset of EIS on the real axis represents the ohmic resistance equal to 3.07 Ω cm^2, 1.13 Ω cm^2 and 0.69 Ω cm^2 at 600 °C, 700 °C and 800 °C, respectively. These resistance values are in good agreement with the conductivity of a 0.25 mm-thick YSZ pellet

at these temperatures[325, 326], indicating that the ohmic resistance mainly comes from the YSZ electrolyte and that the electron conducting phase in the FMS electrode is fully percolating. As previously discussed above, and as evident from EIS at high temperature (figure 5.3.3e), three impedance contributions are present. Thus, the EIS data was fitted by the same equivalent circuit $LR_s(R_1CPE_1)(R_2CPE_2)(R_3CPE_3)$ used also for impregnated and cermet electrodes. A good fit was obtained across the entire temperature range (see red line in figure 5.3.3c-e), resulting in R_2 values of the FMS electrode equal to 1.62, 0.26 and 0.024 Ω cm^2 at 600, 700 and 800 °C, respectively. A comprehensive summary of the fitting results is reported in table 5.3.4

Table 5.3.4 The summary of fitted EIS result of FMS Ni/CGO electrode at 600, 700 and 800°C

	R_s/ Ωcm^2	R_1/ Ωcm^2	R_2/ Ωcm^2	R_3/ Ωcm^2
600 °C	3.07	0.039	1.62	0.21
700 °C	1.13	0.065	0.26	0.22
800 °C	0.69	0.08	0.024	0.21

Figure 5.3.3f compares the impedance spectra of FMS, impregnated and cermet 1 Ni/CGO at 600 °C: the FMS shows the lowest overall polarisation resistance. More specifically, the microstructure-related contribution R_2 of FMS is 1.62 Ω cm^2, being 20 % and 57 % lower than the MF resistance of impregnated and cermet electrodes, respectively. This indicates that the new FMS electrode does have an improved overall electrochemical activity compared to conventional electrode designs.

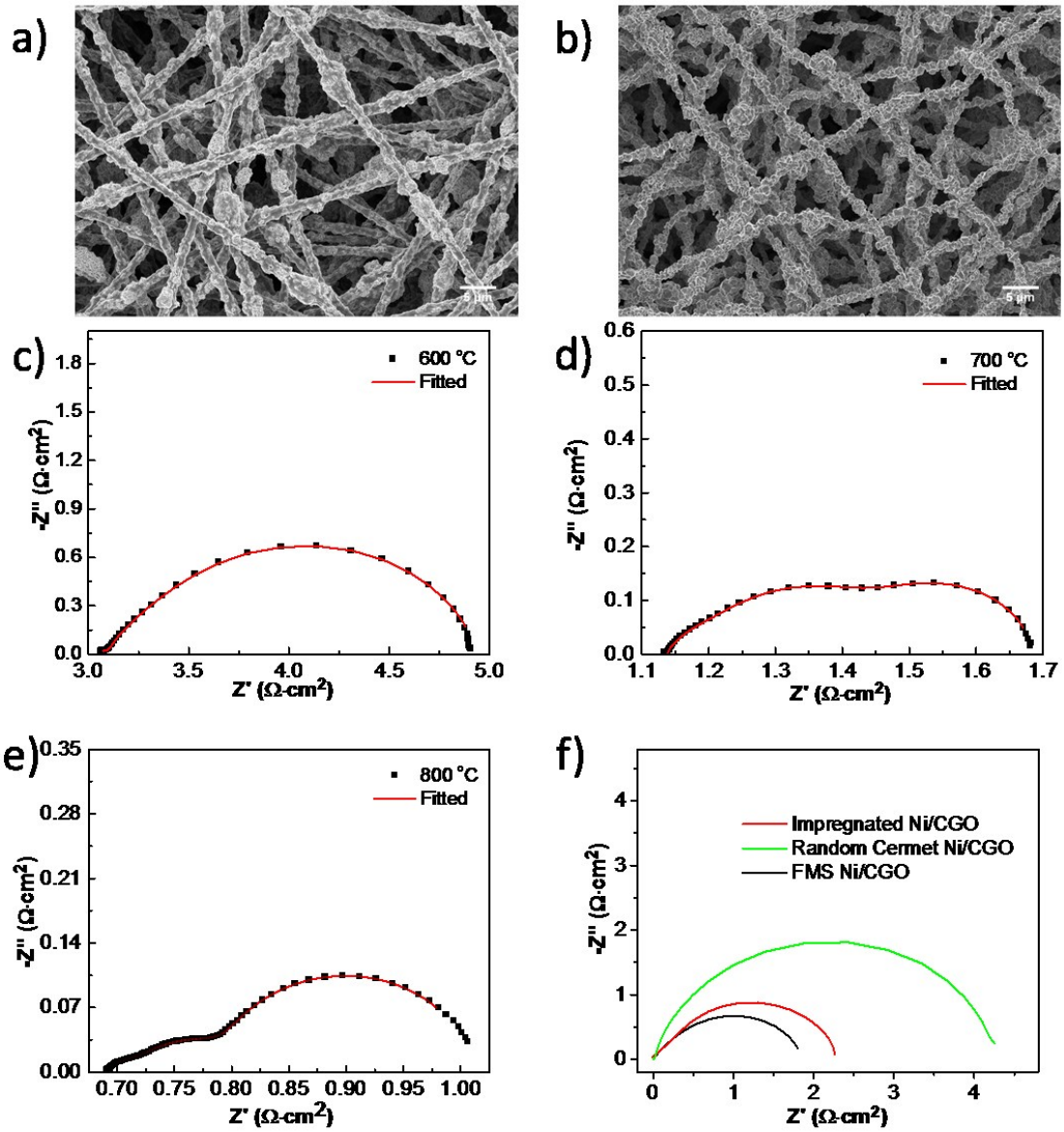


Figure 5.3.3 SEM image of a) Carbonized NiO fibre membrane; b) Precalcined Ni fibre membrane; EIS and fitted impedance of Ni/CGO fibre electrode at c) 600°C; d) 700°C; e) 800°C; f) EIS of FMS, impregnated and cermet 1 Ni/CGO at 600°C.

5.3.2.2 Microstructural and Electrochemical Characterization of FMS Ni/CGO

The 3D reconstruction through FIB-SEM images (figure 5.3.4a-c) indicates that pore and ceria phases are entirely percolating in the FMS electrode. Ni fibres retain structural integrity after embedding and calcination with the CGO backbone, forming a connected Ni network. Only a small part (~12 vol %) of the fibres appear to be separated from the main network.

However, these separated fibres extend beyond the edge of cross-section images, so are not fully captured in the scale of 3D reconstruction and are likely part of the percolating network since, according to SEM images, Ni fibres extend over 20 μm without breakage. For these reasons, all Ni fibres are considered connected to the Ni network and hence percolating. As a consequence, all TPBs are considered active. As shown in table 5.3.5, the Ni volume fraction is 11.5 vol% for FMS Ni/CGO, suggesting the Ni percolation threshold is low in FMS, much lower than in conventional cermets (c. 30 vol%)[327].

According to the microstructural analysis reported in Table 5.3.5, the FMS has a TPB density 4.7 times lower than impregnated Ni/CGO (8.8 vs 41.6 μm^{-2}). However, FMS was specifically designed to maximise the DPB distribution rather than the TPB density. In fact, the total DPB density of the FMS electrode is 7.4 μm^{-1}, 4.3 times larger than impregnated (1.7 μm^{-1}) and 3.2 times larger than conventional cermet 1 (2.3 μm^{-1}). In particular, as evaluated by the cellular automaton algorithm, the FMS electrode shows a better DPB distribution. As reported in figure 5.3.6c,d, which shows the cumulative and density DPB distributions, respectively, the FMS electrode presents an extended DPB which stretches out for more than 1.5 μm from a Ni contact, thus being significantly larger than any other electrode microstructures here analysed. The drop in DPB density distribution at 0.25 μm for FMS (figure 5.3.6d) is likely due to the shrinkage during the reduction of NiO to Ni. In any case, for FMS, 90% of the DPB is within 1.1 μm from the Ni phase and 99.2% is within 2 μm; on the other hand, for the impregnated sample, 92% of DPB is within 0.25 μm and all the DPB is confined within 0.6 μm from Ni. The wider extension of the DPB in FMS is visually depicted in figure 5.3.6a,b, which shows the 3D reconstruction of a single nickel fibre extracted from the Ni network (in grey, figure 5.3.6a) and the CGO phase located within 1 μm from nickel (in yellow-red, figure 5.3.6b). These structural parameters indicate that the design of the FMS electrode is successful in maximizing the ceria-pore DPB and that such a structure is valid for the use in MIEC-based SOFC anodes.

Table. 5.3.5 Summary of structural parameters of FMS, impregnated and cermet Ni/CGO electrodes

	Ni content / vol%	**Porosity / vol%**	**Effective TPB Density L_{TPB}^{v} / µm^{-2}**	**CGO-Pore DPB Density /µm^{-1}**
FMS	11.5	48.4	8.8	7.4
Impregnated	16.3	30.2	41.6	1.7
Cermet 1	24.1	46.3	3.0	2.3
Cermet 2	26.0	50.7	3.8	1.9

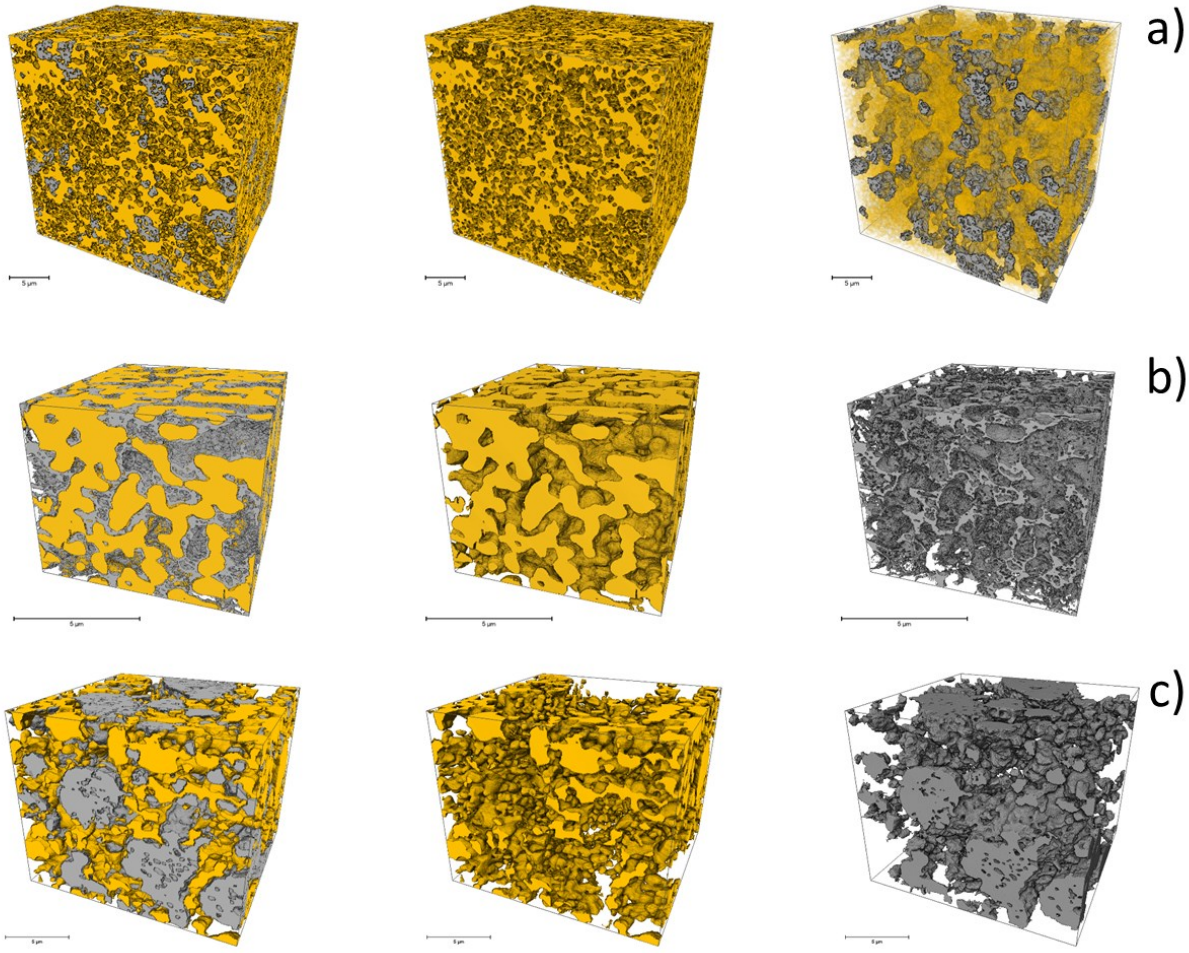


Figure 5.3.4 3D construction of a) FMS; b) Impregnated; c) Cermet 1 Ni/CGO electrode; In 3D reconstruction, the orange parts are CGO, grey parts are nickel.

The effect of the improved microstructural properties on the electrochemical response is corroborated by the model. By using the same kinetic parameters k_{TPB} = 6·10^{-6} S m^{-1} and $k_{DPB,0}$ = 3.6·10^{-5} S atm$^{1/4}$ m^{-2} fitted above in impregnated and cermet electrodes, without adjusting

any other parameters the model predicts an electrode resistance R_2 equal to 1.61 Ω cm^2, which compares very well with the experimental R_2 value of 1.62 Ω cm^2. The satisfactory comparison between modelling and experimental results in four different electrode microstructures, as shown in Figure 5.3.6e, with only two fitting parameters supports the validity of the physically-based model presented here.

According to the model, 88.6 % of the current produced in the FMS electrode comes from the DPB reaction pathway. This means that FMS shows the largest DPB vs TPB current contribution among all the electrode designs here investigated. In such regard, the FMS makes efficient use of the extended DPB distribution discussed in Figure 5.3.6c,d, thus meeting the target for which the FMS design was conceived. Therefore, the efficient utilization of the ceria-pore DPB justifies the superior electrochemical performance of the FMS electrode.

In this section the structural parameters and polarization resistances of three different structures were put into the 2D physical model to fit two kinetic parameters: k_{TPB} and $k_{DPB,0}$. Then the parameters were used to calculate the polarization resistance of FMS and compared with experimental data. The good fitting results in turns verified the availability of the model, as shown in the diagram figure 5.3.5.

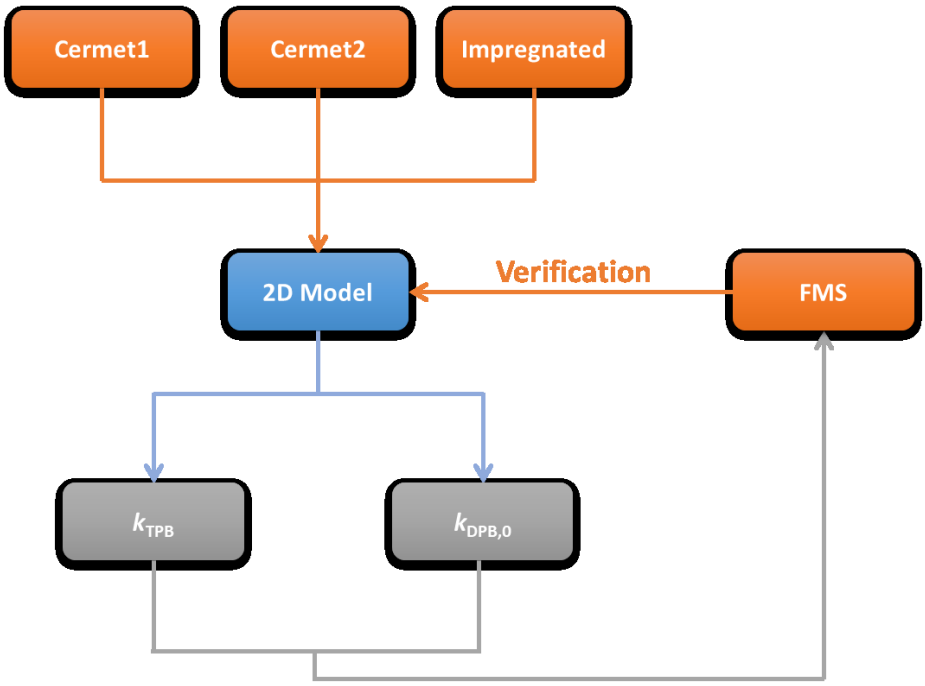


Figure 5.3.5 The diagram of the model-verification procedures presented in section 5.3.1 and 5.3.2.

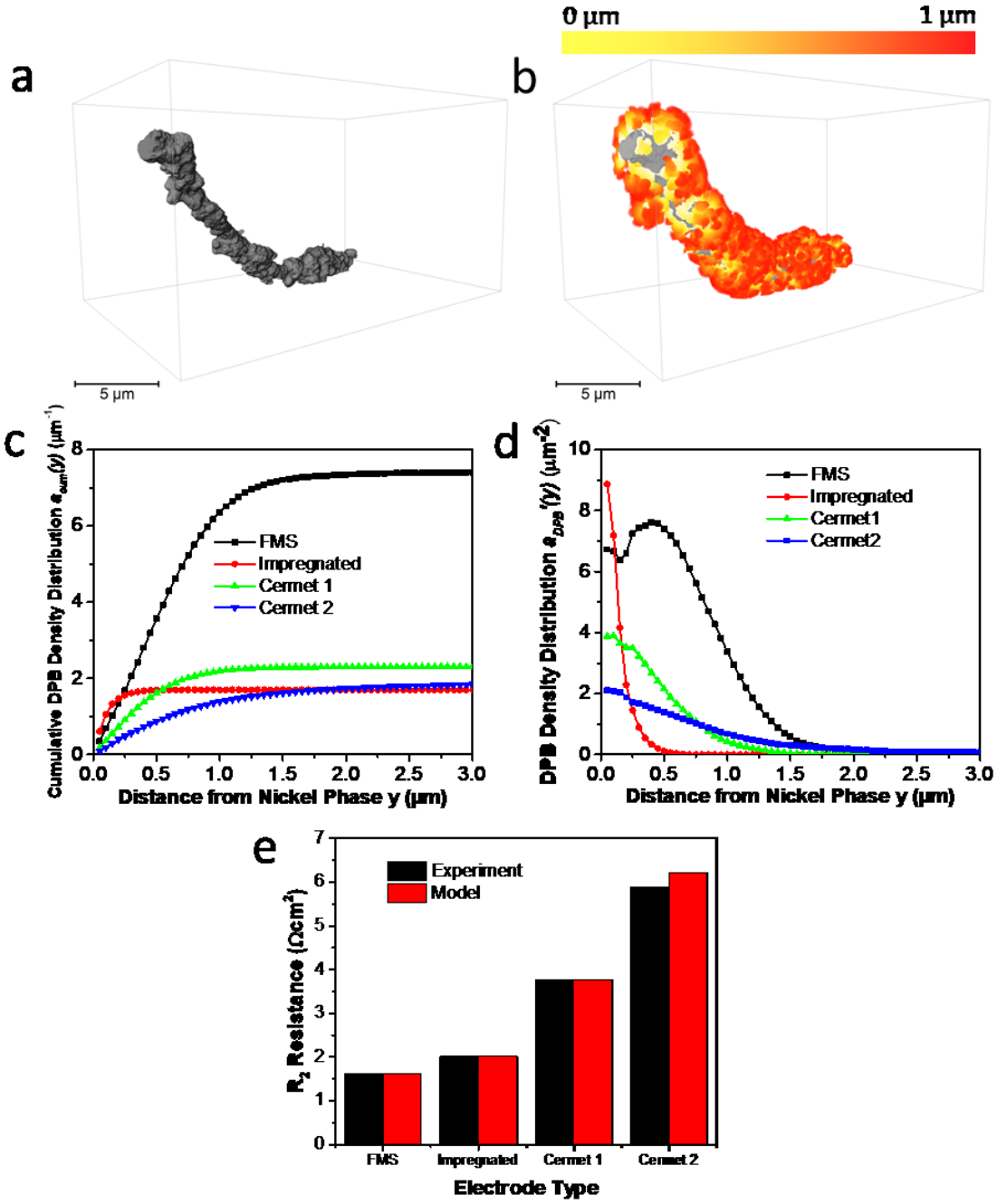


Figure 5.3.6 The 3D reconstruction of a) A single nickel fibre extracted from nickel network; b) The nickel fibre (grey) and CGO that is within 1µm from nickel surface (yellow-red phase), calculated by the cellular automaton algorithm. c) The cumulative distribution of ceria-pore DPB density with distance to nickel phase; d) Distribution of ceria-pore DPB density with distance to nickel phase; e) The comparison of R_2 as obtained from EIS experiments and modelling for FMS, impregnated and cermets Ni/CGO.

5.3.2.3 Performance Stability during Degradation

The previous sections assessed the superior electrochemical performance of FMS design compared to impregnated and cermet CGO-based electrodes. The last requirement to meet concerns the ability of FMS design to inhibit the nickel microstructural evolution at operation temperature, thus ensuring structural and electrochemical stability over time.

The thermal stability of the FMS and impregnated electrodes was investigated by keeping symmetrical cells in 3% H_2O/9.7% H_2/87.3% N_2 gas atmosphere at 600 °C and 800 °C for up to 233 h and 100 h, respectively, measuring the EIS response during degradation. 600 °C was selected for the degradation test because CGO is typically used in intermediate-temperature SOFCs (IT-SOFCs) at 600°C or below. 800 °C was selected, instead, to purposely induce an accelerated degradation, enabling verification of the hypothesis adopted in the previous analysis, as discussed later in this section.

The main results are reported in figure 5.3.7a. At 600 °C, the MF-resistance R_2 of FMS (black curve), equal to 1.62 Ω cm^2 at time zero, stabilized at ~1.75 Ω cm^2 after a few hours without showing any obvious changes for the whole duration of the test (233 h). This corresponds to an increase in polarisation resistance R_2 of only 8 %. Notably, the polarisation resistance R_2 of FMS after ageing (1.75 Ω cm^2) is lower than the resistance values of pristine impregnated (2.02 Ω cm^2) and cermet electrodes (3.77 and 6.21 Ω cm^2). Such an electrochemical stability was corroborated by microstructural analysis of the FMS sample after the degradation test: FIB-SEM cross-section images (figure 5.3.7b) did not show visible changes after aging, with Ni fibres still intact, well percolating and in good contact with CGO particles. On the contrary, the impregnated Ni/CGO electrode showed a dramatic degradation (figure 5.3.7a, red curve): R_2 increased by 55 % within the first 10 h of operation. Afterwards the degradation rate slowed down, nevertheless R_2 increased by an additional 17.9 % from the 10^{th} h to 100^{th} h of aging. This comparison indicates that the FMS electrode is much more stable than impregnated electrodes and has the potential to withstand long-term operation in real SOFC conditions. In addition, the better stability of FMS compared to the impregnated anode confirms that the strategy of increasing the DPB current contribution via extended ceria-pore

surface is a more stable solution than maximizing the TPB density via nano-structuring the Ni phase.

The degradation behaviour of the FMS electrode was studied by accelerating the cell degradation at 800°C for a total of 100 h. The degradation was more pronounced compared with 600 °C, as shown by the green curve in figure 5.3.7a. In the first 15 h the FMS anode went through a quick degradation, as R_2 increased significantly from 0.024 to 0.3 Ω cm^2. After this initial degradation, R_2 stabilized until the end of the test. Despite this significant performance deterioration, the polarisation resistance R_2 of degraded FMS anode is still lower than the R_2 values of pristine cermets 1 and 2, which is 0.49 and 0.57 Ω cm^2 at 800°C. The impregnated electrode, on the other hand, is not usable at 800°C due to its well-known rapid degradation (not shown here). Thus, the FMS electrode shows better EIS performance after stabilization than conventional cermet and impregnated electrodes even at 800 °C.

The full EIS aging profile of FMS Ni/CGO at 800°C is shown in figure 5.3.7c (supplementary information), which enables verification of the hypothesis made above during the EIS interpretation. The ohmic resistance R_s increased from 0.69 to 1.02 Ω cm^2 within the first 15 h, followed by a steady increase up to 1.44 Ω cm^2 towards the 100th h. Such a degradation pattern of the ohmic resistance R_s is similar to that of electrodes degraded at 600 °C, suggesting that the degradation after the 15th hour mainly comes from sintering of current collector. The high-frequency and low-frequency resistance contributions R_1 and R_3, which were assumed to not be related to electrode microstructure, did remain stable over the duration of the degradation test, confirming their attribution to processes occurring outside the electrode.

A closer insight into the ageing mechanisms at 800 °C is offered by 3D microstructural analysis of the FMS electrode after degradation (figure 5.3.7c). Although total TPB and ceria-pore DPB densities remained almost the same, huge changes in microstructure and effective electrical conductivity were detected. Significant nickel agglomeration was observed, resulting in the disappearance of pores inside the Ni fibres and the breakage of the percolating network of the nickel phase, which turned into near-spherical particles with 1-3 µm diameter. This resulted in a major loss in Ni percolation, with further decrease in accessible DPB and active TPB. These microstructural changes probably took place during the first 15 h of

degradation at 800 °C, which showed the rapid increase in R_2. These results indicate that the medium-frequency process (R_2) in impedance is affected by electrode microstructure and, more specifically, is related to the electrochemical reaction at active sites, both on DPBs and TPBs.

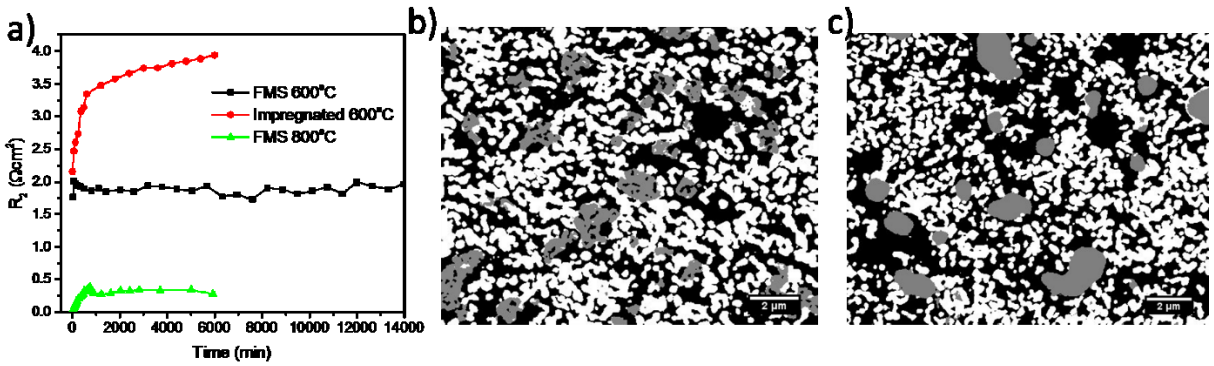


Figure 5.3.7 a) Impedance of FMS Ni/CGO aged in 3%H_2O-9.7% H_2-97%N_2 at 600 °C for 233 h, at 800 °C for 100 h, impregnated Ni/CGO aged in the same condition at 600 °C for 100 h; A slice of FIB-SEM cross-section image of FMS Ni/CGO electrode b) after aging at 600 °C; c) after aging at 800°C, with nickel phase shown in grey, CGO in white and pore in black.

5.3.2.4 Implications from the Pseudo-2D Model for FMS Electrode Optimisation

Similar to conventional electrodes, by applying the electrochemical model to the FMS electrode with or without DPB distribution, negligible differences arise in the prediction of the polarisation contribution $\boldsymbol{R_2}$ (less than 0.5 % difference), suggesting that electron transport in CGO is not rate limiting even with a wider DPB distribution, and all DPB has basically the same reactivity in the FMS electrode. The Pseudo-2D model predictions suggest that, in the specific conditions of the FMS electrode and while keeping the same total DPB density, the DPB distribution can spread up to 6 µm from Ni without any noticeable influence of the CGO electronic resistance on the polarisation contribution $\boldsymbol{R_2}$ (namely, a 2.5 % increase in polarisation resistance). Nevertheless, this indicates that there may be situations for which the DPB distribution from the Ni phase, and so the MIEC electronic resistivity, may become critical in the optimisation of the FMS electrode design. We report below three possible directions for further improvement of the FMS performance along with the corresponding predictions of the pseudo-2D model (all results refer to an operation temperature of 600 °C and 10% H_2):

1. **Reduce CGO particle size for more available DPB density.** A calculation via pseudo-2D model is performed to simulate the situation when smaller particle-size CGO is used as matrix. Let us consider when the DPB density is increased by a factor 5 and extended up to 6 µm away from Ni as discussed above. In such a case, the $\boldsymbol{R_2}$ value calculated from the pseudo-2D model is 0.53 Ω cm^2, thus 3 times smaller than currently obtained. Notably, should the CGO electronic resistance and DPB density distribution be neglected, the polarisation resistance would be underpredicted by 10 %. This implies that the DPB distribution from Ni matters as soon as the DPB density is increased and that there is room for performance improvement by increasing the DPB density without changing the Ni morphology;
2. **Apply materials with higher DPB kinetics.** As the rate-determining step of the process, increasing the surface reaction rate could effectively enhance the overall electrochemical performance. We simulated materials with higher $k_{DPB,0}$ with the same ion/electron conductivity as CGO and found that, when $k_{DPB,0}$ is increased by an order of magnitude, the calculated $\boldsymbol{R_2}$ is 0.31 Ω cm^2, corresponding to a fivefold improvement in performance. By increasing further the catalytic properties of the MIEC material, model predictions show that as soon as the simulated polarisation resistance falls below 0.1 Ω cm^2, the MIEC electronic resistance contributes up to c. 10 % of the polarisation resistance. This indicates that while improving the catalytic properties of the MIEC material towards the DPB reaction is surely essential, the benefits start to fade if the electronic conductivity (and, equivalently, the DPB density distribution from Ni) is not concurrently tailored;
3. **Decrease the fibre diameter while increasing the fibre density.** We have shown that TPB and DPB both contribute to hydrogen conversion. Due to the nature of electrospinning, it is possible to implant membranes composed of thinner and more closed-packed Ni fibres in order to increase the TPB density while maintaining the same exposed DPB, thus enhancing the electrochemical performance. The calculated $\boldsymbol{R_2}$ is 1.46 Ω cm^2 when the TPB density is doubled and 0.88 Ω cm^2 when the TPB density is increased by an order of magnitude, thus being comparatively less effective than the reduction in CGO particle size or the use of more catalytic MIEC materials as discussed in the previous points. Moreover, care needs to be taken as the thermal stability might worsen with thinner Ni fibers.

5.4 Conclusions

This chapter addressed the microstructural optimization strategy of MIEC-based SOFC anodes by quantifying the DPB vs TPB current contribution through the integration of EIS, FIB-SEM 3D reconstruction, and modelling.

Analysis of impregnated and cermet electrodes revealed that the effect of different microstructures on the polarisation resistance of Ni/CGO anodes cannot be solely attributed to the active TPB density. In order to take into account the activity of ceria-pore DPB towards hydrogen electrochemical oxidation, a novel cellular automata algorithm was implemented to evaluate the accessible DPB distribution as a function of the distance from nickel phase from 3D tomographic datasets. This information was used in a physically-based model that, in addition to ionic and electronic current transport, took into account both the TPB and DPB reaction pathways through two length scales along the thickness and the CGO surface, respectively. Results showed that the contribution of ceria-pore DPB on electrochemical activity is significant in a conventional cermet. On the other hand, in impregnated Ni/CGO electrodes most of the DPB is blocked by nickel, so that the TPB reaction pathway compensates for the lack of DPB.

Inspired by these model results, a new structure was designed based on the principle of maximizing the DPB density distribution. The novel structure was prepared by the combination of electrospinning and tape-casting of commercial NiO and CGO powders, consisting of continuous Ni fibre in CGO matrices (FMS). The new FMS Ni/CGO anode exhibited lower polarization resistance compared with other conventional structures, in excellent quantitative agreement with model predictions. In addition, degradation tests revealed the good stability of the FMS electrode at 600 °C, suggesting FMS as a promising electrode design for technological applications.

The study highlights that, by combining electrochemical modelling with microstructural analysis, novel and effective optimization strategies for MIEC-based electrodes can be inspired, going beyond the conventional paradigm of high TPB via nano-sized particles. FMS might only be one of many structures that is capable of efficiently activate the DPB. In fact, there is still large potential to improve the performance and thermal stability of FMS

electrodes, considering that the materials used were all commercial micro-sized powders. On the other hand, electrospinning is a technique with huge flexibility. By adjusting the condition of electrospinning (extraction voltage, distance from syringe to metal plate, composition of slurry etc.), it is easy to control multiple structure parameters, including the fibres diameter and densities. It is also easy to replace the metal and ceramic phase in FMS with other materials due to the large variety of available materials for both electrospinning and casting methods. Little efforts have been conducted in this work on finding the optimal condition and materials of FMS and further enhance the performance of FMS structure, this will surely be done in future.

Chapter 6 Conclusion and Future Prospects

6.1 Conclusion

This thesis is focused on the development of characterization method for CGO-based anodes of solid oxide fuel cells (SOFCs). The mechanism and implications extracted from the method are also addressed.

In the second chapter:

- A facile transient methane pulse method is developed based on the already existing pulse chemisorption method.
- The methane catalytic oxidation mechanism and carbon resistance of CGO is explored in detail through both quantitative and qualitative analysis of results and in-situ Raman spectroscopy.
- Methane is oxidized on Ni/CGO in a Mars van-Krevelen type mechanism in an oxygen-free condition, instead of L-H or E-R mechanism, in which the methane was first decomposed on Ni surface and then oxidized by oxygen spilled-over from CGO. The rate-determining step of the whole oxidation process is the migration of oxygen from bulk to surface.
- The carbon resistivity is found to be closely related with ceria oxidation state.
- With unambiguous mechanism and rate determining step, a great deal of quantitative information can potentially be extracted from methane pulse experiments, such as integrated intensity of peaks and fitting of decay of peaks.

Cu and Ni impregnated CGO is investigated using the methane pulse experiment in chapter 3:

- Cu and Cu-Ni/CGO were investigated by the methane pulse experiment combined with in-situ Raman spectroscopy.
- The results showed that the Cu itself on CGO is not active for methane activation, because of its activity towards water-gas shifting, the methane oxidation was shifted towards the total oxidation route.

- In Ni-Cu/CGO, negligible carbon is deposited after methane pulse, however the methane conversion rate is reduced, there is no evidence that the addition of Cu have positive effect in methane oxidation.

In chapter 4, EIS is combined with methane pulse method to investigate the degradation of Ni/CGO:

- The results from chapter two are further correlated with EIS tests and FIB-SEM to explore the influence of degradation towards the performance and carbon resistance when Ni/CGO is used as the anode of SOFCs.
- It was found that the aggregation of Ni is the major structural change.
- The aggregation of nickel causes the loss of percolation and decrease of metal surface area, as shown by FIB-SEM
- From the peak of methane pulse method, the decrease of metal surface area result in lower conversion of methane, as mentioned in literatures.
- The aggregation of nickel also reduces the metal-oxide interface density, and thus reduces the activity of CGO surface oxygen by increasing the VO formation energy. The carbon resistance when methane is used as fuel is significantly lower. This effect has not been investigated in literatures.

In chapter five, we turned our attention to the characterization of the electrochemical performance of the Ni/CGO anode:

- A novel cellular automata algorithm was implemented to evaluate the accessible DPB distribution as a function of the distance from nickel phase from 3D tomographic datasets.
- A physically-based model that, in addition to ionic and electronic current transport, took into account both the TPB and DPB reaction pathways through two length scales along the thickness and the CGO surface, has been set up based on the microstructural parameters extracted from FIB-SEM. The model acquired good fit on four different Ni/CGO electrode microstructure.
- Inspired by these model results, a new structure was designed based on the principle of maximizing the DPB density distribution, by using electrospinning and tape-casting. The novel structure shows better electrochemical performance and thermal stability

compared with conventional structures, and in turn verifies the feasibility of physical model.

- The high precision of the model enables the prediction of electrochemical performance through microstructures, and can significantly accelerate the efficiency of electrode design.

To conclude, in this thesis, the catalytic reactivity of methane oxidation on Ni/CGO catalyst and electrochemical performance of Ni/CGO electrode is characterized by modified techniques, in which the influence of support has been determined in detail. As the support of catalyst for methane oxidation, CGO itself provides little activity for methane activation, but the oxygen spilled-over to Ni oxidized methane decomposed on Ni surface. The carbon deposition is also “cleansed” by this migrated oxygen, whose migration rate decreases with decreasing oxidation state of CGO. When used in a symmetrical cell in hydrogen, CGO itself has sufficient reactivity for hydrogen oxidation. Combined with its mixed ion and electron conductivity (MIEC) property, we have found that all DPB is electrochemically active without being limited by CGO’s electron conductivity at 600 °C. Furthermore, a design scheme is developed based on previous analysis and able to “predict” Ni/CGO’s performance from its microstructures, the newly designed fibre-matrix structure confirmed the viability of the scheme. This is a useful new tool in the future design of MIEC material based SOFC electrode.

6.2 Future Prospects

Many aspects in the thesis have the potential to be extended in future work.

In the methane transient pulse section (Chapter 2-4), the detailed kinetic data was not interpreted quantitatively. However, they are closely correlated with the intrinsic material parameters of gadolinium doped ceria. Several aspects of the work can be extended in the future:

1. It has been demonstrated that the rate-determining step for carbon oxidation after the major peak is the bulk oxygen migration, so that the rate of CO production in the tail is closely related with the bulk oxygen diffusion rate. By deriving the carbon coverage and oxygen stoichiometry of CGO from mass spectrometry data, it is possible to fit the oxygen diffusion coefficient D_O and oxygen exchange coefficient k_O of different ceria non-stoichiometry (of different pulse numbers) from the CO production tail. If this succeeds, this will provide a facile route to determine D_O, while the conventional transient methods for this purpose such as isotope relaxation method and TAP[328, 329] are usually equipment-demanding or require sample geometries or conditions far from real-world use.
2. Raman spectroscopy is a useful tool for the qualitative determination of surface species and ceria surface oxidation state. However, the signal from the Ce(IV)-O peak is not only related with the concentration of Ce(IV) on surface layer of ceria but also related with the laser penetration depth during the Raman measurements[330, 331]. By reducing the ceria, the penetration depth of the Raman spectrometer also changed, and it is difficult to directly relate the surface oxidation state with Ce(IV)-O peak signal. On the other hand, in-situ X-ray photoelectron spectroscopy (XPS) would allow the Ce(IV) and Ce(III) concentration to be determined directly from the integrated peak intensity, and the penetration depth would be refined to the surface [332, 333]. Therefore, it is possible to establish a schematic of recovery of surface oxygen coverage as a function of time after the pulse, which could be used to calculate the oxygen migration coefficient D_O and oxygen exchange coefficient k_O of different ceria non-stoichiometry.
3. The transient pulse experiment can be done at multiple temperatures, ranging from 300 °C to 1000 °C, because the methane oxidation mechanism can be very different

with different temperatures. For example, at lower temperatures (<400 °C), the bulk oxygen was found not to be active, according to CH_4 TPR by Sadykov et al. [334], the pulse may reveal more information on the surface of ceria and nickel.

4. The transient pulse experiment can be used to compare the catalytic activity and carbon resistivity of combination of different metals and supports, such as Co, Fe, Cu, with different rare earth element doped ceria.

In the fibre electrode section (Chapter 5), the contribution of DPB on Ni/CGO is demonstrated, and a novel structure designed. The work done here is just a preliminary contribution to possible future work listed below:

1. Less effort was put on the optimization of FMS structure, such as the porosity, Ni/ceria ratio, Ni fibre diameter, electrode thickness, percolation and so on. These parameters can be altered by changing the electrospinning parameters and calcination procedures. By looking for an optimal combination of structure parameters, it is possible to further enhance the performance and stability of electrode.
2. The FMS structure has only been applied on Ni/CGO for now, where Ni presents as fibre and CGO as a matrix. There are large varieties of materials that can be used as either fibre or matrices and can serve different applications. More stable but less active metals (Mo, W, Ti, Fe) or electron conducting inorganic materials (LST etc) can be used to replace nickel, because of the high catalytic activity of ceria surface, this will further increase the stability of anode materials; FMS structured LSCF/Ceria can also be considered, where LSCF serve as fibre and ceria as matrices, for SOFC cathodes. In this way, LSCF provides electron conductivity and minor ion conductivity, ceria provides ion conductivity and ORR reactivity.
3. The FMS structure is just one of the possible structure that utilizes the ceria DPB efficiently. Haile's group has presented a column ceria structure based on a similar concept[24]. However, the effort on this is still rare, and there is a large gap to be filled. In the designing of new structures, the model presented in the thesis can be used to examine the viability of it before it is actually prepared, and it will efficiently accelerate the whole design-experiment process.
4. The model presented in Chapter 5 allow the performance of different Ni/CGO structures to be predicted. It is possible to find the optimal structure with the model

and then find the suitable method of material synthesis to realise it. Moreover, different materials combinations in different conditions of application are likely to have different optimal structures, an algorithm could therefore be developed based on the model where the intrinsic properties of materials (ion conductivity, electron conductivity, rate constant of catalytic reaction etc.) and condition parameters (temperature, oxygen partial pressure etc.) are input to generate the most suitable microstructural parameters.

Reference

1. Grove, W.R., *XXIV. On voltaic series and the combination of gases by platinum.* The London and Edinburgh philosophical magazine and journal of science, 1839. **14**(86): p. 127-130.
2. Baur, E. and H. Preis, *Über Brennstoff‐Ketten mit Festleitern.* Zeitschrift für Elektrochemie und angewandte physikalische Chemie, 1937. **43**(9): p. 727-732.
3. Weissbart, J. and R. Ruka, *A solid electrolyte fuel cell.* Journal of the Electrochemical Society, 1962. **109**(8): p. 723-726.
4. Mahato, N., et al., *Progress in Material Selection for Solid Oxide Fuel Cell Technology: A Review.* Progress in Materials Science, 2015.
5. Kan, W.H. and V. Thangadurai, *Challenges and prospects of anodes for solid oxide fuel cells (SOFCs).* Ionics, 2015. **21**(2): p. 301-318.
6. Winkler, W. and H. Lorenz, *The design of stationary and mobile solid oxide fuel cell–gas turbine systems.* Journal of Power Sources, 2002. **105**(2): p. 222-227.
7. Singhal, S.C. and K. Kendall, *High-temperature solid oxide fuel cells : fundamentals, design and applications*. 2002, Oxford: Elsevier Advanced Technology.
8. De Paepe, M., P. D'Herdt, and D. Mertens, *Micro-CHP systems for residential applications.* Energy Conversion and Management, 2006. **47**(18): p. 3435-3446.
9. Boldrin, P., et al., *Strategies for Carbon and Sulfur Tolerant Solid Oxide Fuel Cell Materials, Incorporating Lessons from Heterogeneous Catalysis.* Chemical Reviews, 2016. **116**(22): p. 13633-13684.
10. Shao, Z., W. Zhou, and Z. Zhu, *Advanced synthesis of materials for intermediate-temperature solid oxide fuel cells.* Progress in Materials Science, 2012. **57**(4): p. 804-874.
11. Deng, Z.Q., et al., *Highly Conducting Redox Stable Pyrochlore Oxides.* Chemistry of Materials, 2008. **20**(22): p. 6911-6916.
12. Lu, X.C., et al., *Pd-impregnated SYT/LDC composite as sulfur-tolerant anode for solid oxide fuel cells.* Journal of Power Sources, 2009. **192**(2): p. 381-384.
13. Huang, Y.-H., et al., *Double-perovskite anode materials Sr2MMoO6 (M= Co, Ni) for solid oxide fuel cells.* Chemistry of Materials, 2009. **21**(11): p. 2319-2326.
14. Xiao, G., et al., *Sr 2 Fe 4/3 Mo 2/3 O 6 as anodes for solid oxide fuel cells.* Journal of Power Sources, 2010. **195**(24): p. 8071-8074.
15. Hua, B., et al., *Improved microstructure and performance of Ni-based anode for intermediate temperature solid oxide fuel cells.* Journal of Power Sources, 2014. **247**: p. 170-177.
16. Ruiz-Trejo, E., et al., *Novel Composite Cermet for Low-Metal-Content Oxygen Separation Membranes.* Chemistry of Materials, 2014. **26**(13): p. 3887-3895.
17. Meng, X., et al., *Highly stable microtubular solid oxide fuel cells based on integrated electrolyte/anode hollow fibers.* Journal of Power Sources, 2015. **275**: p. 362-369.
18. Thalinger, R., et al., *Exsolution of Fe and Sro Nanorods and Nanoparticles from Lanthanum Strontium Ferrite La0.6Sr0.4FeO3-delta Materials by Hydrogen Reduction.* Journal of Physical Chemistry C, 2015. **119**(38): p. 22050-22056.
19. Lai, K., et al., *A quasi-two-dimensional electrochemistry modeling tool for planar solid oxide fuel cell stacks.* Journal of Power Sources, 2011. **196**(6): p. 3204-3222.
20. Qu, Z., et al., *Three-dimensional computational fluid dynamics modeling of anode-supported planar SOFC.* International Journal of Hydrogen Energy, 2011. **36**(16): p. 10209-10220.
21. Shen, S., L. Guo, and H. Liu, *Theoretical analysis of the characteristics of the solid oxide fuel cells with a bi-layer electrolyte.* International Journal of Hydrogen Energy, 2013. **38**(29): p. 13084-13090.
22. Pecho, O.M., et al., *3D microstructure effects in Ni-YSZ anodes: influence of TPB lengths on the electrochemical performance.* Materials, 2015. **8**(10): p. 7129-7144.

23. Brown, M., S. Primdahl, and M. Mogensen, *Structure/Performance Relations for Ni/Yttria - Stabilized Zirconia Anodes for Solid Oxide Fuel Cells.* Journal of The Electrochemical Society, 2000. **147**(2): p. 475-485.
24. Chueh, W.C., et al., *High electrochemical activity of the oxide phase in model ceria-Pt and ceria-Ni composite anodes.* Nat Mater, 2012. **11**(2): p. 155-61.
25. Chueh, W.C. and S.M. Haile, *Electrochemistry of mixed oxygen ion and electron conducting electrodes in solid electrolyte cells.* Annual review of chemical and biomolecular engineering, 2012. **3**: p. 313-341.
26. Standing, A., et al., *Efficient water reduction with gallium phosphide nanowires.* Nat Commun, 2015. **6**: p. 7824.
27. Dominguez-Benetton, X., et al., *The accurate use of impedance analysis for the study of microbial electrochemical systems.* Chemical Society Reviews, 2012. **41**(21): p. 7228-7246.
28. Möbius, H.-H., *On the history of solid electrolyte fuel cells.* Journal of Solid State Electrochemistry, 1997. **1**(1): p. 2-16.
29. Mogensen, M. and S. Skaarup, *Kinetic and geometric aspects of solid oxide fuel cell electrodes.* Solid State Ionics, 1996. **86-88**: p. 1151-1160.
30. Andersson, D.A., et al., *Optimization of ionic conductivity in doped ceria.* Proceedings of the National Academy of Sciences of the United States of America, 2006. **103**(10): p. 3518-3521.
31. Zhu, W.Z. and S.C. Deevi, *Development of interconnect materials for solid oxide fuel cells.* Materials Science and Engineering: A, 2003. **348**(1): p. 227-243.
32. Weil, K.S., et al., Fuel Cells Bull., 2004: p. 12-16.
33. Wincewicz, K.C. and J.S. Cooper, *Taxonomies of SOFC material and manufacturing alternatives.* Journal of Power Sources, 2005. **140**(2): p. 280-296.
34. Taylor, M.A., et al., *96Zr diffusion in polycrystalline scandia stabilized zirconia.* Journal of the European Ceramic Society, 2005. **25**(9): p. 1591-1595.
35. Etsell, T.H. and S.N. Flengas, *Electrical properties of solid oxide electrolytes.* Chemical Reviews, 1970. **70**(3): p. 339-376.
36. Spacil, H.S., *Electrical device including nickel-containing stabilized zirconia electrode*. 1970, Google Patents.
37. Somalu, M.R., et al., *Fabrication and characterization of Ni/ScSZ cermet anodes for IT-SOFCs.* International Journal of Hydrogen Energy, 2011. **36**(9): p. 5557-5566.
38. Badwal, S.P.S., F.T. Ciacchi, and D. Milosevic, *Scandia–zirconia electrolytes for intermediate temperature solid oxide fuel cell operation.* Solid State Ionics, 2000. **136-137**: p. 91-99.
39. Gu, H., et al., *Anode-supported ScSZ-electrolyte SOFC with whole cell materials from combined EDTA–citrate complexing synthesis process.* Journal of Power Sources, 2007. **172**(2): p. 704-712.
40. Koide, H., et al., *Properties of Ni/YSZ cermet as anode for SOFC.* Solid State Ionics, 2000. **132**(3): p. 253-260.
41. Sato, K., et al., *Enhanced electrochemical activity and long-term stability of Ni–YSZ anode derived from NiO–YSZ interdispersed composite particles.* Journal of the European Ceramic Society, 2009. **29**(6): p. 1119-1124.
42. Cho, H.J. and G.M. Choi, *Effect of milling methods on performance of Ni-Y2O3-stabilized ZrO2 anode for solid oxide fuel cell.* Journal of Power Sources, 2008. **176**(1): p. 96-101.
43. Shri Prakash, B., S. Senthil Kumar, and S.T. Aruna, *Properties and development of Ni/YSZ as an anode material in solid oxide fuel cell: A review.* Renewable and Sustainable Energy Reviews, 2014. **36**: p. 149-179.
44. Morsi, K., *The diversity of combustion synthesis processing: a review.* Journal of Materials Science, 2012. **47**(1): p. 68-92.
45. Marinšek, M., K. Zupan, and J. Maèek, *Ni–YSZ cermet anodes prepared by citrate/nitrate combustion synthesis.* Journal of Power Sources, 2002. **106**(1–2): p. 178-188.

46. Chen, M., et al., *Synthesis and performances of Ni–SDC cermets for IT-SOFC anode.* Journal of the European Ceramic Society, 2008. **28**(15): p. 2947-2953.
47. Ringuedé, A., J.A. Labrincha, and J.R. Frade, *A combustion synthesis method to obtain alternative cermet materials for SOFC anodes.* Solid State Ionics, 2001. **141–142**: p. 549-557.
48. Grgicak, C.M., et al., *Synthesis and Characterization of NiO–YSZ Anode Materials: Precipitation, Calcination, and the Effects on Sintering.* Journal of the American Ceramic Society, 2005. **88**(11): p. 3081-3087.
49. Tian, N., et al., *Electrical properties of Ce0.85SM0.15O1.925-Fe2O3 electrolytes for IT-SOFCs.* Journal of Alloys and Compounds, 2016. **655**: p. 215-219.
50. Tian, D., et al., *A robust NiO-Sm0.2Ce0.8O1.9 anode for direct-methane solid oxide fuel cell.* Materials Research Bulletin, 2015. **71**: p. 1-6.
51. Sun, J.L., et al., *Synthesis and electrical properties of screen-printed doped ceria interlayer for IT-SOFC applications.* Journal of Alloys and Compounds, 2015. **628**: p. 450-457.
52. Pelosato, R., et al., *Electrical characterization of co-precipitated LaBaCo2O5+delta and YBaCo2O5+delta oxides.* Journal of the European Ceramic Society, 2014. **34**(16): p. 4257-4272.
53. Rida, K., et al., *Effect of calcination temperature on structural properties and catalytic activity in oxidation reactions of LaNiO3 perovskite prepared by Pechini method.* Journal of Rare Earths, 2012. **30**(3): p. 210-216.
54. Lin, J., et al., *Multiform oxide optical materials via the versatile Pechini-type sol-gel process: Synthesis and characteristics.* Journal of Physical Chemistry C, 2007. **111**(16): p. 5835-5845.
55. Zarkov, A., et al., *On the synthesis of yttria-stabilized zirconia: a comparative study.* Journal of Sol-Gel Science and Technology, 2015. **76**(2): p. 309-319.
56. Majedi, A., A. Abbasi, and F. Davar, *Green synthesis of zirconia nanoparticles using the modified Pechini method and characterization of its optical and electrical properties.* Journal of Sol-Gel Science and Technology, 2016. **77**(3): p. 542-552.
57. Kim, H.S., et al., *Sr0.92Y0.08TiO3-delta/Sm0.2Ce0.8O2-delta anode for solid oxide fuel cells running on methane.* International Journal of Hydrogen Energy, 2012. **37**(21): p. 16130-16139.
58. Arabaci, A. and O. Serin, *Characteristics of Samaria-Doped Ceria Prepared by Pechini Method.* Acta Physica Polonica A, 2015. **128**(2B): p. B118-B121.
59. Yoon, J.S., et al., *Catalytic activity of perovskite-type doped La0.08Sr0.92Ti1-xMxO3-delta (M = Mn, Fe, and Co) oxides for methane oxidation.* International Journal of Hydrogen Energy, 2014. **39**(15): p. 7955-7962.
60. Yaqub, A., et al., *Synthesis and characterization of B-site doped La0.20Sr0.25Ca0.45TiO3 as SOFC anode materials.* International Journal of Hydrogen Energy, 2015. **40**(1): p. 760-766.
61. Vogler, M., et al., *Modelling Study of Surface Reactions, Diffusion, and Spillover at a Ni/YSZ Patterned Anode.* Journal of The Electrochemical Society, 2009. **156**(5): p. B663-B672.
62. Bieberle, A., L.P. Meier, and L.J. Gauckler *The Electrochemistry of Ni Pattern Anodes Used as Solid Oxide Fuel Cell Model Electrodes.* Journal of The Electrochemical Society, 2001. **148**(6): p. A646-A656.
63. Mizusaki, J., et al., *Kinetic studies of the reaction at the nickel pattern electrode on YSZ in H2 ・ H2O atmospheres.* Solid State Ionics, 1994. **70-71**: p. 52-58.
64. Tanner, C.W., K.Z. Fung, and A.V. Virkar, *The Effect of Porous Composite Electrode Structure on Solid Oxide Fuel Cell Performance: I. Theoretical Analysis.* Journal of The Electrochemical Society, 1997. **144**(1): p. 21-30.
65. Khan, M.S., et al., *Fundamental mechanisms involved in the degradation of nickel yttria stabilized zirconia (Ni-YSZ) anode during solid oxide fuel cells operation: A review.* Ceramics International, 2016. **42**(1): p. 35-48.
66. Vaßen, R., D. Simwonis, and D. Stöver, *Modelling of the agglomeration of Ni-particles in anodes of solid oxide fuel cells.* Journal of Materials Science, 2001. **36**(1): p. 147-151.

67. Holzer, L., et al., *Microstructure degradation of cermet anodes for solid oxide fuel cells: Quantification of nickel grain growth in dry and in humid atmospheres.* Journal of Power Sources, 2011. **196**(3): p. 1279-1294.
68. Ioselevich, A., A.A. Kornyshev, and W. Lehnert, *Degradation of Solid Oxide Fuel Cell Anodes Due to Sintering of Metal Particles: Correlated Percolation Model.* Journal of The Electrochemical Society, 1997. **144**(9): p. 3010-3019.
69. Hecht, E.S., et al., *Methane reforming kinetics within a Ni–YSZ SOFC anode support.* Applied Catalysis A: General, 2005. **295**(1): p. 40-51.
70. Alzate-Restrepo, V. and J.M. Hill, *Effect of anodic polarization on carbon deposition on Ni/YSZ anodes exposed to methane.* Applied Catalysis A: General, 2008. **342**(1): p. 49-55.
71. Jiang, S.P., *A review of wet impregnation—An alternative method for the fabrication of high performance and nano-structured electrodes of solid oxide fuel cells.* Materials Science and Engineering: A, 2006. **418**(1–2): p. 199-210.
72. Minh, N.Q., *Ceramic fuel cells.* Journal of the American Ceramic Society, 1993. **76**(3): p. 563-588.
73. Liu, Z., et al., *Fabrication and modification of solid oxide fuel cell anodes via wet impregnation/infiltration technique.* Journal of Power Sources, 2013. **237**: p. 243-259.
74. Boldrin, P., M. Millan-Agorio, and N.P. Brandon, *Effect of Sulfur- and Tar-Contaminated Syngas on Solid Oxide Fuel Cell Anode Materials.* Energy & Fuels, 2015. **29**(1): p. 442-446.
75. Park, S., J.M. Vohs, and R.J. Gorte, *Direct oxidation of hydrocarbons in a solid-oxide fuel cell.* Nature, 2000. **404**(6775): p. 265-267.
76. Marina, O.A., et al., *A solid oxide fuel cell with a gadolinia-doped ceria anode: preparation and performance.* Solid State Ionics, 1999. **123**(1–4): p. 199-208.
77. Murray, E.P., T. Tsai, and S.A. Barnett, *A direct-methane fuel cell with a ceria-based anode.* Nature, 1999. **400**(6745): p. 649-651.
78. He, H., R.J. Gorte, and J.M. Vohs, *Highly Sulfur Tolerant Cu-Ceria Anodes for SOFCs.* Electrochemical and Solid-State Letters, 2005. **8**(6): p. A279-A280.
79. Gorte, R.J., H. Kim, and J.M. Vohs, *Novel SOFC anodes for the direct electrochemical oxidation of hydrocarbon.* Journal of Power Sources, 2002. **106**(1–2): p. 10-15.
80. Marrocchelli, D., et al., *Understanding Chemical Expansion in Non-Stoichiometric Oxides: Ceria and Zirconia Case Studies.* Advanced Functional Materials, 2012. **22**(9): p. 1958-1965.
81. Tuller, H.L. and A.S. Nowick, *Small polaron electron transport in reduced CeO2 single crystals.* Journal of Physics and Chemistry of Solids, 1977. **38**(8): p. 859-867.
82. Yahiro, H., et al., *Oxygen ion conductivity of the ceria-samarium oxide system with fluorite structure.* Journal of Applied Electrochemistry, 1988. **18**(4): p. 527-531.
83. Wang, S., et al., *Electrical and Ionic Conductivity of Gd‐Doped Ceria.* Journal of The Electrochemical Society, 2000. **147**(10): p. 3606-3609.
84. Tao, Z.T., et al., *The co-doping effect of Sm and In on ceria for electrolyte application in IT-SOFC.* Journal of Alloys and Compounds, 2016. **663**: p. 750-754.
85. Inaba, H. and H. Tagawa, *Ceria-based solid electrolytes - Review.* Solid State Ionics, 1996. **83**(1-2): p. 1-16.
86. Yahiro, H., K. Eguchi, and H. Arai, *Electrical properties and reducibilities of ceria-rare earth oxide systems and their application to solid oxide fuel cell.* Solid State Ionics, 1989. **36**(1): p. 71-75.
87. Zha, S.W., C.R. Xia, and G.Y. Meng, *Effect of Gd (Sm) doping on properties of ceria electrolyte for solid oxide fuel cells.* Journal of Power Sources, 2003. **115**(1): p. 44-48.
88. Kobi, S., et al., *Ionic conductivity of Nd3+ and Y3+ co-doped ceria solid electrolytes for intermediate temperature solid oxide fuel cells.* Journal of Alloys and Compounds, 2016. **658**: p. 513-519.
89. Prado-Gonjal, J., et al., *Microwave synthesis & sintering of Sm and Ca co-doped ceria ceramics.* International Journal of Hydrogen Energy, 2015. **40**(45): p. 15640-15651.

90. Adachi, G.-y. and N. Imanaka, *The Binary Rare Earth Oxides.* Chemical Reviews, 1998. **98**(4): p. 1479-1514.
91. Yao, H.C. and Y.F.Y. Yao, *Ceria in automotive exhaust catalysts: I. Oxygen storage.* Journal of Catalysis, 1984. **86**(2): p. 254-265.
92. Kacimi, S., et al., *Oxygen storage capacity of promoted Rh/CeC2 catalysts. Exceptional behavior of RhCu/CeO2.* Catalysis Letters, 1993. **22**(4): p. 343-350.
93. Sevcikova, K., et al., *Impact of Rh-CeOx interaction on CO oxidation mechanisms.* Applied Surface Science, 2015. **332**: p. 747-755.
94. Vayssilov, G.N., et al., *Support nanostructure boosts oxygen transfer to catalytically active platinum nanoparticles.* Nature Materials, 2011. **10**: p. 310.
95. Ciucci, F., et al., *Surface reaction and transport in mixed conductors with electrochemically-active surfaces: a 2-D numerical study of ceria.* Physical Chemistry Chemical Physics, 2011. **13**(6): p. 2121-2135.
96. Jung, W., et al., *High electrode activity of nanostructured, columnar ceria films for solid oxide fuel cells.* Energy & Environmental Science, 2012. **5**(9): p. 8682-8689.
97. Murray, E.P., T. Tsai, and S.A. Barnett, *A direct-methane fuel cell with a ceria-based anode.* Nature, 1999. **400**: p. 649.
98. Zhang, L., et al., *A comparative study of H2S poisoning on electrode behavior of Ni/YSZ and Ni/GDC anodes of solid oxide fuel cells.* International Journal of Hydrogen Energy, 2010. **35**(22): p. 12359-12368.
99. Fuerte, A., et al., *Effect of cobalt incorporation in copper-ceria based anodes for hydrocarbon utilisation in Intermediate Temperature Solid Oxide Fuel Cells.* Journal of Power Sources, 2011. **196**(9): p. 4324-4331.
100. Resini, C., et al., *Yttria-stabilized zirconia (YSZ) supported Ni–Co alloys (precursor of SOFC anodes) as catalysts for the steam reforming of ethanol.* International Journal of Hydrogen Energy, 2008. **33**(14): p. 3728-3735.
101. You, H., et al., *Fabrication of Ni0.5Cu0.5Ox coated YSZ anode by hard template method for solid oxide fuel cells.* Journal of Alloys and Compounds, 2016. **669**: p. 46-54.
102. Li, M., et al., *Electrochemical performance and carbon deposition resistance of M-BaZr0.1Ce0.7Y0.1Yb0.1O3-δ (M = Pd, Cu, Ni or NiCu) anodes for solid oxide fuel cells.* Scientific Reports, 2015. **5**: p. 7667.
103. Zhao, K., et al., *Electrochemical performance of a copper-impregnated Ni–Ce0.8Sm0.2O1.9 anode running on methane.* International Journal of Hydrogen Energy, 2013. **38**(9): p. 3750-3756.
104. Hornés, A., et al., *Electrochemical performance of a solid oxide fuel cell with an anode based on Cu–Ni/CeO2 for methane direct oxidation.* Journal of Power Sources, 2014. **249**: p. 520-526.
105. Liu, M., et al., *Performance of the nano-structured Cu–Ni (alloy) -CeO2 anode for solid oxide fuel cells.* Journal of Power Sources, 2015. **274**: p. 730-735.
106. Park, K., et al., *Performance analysis of Cu, Sn and Rh impregnated NiO/CGO91 anode for butane internal reforming SOFC at intermediate temperature.* Renewable Energy, 2015. **83**: p. 483-490.
107. Kaur, G. and S. Basu, *Physical characterization and electrochemical performance of copper–iron–ceria–YSZ anode-based SOFCs in H2 and methane fuels.* International Journal of Energy Research, 2015. **39**(10): p. 1345-1354.
108. Liu, Y., et al., *Development of micro-tubular SOFCs with an improved performance via nano-Ag impregnation for intermediate temperature operation.* Electrochemistry Communications, 2007. **9**(8): p. 1918-1923.
109. Ruiz-Trejo, E., A. Atkinson, and N.P. Brandon, *Metallizing porous scaffolds as an alternative fabrication method for solid oxide fuel cell anodes.* Journal of Power Sources, 2015. **280**: p. 81-89.

110. Katikaneni, S.P., J. Bae, and S. Lee, *Ni/CGO and Ni-Ru/CGO based pre-reforming catalysts formulation for methane rich gas production from diesel processing for fuel cell applications*. 2015, Google Patents.
111. Lu, X.C. and J.H. Zhu, *Cu(Pd)-impregnated La0.75Sr0.25Cr0.5Mn0.5O3 − δ anodes for direct utilization of methane in SOFC.* Solid State Ionics, 2007. **178**(25–26): p. 1467-1475.
112. Lu, C., et al., *A Comparison of Cu-Ceria-SDC and Au-Ceria-SDC Composites for SOFC Anodes.* Journal of The Electrochemical Society, 2003. **150**(10): p. A1357-A1359.
113. Singh, A. and J.M. Hill, *Carbon tolerance, electrochemical performance and stability of solid oxide fuel cells with Ni/yttria stabilized zirconia anodes impregnated with Sn and operated with methane.* Journal of Power Sources, 2012. **214**: p. 185-194.
114. Bae, G., et al., *Performance of SOFC coupled with n-C4H10 autothermal reformer: Carbon deposition and development of anode structure.* International Journal of Hydrogen Energy, 2010. **35**(22): p. 12346-12358.
115. Li, Y., et al., *Cobalt-impregnated La0.75Sr0.25Cr0.5Mn0.5O3−δ anodes for solid oxide fuel cells.* International Journal of Hydrogen Energy, 2014. **39**(15): p. 7980-7987.
116. Gross, M.D., J.M. Vohs, and R.J. Gorte, *A study of thermal stability and methane tolerance of Cu-based SOFC anodes with electrodeposited Co.* Electrochimica Acta, 2007. **52**(5): p. 1951-1957.
117. Marina, O.A., N.L. Canfield, and J.W. Stevenson, *Thermal, electrical, and electrocatalytical properties of lanthanum-doped strontium titanate.* Solid State Ionics, 2002. **149**(1): p. 21-28.
118. Jung, I., et al., *LSCM–YSZ nanocomposites for a high performance SOFC anode.* Ceramics International, 2013. **39**(8): p. 9753-9758.
119. Aguilar, L., et al., *A solid oxide fuel cell operating on hydrogen sulfide (H2S) and sulfur-containing fuels.* Journal of Power Sources, 2004. **135**(1): p. 17-24.
120. Huang, Y.-H., et al., *Double Perovskites as Anode Materials for Solid-Oxide Fuel Cells.* Science, 2006. **312**(5771): p. 254-257.
121. Holtappels, P., F.W. Poulsen, and M. Mogensen, *Electrical conductivities and chemical stabilities of mixed conducting pyrochlores for SOFC applications.* Solid State Ionics, 2000. **135**(1): p. 675-679.
122. Anderson, H.U., *Review of p-type doped perovskite materials for SOFC and other applications.* Solid State Ionics, 1992. **52**(1): p. 33-41.
123. Richter, J., et al., *Materials design for perovskite SOFC cathodes.* Monatshefte für Chemie - Chemical Monthly, 2009. **140**(9): p. 985-999.
124. Tao, S. and J.T.S. Irvine, *A redox-stable efficient anode for solid-oxide fuel cells.* Nat Mater, 2003. **2**(5): p. 320-323.
125. Chen, X.J., et al., *High-performance cathode-supported SOFC with perovskite anode operating in weakly humidified hydrogen and methane.* Fuel Cells Bulletin, 2007. **2007**(6): p. 12-16.
126. Chen, X.J., et al., *Sulfur tolerance and hydrocarbon stability of La0.75Sr0.25Cr0.5Mn0.5O3/Gd0.2Ce0.8O1.9 composite anode under anodic polarization.* Journal of the Electrochemical Society, 2007. **154**(11): p. B1206-B1210.
127. Ye, Y., et al., *Pd-Promoted La0.75Sr0.25Cr0.5Mn0.5O3 / YSZ Composite Anodes for Direct Utilization of Methane in SOFCs.* Journal of The Electrochemical Society, 2008. **155**(8): p. B811-B818.
128. Craciun, R., et al., *A novel method for preparing anode cermets for solid oxide fuel cells.* Journal of The Electrochemical Society, 1999. **146**(11): p. 4019-4022.
129. Jiang, S.P., *Nanoscale and nano-structured electrodes of solid oxide fuel cells by infiltration: Advances and challenges.* International Journal of Hydrogen Energy, 2012. **37**(1): p. 449-470.
130. Lou, X., et al., *Controlling the morphology and uniformity of a catalyst-infiltrated cathode for solid oxide fuel cells by tuning wetting property.* Journal of Power Sources, 2010. **195**(2): p. 419-424.

131. Zhou, Z., et al., *Fabrication of planar-type SOFC single cells by a novel vacuum dip-coating method and co-firing/infiltration techniques.* International Journal of Hydrogen Energy, 2014. **39**(5): p. 2274-2278.
132. Sholklapper, T.Z., et al., *LSM-infiltrated solid oxide fuel cell cathodes.* Electrochemical and Solid State Letters, 2006. **9**(8): p. A376-A378.
133. Li, X., et al., *Performance of a commercial cathode-supported solid oxide fuel cells prepared by single-step infiltration of an ion-conducting electrocatalyst.* Journal of Power Sources, 2012. **199**: p. 132-137.
134. Li, W., et al., *Effect of adding urea on performance of Cu/CeO2/yttria-stabilized zirconia anodes for solid oxide fuel cells prepared by impregnation method.* Electrochimica Acta, 2011. **56**(5): p. 2230-2236.
135. Jung, S., et al., *Influence of composition and Cu impregnation method on the performance of Cu/CeO2/YSZ SOFC anodes.* Journal of Power Sources, 2006. **154**(1): p. 42-50.
136. González-Cortés, S.L., et al., *Urea–organic matrix method: an alternative approach to prepare Co·MoS2/γ-Al2O3 HDS catalyst.* Applied Catalysis A: General, 2004. **270**(1–2): p. 209-222.
137. Zhu, X., et al., *Development of La0.6Sr0.4Co0.2Fe0.8O3−δ cathode with an improved stability via La0.8Sr0.2MnO3-film impregnation.* International Journal of Hydrogen Energy, 2013. **38**(13): p. 5375-5382.
138. Jung, S.-W., J.M. Vohs, and R.J. Gorte, *Preparation of SOFC anodes by electrodeposition.* Journal of the Electrochemical Society, 2007. **154**(12): p. B1270-B1275.
139. Nicholas, J.D. and S.A. Barnett, *Measurements and Modeling of Sm0. 5Sr0. 5CoO3− x–Ce0. 9Gd0. 1O1. 95 SOFC Cathodes Produced Using Infiltrate Solution Additives.* Journal of the Electrochemical Society, 2010. **157**(4): p. B536-B541.
140. Haberko, K., et al., *Structural and electrical properties of Ni–YSZ cermet materials.* Journal of Power Sources, 2010. **195**(17): p. 5527-5533.
141. Okawa, Y. and Y. Hirata, *Sinterability, microstructures and electrical properties of Ni/Sm-doped ceria cermet processed with nanometer-sized particles.* Journal of the European Ceramic Society, 2005. **25**(4): p. 473-480.
142. Kikuchi, R., et al., *Low Ni-Containing Anodes Using Titanate-Based Perovskites for Methane Direct Internal Reforming Power Generation.* ECS Transactions, 2015. **68**(1): p. 1489-1498.
143. Zhu, W., D. Ding, and C. Xia, *Enhancement in Three-Phase Boundary of SOFC Electrodes by an Ion Impregnation Method: A Modeling Comparison.* Electrochemical and Solid-State Letters, 2008. **11**(6): p. B83.
144. Wang, W., et al., *GDC-impregnated Ni anodes for direct utilization of methane in solid oxide fuel cells.* Journal of Power Sources, 2006. **159**(1): p. 68-72.
145. Clemmer, R.M.C. and S.F. Corbin, *The influence of pore and Ni morphology on the electrical conductivity of porous Ni/YSZ composite anodes for use in solid oxide fuel cell applications.* Solid State Ionics, 2009. **180**(9–10): p. 721-730.
146. Klemenso, T., et al., *Stability of Ni-yttria stabilized zirconia anodes based on Ni-impregnation.* Journal of Power Sources, 2010. **195**(21): p. 7295-7301.
147. Busawon, A.N., D. Sarantaridis, and A. Atkinson, *Ni Infiltration as a Possible Solution to the Redox Problem of SOFC Anodes.* Electrochemical and Solid-State Letters, 2008. **11**(10): p. B186.
148. Xia, T., et al., *Optimization of the electrochemical performance of a Ni/Ce0.9Gd0.1O2−δ-impregnated La0.57Sr0.15TiO3 anode in hydrogen.* Solid State Sciences, 2014. **35**: p. 1-9.
149. Li, Y., et al., *Performance and sulfur poisoning of Ni/CeO2 impregnated La0.75Sr0.25Cr0.5Mn0.5O3−δ anode in solid oxide fuel cells.* Journal of Power Sources, 2015. **285**: p. 354-359.
150. Othman, M.H.D., et al., *High-Performance, Anode-Supported, Microtubular SOFC Prepared from Single-Step-Fabricated, Dual-Layer Hollow Fibers.* Advanced Materials, 2011. **23**(21): p. 2480-2483.

151. Almar, L., et al., *High-temperature long-term stable ordered mesoporous Ni-CGO as an anode for solid oxide fuel cells.* Journal of Materials Chemistry A, 2013. **1**(14): p. 4531-4538.
152. Aruna, S.T., et al., *Electrospinning in solid oxide fuel cells – A review.* Renewable and Sustainable Energy Reviews, 2017. **67**: p. 673-682.
153. Li, L., et al., *Preparation of fibrous Ni-coated-YSZ anodes for solid oxide fuel cells.* Journal of Power Sources, 2011. **196**(3): p. 1242-1247.
154. Pan, W., et al., *Novel polymer fibers prepared by electrospinning for use as the pore-former for the anode of solid oxide fuel cell.* Electrochimica Acta, 2010. **55**(20): p. 5538-5544.
155. Marrero-Jerez, J., et al., *TPR-TPD-TPO studies on CGO/NiO and CGO/CuO ceramics obtained from freeze-dried precursors.* Ceramics International, 2014. **40**(9): p. 15175-15182.
156. Falconer, J.L. and J.A. Schwarz, *Temperature-Programmed Desorption and Reaction: Applications to Supported Catalysts.* Catalysis Reviews, 1983. **25**(2): p. 141-227.
157. Hinrichsen, O., T. Genger, and M. Muhler, *Chemisorption of N2O and H2 for the Surface Determination of Copper Catalysts.* Chemical Engineering & Technology, 2000. **23**(11): p. 956-959.
158. Bond, G.C. and S.N. Namijo, *An improved procedure for estimating the metal surface area of supported copper catalysts.* Journal of Catalysis, 1989. **118**(2): p. 507-510.
159. Cordatos, H., et al., *Effect of Ceria Structure on Oxygen Migration for Rh/Ceria Catalysts.* The Journal of Physical Chemistry, 1996. **100**(2): p. 785-789.
160. Richards, R.E., Wallace, W., Nagabhushana, K., Parvulescu, V., Schmidt, W., Hocevar, S., Levec, J., Schunk, S., Regalbuto, J., Smith, A., Goodman, D., Iwasawa, Y., Tada, M., Coman, S., Klabunde, K., Ranjit, K., Yamaguchi, K., Kamata, K., Fenelonov, V., Mel'gunov, M., Bonnemann, H., Poncelet, G., Marcu, V., Busch, O., Demuth, D., Gerlach, O., Haas, A., Klein, J., Zech, T., Zaera, F., Ma, Z., Mizuno, N. , *Surface and Nanomolecular Catalysis*. 2006: CRC Press.
161. Soick, M., D. Wolf, and M. Baerns, *Determination of kinetic parameters for complex heterogeneous catalytic reactions by numerical evaluation of TAP experiments.* Chemical Engineering Science, 2000. **55**(15): p. 2875-2882.
162. 駒井慎一, et al., *Determination of metal dispersion of Pt/CeO2 catalyst by CO-pulse method.* Journal of the Japan Petroleum Institute, 2005. **48**(3): p. 173-177.
163. Song, Z., et al., *The Pr promotion effect on oxygen storage capacity of Ce–Pr oxides studied using a TAP reactor.* Applied Catalysis A: General, 2007. **329**: p. 86-92.
164. van den Bossche, M. and S. McIntosh, *Pulse Reactor Studies to Assess the Potential of La0.75Sr0.25Cr0.5Mn0.4X0.1O3-δ(X = Co, Fe, Mn, Ni, V) as Direct Hydrocarbon Solid Oxide Fuel Cell Anodes.* Chemistry of Materials, 2010. **22**(21): p. 5856-5865.
165. Netzer, F.P. and R.A. Wille, *The surface reaction of carbon and oxygen on a stepped Pt(111) surface.* Journal of Catalysis, 1978. **51**(1): p. 18-25.
166. Gleaves, J.T., J.R. Ebner, and T.C. Kuechler, *Temporal Analysis of Products (TAP)—A Unique Catalyst Evaluation System with Submillisecond Time Resolution.* Catalysis Reviews, 1988. **30**(1): p. 49-116.
167. Dewaele, O. and G.F. Froment, *TAP Study of the Mechanism and Kinetics of the Adsorption and Combustion of Methane on Ni/Al2O3 and NiO/Al2O3.* Journal of Catalysis, 1999. **184**(2): p. 499-513.
168. Macdonald, D.D., *Review of mechanistic analysis by electrochemical impedance spectroscopy.* Electrochimica Acta, 1990. **35**(10): p. 1509-1525.
169. Hauch, A., M. Mogensen, and A. Hagen, *Ni/YSZ electrode degradation studied by impedance spectroscopy — Effect of p(H2O).* Solid State Ionics, 2011. **192**(1): p. 547-551.
170. Zhu, B., I. Albinsson, and B.-E. Mellander, *Impedance spectroscopy study of gadolinia-doped ceria.* Ionics, 1999. **5**(3): p. 286-291.
171. Rösch, B., et al., *Electrochemical characterization of Ni-Ce0.9Gd0.1O2−δ for SOFC anodes.* Solid State Ionics, 2004. **175**(1): p. 113-117.

172. Lohsoontorn, P., D.J.L. Brett, and N.P. Brandon, *The effect of fuel composition and temperature on the interaction of H2S with nickel–ceria anodes for Solid Oxide Fuel Cells.* Journal of Power Sources, 2008. **183**(1): p. 232-239.
173. Leonide, A., et al., *Evaluation and Modeling of the Cell Resistance in Anode-Supported Solid Oxide Fuel Cells.* Journal of The Electrochemical Society, 2008. **155**(1): p. B36-B41.
174. Bieberle, A. and L.J. Gauckler, *Reaction mechanism of Ni pattern anodes for solid oxide fuel cells.* Solid State Ionics, 2000. **135**(1): p. 337-345.
175. Verkerk, M.J. and A.J. Burggraaf, *Oxygen Transfer on Substituted ZrO2, Bi2 O 3, and CeO2 Electrolytes with Platinum Electrodes: II . A ‐ C Impedance Study.* Journal of The Electrochemical Society, 1983. **130**(1): p. 78-84.
176. Jamnik, J. and J. Maier, *Generalised equivalent circuits for mass and charge transport: chemical capacitance and its implications.* Physical Chemistry Chemical Physics, 2001. **3**(9): p. 1668-1678.
177. Lai, W. and S.M. Haile, *Impedance Spectroscopy as a Tool for Chemical and Electrochemical Analysis of Mixed Conductors: A Case Study of Ceria.* Journal of the American Ceramic Society, 2005. **88**(11): p. 2979-2997.
178. Bunaciu, A.A., E.g. Udriştioiu, and H.Y. Aboul-Enein, *X-Ray Diffraction: Instrumentation and Applications.* Critical Reviews in Analytical Chemistry, 2015. **45**(4): p. 289-299.
179. Leng, Y.J., et al., *Low-temperature SOFC with thin film GDC electrolyte prepared in situ by solid-state reaction.* Solid State Ionics, 2004. **170**(1): p. 9-15.
180. Bansal, N.P. and Z. Zhong, *Combustion synthesis of Sm0.5Sr0.5CoO3−x and La0.6Sr0.4CoO3−x nanopowders for solid oxide fuel cell cathodes.* Journal of Power Sources, 2006. **158**(1): p. 148-153.
181. Maher, R.C., et al., *Reduction Dynamics of Doped Ceria, Nickel Oxide, and Cermet Composites Probed Using In Situ Raman Spectroscopy.* Advanced Science, 2016. **3**(1): p. 1500146-n/a.
182. B. Imelik, J.C.V.E., *Catalyst Characterization: Physical Techniques for Solid Materials*. 1994: Plenum Press.
183. McIntosh, S. and R.J. Gorte, *Direct Hydrocarbon Solid Oxide Fuel Cells.* Chemical Reviews, 2004. **104**(10): p. 4845-4866.
184. Ge, X.M., et al., *Solid Oxide Fuel Cell Anode Materials for Direct Hydrocarbon Utilization.* Advanced Energy Materials, 2012. **2**(10): p. 1156-1181.
185. Steele, B., et al., *Oxidation of methane in solid state electrochemical reactors.* Solid State Ionics, 1988. **28**: p. 1547-1552.
186. Thallam Thattai, A., L. van Biert, and P.V. Aravind, *On direct internal methane steam reforming kinetics in operating solid oxide fuel cells with nickel-ceria anodes.* Journal of Power Sources, 2017. **370**: p. 71-86.
187. Silverwood, I.P., et al., *Quantification of surface species present on a nickel/alumina methane reforming catalyst.* Physical Chemistry Chemical Physics, 2010. **12**(13): p. 3102-3107.
188. Pruksawan, S., B. Kitiyanan, and R.M. Ziff, *Partial oxidation of methane on a nickel catalyst: Kinetic Monte-Carlo simulation study.* Chemical Engineering Science, 2016. **147**: p. 128-136.
189. Maier, L., et al., *Steam Reforming of Methane Over Nickel: Development of a Multi-Step Surface Reaction Mechanism.* Topics in Catalysis, 2011. **54**(13): p. 845.
190. Chin, Y.-H., et al., *Reactivity of Chemisorbed Oxygen Atoms and Their Catalytic Consequences during CH4–O2 Catalysis on Supported Pt Clusters.* Journal of the American Chemical Society, 2011. **133**(40): p. 15958-15978.
191. Seimanides, S. and M. Stoukides, *Solid-electrolyte-aided study of methane oxidation on polycrystalline silver.* Journal of Catalysis, 1984. **88**(2): p. 490-498.
192. Nagamoto, H., K. Hayashi, and H. Inoue, *Methane oxidation by oxygen transported through solid electrolyte.* Journal of Catalysis, 1990. **126**(2): p. 671-673.
193. Hurtado, P., et al., *Development of a kinetic model for the oxidation of methane over Pd/Al2O3 at dry and wet conditions.* Applied Catalysis B: Environmental, 2004. **51**(4): p. 229-238.

194. Schwartz, W.R. and L.D. Pfefferle, *Combustion of Methane over Palladium-Based Catalysts: Support Interactions.* The Journal of Physical Chemistry C, 2012. **116**(15): p. 8571-8578.
195. Cargnello, M., et al., *Control of metal nanocrystal size reveals metal-support interface role for ceria catalysts.* Science, 2013. **341**(6147): p. 771-773.
196. Ruiz Puigdollers, A., et al., *Increasing Oxide Reducibility: The Role of Metal/Oxide Interfaces in the Formation of Oxygen Vacancies.* ACS Catalysis, 2017. **7**(10): p. 6493-6513.
197. Kundakovic, L. and M. Flytzani-Stephanopoulos, *Cu- and Ag-Modified Cerium Oxide Catalysts for Methane Oxidation.* Journal of Catalysis, 1998. **179**(1): p. 203-221.
198. Lykhach, Y., et al., *Microscopic insights into methane activation and related processes on Pt/ceria model catalysts.* ChemPhysChem, 2010. **11**(7): p. 1496-1504.
199. Zafiris, G.S. and R.J. Gorte, *Evidence for Low-Temperature Oxygen Migration from Ceria to Rh.* Journal of Catalysis, 1993. **139**(2): p. 561-567.
200. Zhao, S. and R.J. Gorte, *A comparison of ceria and Sm-doped ceria for hydrocarbon oxidation reactions.* Applied Catalysis a-General, 2004. **277**(1-2): p. 129-136.
201. Laosiripojana, N. and S. Assabumrungrat, *Catalytic dry reforming of methane over high surface area ceria.* Applied Catalysis B: Environmental, 2005. **60**(1): p. 107-116.
202. Ahmed, S., et al., *Decomposition of hydrocarbons to hydrogen and carbon.* Applied Catalysis a-General, 2009. **359**(1-2): p. 1-24.
203. Dissanayake, D., et al., *PARTIAL OXIDATION OF METHANE TO CARBON-MONOXIDE AND HYDROGEN OVER A NI/AL2O3 CATALYST.* Journal of Catalysis, 1991. **132**(1): p. 117-127.
204. Helveg, S., et al., *Atomic-scale imaging of carbon nanofibre growth.* Nature, 2004. **427**(6973): p. 426-429.
205. Holstein, W.L., *The roles of ordinary and soret diffusion in the metal-catalyzed formation of filamentous carbon.* Journal of catalysis, 1995. **152**(1): p. 42-51.
206. Sehested, J., *Four challenges for nickel steam-reforming catalysts.* Catalysis Today, 2006. **111**(1–2): p. 103-110.
207. Sasaki, K. and Y. Teraoka, *Equilibria in fuel cell gases I. Equilibrium compositions and reforming conditions.* Journal of The Electrochemical Society, 2003. **150**(7): p. A878-A884.
208. Sasaki, K. and Y. Teraoka, *Equilibria in fuel cell gases II. The CHO ternary diagrams.* Journal of The Electrochemical Society, 2003. **150**(7): p. A885-A888.
209. Ermakova, M., et al., *New nickel catalysts for the formation of filamentous carbon in the reaction of methane decomposition.* Journal of catalysis, 1999. **187**(1): p. 77-84.
210. Chen, D., et al., *Synthesis of carbon nanofibers: effects of Ni crystal size during methane decomposition.* Journal of Catalysis, 2005. **229**(1): p. 82-96.
211. Kim, J.-H., et al., *Effect of metal particle size on coking during CO 2 reforming of CH 4 over Ni–alumina aerogel catalysts.* Applied Catalysis A: General, 2000. **197**(2): p. 191-200.
212. Galea, N.M., D. Knapp, and T. Ziegler, *Density functional theory studies of methane dissociation on anode catalysts in solid-oxide fuel cells: Suggestions for coke reduction.* Journal of Catalysis, 2007. **247**(1): p. 20-33.
213. Zhao, L., et al., *Ni-Co alloy catalyst from LaNi1-xCoxO3 perovskite supported on zirconia for steam reforming of ethanol.* Applied Catalysis B-Environmental, 2016. **187**: p. 19-29.
214. Kan, H. and H. Lee, *Enhanced stability of Ni–Fe/GDC solid oxide fuel cell anodes for dry methane fuel.* Catalysis Communications, 2010. **12**(1): p. 36-39.
215. Nikolla, E., J.W. Schwank, and S. Linic, *Hydrocarbon steam reforming on Ni alloys at solid oxide fuel cell operating conditions.* Catalysis Today, 2008. **136**(3): p. 243-248.
216. Kan, H. and H. Lee, *Sn-doped Ni/YSZ anode catalysts with enhanced carbon deposition resistance for an intermediate temperature SOFC.* Applied Catalysis B: Environmental, 2010. **97**(1): p. 108-114.
217. Jeong, J.H., et al., *Ru-doped Ni catalysts effective for the steam reforming of methane without the pre-reduction treatment with H2.* Applied Catalysis A: General, 2006. **302**(2): p. 151-156.

218. Farrell, B. and S. Linic, *Direct electrochemical oxidation of ethanol on SOFCs: Improved carbon tolerance of Ni anode by alloying.* Applied Catalysis B: Environmental, 2016. **183**: p. 386-393.
219. Guo, J., et al., *The reactivity of surface active carbonaceous species with CO 2 and its role on hydrocarbon conversion reactions.* Journal of Molecular Catalysis A: Chemical, 2010. **316**(1): p. 1-7.
220. Lemonidou, A.A. and I.A. Vasalos, *Carbon dioxide reforming of methane over 5 wt.% Ni/CaO-Al 2 O 3 catalyst.* Applied Catalysis A: General, 2002. **228**(1): p. 227-235.
221. Horiuchi, T., et al., *Suppression of carbon deposition in the CO 2-reforming of CH 4 by adding basic metal oxides to a Ni/Al 2 O 3 catalyst.* Applied Catalysis A: General, 1996. **144**(1): p. 111-120.
222. Amin, M.H., et al., *Highly stable ytterbium promoted Ni/γ-Al 2 O 3 catalysts for carbon dioxide reforming of methane.* Applied Catalysis B: Environmental, 2012. **119**: p. 217-226.
223. Therdthianwong, S., C. Siangchin, and A. Therdthianwong, *Improvement of coke resistance of Ni/Al 2 O 3 catalyst in CH 4/CO 2 reforming by ZrO 2 addition.* fuel processing technology, 2008. **89**(2): p. 160-168.
224. Wang, W., et al., *A new Gd-promoted nickel catalyst for methane conversion to syngas and as an anode functional layer in a solid oxide fuel cell.* Journal of Power Sources, 2011. **196**(8): p. 3855-3862.
225. Laosiripojana, N., S. Assabumrungrat, and S. Charojrochkul, *Steam reforming of ethanol with co-fed oxygen and hydrogen over Ni on high surface area ceria support.* Applied Catalysis A: General, 2007. **327**(2): p. 180-188.
226. Watwe, R., et al., *Theoretical studies of stability and reactivity of CH x species on Ni (111).* Journal of Catalysis, 2000. **189**(1): p. 16-30.
227. Nikooyeh, K., et al., *Effect of hydrogen on carbon formation on Ni/YSZ composites exposed to methane.* Applied Catalysis A: General, 2008. **347**(1): p. 106-111.
228. Lin, Y., et al., *Direct operation of solid oxide fuel cells with methane fuel.* Solid State Ionics, 2005. **176**(23): p. 1827-1835.
229. Horita, T., et al., *Imaging of CH 4 decomposition around the Ni/YSZ interfaces under anodic polarization.* Journal of power sources, 2005. **145**(2): p. 133-138.
230. Dole, H.A.E., et al., *Quantifying metal support interaction in ceria-supported Pt, PtSn and Ru nanoparticles using electrochemical technique.* Journal of Catalysis, 2016. **333**: p. 40-50.
231. Liu, Z., et al., *In Situ Investigation of Methane Dry Reforming on Metal/Ceria(111) Surfaces: Metal–Support Interactions and C−H Bond Activation at Low Temperature.* Angewandte Chemie International Edition, 2017. **56**(42): p. 13041-13046.
232. Gleaves, J.T., et al., *Temporal analysis of products (TAP)—Recent advances in technology for kinetic analysis of multi-component catalysts.* Journal of Molecular Catalysis A: Chemical, 2010. **315**(2): p. 108-134.
233. Morgan, K., et al., *Forty years of temporal analysis of products.* Catalysis Science & Technology, 2017. **7**(12): p. 2416-2439.
234. Balcaen, V., et al., *TAP study on the active oxygen species in the total oxidation of propane over a CuO–CeO2/γ-Al2O3 catalyst.* Catalysis Today, 2010. **157**(1): p. 49-54.
235. Song, Z., W. Liu, and H. Nishiguchi, *Quantitative analyses of oxygen release/storage and CO2 adsorption on ceria and Pt–Rh/ceria.* Catalysis Communications, 2007. **8**(4): p. 725-730.
236. Duarte, R.B., et al., *Transient Mechanistic Studies of Methane Steam Reforming over Ceria-Promoted Rh/Al2O3 Catalysts.* ChemCatChem, 2014. **6**(10): p. 2898-2903.
237. Gopal, C.B. and S.M. Haile, *An electrical conductivity relaxation study of oxygen transport in samarium doped ceria.* Journal of Materials Chemistry A, 2014. **2**(7): p. 2405-2417.
238. Falkenstein, A., et al., *Chemical relaxation experiments on mixed conducting oxides with large stoichiometry deviations.* Solid State Ionics, 2015. **280**: p. 66-73.
239. Katsuki, M., et al., *The oxygen transport in Gd-doped ceria.* Solid State Ionics, 2002. **154–155**: p. 589-595.

240. Yashiro, K., et al., *Mass transport properties of Ce0.9Gd0.1O2−δ at the surface and in the bulk.* Solid State Ionics, 2002. **152-153**: p. 469-476.
241. Sadykov, V.A., et al., *Partial oxidation of methane on Pt-supported lanthanide doped ceria–zirconia oxides: Effect of the surface/lattice oxygen mobility on catalytic performance.* Catalysis Today, 2011. **169**(1): p. 125-137.
242. Forrester, J. and G. Schaffer, *The chemical kinetics of mechanical alloying.* Metallurgical and Materials Transactions A, 1995. **26**(3): p. 725.
243. Bickerton, G.R., et al., *Quantifying the chemical beauty of drugs.* Nature chemistry, 2012. **4**(2): p. 90.
244. Skalar, T., et al., *Oxidation of carbon deposits on anode material Ni–YSZ in solid oxide fuel cells.* Journal of Thermal Analysis and Calorimetry, 2017. **127**(1): p. 265-271.
245. Hofmann, S., et al., *In situ Observations of Catalyst Dynamics during Surface-Bound Carbon Nanotube Nucleation.* Nano Letters, 2007. **7**(3): p. 602-608.
246. Audier, M., et al., *Morphology and crystalline order in catalytic carbons.* Carbon, 1981. **19**(3): p. 217-224.
247. Feigerle, C.S., S.R. Desai, and S.H. Overbury, *The kinetics of CO desorption from Ni(110).* The Journal of Chemical Physics, 1990. **93**(1): p. 787-794.
248. Chorkendorff, I., J.N. Russell, and J.T. Yates, *Hydrogen implantation in Ni(111) — A study of H2 desorption dynamics from the bulk.* Surface Science, 1987. **182**(3): p. 375-389.
249. Holmgren, A., D. Duprez, and B. Andersson, *A model of oxygen transport in Pt/ceria catalysts from isotope exchange.* Journal of Catalysis, 1999. **182**(2): p. 441-448.
250. Ren, X.-B., H.-Y. Li, and X.-Y. Guo, *Monte Carlo simulation of the oscillatory behavior in partial oxidation of methane on nickel catalyst.* Surface Science, 2008. **602**(1): p. 300-306.
251. Jørgensen, M. and H. Grönbeck, *First-Principles Microkinetic Modeling of Methane Oxidation over Pd(100) and Pd(111).* ACS Catalysis, 2016. **6**(10): p. 6730-6738.
252. Bhavsar, S. and G. Veser, *Reducible Supports for Ni-based Oxygen Carriers in Chemical Looping Combustion.* Energy & Fuels, 2013. **27**(4): p. 2073-2084.
253. Xu, J., et al., *Size dependent oxygen buffering capacity of ceria nanocrystals.* Chemical Communications, 2010. **46**(11): p. 1887-1889.
254. Ichikawa, M. and T. Fukushima, *Infrared studies of metal additive effects on carbon monoxide chemisorption modes on silicon dioxide-supported rhodium-manganese,-titanium and iron catalysts.* The Journal of Physical Chemistry, 1985. **89**(9): p. 1564-1567.
255. Boffa, A., A. Bell, and G. Somorjai, *Vanadium Oxide Deposited on an Rh Foil: CO and CO2 Hydrogenation Reactivity.* Journal of Catalysis, 1993. **139**(2): p. 602-610.
256. Wei, J. and E. Iglesia, *Mechanism and Site Requirements for Activation and Chemical Conversion of Methane on Supported Pt Clusters and Turnover Rate Comparisons among Noble Metals.* The Journal of Physical Chemistry B, 2004. **108**(13): p. 4094-4103.
257. Christmann, K., O. Schober, and G. Ertl, *Adsorption of CO on a Ni(111) surface.* The Journal of Chemical Physics, 1974. **60**(12): p. 4719-4724.
258. Datta, P., P. Majewski, and F. Aldinger, *Synthesis and reactivity study of gadolinia doped ceria–nickel: A potential anode material for solid oxide fuel cell.* Journal of Alloys and Compounds, 2008. **455**(1): p. 454-460.
259. Fuerte, A., et al., *Study of a SOFC with a bimetallic Cu–Co–ceria anode directly fuelled with simulated biogas mixtures.* International Journal of Hydrogen Energy, 2014. **39**(8): p. 4060-4066.
260. Park, H.C. and A.V. Virkar, *Bimetallic (Ni–Fe) anode-supported solid oxide fuel cells with gadolinia-doped ceria electrolyte.* Journal of Power Sources, 2009. **186**(1): p. 133-137.
261. Bao, Z., et al., *Kinetic separation of carbon dioxide and methane on a copper metal–organic framework.* Journal of Colloid and Interface Science, 2011. **357**(2): p. 504-509.
262. Sinfelt, J.H., J.L. Carter, and D.J.C. Yates, *Catalytic hydrogenolysis and dehydrogenation over copper-nickel alloys.* Journal of Catalysis, 1972. **24**(2): p. 283-296.

263. Pal, D.B., et al., *Performance of water gas shift reaction catalysts: A review.* Renewable and Sustainable Energy Reviews, 2018. **93**: p. 549-565.
264. Koryabkina, N.A., et al., *Determination of kinetic parameters for the water–gas shift reaction on copper catalysts under realistic conditions for fuel cell applications.* Journal of Catalysis, 2003. **217**(1): p. 233-239.
265. Grenoble, D.C., M.M. Estadt, and D.F. Ollis, *The chemistry and catalysis of the water gas shift reaction: 1. The kinetics over supported metal catalysts.* Journal of Catalysis, 1981. **67**(1): p. 90-102.
266. Binet, C., et al., *FTIR study of carbon monoxide adsorption on ceria: CO carbonite dianion adsorbed species.* Journal of the Chemical Society, Faraday Transactions, 1994. **90**(7): p. 1023-1028.
267. Gokhale, A.A., J.A. Dumesic, and M. Mavrikakis, *On the Mechanism of Low-Temperature Water Gas Shift Reaction on Copper.* Journal of the American Chemical Society, 2008. **130**(4): p. 1402-1414.
268. Knapp, D. and T. Ziegler, *Methane Dissociation on the Ceria (111) Surface.* The Journal of Physical Chemistry C, 2008. **112**(44): p. 17311-17318.
269. Ramírez-Cabrera, E., A. Atkinson, and D. Chadwick, *Catalytic steam reforming of methane over Ce0.9Gd0.1O2−x.* Applied Catalysis B: Environmental, 2004. **47**(2): p. 127-131.
270. Tang, X., et al., *CuO/CeO2 catalysts: Redox features and catalytic behaviors.* Applied Catalysis A: General, 2005. **288**(1): p. 116-125.
271. Tanasini, P., et al., *Experimental and Theoretical Investigation of Degradation Mechanisms by Particle Coarsening in SOFC Electrodes.* Fuel Cells, 2009. **9**(5): p. 740-752.
272. Mitterdorfer, A. and L.J. Gauckler, *La2Zr2O7 formation and oxygen reduction kinetics of the La0.85Sr0.15MnyO3, O2(g)|YSZ system.* Solid State Ionics, 1998. **111**(3): p. 185-218.
273. Horita, T., et al., *Effects of impurities on the degradation and long-term stability for solid oxide fuel cells.* Journal of Power Sources, 2009. **193**(1): p. 194-198.
274. Jiang, S.P., *Sintering behavior of Ni/Y2O3-ZrO2cermet electrodes of solid oxide fuel cells.* Journal of Materials Science, 2003. **38**(18): p. 3775-3782.
275. Sehested, J., et al., *Sintering of Nickel Steam-Reforming Catalysts on MgAl2O4 Spinel Supports.* Journal of Catalysis, 2001. **197**(1): p. 200-209.
276. Khan, M.S., et al., *Fundamental mechanisms involved in the degradation of nickel–yttria stabilized zirconia (Ni–YSZ) anode during solid oxide fuel cells operation: A review.* Ceramics International, 2016. **42**(1, Part A): p. 35-48.
277. Matsui, T., et al., *Performance Deterioration of Ni–YSZ Anode Induced by Electrochemically Generated Steam in Solid Oxide Fuel Cells.* Journal of The Electrochemical Society, 2010. **157**(5): p. B776-B781.
278. Cronin, J.S., J.R. Wilson, and S.A. Barnett, *Impact of pore microstructure evolution on polarization resistance of Ni-Yttria-stabilized zirconia fuel cell anodes.* Journal of Power Sources, 2011. **196**(5): p. 2640-2643.
279. Zekri, A., et al., *Nickel Depletion and Agglomeration in SOFC Anodes During Long-Term Operation.* Fuel Cells, 2017. **17**(3): p. 359-366.
280. Suzuki, S., H. Uchida, and M. Watanabe, *Interaction of samaria-doped ceria anode with highly dispersed Ni catalysts in a medium-temperature solid oxide fuel cell during long-term operation.* Solid State Ionics, 2006. **177**(3): p. 359-365.
281. Steve, R. and P. Robert, *A review of focused ion beam applications in microsystem technology.* Journal of Micromechanics and Microengineering, 2001. **11**(4): p. 287.
282. Wilson, J.R., et al., *Three-dimensional reconstruction of a solid-oxide fuel-cell anode.* Nature Materials, 2006. **5**: p. 541.
283. Iwai, H., et al., *Quantification of SOFC anode microstructure based on dual beam FIB-SEM technique.* Journal of Power Sources, 2010. **195**(4): p. 955-961.

284. Shikazono, N., et al., *Numerical Assessment of SOFC Anode Polarization Based on Three-Dimensional Model Microstructure Reconstructed from FIB-SEM Images.* Journal of The Electrochemical Society, 2010. **157**(5): p. B665-B672.
285. Kishimoto, M., et al., *Enhanced triple-phase boundary density in infiltrated electrodes for solid oxide fuel cells demonstrated by high-resolution tomography.* Journal of Power Sources, 2014. **266**: p. 291-295.
286. Gostovic, D., et al., *Three-Dimensional Reconstruction of Porous LSCF Cathodes.* Electrochemical and Solid-State Letters, 2007. **10**(12): p. B214-B217.
287. Oh, T.-S. and S.M. Haile, *Electrochemical behavior of thin-film Sm-doped ceria: insights from the point-contact configuration.* Physical Chemistry Chemical Physics, 2015. **17**(20): p. 13501-13511.
288. Nielsen, J., T. Klemensø, and P. Blennow, *Detailed impedance characterization of a well performing and durable Ni:CGO infiltrated cermet anode for metal-supported solid oxide fuel cells.* Journal of Power Sources, 2012. **219**: p. 305-316.
289. Adler, S.B., *Mechanism and kinetics of oxygen reduction on porous La1−xSrxCoO3−δ electrodes.* Solid State Ionics, 1998. **111**(1): p. 125-134.
290. Bertei, A., et al., *Validation of a physically-based solid oxide fuel cell anode model combining 3D tomography and impedance spectroscopy.* International Journal of Hydrogen Energy, 2016. **41**(47): p. 22381-22393.
291. Primdahl, S. and M. Mogensen, *Mixed conductor anodes: Ni as electrocatalyst for hydrogen conversion.* Solid State Ionics, 2002. **152-153**: p. 597-608.
292. Primdahl, S. and M. Mogensen, *Gas diffusion impedance in characterization of solid oxide fuel cell anodes.* Journal of the electrochemical society, 1999. **146**(8): p. 2827-2833.
293. Primdahl, S. and M. Mogensen, *Gas conversion impedance: A test geometry effect in characterization of solid oxide fuel cell anodes.* Journal of the Electrochemical Society, 1998. **145**(7): p. 2431-2438.
294. Chen, J., et al., *Characterization of Degradation in Nickel Impregnated Scandia-Stabilize Zirconia Electrodes during Isothermal Annealing.* Journal of The Electrochemical Society, 2017. **164**(9): p. F935-F943.
295. Song, B., et al., *Quantification of the degradation of Ni-YSZ anodes upon redox cycling.* Journal of Power Sources, 2018. **374**: p. 61-68.
296. Aravind, P.V., J.P. Ouweltjes, and J. Schoonman, *Diffusion Impedance on Nickel/Gadolinia-Doped Ceria Anodes for Solid Oxide Fuel Cells.* Journal of The Electrochemical Society, 2009. **156**(12): p. B1417-B1422.
297. Kim, P., D.J.L. Brett, and N.P. Brandon, *The effect of water content on the electrochemical impedance response and microstructure of Ni-CGO anodes for solid oxide fuel cells.* Journal of Power Sources, 2009. **189**(2): p. 1060-1065.
298. Klemensø, T., et al., *Stability of Ni–yttria stabilized zirconia anodes based on Ni-impregnation.* Journal of Power Sources, 2010. **195**(21): p. 7295-7301.
299. Badwal, S.P.S., F.T. Ciacchi, and J. Drennan, *Investigation of the stability of ceria-gadolinia electrolytes in solid oxide fuel cell environments.* Solid State Ionics, 1999. **121**(1): p. 253-262.
300. Vayssilov, G.N., et al., *Support nanostructure boosts oxygen transfer to catalytically active platinum nanoparticles.* Nat Mater, 2011. **10**(4): p. 310-315.
301. Dong, W.-S., et al., *Methane reforming over Ni/Ce-ZrO2 catalysts: effect of nickel content.* Applied Catalysis A: General, 2002. **226**(1): p. 63-72.
302. Beck, R.D., et al., *Vibrational Mode-Specific Reaction of Methane on a Nickel Surface.* Science, 2003. **302**(5642): p. 98.
303. Huang, Z.-M., et al., *A review on polymer nanofibers by electrospinning and their applications in nanocomposites.* Composites Science and Technology, 2003. **63**(15): p. 2223-2253.
304. Formalas, A., *Process and apparatus for preparing artificial threads* 1934.

305. Cherney, L.T., *Structure of Taylor cone-jets: limit of low flow rates.* Journal of Fluid Mechanics, 1999. **378**: p. 167-196.
306. Fong, H., I. Chun, and D.H. Reneker, *Beaded nanofibers formed during electrospinning.* Polymer, 1999. **40**(16): p. 4585-4592.
307. Cavaliere, S., et al., *Electrospinning: designed architectures for energy conversion and storage devices.* Energy & Environmental Science, 2011. **4**(12): p. 4761-4785.
308. Park, J.-H., et al., *Effects of electrospun polyacrylonitrile-based carbon nanofibers as catalyst support in PEMFC.* Journal of Applied Electrochemistry, 2009. **39**(8): p. 1229.
309. Li, M., et al., *Electrospinning-derived carbon fibrous mats improving the performance of commercial Pt/C for methanol oxidation.* Journal of Power Sources, 2009. **191**(2): p. 351-356.
310. Zhi, M., et al., *Nanofiber scaffold for cathode of solid oxide fuel cell.* Energy & Environmental Science, 2011. **4**(2): p. 417-420.
311. Cooper, S.J., et al., *TauFactor: An open-source application for calculating tortuosity factors from tomographic data.* SoftwareX, 2016. **5**: p. 203-210.
312. al., R.e., *Characterization of the local morphology at triple-phase boundaries after SOFC/SOEC operation*, in *13th European SOFC & SOE Forum*. 2018: Lucerne/Switzerland. p. 28-36.
313. Wolfram, S., *Cellular automata as models of complexity.* Nature, 1984. **311**: p. 419.
314. Bessler, W.G., S. Gewies, and M. Vogler, *A new framework for physically based modeling of solid oxide fuel cells.* Electrochimica Acta, 2007. **53**(4): p. 1782-1800.
315. Lai, W. and F. Ciucci, *Mathematical modeling of porous battery electrodes—Revisit of Newman's model.* Electrochimica Acta, 2011. **56**(11): p. 4369-4377.
316. Costamagna, P., P. Costa, and V. Antonucci, *Micro-modelling of solid oxide fuel cell electrodes.* Electrochimica Acta, 1998. **43**(3): p. 375-394.
317. Atkinson, A., S.A. Baron, and N.P. Brandon, *AC Impedance Spectra Arising from Mixed Ionic Electronic Solid Electrolytes.* Journal of The Electrochemical Society, 2004. **151**(5): p. E186-E193.
318. Bertei, A., et al., *The fractal nature of the three-phase boundary: A heuristic approach to the degradation of nanostructured solid oxide fuel cell anodes.* Nano Energy, 2017. **38**: p. 526-536.
319. Bertei, A., et al., *Microstructural Modeling and Effective Properties of Infiltrated SOFC Electrodes.* ECS Transactions, 2013. **57**(1): p. 2527-2536.
320. de Boer, B., *SOFC anode. Hydrogen oxidation at porous nickel and nickel/zirconia electrodes.* 1998.
321. Tucker, M.C., et al., *Performance of metal-supported SOFCs with infiltrated electrodes.* Journal of Power Sources, 2007. **171**(2): p. 477-482.
322. Jung, W., et al., *Robust nanostructures with exceptionally high electrochemical reaction activity for high temperature fuel cell electrodes.* Energy & Environmental Science, 2014. **7**(5): p. 1685-1692.
323. Muecke, U.P., et al., *Microstructure and electrical conductivity of nanocrystalline nickel- and nickel oxide/gadolinia-doped ceria thin films.* Acta Materialia, 2008. **56**(4): p. 677-687.
324. Yu, M., et al., *Influence of Precursor Properties on the Thermal Stabilization of Polyacrylonitrile Fibers.* Polymer Bulletin, 2006. **57**(5): p. 757-763.
325. Zhang, C., et al., *Ionic conductivity and its temperature dependence of atmospheric plasma-sprayed yttria stabilized zirconia electrolyte.* Materials Science and Engineering: B, 2007. **137**(1): p. 24-30.
326. McIntosh, S., J.M. Vohs, and R.J. Gorte, *Impedance Spectroscopy for the Characterization of Cu-Ceria-YSZ Anodes for SOFCs.* Journal of The Electrochemical Society, 2003. **150**(10): p. A1305-A1312.
327. Kenney, B., et al., *Computation of TPB length, surface area and pore size from numerical reconstruction of composite solid oxide fuel cell electrodes.* Journal of Power Sources, 2009. **189**(2): p. 1051-1059.

328. Lacombe, S., H. Zanthoff, and C. Mirodatos, *Oxidative coupling of methane over lanthana catalysts: II. A mechanistic study using isotope transient kinetics.* Journal of Catalysis, 1995. **155**(1): p. 106-116.
329. Guillodo, M., et al., *Oxygen diffusion coefficient and oxygen exchange coefficient of BIMEVOX.10 (ME=Cu, Co) ceramic membranes.* Solid State Ionics, 2003. **164**(1): p. 87-96.
330. Pu, Z.-Y., et al., *Study of oxygen vacancies in Ce0. 9Pr0. 1O2-δ solid solution by in situ X-ray diffraction and in situ Raman spectroscopy.* The Journal of Physical Chemistry C, 2007. **111**(50): p. 18695-18702.
331. McBride, J.R., et al., *Raman and x‐ray studies of Ce1−xRExO2−y, where RE=La, Pr, Nd, Eu, Gd, and Tb.* Journal of Applied Physics, 1994. **76**(4): p. 2435-2441.
332. DeCaluwe, S.C., et al., *In Situ Characterization of Ceria Oxidation States in High-Temperature Electrochemical Cells with Ambient Pressure XPS.* The Journal of Physical Chemistry C, 2010. **114**(46): p. 19853-19861.
333. Pakharukov, I.Y., et al., *In situ XPS studies of kinetic hysteresis in methane oxidation over Pt/γ-Al2O3 catalysts.* Catalysis Today, 2016. **278**: p. 135-139.
334. Sadykov, V.A., et al., *Mobility and reactivity of the lattice oxygen of Pr-doped ceria promoted with Pt.* Reaction Kinetics and Catalysis Letters, 2005. **86**(1): p. 21-28.

Appendix A List of abbreviations and symbols

Abbreviations

CGO Gadolinium-doped Ceria

CLR Chemical Looping Reforming

CPE Constant Phase Element

CSO Samarium-doped Ceria

CTE Coefficient of Thermal Expansion

CUDA Compute Unified Device Architecture

DPB Dual Phase Boundary

DRT Distribution of Relaxation Time analysis

EC Equivalent Circuit

EIS Electrochemical Impedance Spectroscopy

E-R Eley-Rideal mechanism

FIB Focused Ion Beam

FMS Fiber-Matrix Structure

HF High Frequency

L Inductor

L-H Langmuir–Hinshelwood mechanism

LF Low Frequency

MIEC Mixed Ionic and Electronic Conductivity

MP Methane Pulse

MvK Mars-Van Krevelen mechanism

OSC Oxygen Storage Capacity

POM Partial Oxidation of Methane

R Resistor

ScSZ Scandium-Stabilized Zirconia

SEM Scanning Electron Microscope

SOFC Solid Oxide Fuel Cell

SRM Steam Reforming of Methane

TAP Temporal Analysis of Products

TPB Triple Phase Boundary

TPD Temperature-Programmed Desorption

TPO Temperature-Programmed Oxidation

TPR Temperature-Programmed Reduction

TOM Total Oxidation of Methane

XPS X-ray Photoelectron Spectroscopy

XRD X-Ray powder Diffraction

YSZ Yttrium-Stabilized Zirconia

Symbols

a'_{DPB} DPB distribution with distance from Ni

C^* State of cellular automata evolution

d Spacing between diffracting planes, nm

D_{Chem} Chemical diffusion coefficient

D^{eff} Effective diffusion coefficient of gas in electrode

$D(i,j)$ Non-Euclidean distance between two cellular automata cells

$E(i,k)$ Euclidean distance between two cellular automata cells

F Faraday constant, $C \cdot mol^{-1}$

h Planck Constant, $m^2 \cdot$

h_{ed} Electrode thickness, µm

i Current density, $A \cdot m^{-2}$

i_0 Exchange current density, $A \cdot m^{-2}$

i_{DPB}^{v} Current density produced by the DPB reaction path, $A \cdot m^{-2}$

i_L Mximum current density at maximum reactant concentration gradient, $A \cdot m^{-2}$

i_{TPB}^{v} Current density produced by the TPB reaction path, $A \cdot m^{-2}$

I_δ Ion current of species with a charge to mass ratio of δ

j Imaginary unit

J_e Electronic current flux, $A \cdot m^{-1}$

J_O Ionic current flux, $A \cdot m^{-1}$

k_s Surface exchange coefficient

k_{TPB} Kinetic constant of reaction at TPB, $A \cdot \mu m^2 \cdot V^{-1} \cdot m^{-2}$

L_{TPB}^{v} TPB length density, μm^{-2}

n Number of electrons involved in the electrode reaction, mol

pO_2 Oxygen partial pressure, Pa

px Partial pressure of gas x, Pa

r_x Flow rate of gas x, $mL \cdot min^{-1}$

R Universal gas constant, $J \cdot mol^{-1} \cdot K^{-1}$

R_{elec} Ohmic resistance of electron conduction, $\Omega \cdot cm^2$

R_{ion} Ohmic resistance of ion conduction, $\Omega \cdot cm^2$

S_{cp} Set of all cellular automata cells at DPB

$S_{c\&n}$ Set of all cellular automata cells at the boarder of CGO and Ni

S^x_δ Sensitivity of gas *x* at mass/charge ratio δ, $A \cdot Pa^{-1}$

T Temperature, K or °C

V_x Volume of gas x, mL

$Z(j\omega)$ Complex impedance

Z' Real part of impedance

Z'' Imaginary part of impedance

ΔE Activation energy in the equilibrium state, kJ·mol

ΔH_m Activation entropy of electron diffusion, kJ·mol

α Symmetry factor of Butler-Volmer equation

β Full width of half maximum intensity of given peak

δ Oxygen non-stoichiometry in ceria

ε Charge to mass ratio

η_{Act} Activation polarization, V

η_{Conc} Concentration polarization, V

η_{ed} Electrochemical potential of electrons in Ni, V

η_{Ohmic} Ohmic polarization, V

ϑ Angle of incidence, °

λ Wavelength of X-ray, nm

$\tilde{\mu}_e^*$ Electrochemical potential of electrons ions in CGO, V

$\tilde{\mu}_O^*$ Electrochemical potential of oxygen ions in CGO, V

P_{CGO} Volume fraction of CGO

T_{CGO} Tortuosity factor of CGO

σ_e^{eff} Effective electronic conductivity of CGO

$\sigma_O{}^{eff}$ Effective ionic conductivity of CGO

τ *Mean* crystallite size, nm

ω Angular frequency, s^{-1}

Appendix B List of Figures

Figure. 1.1.1 Schematic diagram of a fuel cell single cell with an oxygen ion conducting electrolyte 2

Figure. 1.1.2 An ideal i-V curve of SOFC including activation polarization, Ohmic loss and concentration polarization 7

Figure. 1.1.3 Comprehensive lists of materials used in each component of an SOFC 11

Figure. 1.2.1. Arrhenius plots of ionic conductivity of ceria-based oxides doped with rare-earth oxides: (○) $(CeO_2)_{0.8}(SmO_{1.5})_{0.2}$; (Δ) $(CeO_2)_{0.8}(GdO_{1.5})_{0.2}$; (∇) $(CeO_2)_{0.8}(YO_{1.5})_{0.2}$; (□) $(CeO_2)_{0.8}(CaO)_{0.2}$; (▪) CeO_2; (●) $(ZrO_2)_{0.85}(YO_{1.5})_{0.15}$ 17

Figure. 1.2.2. Ionic conductivity of doped ceria at 1073 K against the radius of dopant cation, shown in the horizontal axis is the critical radius of the divalent or trivalent cation 18

Figure. 1.2.3. E_a for dopants sitting next to each other (a) and separated from each other (b) and an effective average of the former two (c) (see text). The results were obtained within the 3*2*2 supercell, which implies a dopant concentration of 4.2%. The experimental values refer to the same doping level. Nd/Sm and Pr/Gd represent a mixture of dopants and have been placed according to their average atomic numbers 18

Figure. 1.2.4 Scanning electrode microscope micrographs of the porous columnar SDC films prepared in 100 mTorr O_2 at 650°C. (a–d) Top view image as a function of the layer thickness (250 nm to 10.8 mm). (e–f) Cross-section view images with the Pt current collector on top. Image (f) was obtained after focused ion beam (FIB) milling of the sample 21

Figure. 1.2.5 Patterned metal on thin-film ceria as a model system to study competing electrochemical reactions. a. Schematic depicting the two macroscopic reaction sites present in a ceria–metal patterned electrode and the corresponding surface reaction and bulk diffusion steps. Bulk pathways involving the metal are not shown. b. Patterned electrode with an embedded current collector that eliminates contribution from the metallic phase. c–h, Planar SEM images of corresponding electrode structures, recorded after electrochemical characterization under H_2–H_2O–Ar atmospheres at 650 ℃. 23

Figure. 1.2.6 Structure of an ideal perovskite ABX_3 with $X = O^{2-}$ (*left hand side A* in origin; *right hand side B* in origin) 24

Figure. 1.2.7 Wetting angles of different SSC precursor solutions on LSCF, LSM, YSZ and GDC substrates (*note*: mixture 1 had a water-to-ethanol volume ratio of 1:0.3 and mixture 2 has a water-to-ethanol volume ratio of 1:0.6)..... 26

Figure. 1.2.8 Typical process for the infiltration of metal salt nitrate solution or nanoparticle suspension into pre-sintered electrode or electrolyte porous structure..... 26

Figure. 1.2.9 SEM images of the i) overall view and ii) cross-section of the dual-layer HFs co-sintered at 1500 ° C for 12 h and reduced at 550 °C for 2.5 h. 29

Figure. 1.2.10 Sketch of the replica resulting from a double gyroid KIT-6 mesoporous template. (a) Two sets of interpenetrating mesoporous channels in the template, Ni and CGO was impregnated separately in these two channels; (b) [111] projection of the mesostructure and (c) bimodal pore size distribution obtained after filling one or two of the channels 30

Figure. 1.3.1 a. The H_2-TPR of Ni/CGO samples with different Ni loading; b. CO-TPR of 40wt% Ni/CGO sample; c. TPD of 40wt% Ni/CGO sample after CO-TPR; d. O_2-TPO of 40wt% Ni/CGO sample..... 32

Figure. 1.3.2 The impedance of the anode in a solid oxide fuel cell using YSZ as electrolyte: (a) Bode plot; (b) Nyquist plot..... 34

Figure. 1.3.3. Equivalent circuit used for fitting the electrochemical impedance spectra of a symmetrical cell made by Ni/YSZ electrodes 35

Figure. 1.3.4 A diagram of diffraction of an x-ray beam scattered at a crystal plane 37

Figure. 1.3.5 XRD pattern of $Ce_{0.8}Gd_{0.2}O_{1.9}$, the brackets above shows the Miller index of the crystal plane 38

Figure. 1.3.6 Jablonski Diagram of Raman Scattering, *h* is the Planck's constant, v_0 is the frequency of in-coming photon. v_m is the frequency difference between in-coming and excited photon..... 39

Figure. 1.3.7 Extended Raman spectra of a) NiO, b) CGO, and c) NiO-CGO cermet taken at 600 °C in flowing nitrogen using a 514 nm laser. Inset to (b) shows the Raman spectrum obtained from CGO at 600 °C emphasizing a small second-order Raman mode at 1170 cm^{-1} close to the position of the principle NiO mode. 40

Figure. 1.3.8 Normalized intensities of the NiO and CGO Raman peaks monitored as a function of time from a NiO-CGO composite exposed to a) dry and b) wet 75% N_2:25% H_2 flowing at 100 ml/min. Reduction of NiO and CGO appears to be strongly coupled in both cases, although the oxidation state of the CGO surface strongly recovers for the cermet exposed to the wet atmosphere. 41

Figure. 2.1.1 Equilibrium products from methane (CH_4) mixed with H_2O in different steam-to-carbon ratios (S/C): (a) S/C = 0, (b) S/C = 1.0, and (c) S/C = 1.5..... 48

Figure. 2.1.2 TPO spectra of Ni/YSZ exposed for 3 h at 1073 K to feed streams with H_2:CH_4 ratios of (a) 0, (b) 0.5, (c) 1 and (d) 1.5. 50

Figure. 2.1.3 TPO analysis of Ni/YSZ anodes exposed to methane for 6 h at 1073 K with current densities of 0 mA/cm^2, 1 mA/cm^2, 10 mA/cm^2 and 50 mA/cm^2: (a) CO_2 production and (b) H_2O production. 51

Figure. 2.2.1 Impregnation process of Ni/CGO using 2 M $Ni(NO_3)_2.6H_2O$ ethanol 55

Figure. 2.2.2 Analysis process of Ni/CGO using Autochem powder analyser 56

Figure.2.2.3 Schematic indication of gas connection in in-situ Raman experiment 59

Figure. 2.2.4 SEM image of reduced a and c. CGO; b and d Ni impregnated CGO powder ... 61

Figure. 2.2.5 XRD pattern of CGO and Ni/CGO, ♦ indicates doped CeO_2 phase, * indicates NiO phase..... 62

Figure. 2.2.6 The products of the first methane pulse on a. Ni/CGO; b. CGO. The y axis is the flow rate of each species in ml/min CH_4 (mass 15), H_2 (mass 2), H_2O (mass 18), CO (mass 28) and CO_2 (mass 44) are monitored. The methane pulse is injected from 0s. After 25s, all species except for CO has escaped from the system 63

Figure. 2.2.7 The products of the second methane pulse on a. Ni/CGO; b. CGO. The y axis is the flow rate of each species in mL/min CH_4 (mass 15), H_2 (mass 2), H_2O (mass 18), CO (mass 28) and CO_2 (mass 44) are monitored.....64

Figure. 2.2.8 The first to fourth CO production peak of a methane pulse on Ni/CGO and on Ni/YSZ. From the second methane pulse, the CO production peak consists of an initial peak and a tail, the length of tail extends with pulsing number.....65

Figure. 2.2.9: Red, green and black lines are the amount of CO and CO_2 produced, and CH_4 consumed, in each methane pulse; the grey line is the proportion of CO produced in initial peak versus the total CO produced in each methane pulse. The methane pulses were injected with 30min intervals 67

Figure. 2.2.10 The Raman spectrum for reduced Ni/CGO sample, recorded from 0-1780 cm^{-1}

.....69

Figure. 2.2.11 Production/consumption amount of gas species in the methane pulse experiment with in-situ Raman by mass spectrometer versus pulse number 70

Figure. 2.2.12 CO signal from the mass spectrometer and integrated Ce^{IV}-O peak intensity with time in methane pulse on a) Ni/CGO; b) CGO 71

Figure. 2.2.13 Proposed mechanism for methane oxidation in given conditions: Methane either decomposes at the surface of ceria or reacts with adsorbed oxygen, then carbon species are oxidized by oxygen spilled-over from the ceria surface; after depletion of surface oxygen, oxygen from the bulk ceria migrates to the surface; If carbon is not oxidized, it will accumulate and form amorphous and eventually crystalized carbon deposits.....72

Figure. 2.2.14 An excerpt from the CO production of methane pulse with 30min interval, showing the CO production from the fifth methane pulse. It indicates the overlaps of the CO tail with the next pulse, inset is the temperature programmed oxidation after the methane pulse with different interval on Ni/CGO and Ni/YSZ indicated by CO_2 production.....74

Figure. 2.2.15 The decrease of H_2O baseline and increase of H_2 baselines after each methane pulse. The y-axis is logarithmic-scaled to better show the low content 75

Figure. 2.2.16 The CO production peaks in the first cycle of methane pulse with steam reoxidation 76

Figure. 2.2.17 The CO production and initial peak ratio in methane pulse with water oxidation experiment. The black line is the CO production amount in each methane pulse; the grey line is the proportion of CO produced in the initial peak versus the total CO production in each pulse 78

Figure. 2.2.18 The CO production amount in the initial peak and selectivity towards POM plotted with changing oxygen non-stoichiometry in four cycles of methane pulse with water reoxidation 79

Figure. 2.2.19 a) An excerpt from water pulse oxidation in the methane pulse with water oxidation. It shows that all water was converted to hydrogen and that the rate of CO oxidation was enhanced. b) An excerpt from water pulse oxidation on Ni/YSZ after methane pulses. In the methane pulse with water re-oxidation experiment 12.3% water/Ar pulses were injected every seven pulses of methane until no hydrogen is produced 80

Figure 3.3.1 Consumption/production of species in methane pulse as a function of pulse number on a) Ni/CGO; b) Ni-Cu/CGO; c) Cu/CGO and d) CGO; The inset of c and d presents figure in a magnified scale to better show the detail 87

Figure 3.3.2 Consumption/production of species in methane pulse as a function of ceria oxygen non-stoichiometry on a) Ni/CGO; b) Ni-Cu/CGO; c) Cu/CGO and d) CGO; The inset of c and d presents figure in a magnified scale to better show the detail 88

Figure 3.3.3 The integrated Raman Ce-O peak and CO/CO_2 production rate with time on a) Ni/CGO, b) Ni-Cu/CGO,c) Cu/CGO and (d) CGO 90

Figure 4.2.1 The structure of custom rig used in the characterization of symmetrical cells .. 97

Fig. 4.3.1 SEM image of Ni/CGO electrode a) and b) as prepared; c) and d) after 100h aging

..... 99

Figure 4.3.2 a) EIS spectrum of non-aged cell and 100h aged cell (inset is the DRT analysis); b) Summary of EIS of aging symmetrical cell, R_s is the ohmic resistance, R_1 is the resistance

corresponding to the high frequency process, R_2 the medium frequency process and R_3 the low frequency process; c) The equivalent circuit used to fit EIS. 101

Figure 4.3.3a) The consumption/production amount of species in methane pulses on 5 h aged Ni/CGO; b) The CO produced in methane pulses on Ni/CGO of different ageing times.....104

Figure 4.3.4 a) The plateau of species in methane pulses on Ni/CGO at different ageing hours; b) The total CO produced c) CO produced in major peaks d) CO produced in tails from methane pulses on Ni/CGO of different ageing times, plotted with oxygen non-stoichiometry.....106

Figure. 5.1.1 A schematic diagram of setup for electrospinning.....110

Figure. 5.1.2 SEM images of cross sections of electrospun CNF carbonized at 1000 °C 112

Fig. 5.2.1 a) a 2D cross section of 3-dimensional Ni/CGO electrode data in grids. Grey, white and black grids represent Ni, CGO, black and pore separately. Euclidean distance from a given point to Ni/CGO DPB is marked in blue, while intra-ceria distance is shown as the red curve (Note this shortest path is not unique in grid space). b) At the convergence of cellular automata, each ceria cell is assigned with a value representing the intra-ceria distance to Ni/CGO DPB.....115

Figure 5.3.1 a) The EIS of cermet 1 electrode at 600, 700 and 800°C; b) The Arrhenius fitting of R_2.....121

Figure 5.3.2 a) The EIS results of impregnated and cermet Ni/CGO at 600°C, 9.7% H_2/97.3% N_2/3%H_2O; b) The distribution of ceria-pore DPB density with distance to nickel phase A slice of FIB-SEM cross-section image of c. Impregnated Ni/CGO; d. Cermet Ni/CGO; white phase represents CGO, grey phase nickel, black phase pore; e) Sketch of the electron transport within the CGO phase and of the electrochemical reaction at the DPB along the y-scale; f) 2-dimensional example for illustration of the distribution of DPB area.....123

Figure 5.3.3 SEM image of a) Carbonized NiO fibre membrane; b) Precalcined Ni fibre membrane; EIS and fitted impedance of Ni/CGO fibre electrode at c) 600°C; d) 700°C; e) 800°C; f) EIS of FMS, impregnated and cermet 1 Ni/CGO at 600°C.....130

Figure 5.3.4 3D construction of a) FMS; b) Impregnated; c) Cermet 1 Ni/CGO electrode; In 3D reconstruction, the orange parts are CGO, grey parts are nickel.....132

Figure 5.3.5 The diagram of the model-verification procedures presented in section 5.3.1 and 5.3.2 133

Figure 5.3.6 The 3D reconstruction of a) A single nickel fibre extracted from nickel network; b) The nickel fibre (grey) and CGO that is within 1µm from nickel surface (yellow-red phase), calculated by the cellular automaton algorithm. c) The cumulative distribution of ceria-pore DPB density with distance to nickel phase; d) Distribution of ceria-pore DPB density with distance to nickel phase; e) The comparison of R_2 as obtained from EIS experiments and modelling for FMS, impregnated and cermets Ni/CGO.....134

Figure 5.3.7 a) Impedance of FMS Ni/CGO aged in 3%H_2O-9.7% H_2-97%N_2 at 600 °C for 233 h, at 800 °C for 100 h, impregnated Ni/CGO aged in the same condition at 600 °C for 100 h; A slice of FIB-SEM cross-section image of FMS Ni/CGO electrode b) after aging at 600 °C; c) after aging at 800°C, with nickel phase shown in grey, CGO in white and pore in black.....137

Appendix C List of Tables

Table 1.1.1 Features, pro and cons, and major applications of different types of fuel cells 3

Table 4.3.1 The measured microstructural parameters of unaged and aged Ni/CGO electrodes 102

Table 5.3.1 Summary of EIS fitting results of cermets and impregnated Ni/CGO. Fitted by the equivalent circuit $\boldsymbol{LR_s(R_1CPE_1)(R_2CPE_2)(R_3CPE_3)}$ 121

Table 5.3.2 Summary of relevant microstructural parameters of impregnated and cermets Ni/CGO 122

Table 5.3.3 The summary of calculation results from pseudo-2D model of impregnated and cermet Ni/CGO anodes 125

Table 5.3.4 The summary of fitted EIS result of FMS Ni/CGO electrode at 600, 700 and 800°C 129

Table. 5.3.5 Summary of structural parameters of FMS, impregnated and cermet Ni/CGO electrodes 132

Acknowledgement

First of all, I would like to express my gratitude to the supervisor Prof. Nigel Brandon, for the continuous support of my PhD research. And also to Dr. Paul Boldrin, for his patience and immense knowledge. Their guidance helped me in all my research project and writing of this thesis.

I would also like to thank my co-authors in my publications: Dr. Antonio Bertei, Dr. Jingyi Chen, Dr. Robert Maher, Dr. Samuel Cooper, Dr. Xiaolong Chen, Dr. Xinhua Liu, for their contribution in the experiment and modelling, their insightful comments in manuscripts, and their encouragement to me in pursuing my degree.

My gratitude also goes to my other colleagues and all friends, Catalina Pino Munoz, Ridwanur Chowdhury, Yuhua Xia… For all the stimulating discussion, and for the fun we have had in my PhD studies.

At last, special thanks to my girlfriend and my parents. Thank you for your whole-heartedly support at the most difficult time of my PhD period. Thank you for all of your comfort and blessing. Without your love there's no way that I can finished it.